RADIOLOGICAL MAPPING BY IN-SITU GAMMA RAY SPECTROMETRY IN KATHMANDU AND MAKAWANPUR DISTRICT

A THESIS SUBMITTED TO THE

CENTRAL DEPARTMENT OF PHYSICS

INSTITUTE OF SCIENCE AND TECHNOLOGY

TRIBHUVAN UNIVERSITY

NEPAL

FOR THE AWARD OF

DOCTOR OF PHILOSOPHY

IN PHYSICS

By

ANITA MISHRA

March 2023

RADIOLOGICAL MAPPING BY IN-SITU GAMMA RAY SPECTROMETRY IN KATHMANDU AND MAKAWANPUR DISTRICT

A THESIS SUBMITTED TO THE

CENTRAL DEPARTMENT OF PHYSICS

INSTITUTE OF SCIENCE AND TECHNOLOGY

TRIBHUVAN UNIVERSITY

NEPAL

FOR THE AWARD OF

DOCTOR OF PHILOSOPHY

IN PHYSICS

By

ANITA MISHRA

March 2023

DECLARATION

Thesis entitled **"Radiological Mapping by In-situ Gamma Ray Spectrometry in Kathmandu and Makawanpur District"** being submitted to the Central Department of Physics, Institute of Science and Technology (IoST), Tribhuvan University, Nepal for the award of the degree of Doctor of Philosophy (Ph.D.); is a research work carried out by me under the supervision of Prof. Raju Khanal, Central Department of Physics, Tribhuvan University, Kirtipur, Kathmandu, Nepal.

This research work is original and has not been submitted earlier in part or full in this or any other form to any university or institute, here or elsewhere, for the award of any degree.

Anita Mishra

RECOMMENDATION

This is to recommend that **Ms. Anita Mishra** has carried out research entitled **"Radiological Mapping by In-situ Gamma Ray Spectrometry in Kathmandu and Makawanpur District"** for the award of Doctor of Philosophy (Ph.D.) in **Physics** under my supervision. To my knowledge, this work has not been submitted for any other degree.

She has fulfilled all the requirements laid down by the Institute of Science and Technology (IoST), Tribhuvan University, Kirtipur for the submission of the thesis for the award of Ph.D. degree.

.....

Dr. Raju Khanal
Supervisor
(Professor)
Central Department of Physics,
Tribhuvan University, Kirtipur,
Kathmandu, Nepal

June 2022

LETTER OF APPROVAL

Date:2022/09/23

On the recommendation of **Prof. Raju Khanal**, this Ph.D. thesis submitted by **Ms. Anita Mishra**, entitled **"Radiological Mapping by In-situ Gamma Ray Spectrometry in Kathmandu and Makawanpur District"** is forwarded by Central Department of Research Committee (CDRC) to the Dean, Institute of Science and Technology (IoST), Tribhuvan University.

.....

Dr. Om Prakash Niraula
(Professor)
Head,
Central Department of Physics,
Tribhuvan University, Kirtipur,
Kathmandu, Nepal

ACKNOWLEDGMENTS

I would like to express the deepest gratitude to my supervisor Prof. Raju Khanal for his valuable guidance, continuous encouragement and precious support throughout the research work. His constant surveillance, valuable motivations, insights and suggestions throughout the period have played the vital role for the completion of this research work.

I would like to express my sincere thanks to Prof. Dr. Om Prakash Niraula, Head of Central Department of Physics, Tribhuvan University, Kirtipur, Kathmandu, Nepal. I am also thankful to all faculty members and staffs. Also, I would like to acknowledge with much appreciation to Prof. Dr. Binil Aryal and Prof. Dr. Narayan Prasad Adhikari for their worthy suggestions during viva of biannual progress report.

I also express my sincere thanks to Dr. Iain Darby (IAEA) and Mr. Yii Mei Wo (Malaysian Nuclear Agency) for their guidance during the visit.

I express my warm appreciation to Dr. Suresh Basnet and to Nuclear and Plasma Lab Group members in the Department: Mr. Anish Maskey, Mr. Atit Deuja, Mr. Bal Vikram Khatri , Mr. Devendra Raj Upadhyay, Mr. Num Prasad Acharya, Mr. Ram Sharan Karki and Mr. Roshan Chalise. I express my thanks to all colleagues and friends.

It would not have possible without the kind support and help of many individuals. I am very much thankful to Mr. Krishna Prasad Rimal, Mr. Prakash Baniya, Mr. Ram Kumar Bhattarai, Mr. Suresh Majhi and Mr. Avishkar Karki for their effortful support during the data collections.

I would like to acknowledge the support from IAEA (through TC project NEP0002) and Ministry of Education, Science and Technology, Government of Nepal (for coordination with IAEA). I also acknowledge Malaysian Nuclear Agency (for the PGEC course organised by IAEA) and Department of Mines and Geology, Nepal (for providing geological map). I would also like to acknowledge University Grants Commission (UGC), Nepal for PhD fellowship, award number PhD74/75-S&T-15.

Finally, I would like to express my hearty thanks to my parents, in-laws and family who always encouraged and supported me. Special vote of thanks goes to my husband Er. Laxameshwar Mishra for his kind supports and inspirational words throughout the period which made it possible to complete this research work. I would like to thank all my well wishers.

Anita Mishra
June 2022

ABSTRACT

The ionizing radiation has health effect and hence the estimation of exposures from various sources of radiation is important. In this work, radiological mapping of various regions of Kathmandu and Makawanpur district was performed using in-situ gamma ray spectrometry. The exposure was estimated from gamma radionuclides concentrations and also the radiological risk factors to human health were estimated. The radiological maps of the region between Kathmandu and Makawanpur along the road via Kulekhani and adjoining areas were prepared using PGIS 2 spectrometer from Pico Envirotec Inc., a NaI(Tl) detector equipped with GPS. The study area has a complex geological and topographical formation and contains more than nineteen types of rocks and has many upward and downward slopes. In addition to geological variation and topography of the area, anthropogenic activities like land cultivation, road construction and disasters (soil erosion), the exact description of radiogenic and radiological characteristics of the area is challenging.

The measured outdoor absorbed gamma dose rates were overlaid on georeferenced "geological map and topographical map" to capture spatial variability of the measured data with geology and landscape. The dose rate of Kathmandu and Makawanpur varies from 45 to 206 nGy/h with an average of 119$\pm$23 nGy/h which is higher than the world average (59 nGy/h). The mass concentration of ^{40}K varies from 0.1 to 8% with an average of 3$\pm$1%. The mass concentration of ^{238}U and ^{232}Th varies from 0.05 to 28 ppm with an average of 6$\pm$3 ppm and 0.1 to 57 ppm with an average of 18$\pm$7 ppm respectively. The concentration of ^{40}K, ^{238}U and ^{232}Th are found higher than the world average (1.3%, 2.7 ppm and 11.1 ppm respectively). The activity ratios (Th/U, Th/K and U/K) of studied area are found (0.99, 0.09 and 0.09) in good agreement with environmental samples which indicates no relocation of rocks and soils. The results of exposures inferred from the soil concentration show reasonable agreement with the measured outdoor dose rate in air. The homogeneous distribution and low surface activity of ^{137}Cs indicates no contamination in the environment and the trace present is attributed to global fallout from weapon testings and nuclear accidents. The dose rates in the studied area showed strong and positive correlation with the concentrations of gamma radionuclides which indicates that high dose rates are due to elevated radionuclides concentrations. In addition, principal component analysis and ternary plots were used to study the variability of measured data in the studied area. The spatial variability of the data in the Kathmandu and Makawanpur district is mainly due to underlying geology and geochemical process in the terrestrial environment. The finding of the study are

useful to establish baseline data for radioactivity levels and exposure.

The associated risk factors, outdoor annual effective dose and excess lifetime cancer risk are found higher than the world average 0.07 mSv and 0.29 $\times 10^{-3}$ respectively. The annual effective dose was found nearly twice of the world average but was lower than recommended dose limit for public ($<$ 1 mSv). External radiation hazard was calculated to be $<$ 1 which indicates no significant radiological hazard in the area.

The depth profile of gamma radionuclides concentrations in soil were also studied for understanding migration and distribution of radionuclides as they are important for environmental studies. The activity ratios in the depth profile of natural gamma radionuclides in soil were found approximately constant indicating same geochemical origin of the radionuclides. The vertical distribution of ^{137}Cs for all soil profiles were found unnatural and homogeneous due to disturbed soil. The scattering of gamma radiation in air was measured and also calculated using computer program NIST XCOM. The gamma ray intensity was found decreasing with the increase in thickness of air and energy of gamma ray. No significant attenuation was noticed up to 100 cm.

The obtained results of the present work can be used as a baseline data for gamma radionuclides concentrations and exposures in Kathmandu and Makawanpur district. The findings can be used as a base map to assess any changes in background radiation levels due to weathering, geological and anthropogenic activities. The study is mainly conducted along the road and in some selected adjoining area and water resources due to time and technical constraint. More comprehensive study is recommended for broad information in the area. All villages between Kathmandu and Makawanpur district should be studied. The indoor gamma survey and gamma ray spectrometric study for ground water is also recommended to assess more information about exposure. Moreover, the study related to simulation and modelling of environmental gamma photon energy using Monte Carlo techniques or others are desirable.

LIST OF ACRONYMS AND ABBREVIATIONS

A	Activity
ADC	Analog to Digital Converter
AED	Annual Effective Dose
AGRS	Advanced Gamma Ray Spectrometer
ASL	Above Sea Level
BDL	Below Detection Limit
B-H	Bhimphedi to Hetauda
Br	Basic rocks
Ca	Chandragiri formation
Ch	Chitlang formation
CS	Compton scattering
D	Absorbed dose
DD	Digital Derivative
D-K	Dakshinkali to Kulekhani (via Sisneri)
Du	Dunga quartzites
E	Effective dose
EDA	Exploratory Data Analysis
ELCR	Excess Lifetime Cancer Risk
fm	femto meter
GIS	Geographic Information System
Gl	Galyang Formation
GPS	Global Positioning System
Gr	Granites
Gy	Gray
H	Dose equivalent
HBRA	High Background Radiation Area
H_{ex}	External hazard index
H_T	Equivalent dose
IAEA	International Atomic Energy Agency
ICRP	International Commission on Radiological Protection
K-B	Kulekhani to Bhimphedi
K-L	Kathmandu to Lamagaun (Pharping)
L-K	Lamagaun to Kulekhani
Ls	Lower Siwalik
LSQ	Least Square Fitting

MCA	Multi Channel Analyser
Mk	Maksang formation
Mr	Markhu formation
MS1	Lower middle Siwalik
MS2	Upper middle Siwalik
NaI(Tl)	Thallium activated sodium iodide
NCRP	National Council on Radiation Protection and Measurement
NG	Nepal Government
Pa	Pandrang Quartzite
PCA	Principal Component Analysis
PE	Photoelectric absorption
PEI	Pico Envirotec Inc.
PGIS	Portable Gamma Spectrometer Information System
PMT	Photo Multiplier Tube
PP	Pair Production
ppm	Part per million
Q	Quaternary
QC	Quality Control
SD	Standard Deviation
Sk	Sarung Khola formation
So	Sopyang formation
Sp	Shiprin Khola formation
Sv	Sievert
Ta	Tawa Khola formation
Ti	Tistung formation
Ud	Udaipur formation
UNSCEAR	United Nations Scientific Committee on the Effects of Atomic Radiation

LIST OF SYMBOLS

α	Alpha particle
Z	Atomic number
μ	Attenuation coefficient
N_{A}	Avogadro's number
β	Beta particle
^{137}Cs	Cesium-137
λ	Decay constant
m_{e}	Electron mass
eTh	Equivalent thorium
eU	Equivalent uranium
Φ	Flux (Fluence rate)
γ	Gamma ray
$t_{1/2}$	Half life
A	Mass number
%	Percent
dI	Photo peak intensity
^{40}K	Potassium-40
m_{p}	Proton mass
^{232}Th	Thorium-232
^{238}U	Uranium-238

LIST OF TABLES

Page No.

LIST OF FIGURES

TABLE OF CONTENTS

CHAPTER 1

INTRODUCTION

1.1 Environmental Radiation and Gamma Spectrometry

Human beings are always exposed to natural ionizing radiation present in environment (UNSCEAR, 2000). The flux of energy and elementary particles forms the radiation environment. The sources of exposure from natural sources are cosmic rays, terrestrial radiation and internal radiation. In addition to the natural exposure, human activities (using radioactive substances or sources) also cause radiation exposure. The source of exposure from artificial sources are artificially generated radionuclides, reactors, instruments emitting radiation and natural radioactive materials concentrated or relocated by human activity. The radioactive residue from nuclear weapons testing is also a global source of radiation exposure. Radiation exposure can damage cells and has potential to cause hereditary effects in the offspring and even can cause death and cancer in some of them. Since, the ionizing radiation has health effect, the estimation of exposures from various sources of radiation is important. The gamma rays measurement are conducted as it is the most penetrating ionizing radiation from natural and artificial sources. Both manmade and natural sources of radiation are studied by their capacity to cause ionization in matter (IAEA, 2003).

The gamma ray spectrometry is "Radiometric method based on the proportionality between energy and gamma quanta deposited in the detector and pulse amplitudes at the output of the detector, that enables the qualitative and quantitative analyses of gamma ray emitting sources" (IAEA, 2003). Thus, the method is an important tool for mapping and monitoring radiation present in environment. As the measured gamma fluence rates are affected by source intensity, source-detector geometry and other environmental factors like rainfall, soil moisture, vegetation and airborne sources of radiation, the method requires to consider these factors. The method is also challenging due to low radiation field intensities and complexity in the radionuclides (primordial, cosmogenic, anthropogenic) composition (NCRP, 1976).

The background radiation (from cosmic rays, terrestrial radiation, shielding materials and detector) and instrumental noise also reduces the signal of photon to noise ratio due to which the accuracy of determining radionuclides concentrations in environment

is lowered by this method (Gilmore, 2008). The interference of spectra by coincident summing and pile up effects, Compton scatter and efficiency limitations due to geometry also complicates the measurement. The analysis and interpretation of spectra is time consuming also due to complexities in spectra decomposition. The scintillation detectors NaI(Tl) have high detection efficiency but the Compton continuum and the coincidence photo-peaks present due to their low resolution produces interference in the case of photons with low energy (< 500 keV) detection. The HPGe detectors have high resolution especially at low energies. But these detectors have lower detection efficiency than NaI(Tl) detectors and have high background and Compton scatter interference (Debertin & Helmer, 1988).

In-situ gamma ray spectrometric method is a spatial representative method, and hence represent a large volume source compared to ex-situ (laboratory method). Also, in-situ method is less time consuming than ex-situ analysis. Moreover, high spatial resolution enables in detail and precise assessment of environmental radioactivity and its geospatial mapping (Beamish, 2016; IAEA, 2003).

1.2 Geology of Kathmandu and Makawanpur

Geologically, the Kathmandu and Makawanpur districts consists lesser Himalayan crystallines, lesser Himalayan sediments and Siwalik belt (Figure 1). They comprises a Kathmandu complex and Nawakot complex. The marble, granite and quartzite are found in the area. In the context of the study sites, the area comprises mostly a Kathmandu complex (Figure 2). The Kathmandu complex consists of high grade metasediments (Bhimphedi group) along with weakly metamorphosed and unmetamorphic sediments. The sites contains a coarsely crystal line, strongly garnetiferous two-mica schist, Amphibole and pyroxene minerals (Bhimphedi group), and Chlorite Schist rock towards the base of Mahabharat Thrust along with coarsely crystalline, well-bedded to massive marbles containing mica. It also consists green-gray biotite quartzite, ortho quartzite (Chisapani) and micaceous quartzite (Kulekhani). The schists, quartzites and marbles are found in variable proportion. Sand stone and lime stone also is the part of the sites. The Kathmandu complex also contains gneisses and granite (Stöcklin, 1980). Minerals like copper, zinc, tin, silver, dolomite and limestones are found in the area (NG, 2017).

The predominant rocks in the studied area are granite schist, marble, phyllite, amphibolite, graphite slate. Except for marble and amphibolite, the dose rates were found higher than 90 nGy/h which is higher than the world average value of 59 nGy/h (UNSCEAR, 2000). The maximum absorbed dose rate 228 nGy/h was contributed from granite schist. UNSCEAR summarized the country with the value of absorbed dose rate greater than 80 nGy/h as "countries with the highest values". Thus, the area was classified as delivering high dose rates (Wallova et al., 2010).

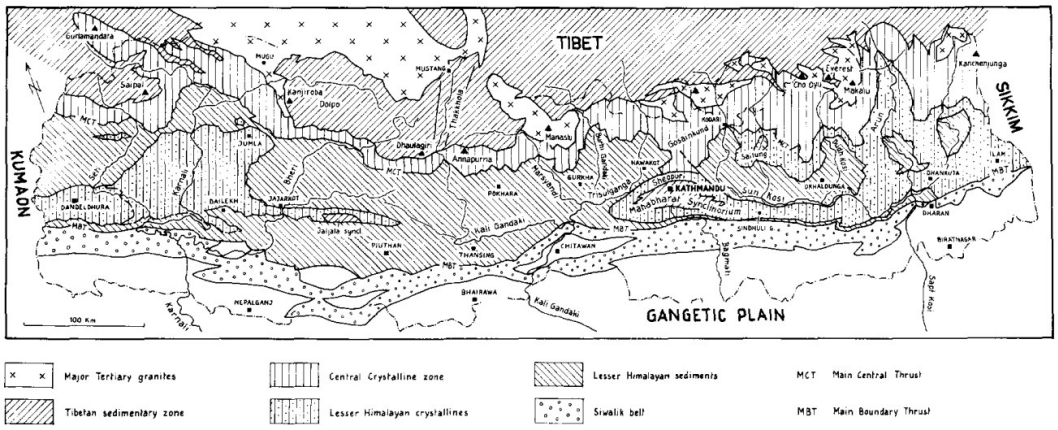

Figure 1: Geological zonation of Nepal (Stöcklin, 1980)

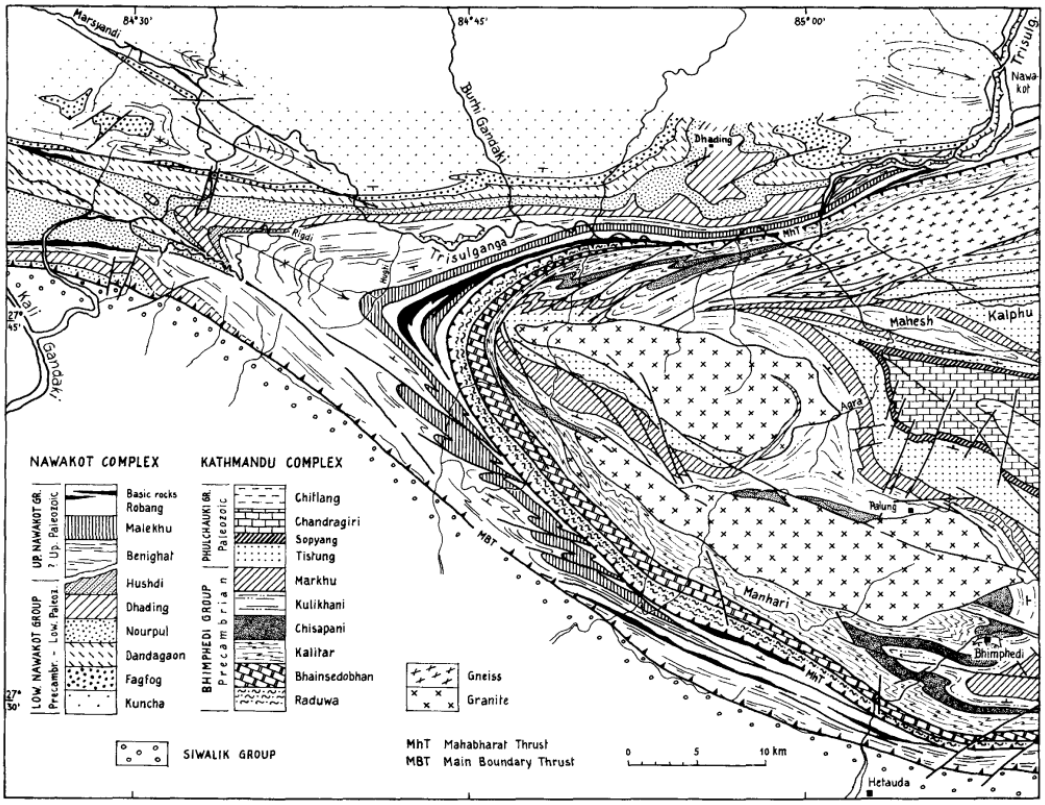

Figure 2: Mahabharat synclinorium in central Nepal (Stöcklin, 1980)

More research is required in the Kathmandu and Makawanpur and its surroundings to assess the radiation level in the environment and to estimate the health hazards associated with NORM (naturally occurring radioactive materials). Moreover, land cultivation, settlements in the area, soil erosion and factory establishment in the area for which risk of radiation exposure needs to be measured.

In this work, the Kathmandu and Makawanpur districts along the road via Kulekhani and the adjoining environments were studied. The longitude and latitude of the study

area varies from 85.023155° to 85.298637° and 27.414093° to 27.684404° respectively. The altitude of the area varies from 395 m to 1879 m ASL. It is hilly area with thick vegetation, rivers and lakes.

1.3 Research Hypothesis

The significant amount of uranium found in rocks, soil and water in the villages of Makawanpur and elevated background radiation in the surrounding area of Hetauda is radiation anomaly (Khabar, 2014) which is regulated and retained by the geological, geographical (altitude variation, hills and valley) and topographical structure as well as human activities (land cultivation, road construction, erosion, hand dug wells). This radiation characteristics of field is feasible for radiological mapping by describing geospatially and to indicate quantitatively.

1.4 Statement of the Research Problem

Though Nepal is a small country, it has geographical diversity. Moreover when we look from south to north, variation in geography and geology is found even for a small distance. As Makawanpur to Kathmandu elongates from south to north, there is significant altitude variation and many upward and downward slopes. So, radiological mapping of Kathmandu and Makawanpur district is necessary to establish baseline data for radioactivity levels to measure and evaluate ionizing radiation and associated radionuclides in the environment. In addition, it is applicable for preparing base for environmental monitoring and exploring mines.

In-situ gamma ray spectrometry offers low cost compare to ex-situ. It can covers large area (spatially representative method) and is useful method for assessment of radioactivity level and exposure in uneven and rocky terrestrial environment. It is also convenient for monitoring contaminated area.

1.5 Objective

General Objective

The aim of this work is mapping of radioelements and assess radioactivity level, radiation exposure and associated radiological hazards in the Kathmandu and Makawanpur district using in-situ gamma ray spectrometry.

Specific Objectives

1. To prepare a radiological map in the region between Kathmandu and Makawanpur along the road via Kulekhani by using NaI(Tl) detector equipped with Global Positioning System and Geographic Information System software.

2. To locate the region of unusual high or low activity by determining activity concentrations of ^{238}U, ^{232}Th and ^{40}K and assess associated radiological risk factors in the study area.
3. To study the presence of radioactive materials in the rock, soil and water in the region of high activity and to seek for the causes of increased activity and possibility of radioactive deposit in those areas.
4. To estimate the concentration of radioactive nuclides in the soil for different burial depth (Radionuclide depth profile).
5. To measure the relative intensity of the gamma (unscattered) to that scattered radiation for different depth.

1.6 Research Justification and Significance

Although high amount of uranium radionuclides and elevated background radiation have been reported in and around Kathmandu and Makawanpur, systematic and detail investigation have not been carried out so far in the area to ascertain and resolve the spatial distribution and variation of higher radiation exposure and radioactivity levels in terms of topography, geology etc.

In addition to geological variation and topography of the area, anthropogenic activities like land cultivation, road construction and disasters (soil erosion), the exact description of radiogenic and radiological characteristics of the area is challenging. The present study was under taken to assess the levels and distribution patterns of gamma radiation and associated radionuclides and to understand their occurrence for the establishment of base line level of natural and global fallout radionuclides in the area using in-situ gamma ray spectrometry.

CHAPTER 2

LITERATURE REVIEW

2.1 Exposure from Background Radiation

Living organisms are continuously exposed to natural ionizing radiation. Background radiation contributes more than 80% of ionizing radiation exposure. The cosmic rays from outer space and sun surface, radionuclides that exists in the Earth's crust, air, water, food, building materials and in human body are the sources of natural exposure. Some of the exposures are uniform everywhere for all persons whereas some exposures vary with location. The world average value of annual effective dose (AED) from natural exposure varies from 1-10 mSv with an average of 2.4 mSv (UNSCEAR, 2000).

External irradiation is an important component of human exposure. It can be from natural radionuclides present in environment or anthropogenic radionuclides released from human practices. External exposure from natural background radiation is more significant for most people compared to exposure caused by artificial sources (UNSCEAR, 2000). Cosmic rays, cosmogenic radionuclides and terrestrial radiation are the contributors of natural radiation. Cosmic ray intensity increases with altitude and slightly with latitude. Cosmogenic radionuclides produced in the atmosphere has no significant contribution to radiation dose. Terrestrial gamma radiation comes from the primordial radionuclides in rocks and soils. ^{40}K, ^{238}U and ^{232}Th are the principal primordial radionuclides in terms of dose as their half-life is comparable to the age of the Earth (IAEA, 2003).

Human exposure to naturally occurring radioactive materials (NORM) in the environment derives primarily from these primordial radionuclides and their decay series, radon in air and water. More than 80% exposure (external and internal) from natural source is from primordial radionuclides, contributing AED of 2 mSv (IAEA, 2003).

2.2 NORM Distribution

The radioactivity levels of terrestrial radiation depends on the types and distribution of rocks and soil and the process of concentration and immobilization. Ideally, the composition of radioactive material should correspond to the original parent rock but

usually this doesn't happen due to erosion and weathering. These geochemical process enhances and redistribute the radioactive material which causes disequilibrium in the decay of uranium series (Navas et al., 2011). Soil pedogenesis, lithological changes and mineralization can also vary the distribution of NORM (Dickson & Scott, 1997). The national regulatory authorities normally implements the ICRP recommended dose limits for control of ionizing radiation exposure to human (ICRP, 2007).

2.3 Dose Rates and Radioactivity Concentrations

The worldwide value of measured absorbed dose rate in air varies from 18 to 93 nGy/h with a typical range of variability from 10 to 200 nGy/h. The average worldwide value of the outdoor absorbed dose rate in air is 59 nGy/h. All the country with the absorbed dose rate less than 40 nGy/h are kept in lowest dose rate area while greater than 80 nGy/h are categorized as highest value area. Cyprus, Egypt, Netherland, Iceland, Brunei and UK have lesser value and Portugal, Malaysia and Australia have greater value of dose rate.

The worldwide average concentration of ^{40}K, ^{232}Th and ^{238}U in soil are 420, 45 and 33 Bq/kg respectively. The average dose rate calculated from these concentrations are 60 nGy/h. The absorbed dose rate in outdoor air calculated from terrestrial gamma radiation (soil concentration) agree with the measured dose rate worldwide except some countries. Luxembourg and Sweden showed more than 30% discrepancies as the level of ^{40}K in soil are higher, Syria and Albania had low levels of radionuclides in soil and Ireland had low measured dose rate. The average outdoor annual effective dose is 0.07 mSv (UNSCEAR, 2000) . However, in some areas high dose are measured due to elevated level of NORM and the areas are known as HBRA (high background radiation areas) (Eisenbud & Gesell, 1997).

Norm levels investigation and measurement of dose rates in the area is thus necessary for establishing the NORM baseline values and to assess associated health risk. In addition, anthropogenic activities like use of stone and bricks as building material, production and use of phosphate fertilizers, uranium and thorium mining, quarrying and energy production from coal and geothermal etc. could lead to NORM levels enhancement and consequently in the environmental exposure (Landa, 2007; Okeji et al., 2012). In such case, it is known as technologically enhanced naturally occurring radioactive materials (TENORM).

O' Brien and Cooper had presented the exposure and TENORM transfer pathways in the environment with associated impacts to ionizing radiation on humans (O'Brien & Cooper, 1998). An informative view of a volume of NORM's waste generated from technological process, regulatory implications, recommendations for disposal of NORM waste and remediation of contaminated sites are explained in many studies (Paschoa,

1998; van Velzen, 2015).

2.4 Anthropogenic Radionuclides in Environment

The radioactive particles (or gases) released in trace quantities in accident were carried in every direction by the wind. Later, they get deposited by precipitation. The time periods that the particles remains airborne depend on height of injection into atmosphere, time and latitude. Radionuclides released to the atmosphere either decay during the transit or are deposited by wet and dry deposition on the Earth's surface within short periods. The isotopes of cesium radionuclides deposited on ground can cause long term exposure as they have longer half-lives (UNSCEAR, 2000).

2.5 Fluctuation in Background Radiation

"In addition to variations from place to place, the ambient background gamma dose rate in air at any specific location is not constant in time". A considerable fluctuation is observed due to soil moisture, snow cover and removal of radon progeny in air by rainfall. In 30 minutes intervals measurement of continuous monitoring recorded $\pm$ 5% variations from daily average level (Klemic, 1996; Smetsers & Blaauboer, 1997). The elevation depends on amount of rainfall and rain interval (Fujitaka et al., 1992). The elevated level remains for several hours and then the decrement is followed by 5% from the average level due to increased soil moisture (shielding). It takes hours or days to return to normal level (soil saturation disappear) after the rainfall. Background levels decreases by 1% for each centimeter of snow cover (Fujimoto, 1986; Hatakka et al., 1998).

2.6 High Background Radiation Area

There are some areas in the world where markedly high dose rates in air are measured. These high dose rates are due to thorium and uranium bearing minerals in soil. The elevated exposure levels in the areas of high natural background is due to various causes. Guarapari in Brazil, Kerala and Madras states in India, Yangiang in China and Nile delta in Egypt have high background radiation due to high levels of thorium in monazite sand deposits. Mineas Gerais in Brazil, Niue Island in the pacific, and some parts of Italy have high radiation level due to volcanic soils. The granitic and schistic rocks and sands of central massive in France and the uranium minerals in soil in the southwest of that country are the cause of high radiation level in that area. The high background radiation level in Ramsar and Mahallat in Iran are due to enhanced ^{226}Ra concentrations in water flowing around from hot springs (UNSCEAR, 2000). As beach sands and deposits are replenished by tides and springs, the exposure can vary in high background areas.

The urbanization and construction of road in these area have moderately decreased the background levels (Sohrabi, 2000; Veiga et al., 1999). The Mrima-Kiruku complex in Kenya was reported as a geogenic high background radiation anomaly (Kaniu, 2017).

2.7 Gamma Ray Spectrometry

The knowledge of the geochemistry of the radioelements in soils and rocks, and the process which causes the change in their distribution and mobility is needed to use the method of gamma ray spectrometry as mapping. The method is widely used in surveying soil, regolith studies, mineral exploration and geological mapping. Geochemical and mineralogical studies of rocks and soils has a fundamental role in supporting gamma ray spectrometry survey interpretation as they explain the way of radioelements existence and their petrogenetic and pedogenetic associations. The gamma radiation mapping depends on integrated approach as the data are interpreted in combination with satellite images, geological maps and others. GIS (Geographical Information System) is the best for integration approach as they provide processing of image and enhances the functionality with the overlay of dynamic map and cartography. The gamma rays of natural sources of radiation within the energy range which are used for mapping can penetrate some meters of air but is totally attenuated by about 50 cm of rocks and soils. Due to which gamma ray spectrometric method is implied for measuring natural sources of terrestrial radiation. As the gamma ray spectrometric method is surface mapping method, the knowledge of surface process is required for data interpretation. The gamma rays from the Earth's crusts mostly comes from upper 30 cm and the fluence rates are affected by the environment (vegetation and soil moisture) (IAEA, 2003).

It is difficult to interpret gamma ray method data in terms of lithology as classification schemes of rock do not accommodate radioelement content except some granites. Therefore, interpretation must be made on correlation with recognized geology and ground truthing to develop framework of lithology. Homogeneous unit mapped on geological map exhibits dividing in the radiometric data for igneous units.

Gamma ray spectrometry method is most useful for regolith and soil mapping when interpreted in conjunction with topography, satellite imagery and aerial photography (Wilford, 1992; Wilford, 1996; Bierwirth, 1996; Cook et al., 1996; Wilford et al., 1997). The gamma ray spectrometric response of soils and rocks varied with the climate of the area surveyed because the response due to weathered rocks, fresh bedrock and transported materials differs. The concentrations and distributions of the radioelement is modified by weathering (Dickson & Scott, 1997). Information on geomorphic process and soil and regolith properties is provided by gamma ray method (Wilford et al., 1997). High quality geochemical databases is considered as an important part of environmental knowledge. The study of the global inventory of geochemical data explained the

radioelement mapping significance (Darnley et al., 1995). Gamma ray spectrometric data have helped in detailed lithological mapping. The lithological units identified with radioelement signatures (volcanic origin) can be used as lithological markers in complex areas in explaining the pattern of the geological map (Jaques et al., 1997). The average content of ^{40}K and ^{232}Th in soils reflect the average ^{40}K and ^{232}Th content of their original rocks. But, the difference in concentrations of soil radioelement were found relatively small. This is not the case with ^{238}U (Dickson & Scott, 1997). For geological mapping, a general strategy is to outline the major lithological unit first and then enhance patterns of the radioelement.

The mapping of activity of the manmade sources in the location is necessary as these sources contribute to the radiation dose to the population. Though there is strict control and regulation on the installation and use of the radiation sources in research, industry, power plant, military and in health services accidents do happen. Reactor accidents at wind scale, UK (1958) and Chernobyl, USSR (1986), Daichhi, Japan (2011), the loss of isotopes sources in Mexico (1985) and Brazil (1917) and reentry of nuclear power satellite in Canada (1978) had significant contribution to terrestrial gamma radiation. Ground gamma ray methods are used for the mapping of area contaminated by fallout and for the location of lost sources. Human activity like mining (Uranium and Thorium) concentrate and redistribute the radio elements. Phosphate and Potassium fertilizer in cultivated land also redistribute radioactive materials (IAEA, 2003).

2.8 In-situ Gamma Ray Spectrometry

In-situ gamma ray spectrometry method is more applicable for environmental radioactivity monitoring as it is representative of large area and integrated the source inhomogeneities and gives instantaneous results and analysis. Therefore, the method is considered spatially representative, less costly, more sensitive and rapid compared to ex-situ method. This is because the collection of samples from environment and preparing them as test sample for ex-situ analysis takes more time and money (Beck et al., 1972). But, as the samples for ex-situ analysis are prepared and measured in controlled environment and geometries, these measurements are considered more reliable compared to in-situ method (Rostron et al., 2014). Because of short counting times and field conditions, analytical uncertainties for in-situ method are 50% (approximately) higher than ex-situ measurement. Sampling and counting statistics are mostly the cause of uncertainties for ex-situ analysis (Tsujimoto, 1988).

For in-situ gamma ray spectrometric method, the accurate interpretation depends on detector's proper calibration, radiation flux that strikes the detector, calculation and knowledge of radioactivity distribution in the sites (Laedermann et al., 1998). The several factors like disequilibrium in ^{238}U decay series, inability to meet standard geometry

conditions, soil moisture and vegetation, instrument stability in rugged environment and contribution of atmospheric ^{222}Rn also influenced the accuracy of the method (Hendriks et al., 2001; Klusoň & Thinova, 2011).

In-situ gamma ray spectrometry's conventional application relies upon the deployment of measuring stations (static) similar to traditional sampling process (Beck et al., 1972; Tyler & Copplestone, 2007). The logistic deployment teams for radiation measurement still carried an overhead cost of the equipment and are also overhead from the personnel time connected to the length of measurements (30 to 60 min) per measurement point due to detectors efficiency. The arrival of mobile computing resources has enabled a detectors equipped with GPS available and deployable for radiometric surveys as an efficient continuous measurement system.

Airborne systems are expensive and provide limited spatial resolution but are effective for mapping large area (Beamish, 2016). Carborne systems are cheaper than airborne and are thus used for mapping contamination of road networks and areas (with off road access) (Bezuidenhout, 2015; Kobayashi et al., 2015), radioactive mineral prospecting (Grasty & Cox, 1997) and radioactive source search and recovery (Aage & Korsbech, 2003). Detailed radiometric mapping is provided by mobile backpack systems in area (with less access to vehicles) as it provides higher spatial resolution of up to few meters (Cresswell & Sanderson, 2009; Nilsson et al., 2014).

As gamma ray interpretation method depends on the survey area, data quality, scope and interpretation purpose, no any universal set of guidelines is defined to interpret the data of gamma ray spectrometry. In interpretation process, the first step is to emphasize the overall radioelement concentration varieties. The second step is to outline the spatially continuous radioelement anomalies and domains. Mean-differencing, regression analysis and principal component analysis are applied within each unit to identify anomalies and to enhance minute responses of gamma ray against the background. The final step is to integrate the geological information available and other related information into the interpretation of gamma ray (IAEA, 2003).

The in-situ radiometric study have been reported recently in Southwestern Nigeria, Ogun state, Nigeria, Japan, Spain and Russia (Akingboye et al., 2021; Olagbaju et al., 2021; Ji et al., 2021; Corbacho & Baeza, 2022; Ramzaev et al., 2021) . The method of rapid in-situ gamma analysis was also studied using numerical integration and Monte Carlo simulation method (Wu et al., 2022).

2.9 Radiometric Study in Nepal

Several radiometric studies were performed in University as Master's thesis. In addition, some reports related to radiometric study were also prepared by the offices of Nepal Government. The many project works related to radiation were also carried out.

Though some work related to radiation have been carried out in Nepal, the systematic, comprehensive and published work is still lacking (Bhatt et al., 2012).

The uranium in rocks and background radiation in Central Siwalik of Nepal (Aryal, 1994) and the rapid determination of ^{40}K in sample of soil from Kathmandu valley using multichannel spectrometer (Shah, 1994) were studied. The radionuclides concentrations in sediments, water of rivers in Kathmandu and underground water were also studied along with the concentration of radon in soil and dwellings of Nepal. The concentrations of uranium in phosphate fertilizer and cement was also studied. The concentration of ^{40}K in the soil of northern Kathmandu valley was measured in the range of 17.48 to 412.26 Bq/Kg (Yadav et al., 2012). The annual effective dose rates in Kathmandu valley were estimated in the range of 0.39 to 0.66 mSv/y (Pantha et al., 2019).

The many preliminary study and investigations of radioactive materials in different parts of Nepal had been reported by Departments of Mines and Geology, Nepal (DMG) and Nepal Academy of Science and Technology (NAST). In addition, many study related to radiation exposure at different hospitals were carried out.

The status of radiation protection in hospitals of Nepal (Adhikari, 2012) and the study of radiation level at hospitals in Nepal and first data about radiation level & doses evaluation to medical staff at the catheterization laboratory at Katmandu, Nepal were also reported (Adhikari et al., 2009, 2013).

2.10 Utility of Exploratory Data Analysis

The radioactivity anomalies interpretation in area with respect to geology, time and space can be a challenging task. Since, the independent variables like geology, mineralogy and NORM are often correlated, multivariate techniques are required to study, untangle and interpret the underlying phenomena. The multivariate exploratory data analysis (EDA) techniques (regression and pattern recognition) may help to overcome these challenges via modelling and data mining due to their multivariate capabilities, versatility and robustness (Varmuza & Filzmoser, 2016). The performance of the techniques is superior to classical data analysis approach in the determination of complex environmental data-sets variability (Einax et al., 1997).

Principal component analysis (PCA), artificial neural networks (ANN) and hierarchical clustering analysis (HCA) have been applied in the spatial distribution investigation and radioactivity contamination origin in the area surrounding the power plants (Tsikritzis, 2005; Charro et al., 2013), classification of soil on the basis of geographical origin (Dragovic & Onjia, 2007), estimation of geogenic radon potential (Dragovic & Onjia, 2007), and determination of coastal sediments and beach sand provenance (De Meijer et al., 2001) etc.

In spite of cost effectiveness and usefulness, EDA techniques have barely been

utilized fully in the data mining and spatial modeling of dataset of in-situ radiological survey e.g. assessment of distribution of NORM and TENORM in terrestrial complex environments. The EDA techniques are more robust compared to conventional geo-statistical modelling techniques (variography) in modelling non-stationery and non-linear spatial trends (Kanevski et al., 2004). Fuzzy logic techniques for environmental applications can be used in the decision support systems development (Astel, 2007).

CHAPTER 3

MATERIALS AND METHODS

3.1 Radioactivity

Atoms are smallest unit of an element that retains its chemical properties. It consists of a central nucleus surrounded by electrons. The electrons are negatively charged and the nucleus are positively charged consisting uncharged neutrons and positively charged protons. The diameter of a nucleus and an atom is of the order of 10^{-15} m (1 fm) and 10^{-10} m respectively. Nuclear size ranges from about 1 to 7 fm for a single nucleon and heaviest nuclei respectively. Nuclear lengths is in the order of 10^{-15} m (1 fm), colloquially know as 1 fermi. Since, the electron mass is negligible compared with the proton mass ($m_p \approx 2000\ m_e$), it is usually ignored (Krane, 1988). The sum of the nucleons (neutrons and protons) in nucleus is the mass number and the number of protons present in nucleus is the atomic number (proton number). The mass number and atomic number is denoted by A and Z respectively. Isotopes are the atoms of an element having same proton number but different number of neutrons. They have same chemical properties but different physical (radioactive) properties.

Some isotopes have an unstable nuclei due to their surplus of energy. These unstable nuclei transforms to more stable nuclei of different isotopes by emitting particles. These nuclides are called radionuclides and the process is known as nuclear (radioactive) decay or disintegration. The disintegration (of unstable nuclides) is accompanied by particles or energy emission known as nuclear radiation. The spontaneous change within the nucleus resulting in the emission of particles (α and β) or electromagnetic radiation (photon) is radioactive decay. The mass change (mass of final product is smaller than mass of the original one) drives the radioactive decay. The decay is exoergic nuclear reaction. The small mass change appear as an energy and is determined by Einstein's equation,

$$\Delta E = \Delta m \times c^2 \tag{3.1}$$

where ΔE is energy difference, c is speed of light and Δm is mass difference (Gilmore, 2008).

The main quantity used to measure the radiation decay is activity of a radioisotope source. It is defined as the rate of disintegration of nuclides and is given by fundamental law of radioactive decay.

$$A = \left.\frac{-dN}{dt}\right|_{\text{decay}} = \lambda N \tag{3.2}$$

where N is the number of radioactive nuclei and a proportionality constant (λ) is a radioactive decay constant (probability that a given nucleus will decay per unit time). The negative sign indicates that N is decreasing with time. Radioactive decay is independent of other physical conditions (IAEA, 2003). The reciprocal of decay constant is known as mean life time (T) = 1/(λ) (Gilmore, 2008).

The historical unit of activity is curie (Ci). 1 Ci = 3.7 $\times$ 10^{10} disintegration/ second. It is the best estimate of activity of 1 g of ^{226}Ra. The curie is gradually replaced by its S.I. equivalent becquerel (Bq). The general conference on Weights and Measures (GCPM) in 1975, declares becquerel as one disintegration per second as the standard unit of activity. 1 Bq = 2.703 $\times$ 10^{-11} Ci

The activity actually measures the disintegration rate of source, not the emission rate of radiation produced in decay. A radiation is often emitted in only a fraction of the decays, so a decay scheme of the particular isotope should be known to infer a radiation emission rate from its activity. The decay of radioisotopes produces daughter nuclei whose activity may also have contribution to the radiation from the source. The activity per unit mass of the sample of radioisotope is known as the specific activity.

$$\text{specific activity} = \frac{\text{activity}}{\text{mass}} \tag{3.3}$$

If a sample is pure (unmixed with other nuclear species) or "carrier free", its specific activity can be obtained from

$$\text{specific activity } = \frac{\text{activity}}{\text{mass}} = \frac{\lambda N}{\frac{NM}{N_A}} = \frac{\lambda N_A}{M} \tag{3.4}$$

where M is molecular weight of sample, N_A (= 6.02 $\times$ 10^{23} nuclei/mole) is the Avogadro's number. From equation 3.4, it is clear that high specific activity is obtained for radionuclides with large λ (i.e. small half life) (Knoll, 2010). The radiation energy is conventionally and traditionally measured in electron volt or eV. The SI unit of energy is the Joule. 1 eV = 1.602 $\times$ 10^{-19} J

The electron volt is more convenient unit for particulate radiation. The energy of photon (gamma ray or X ray) is related to the frequency of radiation,

$$E = h\nu \tag{3.5}$$

where h (6.626 $\times$ 10^{-34} Js) is Planck's constant and ν is the frequency (Knoll, 2010). Since, the number of atoms of radionuclide decreases with time, integrating equation (3.2) gives

$$N_t = N_0 e^{-\lambda t} \tag{3.6}$$

where N_t is the number of atoms at time t, N_0 is the number of atoms present at time $t = 0$. In practice, number of atoms is replaced by activity as activity is proportional to number of atoms (A_t=A_0 $e^{-\lambda t}$). The decay constant (λ) is related to the half-life ($t_{1/2}$) of the radionuclides by

$$t_{1/2} = \frac{0.693}{\lambda} \tag{3.7}$$

Half-life is defined as the average time required to lose half of activity for a given radionuclides. Radionuclides have its unique half-life (independent of its physical or chemical states). Half-lives of radionuclides can be as long as billions of years and as small as nanoseconds.

There are several types of radioactive decay. The types of decay of unstable nuclides determines the nature of the atom formed after decay. The most common decays involves the emission of particles alpha (α), beta (β) and high energy electromagnetic rays (γ-rays and X-rays). The neutron-proton ratio (N/Z) determines the nuclear stability. The unstable nucleus reach stability after several decay process. A large imbalance of the ratio causes radionuclides to undergo α-decay where as a slight imbalance causes β-decay. Many heavy nuclei (naturally occurring ($82<Z\leq92$) decay by α particle (^{4}He nucleus) emission. An α decay process is schematically written as

$${}^{A}_{Z}X \rightarrow {}^{A-4}_{Z-2}Y + {}^{4}_{2}\alpha \tag{3.8}$$

where X and Y represents parent and daughter nuclides respectively (Mlwilo, 2010).

Beta (β) particle decay takes place in nuclear transition modes when the atomic number Z of the nucleus increases or decreases by one and the mass number remains same. Unstable nuclei (rich in neutron or proton) decay by negative or positive β particle emission respectively. β^- (negatron, e^-) particle emission occurs in a neutron rich nuclides and during emission the charge on nucleus increases by one unit. During this transition, a neutron is converted into proton and anti-neutrino ($\bar{\nu}$). The transition is represented schematically as

$${}^{A}_{Z}X \rightarrow {}^{A}_{z+1}Y + \beta^- + \bar{\nu} \tag{3.9}$$

A β^+ particle or positron (e^+) emission (less frequent) occurs in proton-rich nuclides and

during transition, a proton is converted in to neutron, positron (β^+) and a neutrino (ν) . In β^+ emission, the nuclear charge decreases by one unit. Schematically, the transition is written as

$$ {}^{A}_{Z}X \rightarrow {}^{A}_{z-1}Y + \beta^+ + \nu \tag{3.10} $$

The anti-neutrinos and neutrinos have an extremely small interaction probability with matter and are not detectable for practical purposes. The recoil energy of recoil nucleus Y is very small (below the ionization threshold) which cannot be detected by conventional means. Thus, only beta particle itself produce a significant ionizing radiation in beta decay.

Electron capture occurs (as an alternative of β^+ decay for proton rich nuclides) when the nucleus absorbs the orbital electron of an atom. The electrons from the innermost orbit (K-shell) is usually captured in this process, and hence it is also known as K-capture (Lilley, 2013). The vacant electron position is replaced by the emission of characteristic electromagnetic radiation of low energy. The process is schematically written as (IAEA, 2003)

$$ {}^{A}_{Z}X + \mathrm{e}^- \rightarrow {}^{A}_{z-1}Y + \text{ photon (electron capture)} \tag{3.11} $$

The excited daughter nucleus are produced in both α and β decay mode. The excited daughter nucleus de excite to reach ground state instantaneously ($\approx 10^{-12}$ s) by the process of gamma emission or internal conversion.

Internal conversion occurs when excited parent nucleus (often preceded by beta decay of parent species) de excites by transferring energy to an orbital electron of the same atom. The process is schematically written as

$$ {}^{A}_{Z}X^* \rightarrow {}^{A}_{Z}X^+ + \mathrm{e}^- + E_{\mathrm{e}^-} \tag{3.12} $$

Usually, the excited nucleus de excites through the emission of gamma ray photon but for some case, gamma emission somewhat inhibited and internal conversion becomes significant. After, internal conversion, the energy of the electron is given by

$$ E_{\mathrm{e}^-} = E_{ex} - E_b \tag{3.13} $$

where E_{ex} is the nuclear excitation energy transferred to orbital electrons, E_b is binding energy of the electron in the original shell. Auger electrons are roughly the analogue of internal conversion electrons when the excitation energy does not originate in the nucleus but in the atom.

Alpha (α) and β^- particle emissions is followed by the emission of one or more

gamma (γ) rays (photons of electromagnetic radiation). Gamma emission occurs when the nucleus is left unstable after particle decay. When the daughter product is left in excited state, either it can fall directly to ground state or descends in steps to lower energy states through the emission of gamma radiation energy. The de excitation of the daughter nucleus is by the emission of the excitation energy in the form of gamma ray (photon). There is no change in Z, N or A. Gamma ray emission is not a decay but a de excitation of the nucleus. The process is schematically written as

$$ {}^{A}_{Z}X^{*} \rightarrow {}^{A}_{Z}X + \gamma + E_{\gamma} \tag{3.14} $$

The energy of a gamma ray energy E_{γ} is the difference in energy of nuclear states.

$$ E_{\gamma} = hv = E_1 - E_2 = {}^{A}_{Z}X^{*} - {}^{A}_{Z}X \tag{3.15} $$

where $h\nu$ is the energy of electromagnetic radiation and E_1 and E_2 are the energy levels. This method is preferred for identifying radioactive isotopes of energies within 100 keV to 10 MeV range (Gilmore, 2008).

Radioactive decay also occurs in a series (chain) with a number of radioactive daughter products and ends in a stable isotope. Starting with a specified amount of parent radionuclides and in a closed system, the activity and the number of atoms of daughter elements grows gradually until radioactive equilibrium of series is reached. At this stage, the activities of all the radionuclides are similar. Thus, the measurement of the concentration of daughter element can give the estimation of concentration of other element in decay series. Under equilibrium conditions (IAEA, 2003),

$$ \lambda_1 N_1 = \lambda_2 N_2 = \cdots \quad \lambda_N N_N \tag{3.16} $$

Decay chain is more complex when daughters and its progenies are also radioactive. When a daughter radionuclides decays from parent radionuclides, the difference between the rate of growth from the parent radionuclides and the rate of decay of the daughter radionuclides is equal to the rate of change of number of daughter atoms.

$$ \frac{dN_D}{dt} = \lambda_P N_P - \lambda_D N_D \tag{3.17} $$

$$ = \lambda_P N_{P0} e^{-\lambda P t} - \lambda_D N_D \left[\because N_P = N_0 e^{-\lambda t}\right] $$

where D and P are daughter and parent respectively. Solving, this linear differential equation gives

$$ N_D = N_{P0}\left[e^{-\lambda_P t} - e^{-\lambda_D t}\right]\frac{\lambda_P}{\lambda_D - \lambda_P} + N_{D0}e^{-\lambda_D t} \tag{3.18} $$

$\because A = \lambda N$, the above equation in terms of activity is

$$A_D = A_{P0}\left[e^{-\lambda_p t} - e^{-\lambda_D t}\right]\frac{\lambda_p}{\lambda_D - \lambda_P} + A_{D0}e^{-\lambda_D t} \tag{3.19}$$

If the parent and daughter are separated chemically, as ratio of parent to daughter half-lives varies, the second term of equation is zero

$$A_D = A_{P0}\left[e^{-\lambda_p t} - e^{-\lambda_D t}\right]\frac{\lambda_p}{\lambda_D - \lambda_p} \tag{3.20}$$

From above equation, the change in activities in pure parent form is obtained. There are three particular case for growth of activity from decay of a parent. It depends upon whether the half-life of parent is greater or less than the half-life of daughter (Gilmore, 2008).

If the half-life of parent is longer than daughter, then it is in transient equilibrium. In this equilibrium, the daughter nuclides is in constant ratio to that of parent radionuclides and decays apparently with the half-life of the parent. After about 10 half-lives of the daughter nuclides, transient equilibrium is established after which daughter decays with the parent half-life. The sum of daughter and parent activities is total activity.

If t in equation (3.20) is set greater than the half-life of the daughter, the relative numbers of daughter and parent atoms at equilibrium is

$$\frac{N_D}{N_P} = \frac{\lambda_P}{\lambda_D - \lambda_P}, \quad [\lambda_D > \lambda_P] \text{ in transient equilibrium} \tag{3.21}$$

The equilibrium activity of daughter relative to parent is

$$A_D = \frac{A_P \lambda_D}{\lambda_D - \lambda_P} \tag{3.22}$$

[This equilibrium states varies with time and activity of daughter product peaks before it starts to decay]

$$A_D = \frac{A_P t_{1/2}}{t_{1/2P} - t_{1/2D}} \tag{3.23}$$

If the half-life of the parent nuclides is very very longer than daughter, the equilibrium state is secular equilibrium. In this case, $t_{1/2D}$ becomes negligible and above equation becomes

$$A_D = A_p \quad [\text{ or } \lambda_D N_D = \lambda_p N_p] \tag{3.24}$$

i.e. the activity of daughter equals the activity of parent. In this case, each daughter activity will be equal to its parent and the total activity (Gilmore, 2008). The natural

decay series, uranium and thorium decay series are assumed in secular equilibrium. ^{238}U and ^{232}Th activity concentrations are estimated using radioactive decay and emissions from the daughter products of ^{238}U and ^{232}Th. However, in uranium decay series disequilibrium occurs due to escape of radon gas ^{222}Rn. The complete or partial addition and removal of members of series by dissolution or precipitation (e.g. leaching of ^{222}Rn and ^{230}Th) also causes disequilibrium in the series. The equilibrium is restored in days, weeks or millions of years depending on half-lives of the radioisotopes (IAEA, 2003).

Natural terrestrial radiation originates from long lived primordial radionuclides present in the Earth's crust since its formation. The half-lives of the radionuclides is very long (several billion years) and they survived since their creation and have not substantially decayed. These radionuclides are found in soil, water, air, plants and even in human bodies. The most abundant long lived primordial radionuclides are uranium (^{238}U and its daughters), thorium (^{232}Th and its daughters), potassium (^{40}K) and actinium (^{235}U and daughters). The soil, rocks, minerals (terrestrial materials) containing these radionuclides are known as naturally occurring radioactive materials (NORM) (Gilmore, 2008). ^{238}U and ^{232}Th are among the four naturally occurring radioactive heavy elements having 4n series. These series begins with the long lived and heavy parent nuclides which has half-life equal to the order of the age of the Earth (Podgorsak & Hendee, 2010). In each of these series, most of the transitions towards the stable nuclides are made by α-decays and few by β-decays. Thorium series is referred as 4n-series as the mass number in each decay series are multiple of 4. Neptunium has completely decayed and no longer occurs naturally.

Many natural elements have radioactive isotopes but only the uranium and thorium decay series and potassium radioisotopes are measured. Only these radioisotopes can produce gamma rays of sufficient intensity and energy to be measured by gamma ray spectrometry as they are relatively abundant in nature. Average crustal abundances are in the range 2-3 ppm U, 8-12 ppm Th and 2-2.5% K (IAEA, 2003). The radioactive isotope (^{40}K) of potassium occurs as 0.012% of natural potassium and decays to ^{40}Ar by emitting gamma rays. Since, the radioisotopes ^{40}K (half-life 1.3×10^9 years) occurs as a fixed proportion of natural K, these gamma rays are used to estimate the total amount of potassium present.

Uranium naturally occurs as ^{238}U ($t_{1/2}$ = 4.468 $\times$ 10^9 years) and ^{235}U ($t_{1/2}$ = 7.04 $\times$ 10^8 years) radioisotopes. The radioisotopes ^{238}U gives rise to decay series with 14 intermediates decay stages and terminate in the stable isotope, ^{206}Pb. ^{235}U radioisotopes decays to the stable isotope, ^{207}Pb. Thorium occurs naturally as ^{232}Th radioisotopes. ^{232}Th ($t_{1/2}$ = 1.405 $\times$ 10^{10} years) radioisotopes gives rise to the decays series with 10 intermediates decay stages and terminate in the stable isotope ^{208}Pb (Table 1).

Table 1: Decay series of NORM (Gilmore, 2008)

series	Type	Parent	First decay	Alpha particle	Half life (years)	Stable end products	*Measurable nuclides	Decay stages
Uranium	4n + 2	^{238}U	^{234}Th + α	8	4.468 $\times 10^9$	^{206}Pb	6	14
Actinium	4n + 3	^{235}U	^{231}Th + α	7	7.04$\times 10^8$	^{207}Pb	1	11
Thorium	4n	^{232}Th	^{228}Ra + α	6	1.405$\times 10^{10}$	^{208}Pb	4	10

* by gamma spectrometry

^{238}U comprises 99.25% of natural uranium. It gives rise to decay chain until stable ^{206}Pb isotope is reached. The half-lives of the nuclides in the series are much less than the half-life of parent nuclides ^{238}U. Also, in natural and undisturbed source of uranium, daughter and parent radionuclide will be in secular equilibrium and the activity of daughter nuclide will be equal to parent activity. In ^{238}U chain series, there are 14 radionuclides. So, the total activity will be 14 times of the parent or any individual nuclide. Among all the nuclides in the series, only the six ^{234}Th, ^{234m}Po, ^{226}Ra, ^{214}Pb, ^{214}Bi and ^{210}Pb emits gamma radiation. The series will be in equilibrium only in undisturbed case. If any or all daughter nuclides are removed, the chain equilibrium will be broken. The decay series is given in Appendix (Figure A.1).

^{235}U comprises 0.72% of natural uranium and decays to stable ^{207}Pb. In ^{235}U chain series, there are 12 nuclides but among the nuclides in the series, only the ^{227}Th, ^{223}Ra and ^{219}Rn emits gamma radiation. The total activity of the nuclides in the series is 11 times the ^{235}U activity. The decay series is given in Appendix (Figure A.2).

^{232}Th comprises 100% natural thorium. ^{232}Th give rise to decay series and terminates to stable isotope ^{208}Pb. Among 10 radionuclides in the series, only ^{228}Ac, ^{224}Ra, ^{212}Pb and ^{212}Bi emits gamma radiation. The decay series is given in Appendix (Figure A.3) (Gilmore, 2008).

3.2 Gamma Ray Interaction

As gamma ray photon is uncharged, no direct ionization or excitation of the material was created (like α and β particles) through which it pass. Therefore, the detection of gamma rays is dependent on causing the photon of gamma ray to undergo an interaction that transfers part or all of the photon energy to an electron within detector material (Knoll, 2010; Gilmore, 2008). These electrons get excited with charge and lost their energy by ionization and excitation of the atoms of the detector which give rise to electron-hole pairs. As the absorption coefficient for gamma radiation is low in gases, the practical detectors for gamma ray depend upon interaction with a solid. The degree of gamma radiation interactions with matter depends upon the radiation energy. Gamma ray interacts by three principal process: photoelectric effect, Compton scattering and

pair production. Photoelectric interactions and pair production are dominant at low and high energy respectively while in the mid-range energy, Compton scattering is important. Gamma ray can also interact by photonuclear reactions and coherent scattering (Rayleigh and Bragg scattering). The cross-sections for photonuclear reactions for gamma energy less than 5 MeV are not significant, and hence this interaction is not taken in consideration in most of the gamma ray measurement. Similarly, coherent scattering is not considered in gamma ray measurement as no energy is transferred to the detector in such interaction and thus, no signal is generated even though such interaction might attenuate gamma rays. Energy of gamma ray is transferred to the electrons in the detector (absorbing medium) in every significant process which represents the absorbed energy in the detector and relates to the output from the detector.

3.2.1 Photoelectric Absorption

In photoelectric absorption, gamma ray photon interacts with the bound electron in an atom and get excited from its shell with a kinetic energy E_e

$$E_{\mathrm{e}} = E_{\gamma} - E_b \tag{3.25}$$

where E_{γ} is the energy of gamma ray and E_b is the binding energy of electron in its shell.

The atom is now in excited state with an excess energy of E_b. The atom de excites by filling the vacancy of photoelectron with high energy electron with the emission of characteristic X-ray. This process continue until all gamma ray energy is absorbed. (A recoiling atom retains a small amount of energy to conserve momentum during ejection of electron which is ignored for practical purposes).

The cross section (τ) of photoelectric absorption varies with gamma energy E_{γ} and atomic number of the absorber (Z)

$$\tau \propto \frac{Z^n}{E_{\gamma}^m} \tag{3.26}$$

where n and m depends on energy and lies within 3 to 5. This equation signifies that more gamma radiation is absorbed by heavier atoms than lighter atoms. Hence, material of ideal detector would be of high Z.

The photoelectric attenuation coefficient (μ_{PE}) is given by

$$\mu_{PE} = \tau \times \rho \times \frac{N_A}{A} \tag{3.27}$$

where A is the atomic mass, ρ is the density of absorbing material and N_A is Avogadro's number (Gilmore, 2008).

3.2.2 Compton Scattering

In Compton scattering, gamma ray interacts with an electrons (free or less tightly bound) directly and transferred part of the energy to it making them recoil electron. The imparted energy of the recoil electron (E_e) is

$$E_{\mathrm{e}} = E_{\gamma} - E'_{\gamma} \tag{3.28}$$

$$E_{\mathrm{e}} = E_{\gamma} \left\{ 1 - \frac{1}{\left[1 + E_{\gamma} \frac{(1-\cos\theta)}{m_0 c^2}\right]} \right\} \tag{3.29}$$

[$m_0 c^2$ is rest mass energy]

The energy absorbed varies with the scattering angle (θ) which lies between θ to π. The term (within the bracket) is less than one even when $\theta = \pi$ (extreme), so only portion of gamma energy is transferred to the recoil electron.

The absorption cross-section (σ) of Compton scattering is related to gamma ray energy and atomic number of absorbing material,

$$\sigma \propto f\left(E_{\gamma}\right) \tag{3.30}$$

where energy function $1/E_{\gamma}$ is considered appropriate

Since, A/Z is reasonably constant (≈ 1) over a large part of periodic table, Compton scattering coefficient is given by

$$\mu_{CS} = \sigma \times \rho \times \frac{N_A}{A} \tag{3.31}$$

$$\mu_{CS} = \text{constant} \times \sigma \times f(E_{\gamma}) \tag{3.32}$$

At given gamma energy, Compton scattering cross section depends strongly on material density and is almost independent of atomic number. Moreover, at particular energy, mass attenuation coefficient (μ_{CS}/ρ) varies slightly with atomic number (Gilmore, 2008).

3.2.3 Pair Production

In pair production, gamma ray interacts with the whole atom (unlike photoelectric absorption and Compton scattering). The gamma ray is converted in to electron-positron pair within the coulomb field of the nucleus. For pair production, the gamma ray energy must be greater than 1022 keV (combined rest mass, 511 keV of two particles).

Pair production can take place in electron field if the energy is greater than 4 rest masses and the probability is also very low, due to which it is not considered in normal gamma spectrometry (0-3 MeV).

The net energy absorbed within detector in this event is given by

$$E_{\mathrm{e}} = E_{\gamma} - 1022 \text{ keV} \tag{3.33}$$

The cross section (K) depends on Z and E_{γ} in complicated manner,

$$K \propto Z^2 f\left(E_{\gamma}, Z\right) \tag{3.34}$$

K varies with Z^2 and the function in parentheses changes slightly with Z (Gilmore, 2008).

The attenuation coefficient (μ_{PP}) is given by

$$\mu_{pp} = K \times \rho \times \frac{N_A}{A} \tag{3.35}$$

The relative importance of major type of gamma ray interactions was shown in Figure 3. The line shows the value where the value of Z and $h\nu$ are just equal for two neighboring effect.

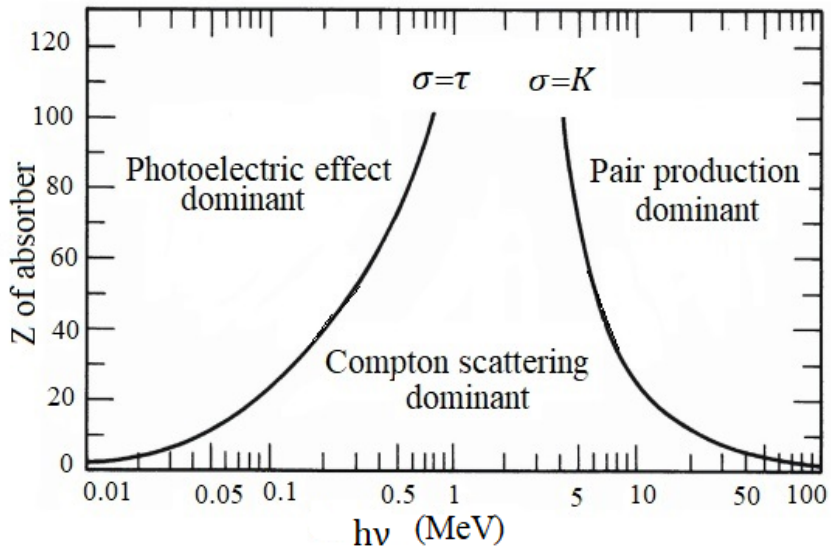

Figure 3: Three major types of gamma ray interactions (Knoll, 2010)

In general, gamma ray photons loses energy through Compton scattering continuously until the resulting photons of low energy are absorbed by photoelectric absorption.

3.2.4 Attenuation Coefficient of Gamma Ray

Gamma ray photon is removed from the beam in each interaction process by scattering or absorption which is characterized by occurrence probability per unit length of path in absorber. These probability per unit length of path that the photon of gamma ray is removed from the beam is known as linear attenuation coefficient. The transmitted

photons number (I) in terms of the original number (I_0) is given by

$$I = I_0 e^{-\mu x} \tag{3.36}$$

where μ is linear attenuation coefficient and x is the length of path (Knoll, 2010).

Mean free path can also characterize the gamma ray photon. It is the average distance travelled before an interaction in the absorber and is the reciprocal of the linear attenuation coefficient. Its value lies from few mm to tens of cm for common gamma ray energy in solid.

As the linear attenuation coefficient varies with absorber density (even if the material is same), the mass attenuation coefficient is used widely.

$$\text{Mass attenuation coefficient} = \frac{\mu}{\rho} \tag{3.37}$$

where ρ is the density of the medium. The mass attenuation coefficient for a given energy of gamma ray does not change with absorber physical state.

Mass thickness of Absorber

The gamma rays attenuation law in terms of mass attenuation coefficient is

$$I = I_0 e^{\left(-\frac{\mu}{\rho}\right)\rho x} \tag{3.38}$$

where ρx is the mass thickness of the absorber which determines the degree of attenuation. It is expressed in mg/cm^2. As mass thickness is more fundamental than physical thickness, it is used to measure the absorber thickness in radiation measurement.

Buildup

Detector can respond to all gamma rays in real case (i.e. directly from source, scattered in absorber or other types of secondary radiation of photon) and is unable to distinguish between them. Due to this, measured signal will be larger than that measured under good geometry (using collimator). To handle this condition, equation 3.36 is replaced by

$$I = I_0 B\left(x, E_\gamma\right) e^{-\mu x} \tag{3.39}$$

where $B(x, E_\gamma)$ is the built up factor. It depends on the type of detector used and on the specific geometry used. Build up factor is unity for the detector which only responds to direct gamma rays. If the detector responds to broad gamma ray energies range, the thick slab absorber's build up factor is nearly equal to absorber thickness in unit of mean free path (Knoll, 2010).

Total Attenuation Coefficient of Gamma Ray

The fraction of mono-energetic photons which penetrate the detector with their original direction and energy (without any interaction) are considered in gamma ray spectrometry. The remaining photons that are either scattered or absorbed in the detector is referred as attenuation (Debertin & Helmer, 1988). The total attenuation coefficient is the sum of coefficient of the significant interaction processes,

$$\mu_T = \mu_{PE} + \mu_{CS} + \mu_{PP} \tag{3.40}$$

This equation in terms of cross section can be written as

$$\mu_T = \left(\rho \times \frac{N_A}{A}\right)(\tau + \sigma + K) \tag{3.41}$$

The equation in term of mass attenuation coefficient,

$$\frac{\mu_T}{\rho} = \left(\frac{N_A}{A}\right)(\tau + \sigma + K) \tag{3.42}$$

After interaction, photon at different energy are emerged as a consequence which is not taken in to account in mass attenuation coefficient. Those incomplete interactions are taken in account in total absorption coefficient (μ_A),

$$\mu_A = \left(\rho \times \frac{N_A}{A}\right)(\tau \times f_{PE} + \sigma \times f_{CS} + K \times f_{PP}) \tag{3.43}$$

where the factor $'f'$ is the ratio of energy imparted to electrons (by the interaction) to the initial energy of the gamma ray (Knoll, 2010). The total mass attenuation coefficient of gamma rays of energy within terrestrial origin for the present study is calculated using computer program NIST XCOM.

3.3 Dose Conversion

Dose is estimated from fluence. Fluence (Φ) is defined as

$$\Phi = \frac{dN}{da} \tag{3.44}$$

where dN is the differential number of photons of gamma ray incident on a differential cross section (da) of a sphere (Knoll, 2010). For a mono directional beam, where the area is perpendicular to the beam direction, the fluence is number of photons per unit area ($\phi = \frac{N}{a}$).

The counts recorded by detector is more related to fluence than dose. So, a dose

conversion from fluence is carried to interpret measurement made with detector (pulse mode) to determine dose.

The attenuation of gamma rays over small distance in air is negligible, so direct (or unscattered) fluence from point source is given by

$$\Phi = \frac{N}{4\pi d^2} \tag{3.45}$$

where N is the photons number emitted from source and d is the distance from the source. The energy dependent probabilities of producing secondary ionizing particles from gamma ray, the quality factor Q (applied for conversion of dose equivalent from energy deposited per unit mass and the kinetic energy deposited by the ionizing particle) must be taken in to account for the conversion of dose from fluence.

Because of attenuation and self-shielding effect within the human body, various tissues and organs differs in radio sensitivity. Due to this, tissue weighting factors were recommended by ICRP. The individual dose component is then added to get the effective dose which represents the estimate of the overall biological effect of whole body for uniform exposure. The effective dose is written as

$$H_E = h_E \Phi \tag{3.46}$$

where h_E is the conversion coefficient for fluence to effective dose. Integrating the conversion coefficient multiplied by fluence (energy dependent) incident on body gives the effective dose (Knoll, 2010).

3.3.1 Absorbed Dose

The mean energy ($d\bar{\varepsilon}$) deposited by any type of radiation per unit mass (dm) of absorber is known as absorbed dose (D). It is expressed in J/kg or Gray (Gy). It is the measure of physical and chemical effects created in an absorbing material by a given radiation exposure. It is the fundamental quantity in dosimetry for radiological protection (ICRP, 2007).

$$D = \frac{d\bar{\varepsilon}}{dm} \tag{3.47}$$

3.3.2 Dose Equivalent

The ionizing radiation changes atoms and molecules temporarily or permanently and can damage cells. The equal amount of absorbed dose have different biological effect under different irradiation conditions. It depends on the magnitude of the energy deposited in the form of electrons or heavy charged particles as the severity of the biological damage depend on LET (linear energy transfer). Large value of LET (heavy charged particle)

result in greater damage than electrons (with lower LET), even if the absorbed dose is same. Therefore, "dose equivalent" term is introduced which gives the biological effect of the radiation exposure. The dose equivalent (H) is given by

$$H = DQ \tag{3.48}$$

where "Q" is the quality factor which increases with LET. Dose equivalent is numerically equal to absorbed dose for gamma rays as LET is so low that Q is equal to 1. The unit of dose equivalent depends on absorbed dose unit. If "D" is expressed in Gy than "H" is expressed in Sievert (Sv) (Knoll, 2010).

3.3.3 Equivalent Dose

ICRP represents equivalent dose (in an tissue T, due to radiation R) by a symbol $H_{T,R}$. The average absorbed dose $D_{T,R}$ multiplied by radiation weighting factor W_R gives equivalent dose and is determined by incident radiation energy. W_R gives the biological effects of various radiations.

$$H_{T,R} = W_R \cdot D_{T,R} \tag{3.49}$$

The equivalent dose is not a point quantity like dose equivalent but an average over a tissue and given by

$$H_T = \sum_R H_{T,R} = \Sigma_R W_R \cdot D_{T,R} \tag{3.50}$$

If different (mix) radiation are present than sum over all radiation types gives H_T (Knoll, 2010).

3.3.4 Effective Dose

The effective dose (E) is given by

$$E = \sum_T W_T \cdot H_T \tag{3.51}$$

where W_T is tissue weighting factors which gives the relative damage to tissue (or organ) from whole body uniform exposure. W_T sums to unity, therefore, one Sievert H_T equals to 1 Sievert E. "E" is the fundamental quantity in radiological protection for providing limit by ICRP. Since, W_T is biological quantities, it cannot be evaluated experimentally. Hence, equation 3.49-3.51 is not used as a basis for measurements (Knoll, 2010).

3.4 Gamma Ray Spectroscopy/Spectrometry

The type of radiation measurement which deals with the measurement of energy distribution of gamma radiation produced by source is gamma ray spectroscopy. A spectrum of gamma energy is a function of particle distribution in terms of energy (Tsoulfanidis & Landsberger, 2021). Since, the detection of gamma ray is relatively easy and can be done with high precision at high resolution, gamma radiation emitted during a radioactive decay process is primary means to study about nuclear excited states, identify radionuclides by determining their energies and activity concentrations quantification. Gamma ray spectroscopy does not require any chemical separation, and hence is direct technique for radionuclide identification and quantifying activity. The photo peak gives the total energy of gamma ray deposited in the detector. This method is used for both in-situ and ex-situ measurement (Gilmore, 2008; Beck et al., 1972; Krane, 1988). A gamma ray spectrum gives the intensities and energies of transitions.

The gamma ray detection depends on gamma ray interaction that transfers all or part of the energy of the photon to an electron of the absorbing material and generate excited energy. Gamma rays interact mainly via photoelectric absorption, Compton scattering and pair production. The excited electrons lose their energy through excitation and ionization of atoms of detector and give rise to electron-hole pairs (Knoll, 2010). The gamma ray spectroscopy is generally realized using scintillation (NaI(Tl)) and semiconductor (HPGe) detectors. These detectors produce electric signals from electron-hole pairs for pulse processing. The number of events in a detector takes place depending on the energy of gamma rays.

Gamma ray spectrometry uses two types of model: physical model and statistical models. Physical models which provides an insight of physics is necessary for effective survey design and for data processing and interpretation procedures. Statistical models estimates or predicts errors (IAEA, 2003).

The semi-empirical model based on mono-energetic (unscattered) radiation is the simplest approach for gamma ray fields modelling. The two-layer model with the earth as an infinite half-space with a constant density and radioelement concentration overlain by constant density of non-radioactive air was used (Clark et al., 1972). The observed photo peak intensity, dI, from gamma ray emissions of photon energy E_0 by a volume element dV within the earth is given by

$$dI = \frac{A\varepsilon}{4\pi R^2} e^{-\mu_e r_e} e^{-\mu_a r_a} N dV \tag{3.52}$$

where NdV = number of gamma rays of energy E_0 emitted per second by the volume element dV;
A = effective cross-sectional area of a detector

ε = photopeak efficiency of the detector for gamma rays of energy E_0
μ_e , μ_a = linear attenuation coefficients for the earth and air respectively
r_e, r_a = the distances through the earth and air that the gamma rays travel
R = r_a+r_e

3.4.1 In-situ Gamma Ray Spectrometry

In-situ gamma ray spectrometry is a powerful and rapid method for determining the concentrations of radioisotopes in the environment (Jacob et al., 1994).

The term in-situ is a Latin word which means "in the original place". Thus, "in-situ gamma ray spectrometry" means that the spectrum of the gamma flux is collected at the site for analysis (to identify and quantify the radionuclides). The in-situ technique was originated during atmospheric nuclear weapon testing time for providing quick and reliable information of the radiation in outdoor environment. It gives quantitative results separating natural background from manmade sources. The in-situ spectrometry is more powerful as gamma radiation from sources can be measured over a several hundred square meters area when a detector is placed over a ground surface. The detector's "field of view" would be larger for source closer to soil surface and for sources of high energy. Due to radiation transport nature through matter (the soil and air), in-situ spectrometry is limited to the measurement of gamma ray emitters. The buried sources are generally not detected with measurements performed above ground due to attenuation properties of soil. e.g. For 662 keV sources, 97% of primary flux will be cut down by 30 cm soil. In such case, detector is lowered in to a hole for measurement. In general, the in-situ measurement indicates the measurements performed near ground level and the source distribution is expected to be spread over a very large area with the source near at the soil surface (Miller & Shebell, 1993).

In-situ gamma ray spectrometry are classified mainly in types: portable, car borne and airborne for radiometric mapping. Portable and car borne gamma ray spectrometry are used for detailed mapping survey and region mapping to estimate the concentration of radionuclides. Since 1960, portable gamma spectrometry has been used for geological mapping, uranium exploration and environmental studies. Air borne gamma spectrometry has been used as the lithological mapping tool and for the direct detection of ore bodies. It is also used for radon measurement and mapping of nuclear fallout. In recent years, the method has also included the application like ground water discharge, salinity studies and soil mapping. The gap between portable and airborne technique is filled by car-borne gamma ray spectrometry. It has much greater coverage than portable system for a given time and cost and has improved resolution and quick mobilization compared to airborne system. It is mostly used for mapping fallout and searching orphan source (IAEA, 2003).

Portable gamma ray spectrometers are used widely in field studies. The priori

assumptions needs to be made about the nuclides distribution in the soil before applying the method to ground level measurement to derive specific activities from spectra. In-situ measurement of ^{40}K, the decay series of ^{238}U and ^{232}Th (naturally occurring terrestrial gamma radiation) and ^{137}Cs (anthropogenic radionuclide, global fallout) are mostly used in Earth sciences mapping and for monitoring purposes.

The portable gamma ray spectrometry depends on the location, size and geometry of sources. Source-detector geometry is kept constant for meaningful measurement. The detector can be either kept on the Earth surface or at a low constant height. If the detector is placed directly on ground, then effective thickness of rock sample is approximately 25 cm, a mass exceeding 100 kg and a radius of 1 m. If the detector height is raised, effective source diameter increases rapidly depending on gamma ray energy from several meters to tens of meters (IAEA, 2003; Kogan et al., 1971). For ideal in-situ gamma ray spectrometry method, the detector is generally kept at a height of nearly 1 m above the ground which enlarge the detector's field of view up to the radius 10 m to 30 m and effective thickness to 30 cm (Kastlander, 2010).

3.4.2 Basic Parameters for Calibration

Fluence rate (Φ), full absorption peak count rate (N) and source activity (A) are fundamental quantities used in in-situ spectrometry (Miller & Shebell, 1993). The measured peak count rate in a spectrum is converted to the source activity level in the soil or dose rate using the relation

$$\frac{N_f}{A} = \frac{N_f}{N_0} \cdot \frac{N_0}{\Phi} \cdot \frac{\Phi}{A} \tag{3.53}$$

where $\frac{N_f}{A}$ = full absorption peak count rate at some energy E, from gamma transition per unit activity of the isotope in soil
$\frac{N_0}{\Phi}$ = full absorption peak count rate per unit fluence rate from plane parallel beam of photons normal to the detector, at energy E
$\frac{N_f}{N_0}$ = correction factor for the detector response at energy E (to account for the fact that fluence from an extended source will not be normal to the detector face but distributed across some range in angles in environment)
$\frac{\Phi}{A}$ = fluence rate of energy E from unscattered photons arriving at the detector due to gamma transition for a isotope per unit activity of that particular isotope in the soil
$\frac{N_0}{\Phi}$ depends only on detector, $\frac{N_f}{N_0}$ depends on characteristics of the detector and the source geometry and $\frac{\Phi}{A}$ depends on the distribution of source in the soil.

3.4.3 Unscattered Flux

Figure 4 illustrates the theoretical model for an in-situ gamma measurement. A detector is kept above a source, considering that the source is distributed in or deposited on a volume of soil. [Let ($\vec{r_D}$) designates the detector position relative to origin O. $\vec{r}$ is the position of differential volume of soil, $\vec{r_i}$ is the air-ground interface location.]

The total unscattered flux for a gamma source of energy E is given by (Miller & Shebell, 1993)

$$\Phi = \int_V \frac{f(r)}{4\pi\,(r_D - r)^2} e^{\left[\frac{-\mu_s}{\rho}\rho(r_i - r) - \frac{\mu_a}{\rho_a}\rho_a(r_D - r_i)\right]} dV \tag{3.54}$$

where $f(r)$ = Source strength at r
$\frac{\mu_s}{\rho}$ = mass attenuation coefficient for soil (cm^{2}g^{-1})
$\frac{\mu_a}{\rho_a}$ = mass attenuation coefficient for air

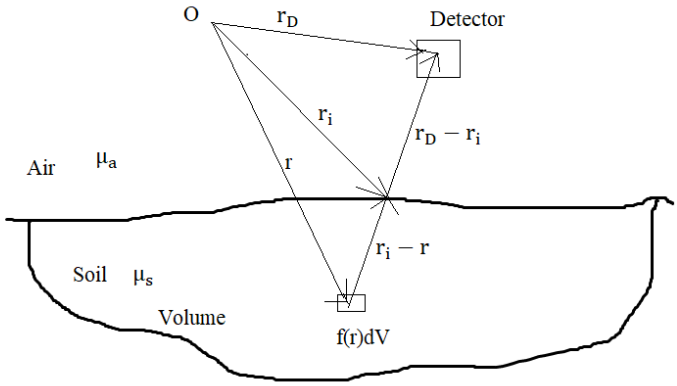

Figure 4: Model for in-situ gamma ray spectrometry for calculating flux (Miller & Shebell, 1993)

^{238}U and ^{232}Th series and ^{40}K are the natural sources of gamma radiation in the environment and the fallout from nuclear weapon testing, and effluents from reactors are the anthropogenic sources. It is assumed that fallout activities in the soil vary with depth while the natural radionuclides is distributed uniformly.

Therefore, distribution of natural gamma radionuclides is expressed as (Miller & Shebell, 1993)

$$f(Z) = S_V \tag{3.55}$$

where S_V = soil activity per unit volume (photons/cm^3-s). In the case of fresh fallout

that has not been driven in to the soil,

$$f(Z) = S_A \delta(Z - Z') \tag{3.56}$$

S_A = Surface activity (photons/cm^2-s)
Z' = distance from a detector to the air-ground interface

In case of aged fallout,

$$f(Z) = S_0 e^{(-\frac{\alpha}{\rho}\rho Z)} \tag{3.57}$$

where α = inverse of relaxation length (cm)
ρ = density of soil (g cm^{-3})
S_0 = surface activity (photon/cm^2-s).

Figure 4 can be made simple by taking infinite half-space geometry assuming infinite volume of soil and a flat air-ground interface (Figure 5). The detector is placed at the origin, at height 'h' above the air-ground interface. For ideal set up, large and flat open field is considered with no obstructions or surface features that can reduce the photon flux.

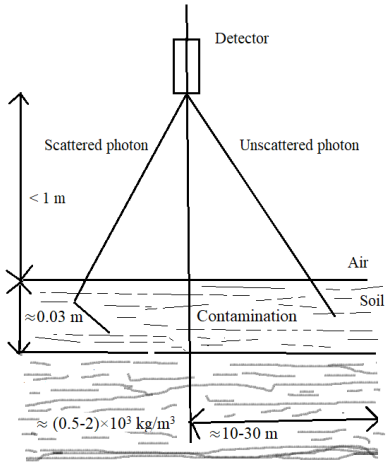

Figure 5: Cross sectional view of ideal model for in-situ measurement (Kastlander, 2010)

For uniform distribution (natural radionuclides in terrestrial environment), equation 3.54 becomes (Miller & Shebell, 1993)

$$\frac{\Phi}{S_{v/\rho}} = \frac{1}{2}\frac{\mu_a}{\rho_a}\frac{\rho}{\mu_s}\rho h \left(\frac{e^{\left[\left(\frac{\mu_a}{\rho_a}\right)\rho_a h\right]}}{(\mu_a/\rho_a)\,\rho_a h} - E_1\left(\frac{\mu_a}{\rho_a}\rho_a h\right)\right) \tag{3.58}$$

For exponential distribution (aged fallout in environment)

$$\frac{\Phi}{S_0} = \frac{1}{2}\left[E_1\left(\frac{\mu_a}{\rho_a}\rho_a h\right) - e^{\left(\frac{\alpha\rho}{\rho\mu_s}\frac{\mu_a}{\rho_a}\rho_a h\right)} E_1\left[\left(1+\frac{\alpha}{\rho}\frac{\rho}{\mu_s}\right)\frac{\mu_a}{\rho_a}\rho_a h\right]\right] \tag{3.59}$$

where $\rho_a h$ = mass depth of air

E_1 is exponential integral and defined as

$$E_1(x) \cong \int_x^\infty \frac{e^{-t}}{t} dt \tag{3.60}$$

Composition of soil and soil density variation have minimal impact on the photon flux but excessive roughness of ground provides additional self-absorption.

The need of cooling, high cost and available size of detector has make difficult to use semiconductor detectors for in-situ measurement. Thus, scintillation detectors are more preferred as they can be operated at ambient temperatures and are cheaper and available in large crystals with moderate resolution (Anspaugh, 1976). NaI(Tl) scintillators are popular because of its high photoelectric absorption by its iodine constituents (Z = 53). The high intrinsic detection efficiency and large photo-fraction makes the sodium iodide scintillation spectrometers important. CsI and BGO have greater detection efficiency and photo fraction but has slow decay and available only in limited sizes. The newer scintillators like $LaBr_3$ (Ce) has fast decay time, higher light output and better energy resolution despite that the availability of NaI(Tl) in large volume at lower cost and reasonable performance has maintained its popularity. Also, $LaBr_3$ (Ce) do not show pulse discrimination properties which reduces their use in mixed radiation field applications (Knoll, 2010). Modern portable gamma spectrometers are mostly differential spectrometers with at least 350 cm^3 of NaI(Tl) detectors. It can record 256 or 512 data channels in the energy range within 0 to 3 MeV. Automatic spectrum stabilization is either by one of the natural radionuclides peaks (^{208}Tl at 2.62 MeV or ^{40}K at 1.46 MeV) or by a low-energy peak from an isotope (reference). The reference isotope is typically ^{137}Cs at 0.662 MeV. For the in-situ estimation of radioelement concentrations of ^{40}K, ^{238}U and ^{232}Th, the full gamma ray spectrum is recorded as well as the instruments record sum channels over broad energy windows. Instruments memory can record several hundreds of full energy spectra or several thousands of field measurements.

The threshold of a spectrometer is set to an energies slightly below 1.76 MeV, 2.62 MeV and 1.46 MeV for ^{238}U, ^{232}Th and ^{40}K measurement respectively and to a low energy for measurement of total count. For instrument gain adjustment, reference gamma source is used.

The acquired spectra are processed using windows method that entails NORM mapping monitoring photo peaks of 1460 keV (^{40}K), 1765 keV (^{214}Bi) and 2614 keV (^{208}Tl) for determination of ^{40}K, ^{238}U and ^{232}Th concentrations respectively. Nuclear fallout

(^{137}Cs) is detected on 662 keV window. NaI(Tl) detector was used in the present work. NaI(Tl) crystals have high density and the detector have a 100% detection efficiency for low gamma energy. The energy resolution for ^{208}Tl is 7% at 2614 keV and 10% for ^{137}Cs at 662 keV (IAEA, 2003).

Gamma rays incident on the detector interacts with the NaI(Tl) crystal to produce charged particles (electrons and positrons) by photoelectric absorption, Compton scattering and pair-production processes. The crystals are excited by these charged particles and thus, scintillates (emits visible light photons). The incident gamma energy (approximately 11%) is converted into photons with 3 eV in 0.23 µs with an emission of wavelength of 415 nm (Knoll, 2010). The distribution of pulse height of a gamma ray incident on detector depends on the relative cross sections (P.E., C.S., P.P.) and the size of detector. The pulse height distribution due to events occurring in NaI(Tl) detector are presented in Table 2 (Ouseph, 1975).

Table 2: Contribution to Pulse height distribution due to events occurring in the NaI(Tl) detector (Ouseph, 1975)

	Interaction process	Energy absorbed E_γ in crystal	Pulse height
1	Photoelectric effect	E_γ	pulses in photo peak
2	Compton effect (scattered γ escapes)	varies from 0 to E_{max} E_{max} = E_γ (1+(m_0c^2)/(2E_γ))	pulses in Compton continuum
3	Compton effect (scattered γ absorbed)	E_γ	pulses in photo peak
4	Pair production (annihilation γ escapes)	kinetic energy of e^-e^+ pair = E_γ - 1.022 MeV	double escape peak (E_γ - 1.022 MeV)
5	Pair production (one annihilation γ escapes)	E_γ-1.022+0.511 MeV	single escape peak (E_γ - 0.511 MeV)
6	Pair production (both photons absorbed)	E_γ	Pulses in photo peak
7	Pair production (one of the γ annihilation produces Compton electron)	Compton contribution of E_γ- 0.511 MeV	pulses in the Compton continuum
8	Compton back scattering	E_γ - E_{max}	back scatter peak
9	Compton angle other than π	energy varies between E_γ and E_γ - E_{max}	Pulse height indistinguishable from Compton distribution
10	Pair production outside, and one γ scattered in detector	0.511 MeV	peak at 0.511 MeV

3.5 Statistical Analysis and Spatial Data Interpolation

3.5.1 Basic Statistics

The activity concentrations of radionuclides were determined using in-situ gamma ray spectrometry. The statistical characteristics of the radionuclides activities were described using basic statistics.

In statistics and probability theory, skewness measures the asymmetry of the distribution of a random variable. The skewness analysis has many benefits. Most of the model assumes that the data are distributed symmetrically about the mean (normal distribution). The normal distribution has zero skewness. However, real data points may be skewed and not be perfectly symmetric. Skewness measures degree of distribution (asymmetry distribution) around its mean (Groeneveld & Meeden, 1984). The distribution with an asymmetric tail extending towards positive values indicates positive skewness. In this case, mean is greater than median which indicates most data values are less than mean. The asymmetric distribution with a tail extending towards negative value indicates negative skewness. In this case, mean is smaller than median i.e. most of the data values are greater than mean. Lower skewness generally indicates normal distribution.

Kurtosis measures the probability distribution peakedness of random variable. The relative distribution peak compared to normal distribution gives kurtosis. Relatively peaked distribution has positive kurtosis while flat distribution has negative kurtosis. The kurtosis value is higher if the variance is due to infrequent extreme deviations (Adam & Eltayeb, 2012). The frequency distribution can be seen in histogram plot. Bell shaped histogram indicates normal distribution.

Generally, univariate statistical analysis is used for radioelement data in environmental samples. The univariate data analysis is simple but it can emerge associated reductionism fallacy (Ashley & Lloyd, 1978). Hence, to minimize such problem, multivariate analysis is used to look correlation without losing information among large number of variables (Jackson, 2005; Meglen, 1992). The multivariate analysis is used to get high data compression efficiency to find some information of the original data which will be useful in interpreting environmental geochemical origins of the studied materials. Also, large data sets are simplified and organized using this method to provide meaningful insight (Laaksoharju et al., 1999). Also, natural correlations between variables (samples) are indicated using this method which highlights the information that cannot been seen at first glance (Wenning & Erickson, 1994).

The multivariate statistical analysis of environmental data is used to interpret relations among variables for the environmental system management (Liu et al., 2003). In present work, radioactive measurements made using gamma ray spectrometric method were subjected to quantitative and qualitative statistical analyses to draw important conclusions regarding the radioelement distribution nature in the environment of Kathmandu and Makawanpur district of Nepal.

For bivariate analysis, correlation analysis is used to find the mutual relations and the associated strength between the variables pairs by calculating linear Pearson correlation coefficients.

For multivariate analysis, principal component analysis technique is carried out. In

this technique, variables of samples set are combined linearly to get new fundamental components which provides a better quantitative interpretation and description of geochemical data (Asfahani et al., 2005, 2007). The original set of data is mean centered and orthogonally decomposed in to loading matrix, score matrix and residual matrix

$$X_c = T \cdot P^T + E \tag{3.61}$$

where X_c = mean centered
T = score matrix
P = loading matrix
E = residual matrix

The score matrix expresses observations (radionuclide concentrations) relationships in new co-ordinate axes (orthogonal) known as principal components. The principal components (first) is the latent linear variable with the maximum variance, and the direction of first principal component is orthogonal to the directions of second principal component. The importance of principal components is explained in terms of percentage of the total variance. The loading matrix describes the structure of data in terms of correlations of variable.

The 2-D graphical scatter plot of the loadings and scores vectors in different combinations gives the description of observations covariance and provides simple interpretable overview of data (Varmuza & Filzmoser, 2016).

3.5.2 Ternary Plot

Ternary plot are used for display and visualization of the three part compositional data variability in which variables are represented as equilateral triangle (Aitchison, 1982). The measurements individual portions are derived by drawing a line through the point investigated which is parallel to the opposite edge (Figure 6).

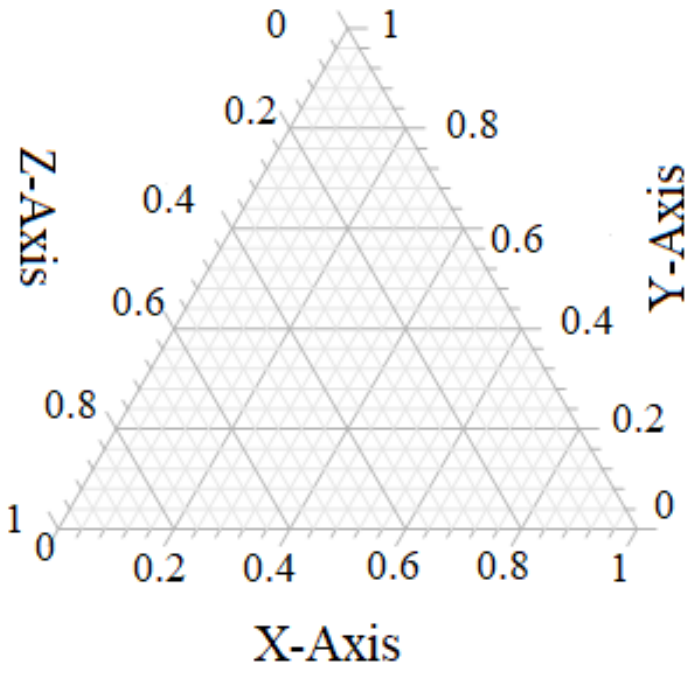

Figure 6: Ternary diagram showing percentage in three component system

The perpendiculars from any point (p) to the opposite sides in a triangle satisfy the relation

$x_i \geq 0\ (i = 1, 2, 3), \quad x_1 + x_2 + x_3 = 1$

The theory and applications of ternary plot in geoscience is explained in detail by Buccianti et al (Buccianti et al., 2006).

3.5.3 Kriging Technique

The variogram and kriging (geo-statistical techniques) are used for interpolation and investigation of the distribution of spatial variables (Webster & Oliver, 2007). In present work, kriging technique was used for interpolating for spatial mapping of the in-situ measurements of radionuclides over locations (non-sampled) to find the spatial dependency in the area surveyed. This technique uses the semi-variogram function for describing spatially correlated data relationship.

$$\gamma(h) = \frac{1}{2N(h)} \sum_{i=1}^{N(h)} \{Z(X_i) - Z(x_i + h)\}^2 \tag{3.62}$$

For present study, Surfer software is used for preparing contour map in which kriging method is used for gridding the data for interpolation and linear variogram is used as estimator type. The 100 of random points (e.g. dose rates) from the input data is cross validated before gridding for contour using point kriging type.

Mapping of the interpolation values is achieved using grid nodes (nearest sampling points) for creating fine figure using GIS software.

3.6 Methods and Site Description

A mobile in-situ radiometric measurement was conducted using portable gamma ray spectrometer. The survey conducted covers more than 120 km along the road between Balkhu and Hetauda via Kulekhani. From Dakshinkali to Kulekhani, both way (via Pharping and via Sisneri) was covered. The survey of Hetauda city and some parts of Kathmandu city (Mishra & Khanal, 2019; Mishra & Khanal, 2023) was also conducted along with some selected adjoining area (Rakash Khola, Bhimphedi, Golping Besi and Bhaise) and along the bank of rivers (Chobhar, Rakash Khola, Mahalaxmi, Bhaise and Samari & Rapati) and around the lakes (Taudaha and Indra Sarovar) within the studied area. The depth distribution profiles of soils were studied at eight different locations (Chobhar, Pharping, Raksh Khola, Salle, Dhorsingh, Chisapani Gadhi, Baghjhora and Hetauda) within the survey sites. The scattering of gamma ray of natural origin in air at different height at ambient temperature was studied in Kathmandu city.

The final survey was planned and conducted after many preliminary samples study, survey and experiments. The survey of Tribhuvan University, Bagh Bhairav temple, ring road, UNESCO sites (Swayambhunath, Pashupatinath, Boudhanath, Kathmandu durbar square, Patan durbar square, Bhaktapur durbar square, Changu Narayan) in Kathmandu (Mishra & Khanal, 2019; Mishra & Khanal, 2023), bridges on Bishnumati river, Rani Pokhari, Sisdol landfill sites and Manjushree statue of Chobhar were conducted previously. The soil depth profile of ^{137}Cs, ^{40}K and ^{238}U in Tribhuvan University were also conducted prior to final survey. The results presented here are based on the final survey that was conducted for seven days from 30 October to 1 November 2019 and on 21 January 2020, 1 Feburary 2020, 12 March 2020 and 14 March 2020 with the help of six field personnel.

The area studied is located between an altitude of 384 m to 1872 m ASL within latitude range N 27.503° to 27.684° and longitude range E 85.042° to 85.330°. The survey was started from Balkhu Chowk of Kathmandu and ends at Buddha chowk of Hetauda. During the survey, the altitude first increases and then decreases and again increases and then decreases as proceeded to Hetauda. The depth distribution of radionuclides in the soil was studied at eight selected locations between the studied areas. The selected locations were Chobhar at 1232 m ASL, Pharping (Dakshinkali) at 1609 m ASL, Rakash Khola (Fakhel) at 1743 m ASL, Salle at 1580 m ASL, Chisapani Gadhi at 1656 m ASL, Dhorsingh at 860 m ASL, Baghjhora at 484 m ASL and Hetauda at 384 m ASL.

3.7 In-situ Measurement

Ground radiometric methods with portable gamma ray spectrometer was used for mapping dose and surface concentrations of radionuclides. The continuous measurement was taken on foot with the detector carried in backpack at 1 sec interval (Figure 7). The distance between the detector and ground is kept less than 1 m with a detector pointing downwards. The measurement was taken at a walking pace of 2 km/h.

Figure 7: In-situ ground based radiometric measurement with detector in backpack pointing downward

The depth distribution profiles of primordial radionuclides (^{40}K, ^{238}U, ^{232}Th) and ^{137}Cs were studied at the depth of (0-10) cm, (10-20) cm, (20-30) cm, (30-40) cm and (40-50) cm by lowering the detector in the hole as shown in appendix (Figure A.4). The radionuclides concentrations at different depth had been studied at eight different locations (Chobhar, Pharping, Raksh Khola, Salle, Chisapani Gadhi, Dhorsingh, Baghjhora and Hetauda) along the survey sites.

The gamma scattering in air at up to 300 cm height at every 50 cm had been studied at ambient temperature in Kathmandu city. The total attenuation mass coefficient for ^{40}K, ^{238}U and ^{232}Th for energy 1.461 MeV, 1.764 MeV and 2.614 MeV respectively for air (considering air mixture of 78.08% N_2, 20.95% O_2, 9.34 $\times$ 10^{-3}% Ar and 3.45 $\times$ 10^{-4}% CO_2 (Allen & Cox, 2000) are also calculated using computer program NIST XCOM to get attenuation length of gamma ray.

3.8 PGIS 2

The portable gamma ray spectrometers PGIS 2 (Portable Gamma spectrometer Information System) from Pico Envirotec Inc. (Figure 8) of 5 kg was used for survey of the area.

The detector is equipped with thallium activated sodium iodide, NaI(Tl) crystal of 0.347 L. The spectrometer consists of scintillation detector unit integrated with GPS and data logger unit (developed for android mobile). The detector has wireless communication with data logger unit via Bluetooth and provides real time navigation guidance to operator. The detector is coupled with multichannel analyser (MCA) of 512 channels and the energy range of the detector is 20 keV to 3 MeV. It can measure per second spectra and its startup stabilization (tuning) time is less than a minute. It can be operated in an environment of -20 to 50 °C (PEI, 2014).

Figure 8: PGIS 2

The instrument is designed for portable or backpack spectrometry surveys in different kind of environments. The PGIS 2 is based on advanced microprocessor and mobile technologies. It consists of a detector unit, integrated with GPS and a data logger unit (PEI Core) based on state-of-the-art portable devices (smart-phone). The user interface and data acquisition system is based on the Android OS. The PGIS 2 is embedded with AGRS (advanced gamma-ray spectrometer) which is useful for geological and geophysical exploration, mapping, and environmental and nuclear surveillance. The detector processing is individual and independent which provides real time gain and linearity correction. The AGRS is fully automated and self-stabilizing on natural radioelements due to which regular and time consuming system checks and recalibration is not required and it assures reliable and accurate gamma-ray measurements. Also, when operating in real time (collecting data) the linearity, the gain and offset of detector is corrected mathematically for each and every measurement. The system is

auto calibrated by natural photo peaks of ^{40}K, ^{238}U or ^{232}Th. The data acquired is synchronized automatically with GPS time and location. The instant spectrum can be displayed on mobile screen in real-time in a waterfall or counts per second mode (Figure 9). The chart view can display data channels: ROI windows, dose rate, cps and ^{40}K, ^{238}U, ^{232}Th activities or concentrations etc. Real time ground navigation allows to follow a survey grid or way-points on a displayed map that can be prepared as a calibrated image (using PEIConvert) or automatically loaded from the internet (using Open Street Maps)[https://www.environmental-expert.com/products/model-PGIS 2-portable-gamma-ray-spectrometer-115412].

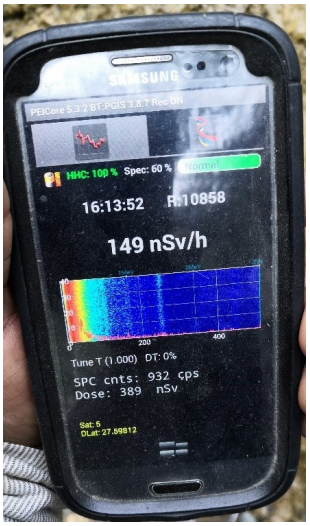

Figure 9: Instant spectrum and dose rate displayed on mobile screen during survey

3.8.1 PEIView Data Viewer

The acquired data is also analysed in laboratory in computer using software PEI Data Viewer (PEIView) provided with the instrument. PEIView provides fast field data verification for Pico Envirotec Inc. (PEI) binary data format files. It converts PEI data format into ASCII which can be used with standard data base programs. It also convert PEI data format into a Geosoft GBN format to be used with supporting data processing software. The data from PEIView can be exported to ASCII format and Google earth format (KMZ Format and GPX Track). The program also provides calculation of stripping ratio and window sensitivities and allows simple data correction (PEI, 2013). PEIView provides different windows (views) to present the data:

1. Charts View: It contains up to six charts and each chart shows one data channel.
2. All Samples View: It presents whole file data.
3. Spectra View: It represents spectral channels. This is the important window for gamma spectrometric data analysis as gamma radiation from specific radionuclides can be identified and analyzed. There are three charts in Spectra View: Color Waterfall

Chart, Spectral Window Chart and Spectral Chart.

4. Table View: It displays numerical data in table form.

The screenshot of chart view, all sample view, spectra view (including color waterfall chart, spectral window chart and spectral chart) and table view during analysis is shown below in Figure 10-16. The chart view gives the first glance of data (Figure 10). The data is checked here and exported to AscII or KMZ format prior to spectral analysis. The sum of spectral channels is displayed in spectral window chart (Figure 13). Spectral window can be generated for any region of interest by changing the lower and upper margin of the window.

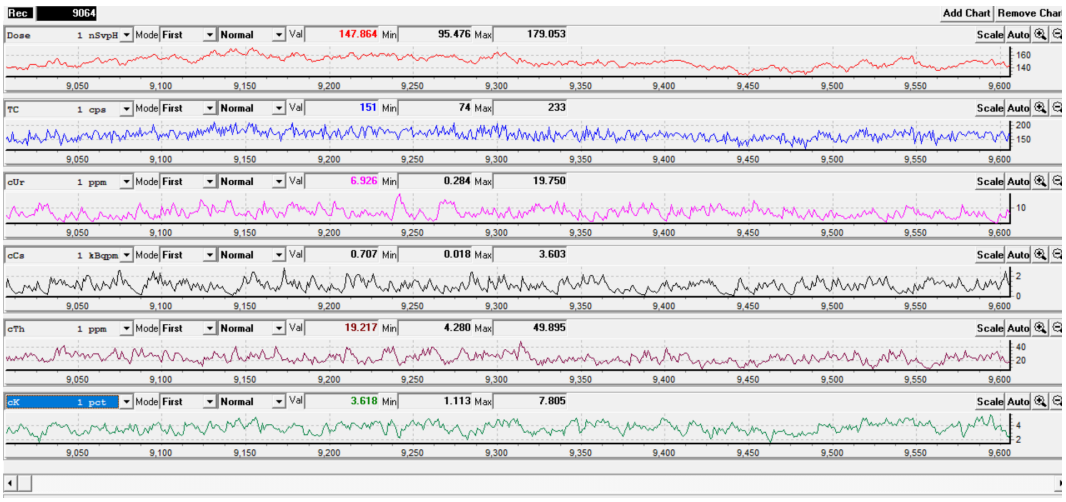

Figure 10: Chart view in PEIView

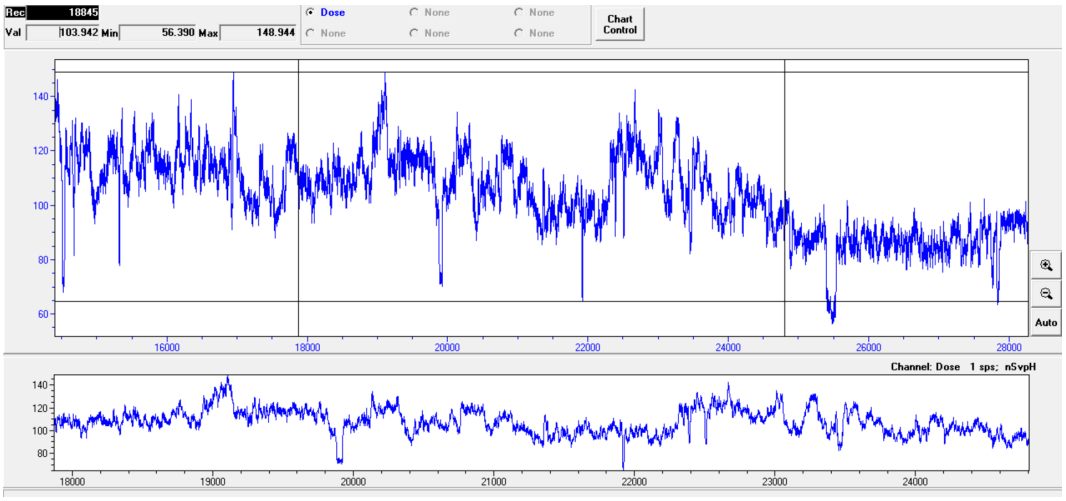

Figure 11: Data channel displayed in all samples view

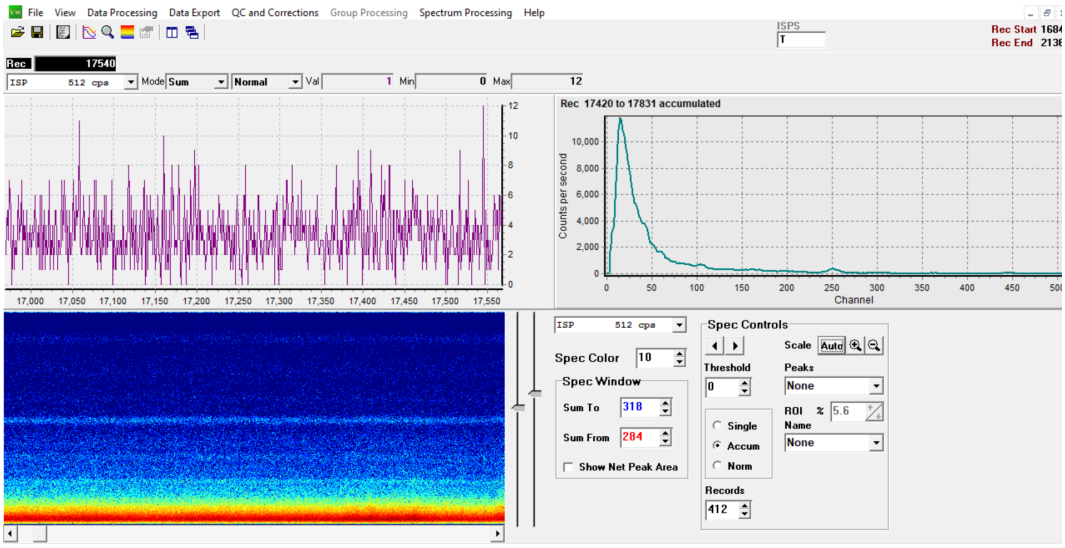

Figure 12: Spectral view in PEIView

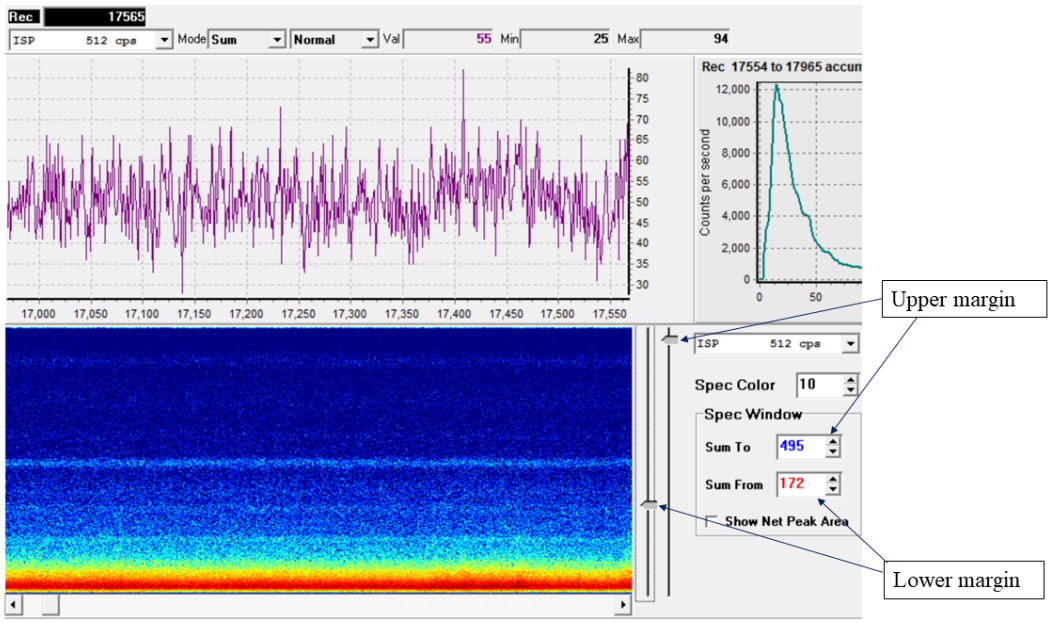

Figure 13: Spectral window chart in spectral view

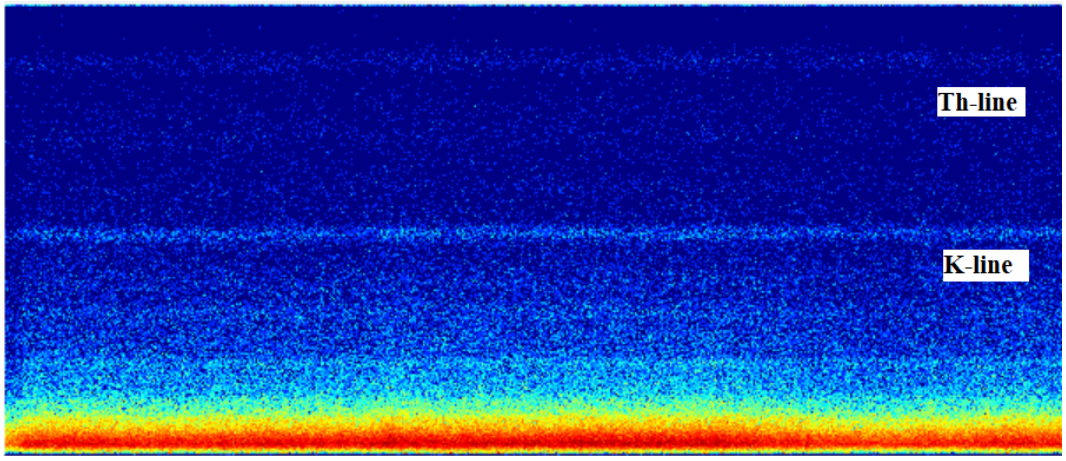

Figure 14: Chart showing ^{232}Th and ^{40}K lines in spectral view

Find Record | 14402 | Go | Find Channel Value | Dose 1 nSvpH | 0.000 | Find | From the Beginning | From the Next Record | Display ASCII

	RECS	Dose	TC	cUr	cTh	cK	Cs
	14532	72.391	71	3.115	6.101	1.687	16
	14533	73.633	76	2.077	6.678	1.646	19
	14534	73.341	67	2.038	6.973	1.500	12
	14535	72.066	62	3.388	7.081	1.070	17
	14536	72.861	70	4.288	7.152	1.317	14
	14537	75.977	81	4.888	7.200	1.268	14
	14538	76.829	72	3.259	12.544	1.117	10
	14539	82.844	93	3.479	13.405	1.336	27
	14540	88.756	102	6.378	13.801	1.564	26
	14541	93.514	107	4.252	14.333	1.966	20
	14542	100.452	124	2.835	19.821	2.412	35
	14543	105.160	111	5.949	18.078	2.281	21
	14544	109.800	133	6.649	17.005	2.740	31
	14545	112.306	122	4.432	19.080	2.845	22
	14546	114.745	137	2.955	20.553	3.460	29
	14547	113.795	125	1.970	18.835	3.337	28
	14548	113.496	116	5.441	12.556	3.255	26
	14549	112.677	105	4.281	10.892	3.105	16
	14550	112.410	123	3.438	14.916	2.970	23

Figure 15: Table view showing dose rate (nGy/h), total count rate (cps), concentration of ^{238}U (ppm), concentration of ^{232}Th (ppm), concentration of ^{40}K (%) and count rate of ^{137}Cs (cps)

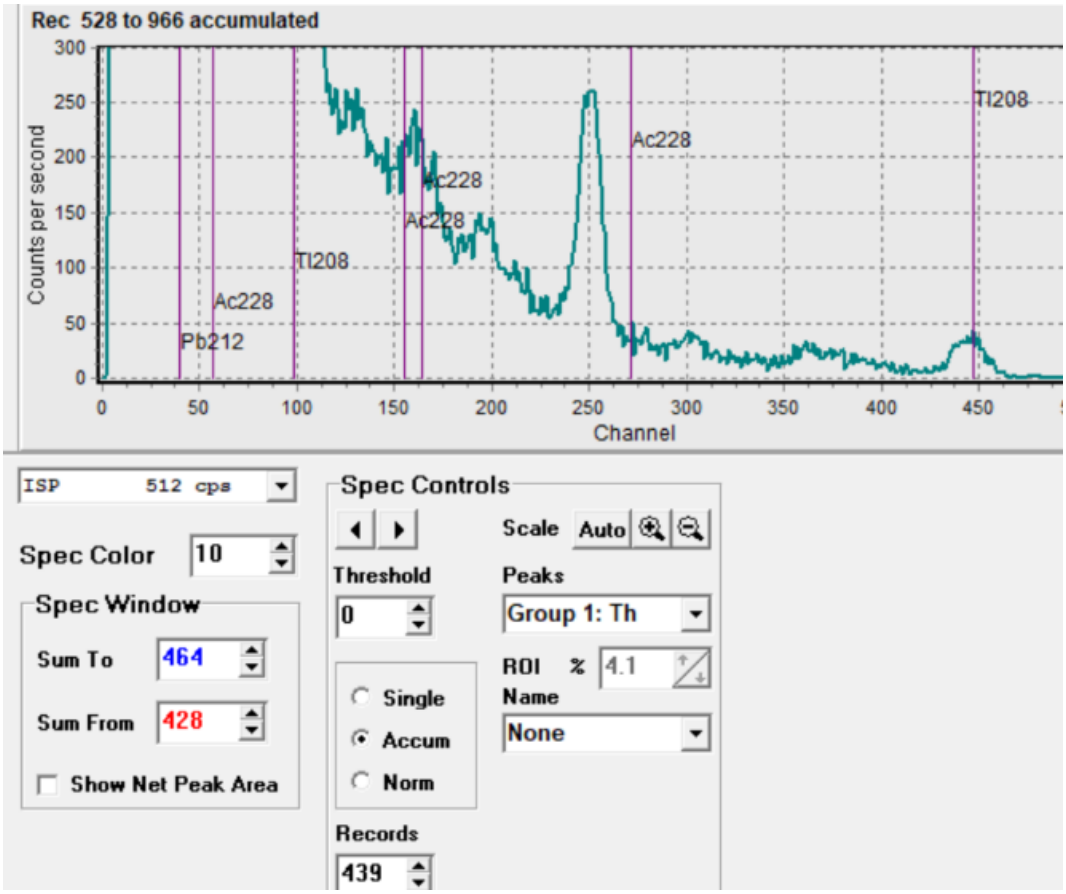

Figure 16: Spectral chart of accumulated spectrum with ^{232}Th peaks

The spectral chart of accumulated spectrum with ^{238}U and ^{40}K peaks is shown in Appendix (Figure A.5).

Data Quality Control

PEIView provides basic quality control of data files recorded by Pico Envirotec data acquisition systems of PGIS. Spectrometer and GPS data should never be repeated as repetition of data occurs in the case when the data was lost. Data repetition can be checked by QC (quality control) of data viewer.

GPS Data

If GPS time channel in Charts View with a data function set to first digital derivative (DD) appear constant (horizontal line), then the data is good (no problem in GPS data). The screenshot of first DD of GPS time channel of surveyed data is shown in Figure 17. The chart values "1" indicates that the rate of sampling of GPS receiver is once per second.

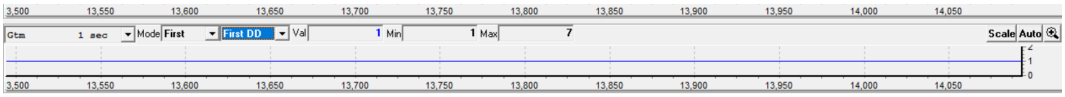

Figure 17: The first digital derivative of GPS time channel of surveyed data

The main problems potentially found in spectrometer data are: potassium line not straight, spikes in total count, individual crystal status problems, gain coefficient not in range and repeated spectral data.

From Figure 11 and 14, we can see that no spikes is seen in total count and the potassium line of surveyed data is straight. The crystal status problem also can be checked from data viewer. Spectrometer status is an ASCII data channel and named as ISPS. Spectrometer status indicates the element that the crystal is tuned on. Each crystal has its own status value. Indication of "N", "A" and "0" means problems. During the survey, the crystal was mainly tuned with element "T" and sometimes with element "K" where T indicates thorium and K indicates potassium element peak (Figure 18). The chart view of tuning status is shown in Appendix (Figure A.6).

Figure 18: Examples of spectrometer status

Automated QC

The automated QC function is also provided in data viewer for fast quality control. The data in a spectrometer and GPS file are checked and are analyzed. Spectrometric status was found ok and there was no repetition of data (Figure 19).

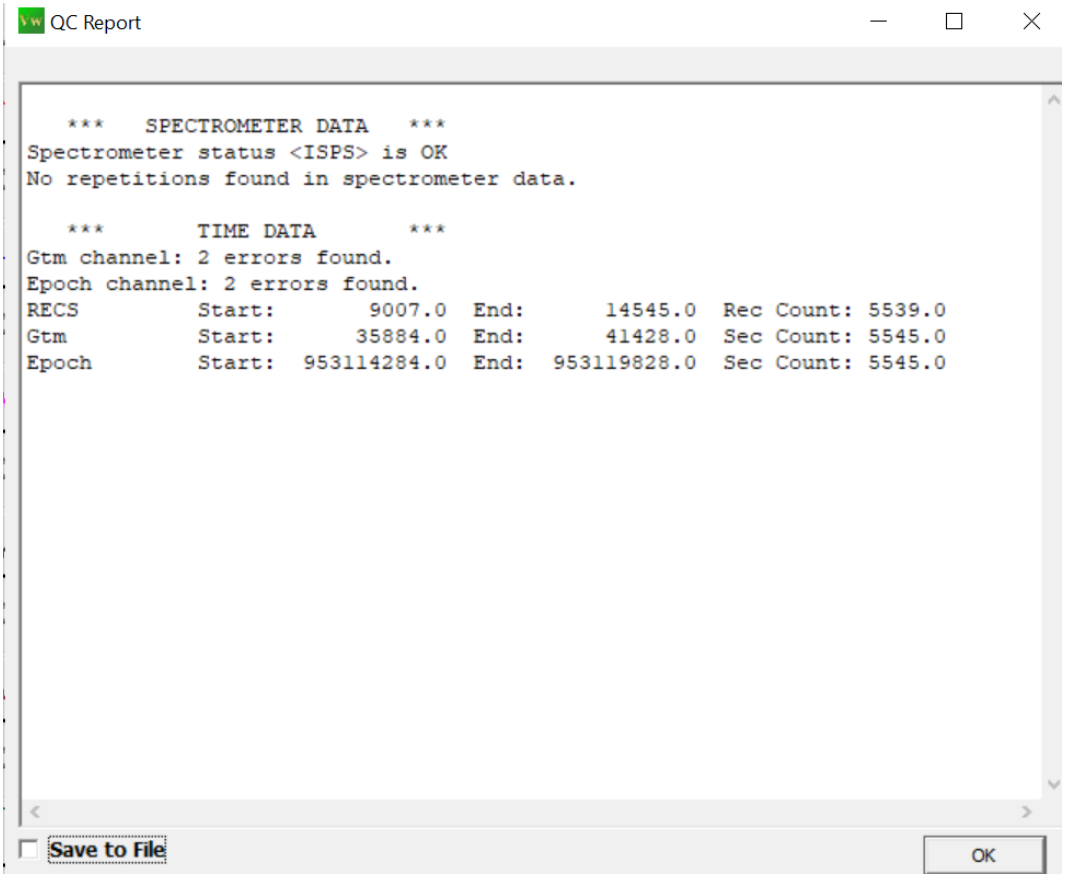

Figure 19: QC Report

3.8.2 Detector and Pulse Processing

The detector comprises a scintillation crystals of NaI(Tl) coupled with a photomultiplier tube (PMT) and high voltage supply. The detector is also coupled with multichannel analyzer (MCA) along with preamplifier and analog to digital converter (ADC). The block diagram is shown in Figure 20.

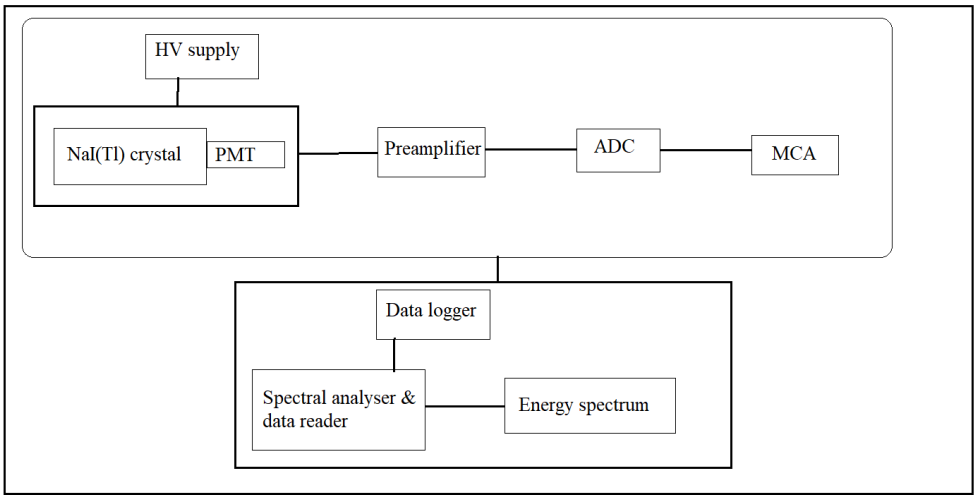

Figure 20: Block diagram of PGIS 2 spectrometer

A gamma ray photons incident on detector interacts with the crystal (NaI(Tl)) and produce scintillations (photons of visible light) which induce the electrons ejection from the photocathode of the PMT. The electron number multiplies progressively and produces an electron cloud at dynode of PMT which strikes the anode. Ultimately, a negative voltage pulse as output is produced with an amplitude proportional to the incident photon energy (Knoll, 2010). The output pulse is integrated by a preamplifier (charge sensitive) producing exponential decaying pulse which is digitized by ADC and processed by MCA.

3.8.3 Instrument Calibration

The estimation of the constants that converts the count rates of spectrometers to dose rates or concentrations of radionuclides is known as calibration of gamma ray spectrometer. The calibration includes the estimation of background radiation, sensitivity constants and stripping ratios. The calibration routine of PGIS 2 is based on defining the natural radiation background peaks (^{40}K, ^{238}U or ^{232}Th) and adjusting the High Voltage (HV) value. PGIS 2 calibration is automated and performed using the AGRS1 software provided with the detector (PEI, 2014). The calibration was done in the ground in open field near Central Department of Physics, Tribhuvan University in Kirtipur, Kathmandu.

Background Correction

Background radiation is from internal radioactivity of an instrument, atmospheric radon and cosmic radiation (IAEA, 2003). Therefore, background correction is made to minimize noise for increasing accuracy of the measurement. The background correction of the PGIS 2 spectrometer is made by adjusting high voltage for linearity with natural

radionuclides peaks which is based on the detector volume and background radiation (PEI, 2010).

Calibration for Assaying ^{40}K, ^{238}U and ^{232}Th

The gamma ray spectrometer calibration for assaying ^{40}K, ^{238}U and ^{232}Th are done using calibration pads. The calibration requires the estimation of stripping ratios and sensitivity constants. A calibration pad is a concrete slab containing known radioelements concentrations. The dimension for cylindrical pads recommended by IAEA is 3 m in diameter and 0.5 m in thickness (IAEA, 1989). The pads are enriched either in ^{40}K, ^{238}U or ^{232}Th. The concentrations recommended by IAEA are 8% K in the K- pad, 125 ppm Th in the Th- pad and 50 ppm U in the U- pad. The fourth pads are for background. The concentrations of pads used for calibration of PGIS 2 are given in Table 3. The geometric correction factors for ^{40}K, ^{238}U and ^{232}Th were 1.17, 1.17 and 1.19 respectively.

Table 3: Concentrations of ^{40}K, ^{238}U and ^{232}Th in transportable calibration pads (PEI, 2014)

Pad	K (%)	eU (ppm)	eTh (ppm)
Blank	1.410 ± 0.010	0.970 ± 0.030	2.260 ± 0.100
^{40}K	8.710 ± 0.090	0.320 ± 0.020	0.740 ± 0.100
^{238}U	1.340 ± 0.020	52.900 ± 1.000	3.400 ± 0.140
^{232}Th	1.340 ± 0.020	2.960 ± 0.060	136.000 ± 2.100

The ^{40}K, ^{238}U and ^{232}Th window count rates obtained over the pads are related linearly to the concentrations of K, Th and U in the pads. If n_i (i=1, 3) be the count rate in the i_{th} energy window (^{40}K, ^{238}U or ^{232}Th), and s_{ij} (i=1, 3; j= 1, 3) be the sensitivity of i$_{th}$ count rate to the concentration of the j$_{th}$ element (^{40}K, ^{238}U or ^{232}Th) then (IAEA, 2003),

$$n_i = S_{i\mathrm{k}}C_{\mathrm{k}} + S_{i\mathrm{U}}C_{\mathrm{U}} + S_{i\mathrm{Th}}C_{\mathrm{Th}} + {}_{ni}BG \tag{3.63}$$

where,

n_i = count rate in the i$_{th}$ energy window (cps), i = 1,2,3

S_{ij} = sensitivity of the spectrometer for the detection of j_{th} element in the i_{th} energy window (cps per unit concentration of the j_{th} element)

C_j = concentration of j_{th} element (% K, ppm U, ppm Th)

${}_{ni}BG$ = background count rate in the i_{th} energy window (cps)

Since, ^{40}K, ^{238}U and ^{232}Th measurement is made in 3 energy window and background

count rates $_{ni}$BG can be subtracted, the equation (3.63) in matrix form can be written as

$$N = SC \tag{3.64}$$

Where,
N = column vector of background - corrected count rates (n_i-n_{iBG})
S = 3×3 matrix of sensitivities (S_{ij})
C = column vector of concentrations (C_K,C_U,C_{Th})
The equation (3.63) can be modified as

$$n_i - n_{iBG} = S_{i\mathrm{k}}\Delta C\mathrm{K} + S_{i\mathrm{U}}\Delta C\mathrm{U} + S_{i\mathrm{Th}}\Delta C\mathrm{Th} \tag{3.65}$$

where,
Δ C_j = difference between the concentrations of the j_{th} element in a calibration pad and the concentrations of the j_{th} element in the background pad. Equation (3.65) in matrix notation can be written as

$$N = S\Delta C \tag{3.66}$$

where,
N = 3×3 matrix of corrected background count rates (n_i- n_{iBG})
S = 3×3 matrix of sensitivities (S_{ij})
ΔC = 3×3 matrix of differential concentrations of ^{40}K, ^{238}U and ^{232}Th in ^{40}K, ^{238}U and ^{232}Th pad minus ^{40}K, ^{238}U and ^{232}Th in background pad. The sensitivity matrix may be estimated by

$$S = N\Delta C^{-1} \tag{3.67}$$

The sensitivities are in units of count rates per unit concentration. The window sensitivities of detector is given in Table 4.

Table 4: Window sensitivities of detector for infinite sources (PEI, 2014)

window	Sensitivities
^{40}K	3.242 ± 0.043 cps per %
^{238}U	0.272 ± 0.003 cps per ppm
^{232}Th	0.127 ± 0.002 cps per ppm

The stripping ratio are used to estimate the net count rate of a one element in an energy window. The stripping ratios is defined as the ratios of count rates caused by one

element in an energy window to the count rate of that element in its principal energy window. The ratio gives the measurement of energy resolution. If the ratio is smaller, better is the resolution of the detector.

For ^{40}K, ^{238}U and ^{232}Th energy windows ($i = 1$, 2 and 3), the stripping ratios ($\alpha, \beta, \gamma, a, b$ and g) are calculated by the ratio of sensitivities:

$$\alpha = \frac{S_{2\text{Th}}}{S_{3\text{Th}}} \quad \beta = \frac{S_{1\text{Th}}}{S_{3\text{Th}}} \quad \gamma = \frac{S_{1\text{U}}}{S_{2\text{U}}} \tag{3.68}$$

$$a = \frac{S_{3\text{U}}}{S_{2\text{U}}} \quad b = \frac{S_{3\text{K}}}{S_{1\text{K}}} \quad g = \frac{S_{2\text{K}}}{S_{1\text{K}}} \tag{3.69}$$

where α is the Th into U stripping ratio, a is the U into Th stripping ratio, β is the Th into potassium stripping ratio, b is the K into Th stripping ratio, γ is the U into K stripping ratio, and g is the K into U stripping ratio (IAEA, 2003). The stripping ratio of the PGIS 2 is given below (PEI, 2014).

α = 0.5267 $\pm$ 0.0100 β = 0.6791 $\pm$ 0.0195 γ = 0.9904 $\pm$ 0.0187

a = 0.0314 $\pm$ 0.0044 b = 0.0017 $\pm$ 0.0020 g = 0.0013 $\pm$ 0.0022

3.8.4 Data Processing

The number of counts N recorded in a particular energy window for a counting time, t can be converted to a count rate, $n = N/t$ (cps). PGIS 2 automatically correct for instrument dead time by extending the counting time. It is also calibrated to give an estimate of the terrestrial dose rate directly by converting radioelement concentrations.

3.8.5 Errors

The main factors reducing assay precision are the statistical nature of radioactivity, variable water contents in rocks and variable background radiation due to atmospheric radon. About 0.1% K, 0.4 ppm eU and 0.6 ppm eTh precision is expected with scintillation gamma ray spectrometer from field survey using 4 minutes sampling time (IAEA, 2003).

3.8.6 Spectral Data Processing

In present work, the window based method (IAEA, 2003) was used to process the PGIS 2 spectra. The elemental activity concentrations are extracted from spectral windows ^{40}K, ^{238}U and ^{232}Th. The results were reported in terms of potassium (K), equivalent uranium (eU) and equivalent thorium (eTh). eU and eTh imply that parent concentrations are inferred from decay products assuming homogeneous distribution and secular equilibrium.

3.8.7 Spectrum Fitting

The least square (LSQ) fitting of natural radionuclides photopeaks in the measurement of spectra utilizing model detector responses was performed using Praga 4 Ground software (PEI, 2008). Praga 4 can perform: Standard window based processing, Principal component analysis (PCA), Least-squares (LSQ) fitting based on model detector responses, spectrum restoration (smoothing) and Radon detection and removal. The Compton scattering and photopeak resolution was derived by Monte Carlo simulation. LSQ fitting determine the net photo-peak areas in specific windows from the sum of squares random error (R^2) (Debertin & Helmer, 1988).

$$R^2 = \Sigma_i \omega_i (N_i - f_i)^2 \tag{3.70}$$

where $Ni \pm \sigma(Ni)$ are the measured peak areas, ω_i = $\sigma(Ni) - 2$ is the weighting factor and f_i is the calculated peak areas. A portable spectrometers with low volume detectors produce a very low number of counts per second and typical accumulated one second spectrum is virtually empty. As standard window or LSQ fitting processing techniques are unsuitable for spectra with zero counts over many channels, either the database should contain accumulated spectra over sufficient time (over 100 seconds for small 3 inch detectors) or if one second spectra were collected, stacking option should be used for processing. The benefit of LSQ fitting is mainly in environmental applications including monitoring of man-made radioactivity. In addition to ^{40}K, ^{238}U and ^{232}Th, Praga 4 can discriminate up to 9 anthropogenic nuclides at once and can gives results in activity or exposure/dose rates. The final model detector responses for natural radionuclides are normalized so that count rates over their respective (IAEA) standard windows are equal to one. Window based sensitivity calibration constants are applied for fitting process output to get results in activity. The final model responses for manmade radionuclides are calculated per 1 Bq/m^2 and therefore the fitting process gives results in activity/area.

The three or four spectral windows is monitored in conventional approach for getting and processing gamma spectrometric data (Figure 21, Table 5). The photo peak energy being monitored is shown after each nuclide in brackets. The energy window "K" monitors the gamma rays energy 1.46 MeV emitted by ^{40}K. The energy windows "U" and "Th" monitor gamma ray emitted from the decay products in the ^{238}U and ^{232}Th decay series. For the measurement of ^{40}K, ^{238}U and ^{232}Th these windows are accepted as the most suitable. The total count window monitors total radioactivity (IAEA, 2003).

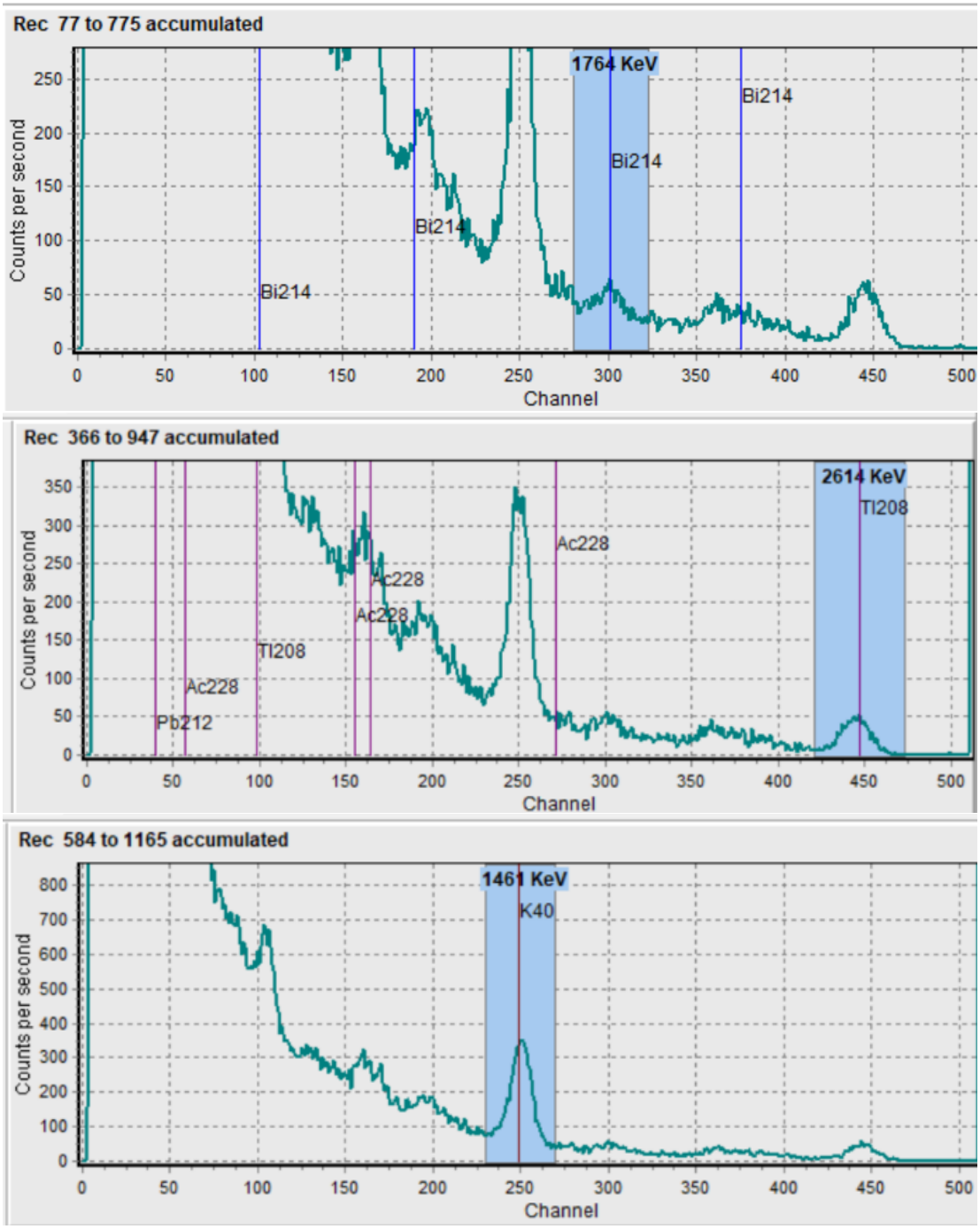

Figure 21: Typical gamma ray spectrum showing the position of energy windows

Table 5: Recommended energy windows for radioelement mapping of gamma rays (IAEA, 2003; PEI, 2014)

Window	Radionuclides	Energy range (keV)	Emission probability (%)
Total count		400 to 2810	
^{238}U	^{214}Bi (1764 keV)	1660 to 1860	15.3
^{232}Th	^{208}Tl (2614 keV)	2410 to 2810	99.7
^{40}K	^{40}K (1461 keV)	1370 to 1570	10.7
^{137}Cs	^{137}Cs (662 keV)	574 to 762	

3.8.8 Specific Activity Determination

The count rates in energy windows and the concentrations of radioelement corresponding to count ratios are estimated from stripping ratios using the stripping method (IAEA, 2003). Assuming the stripping ratio ($b = g = 0$), the net count rates of the j_{th} element in window i are given by equations (3.71-3.73) and the concentrations by equation 3.74.

$$n_{3\text{Th}} = \frac{(n_3 - n_{3BG} - a(n_i - n_{2BG}))}{(1 - \alpha a)} \tag{3.71}$$

$$n_{2\text{U}} = n_2 - n_{2BG} - \alpha n_{3\text{Th}} \tag{3.72}$$

$$n_{1\text{K}} = n_1 - n_{1BG} - \beta n_{3\text{Th}} - \gamma n_{2\text{U}} \tag{3.73}$$

$$C_{\text{K}} = \frac{n_{1\text{K}}}{S_{1\text{K}}} \quad C_{\text{U}} = \frac{n_{2\text{U}}}{S_{2\text{U}}} \quad C_{\text{Th}} = \frac{n_{3\text{Th}}}{S_{3\text{Th}}} \tag{3.74}$$

For PGIS 2 spectrometer, dead time is corrected automatically (PEI, 2013). The number of counts (N) in a specific window for a specific time (t) are directly converted to count rate, $n = N/t$ (cps) and corresponding radioelement concentrations. The conversion factor for radio elemental mass concentration to specific activity is given in Table 6. The theoretical gamma dose rates at 1 m above an infinite and plane homogeneous medium (soil) per unit concentration of radioelements considering equilibrium uranium and thorium decay series is given in Table 7.

Table 6: Radioelement mass concentration conversion to specific activity (IAEA, 2003)

Radioelement concentration	Specific activity
1 ppm eU	12.35 Bq/kg (^{238}U or ^{226}Ra)
1 ppm eTh	4.06 Bq/kg (^{232}Th)
1% K	313 Bq/kg (^{40}K)

Table 7: Theoretical gamma dose rates per unit radioelement concentration (Løvborg, 1984; IAEA, 2003)

Radioelemental concentration	Dose rate (nGy/h)
1% K	13.078
1 ppm U	5.675
1 ppm Th	2.494

3.9 Absorbed Dose Rates and Risk Factors

The total absorbed dose rate in air at 1 m above the ground (assuming infinite homogeneous soil medium) is given directly by a PGIS 2. The dose rates from particular radionuclides are calculated from measured radioelement concentration using the conversion factor given in Table 7 and the mass concentration measured was converted to activity concentrations using conversion factor given in Table 6. The absorbed dose rates can also be calculated from specific activity concentrations of radionuclides (A_U, A_{Th} and A_K) using conversion factors (equation 3.75). The annual effective dose is estimated using equation 3.76 (UNSCEAR, 2000).

$$D(\text{nGy/h}) = 0.462A_{\text{U}} + 0.604A_{\text{T}h} + 0.042A_{\text{K}} \tag{3.75}$$

$$AED(\text{mSv}) = D \times 0.7 \times 0.2 \times 8760 \tag{3.76}$$

where 0.7 is the gamma conversion coefficient from absorbed dose to effective dose in air, 0.2 is outdoors occupancy factor and 8760 is hours in a year.

The collective effect of the activity concentrations of ^{40}K, ^{238}U and ^{232}Th radionuclides in a building materials can be estimated by a single quantity "hazard index" (Bavarnegin et al., 2013). Among different hazard indices, external radiation hazard (H_{ex}), is used for the assessment of radiological hazard of building materials . The rocks and soils in the study area are also used for building purpose. Therefore, to limit the dose from building materials to recommended limit, the external hazard index of gamma radiation from NORM, H_{ex} is calculated using equation (3.77) (Beretka & Matthew, 1985). H_{ex} must be less than one for insignificant radiation hazard as the recommended dose limit for public is 1 mSv (ICRP, 2007). It is obtained from upper limit of radium equivalent activity.

$$H_{ex} = \frac{A_{\text{U}}}{370} + \frac{A_{\text{T}h}}{259} + \frac{A_{\text{K}}}{4810} \tag{3.77}$$

Excess lifetime cancer risk (ELCR) is calculated using equation (3.78). It represents the number of extra cancer expected to ionizing radiation at a given dose in a human

(Taskin et al., 2009).

$$ELCR = AED \times LE \times RF \tag{3.78}$$

where LE is the life expectancy (66.2 years) for Nepali (http://en.worldstat.info/Asia/Nepal) and RF is the risk factor (0.05 /Sv) for public (ICRP, 2007).

For anthropogenic radionuclides (^{137}Cs), surface activity concentration is measured by a PGIS 2. The outdoor absorbed dose rate in air at 1 m above the ground surface for ^{137}Cs is calculated using equation 3.79 (Jacob et al., 1994) and the external annual effective dose is estimated using equation 3.80 (Taira et al., 2013).

$$D(\text{nGy/h}) = 7.6 \times 10^{-4} \times C \tag{3.79}$$

$$AED(\mu Sv) = D \times 0.7 \times 0.2 \times 8760 \times S \tag{3.80}$$

where C is the surface activity concentration in kBq/m^2 and S is the shielding factor for 1 m above the ground (0.7 for usual land) (IAEA, 2000).

3.10 Study Area

The Kathmandu and Makawanpur district lies in Bagmati province in central part of Nepal. The study area is hilly area covered by mountains in north and the plains in south whereas Kathmandu (starting point) and Hetauda (final site) is valley. It lies within the latitude N 27.503° to 27.684° and longitude E 85.042° to 85.330° at an altitude of 384 m to 1872 m ASL.

The survey was carried along the road (more than 100 km) which was unpaved (dirt or gravel road) and somewhere paved. Balkhu, Kirtipur, Chobhar, Dakshinkali, Bansbari, Satikhel, Pharping, Lamagaun, Humane, Bhanjyang, Rakash Khola, Fakhel, Markhu, Sukaura, Mahalakshmi Khola, Salle, Kalanki, Kulekhani, Bhim Khola, Deurali, Chishapani Gadhi, Bhimphedi, Jurikhet, Dhorsingh, Mandu, Ghatte Khola, Golping Beshi, Tansen Bridge, Nibuwatar, Pandrang, Bhaishe, Taubas, Trikhandi, Baghjhora and Hetauda are the places between Kathmandu and Makawanpur district along the road surveyed. Chhaimale, Sundararadevi and Sisneri were also covered during the survey (Figure 22). The sites contains different kinds of rocks and soils (Figure 23) along with thick vegetation. The paddy field, vegetable garden, rivers, lakes and some small villages were observed during the survey. The photos of the rocks, soil, rivers, lake and paddy fields are shown in Appendix (Figure A.7 and A.8). The depth distribution of radionuclides studied at eight different locations within the survey area is shown in appendix (Figure A.9). The survey was also carried in the adjoining area (famous village) along the way and in Hetauda city. The eight locations used for depth profile study and the locations of surveyed adjoining area are shown in Figure 24 and 25 respectively. The

dose rates were also assessed along the bank of the rivers and around the lakes that lies within the studied area. The GPS location of studied area is given in Table 8.

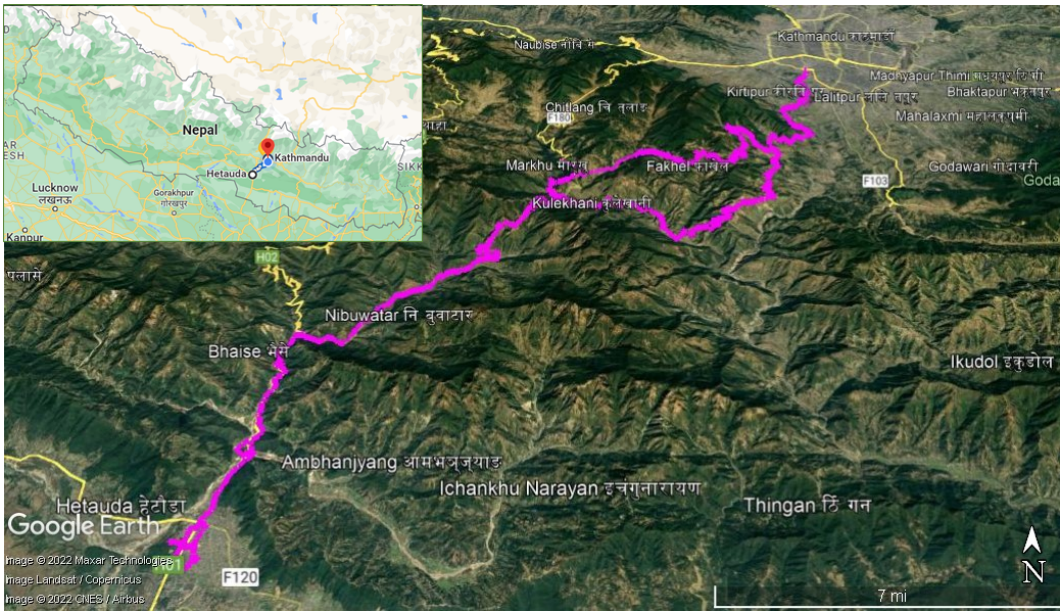

Figure 22: Map showing the surveyed path overlaid on geographical terrain

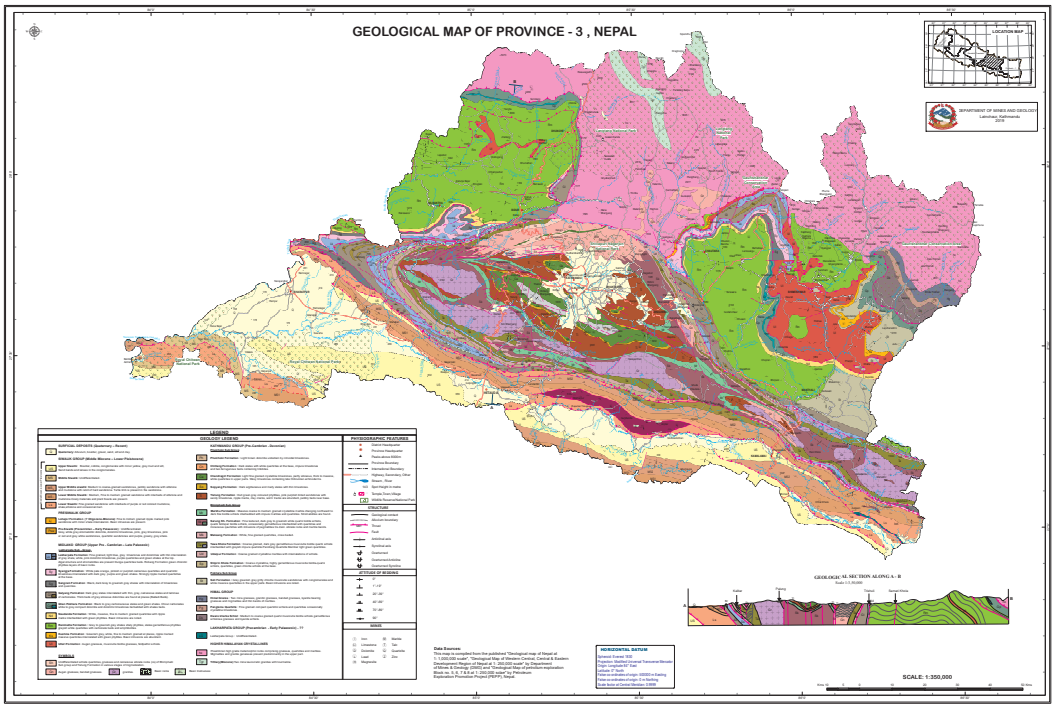

Figure 23: Map indicating geological feature of Bagmati province, Nepal (DMG, 1994)

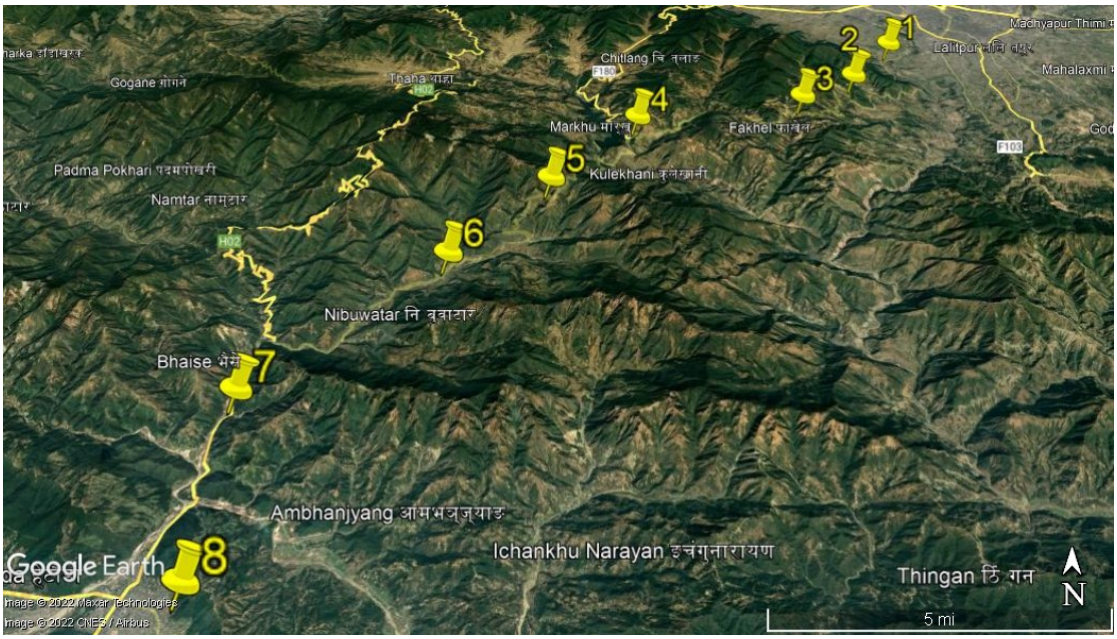

Figure 24: Vertical depth measurement sites (1. Chobhar, 2. Pharping, 3. Rakash Khola, 4. Salle, 5. Chisapani Gadhi, 6. Dhorsingh, 7. Baghjhora, 8. Hetauda)

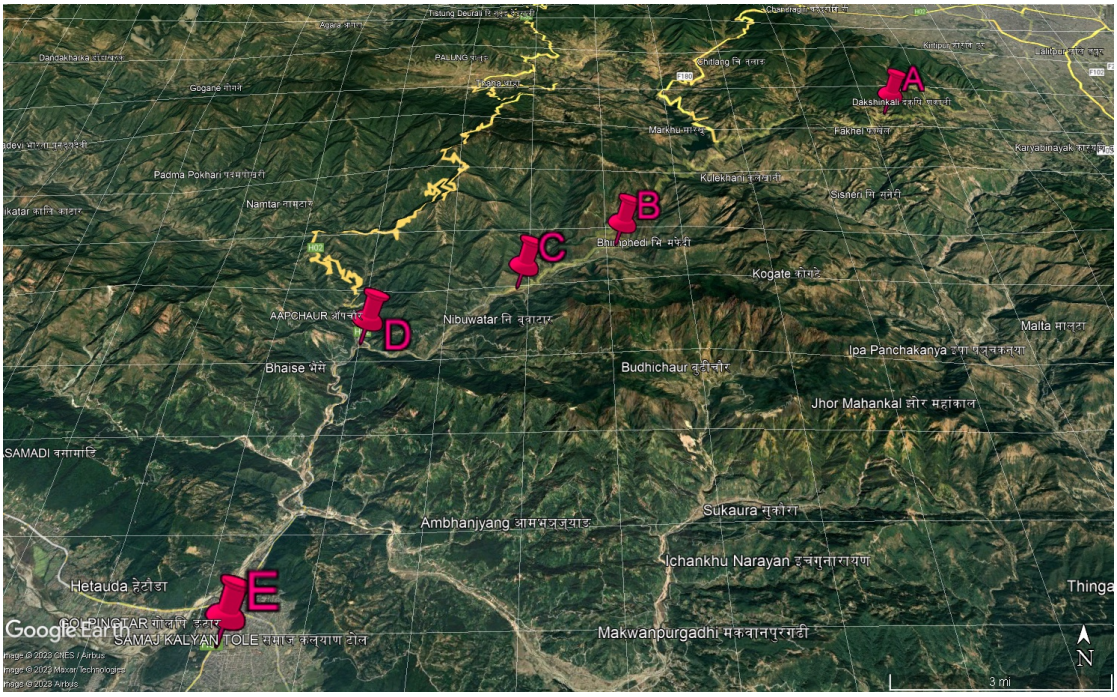

Figure 25: Surveyed adjoining area (A. Rakash Khola, B. Bhimphedi, C. Golping Besi, D. Bhaise and E. Hetauda)

Bare soil, rock outcrops on the hills and farming activity along the hill slopes were observed during the survey. A ground based survey on foot was performed from Balkhu chowk (Kathmandu) to Buddha chowk (Hetauda). The survey was carried from Balkhu to Dakshinkali, from Dakshinkali to Kulekhani (both road was covered i.e. via Pharping

(Lamagaun) and via Sisneri) and from Kulekhani to Hetauda. Both road was covered during the survey as the high dose rate measured was along Kulekhani.

Table 8: GPS location of study area

Sites	N Latitude (deg)		E Longitude (deg)		Altitude (m)	
	Min	Max	Min	Max	Min	Max
Kathmandu to Hetauda	27.414093	27.684404	85.02316	85.298637	395	1879
Kathmandu to Lamagaun	27.606254	27.684404	85.244003	85.298637	1222	1643
Lamagaun to Kulekhani	27.593044	27.609035	85.159900	85.247345	1507	1840
Dakshinkali to Kulekhani	27.556629	27.613056	85.15427	85.268158	1086	1789
Kulekhani to Bhimphedi	27.536581	27.591352	85.10683	85.157623	886	1879
Bhimphedi to Hetauda	27.414093	27.537495	85.02316	85.106827	395	881
Adjoining environs						
Raksh Khola	27.604836	27.609062	85.22903	85.233131	1704	1759
Golping Besi	27.527248	27.532400	85.09033	85.101005	752	845
Bhaise	27.506765	27.510317	85.04713	85.052483	519	569
Hetauda	27.414093	27.430925	85.02316	85.035705	417	469
Water resources						
River						
Chobhar	27.648611	27.65225	85.28697	85.289482	1208	1217
Sisneri (Dakshinkali)	27.556641	27.558187	85.21096	85.21257	1094	1104
Mahalaxmi	27.602148	27.606151	85.18735	85.195869	1533	1608
Sisneri (Kulekhani)	27.577574	27.57905	85.18054	85.182663	1198	1209
Bhaise Dobhan	27.506998	27.510317	85.04713	85.048523	520	556
Samari (Rapati)	27.455564	27.462061	85.03749	85.043579	396	425
Lake						
Taudaha	27.647562	27.649815	85.280334	85.283348	1231	1247
Indra Sarovar	27.589460	27.593477	85.157623	85.166458	1489	1585

3.11 Spatial Dose Rates Mapping

The maps showing gamma dose rate were created using Surfer 14 from Golden software. The spatial distribution of geo-referenced dose rates were shown using classed post map technique using round symbol and grouping them into discrete classes of colour code (Table 9).

Table 9: Colour coding for mapping of gamma dose rates

Colour	Dose rate range (nGy/h)	Description
Blue	0 to 60	up to world average
Green	60 to 120	up to twice of world average
Yellow	120 to 180	up to thrice of world average
Red	> 180	higher than thrice of world average

The measured dose rates in studied area were interpolated (gridding) using Kriging technique. In Kriging technique, the nearest grid nodes (surveyed point) was used

(Software, 2020). The spatial maps of an area was generated using the grids by semi-variogram model (Webster & Oliver, 2007).

3.12 Exploratory Analysis

The conceptual frame work for the exploratory analysis of in-situ radiometric measurements in the studied sites is shown in Figure 26. Exploratory analysis were studied using Grapher except PCA which was performed using XLSTAT from excel. The maps were produced using Surfer software from Golden software and Google pro. The scattering graphs were plotted using python.

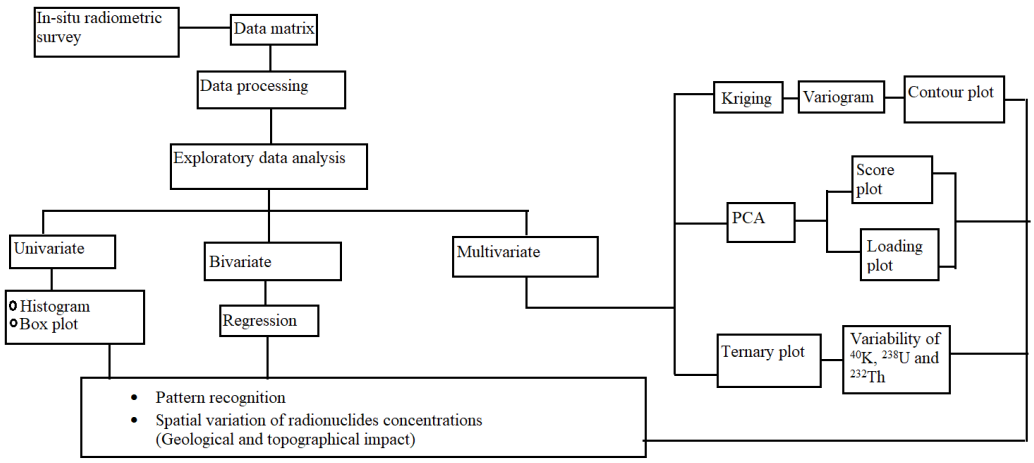

Figure 26: Frame work used in exploratory analysis of in-situ radiometric measurements in the studied sites

CHAPTER 4

RESULTS AND DISCUSSION

The results of mobile in-situ gamma ray spectrometric measurements are presented and compared with the other worldwide related studies. The statistical analysis of the results are presented in addition to radiological map. The average (mean) of the data are presented with SD (standard deviation).

The radiometric study of Kathmandu and Makawanpur district (from Kathmandu to Hetauda via Kulekhani) was conducted. The topographic factors like slope orientation, altitude and gradient have major influence on soil formation (Navas et al., 2005). As the study area from Kathmandu to Hetauda (K-H) is rugged (hills road) and has significant topographical (altitude) and geological variations for even short distance, the surveyed sites is divided in four parts: Kathmandu to Lamagaun (Pharping) (K-L), Lamagaun to Kulekhani (L-K), Kulekhani to Bhimphedi (K-B) and Bhimphedi to Hetauda (B-H) for about approximately 20 km distance for comprehensive study and analysis (Figure 27). Dakshinkali to Kulekhani via Sisneri (D-K) was also surveyed as elevated dose rates was measured in Kulekhani area. Therefore, from Dakshinkali to Kulekhani, both way (via Pharping and via Sisneri) was surveyed. Some selected adjoining environs with inhabited area (Rakash Khola, Bhimphedi, Golping Besi, Bhaise and Hetauda city) and along the water resources (Chobhar river, Taudaha lake, Sisneri (Dakshinkali) river, Mahalaxmi river, Sisneri (Kulekhani) river, Indra Sarovar lake, Bhaise Dobhan river, Samari (Rapati) river) within the study area were also studied for better understanding of gamma radiation in the area. The depth profiles up to 50 cm of soils at eight selected location were studied for understanding migration and distribution of radionuclides as they are important for environmental studies. In addition, the scattering of gamma radiations in air up to 300 cm were also studied.

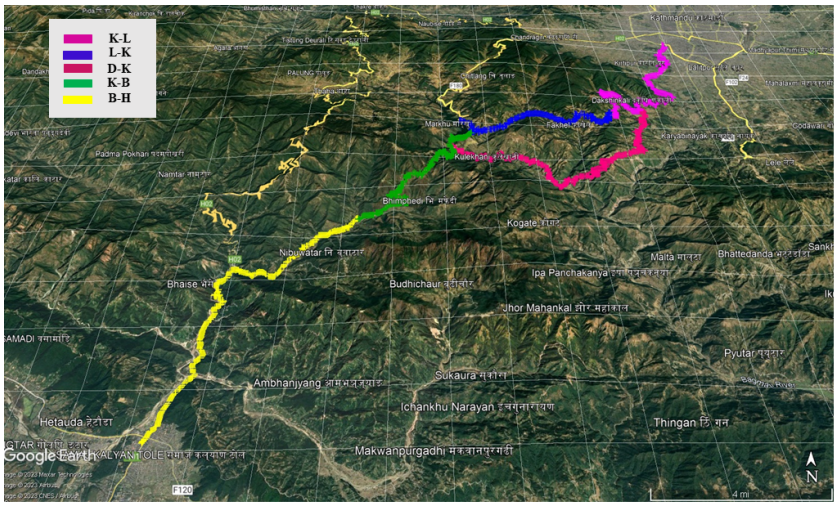

Figure 27: Map showing the sections (K-L, L-K, D-K, K-B and B-H)

4.1 Dose Rates between Kathmandu and Makawanpur District

The radiological map showing air absorbed dose rate gives the estimation of the terrestrial radiation dose to people and can identify the area with natural radiation hazards (IAEA, 1990). The measured outdoor absorbed gamma dose rates from systematic assessments in the study area were overlaid on georeferenced "geological map and topographical map" to produce a radiological map to capture spatial variability of the measured data with geology and landscape. The spatial variability of the measured radionuclides concentrations within the studied area corresponds to the underlying geology, geography and topography. The studied area have a complex geological and topographical formation. It contains more than nineteen category of rocks and have many upward and downward slopes (hill road). The area contains a rocks from surficial deposits, Siwalik group, Lakharpata subgroup of Midland group, Phulchoki and Bhimphedi subgroup of Kathmandu group along with basic rocks (Br) and granites (Gr). The Quaternary (Q) rocks from Surficial Deposits (Quaternary - Recent) group is found in Kathmandu and Hetauda valley. It contains Alluvium, boulder, gravel, sand, silt and clay. The Dunga quartzites beds (Du) and Galyng formation (Gl) from Lakharpata sub group of Midland Group (Upper Pre - Cambrian - Late Paleozoic) is found in B-H. Du contains Algal structure and stromatotites and Gl contains dark grey slates intercalated with thin, grey, calcareous slates and laminae of carbonates. The Chandragiri Formation (Ca), Chitlang Formation (Ch), Sopyang Formation (So) and Tistung Formation (Ti) from Phulchoki sub group of Kathmandu group (Pre-Cambrian - Devonian) are found between Kathmandu and Kulekhani area. Ca contains light fine grained crystalline limestones, partly siliceous, thick to massive white quartzite in upper parts and wavy limestones containing late Ordovician echinoderms, Ch contains Dark slates with white quartzites at the base, impure limestones and two ferrugenous beds containing trilobites, So contains dark

argillaceous and marly slates with thin limestones and Ti contains dull green coloured phyllites, pink purpulish sandstone with sandy limestone, clay cracks and pebbly bed near base. The Markhu Formation (Mr), Maksang Formation (Mk), Sarung Khola Formation (Sk), Tawa Khola Formation (Ta), Pandrang Quartzite (Pa) of Ta, Shiprin Khola Formation (Sp) and Udaipur Formation (Ud) from Bhim Phedi subgroup of Kathmandu group (Pre-Cambrian - Devonian) are found between Kulekhani and Hetauda. Mr contains massive coarse to medium grained crystalline marble changing northward to dark fine biotite schists interbedded with impure marbles, quartzites and stromatolites. Mk contains cross bedded, white and fine grained quartzites. Sk contains fine textured, dark grey to greenish white quartz biotite schists, quartz feldspar biotite schists, occasionally garnetiferous interbedded with quartzites, silicate rocks and marble bands. Ta contains coarse grained, dark grey garnetiferous muscovite biotite quartz schists interbedded with greyish impure quartzite, Pa contains light green quartzites, Sp contains Coarse crystalline, highly garnetiferous muscovite biotite-quartz schists, quartzites, green chlorite schists at the base and Ud contains coarse grained crystalline marbles with intercalations of schists. The Lower Siwalik (Ls), Lower middle Siwalik (MS1) and Upper Middle Siwalik (MS2) from Siwalik group (Middle Miocene-Lower Pleistocene) are also found between Kulekhani and Hetauda. Ls contains fine grained sandstone with interbeds of red coloured mudstone, shale and siltstone. MS1 contains fine to medium grained sandstone with interbeds of siltstone and mudstone along with coaly materials and plant fossils. MS2 contains medium to coarse grained sandstones, peeby sandstones with siltstone and mudstone along with turtle limb in sandstone. Limestones ores are also present within the area (DMG, 1994).

4.1.1 Dose Rates in K-H

The radiological map from Kathmandu (Balkhu Chowk) to Buddha chowk of Hetauda (Makawanpur) was shown in Figure 28 and 29. The altitude of the area varies from 395 m to 1879 m ASL showing large variation in elevation. The average dose rate (119 nGy/h) measured between Kathmandu (Balkhu Chowk) to Makawanpur (Hetauda) was found nearly twice of the world average, 60 nGy/h (UNSCEAR, 2000). The dose rate varies from 44 to 206 nGy/h with 0.8% of dose rates below the world average, 50.1% above the world average, 48.9% above twice of world average and 0.2% above the thrice of world average. The higher dose rates can be seen over Sk, Mr, Ti and Gr rocks (Kulekhani area) which consists quartz, biotite, feldspar, marble, phyllites, sandstone, limestone and granites. The lower dose rates are noticed on Q rocks (Hetauda) which contains alluvium, boulder, gravel, sand, silt and clay.

The increase in dose rate by a factor of 2 to 3 times was noticed in area. The region is mostly overlain by quartz biotite, feldspar, phyllite, sandstones, limestones, clay cracks, grained crystalline limestones, white quartzite, mudstone, marble, shale siltstone, dark

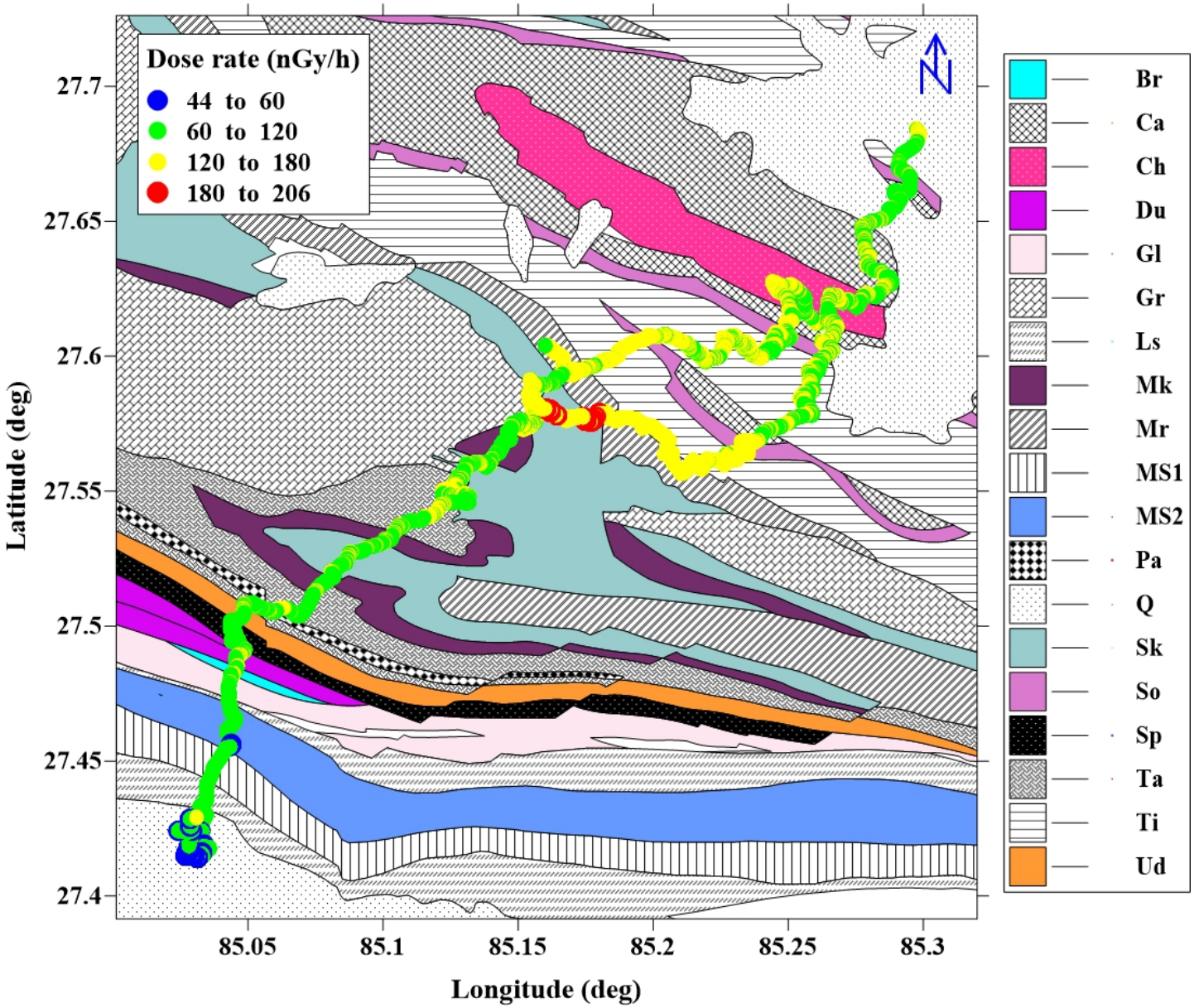

Figure 28: Radiological map of K-H overlaid on geological map

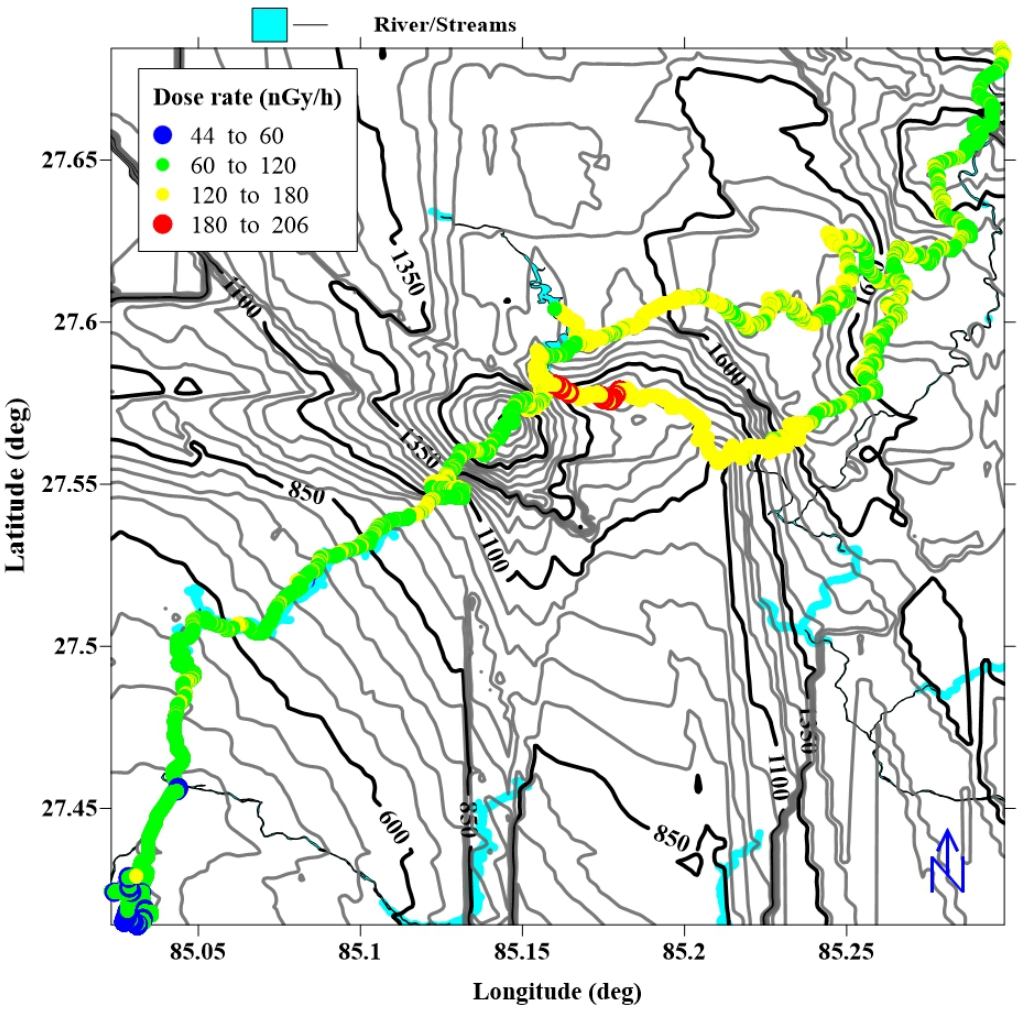

Figure 29: Dose rates in K-H overlaid on topographical map showing altitude contour

slates, grey slates, quartzites, green quartzites, basic rocks, granites, alluvium, boulder, gravel, sand, silt and clay. The radioelement (^{232}Th) have a little greater contribution to dose rates in the area. The measured dose rates are found higher at higher altitude (near Kulekhani) and lower at lower altitude (Hetauda). The kriging method is used for gridding the data for making 2D dose rates map. The smooth spatial distribution of dose rates is noticed within the area from data interpolations (Figure 30). The results obtained show a dependence of gamma dose rates on the geological properties of rocks and soils at higher altitude.

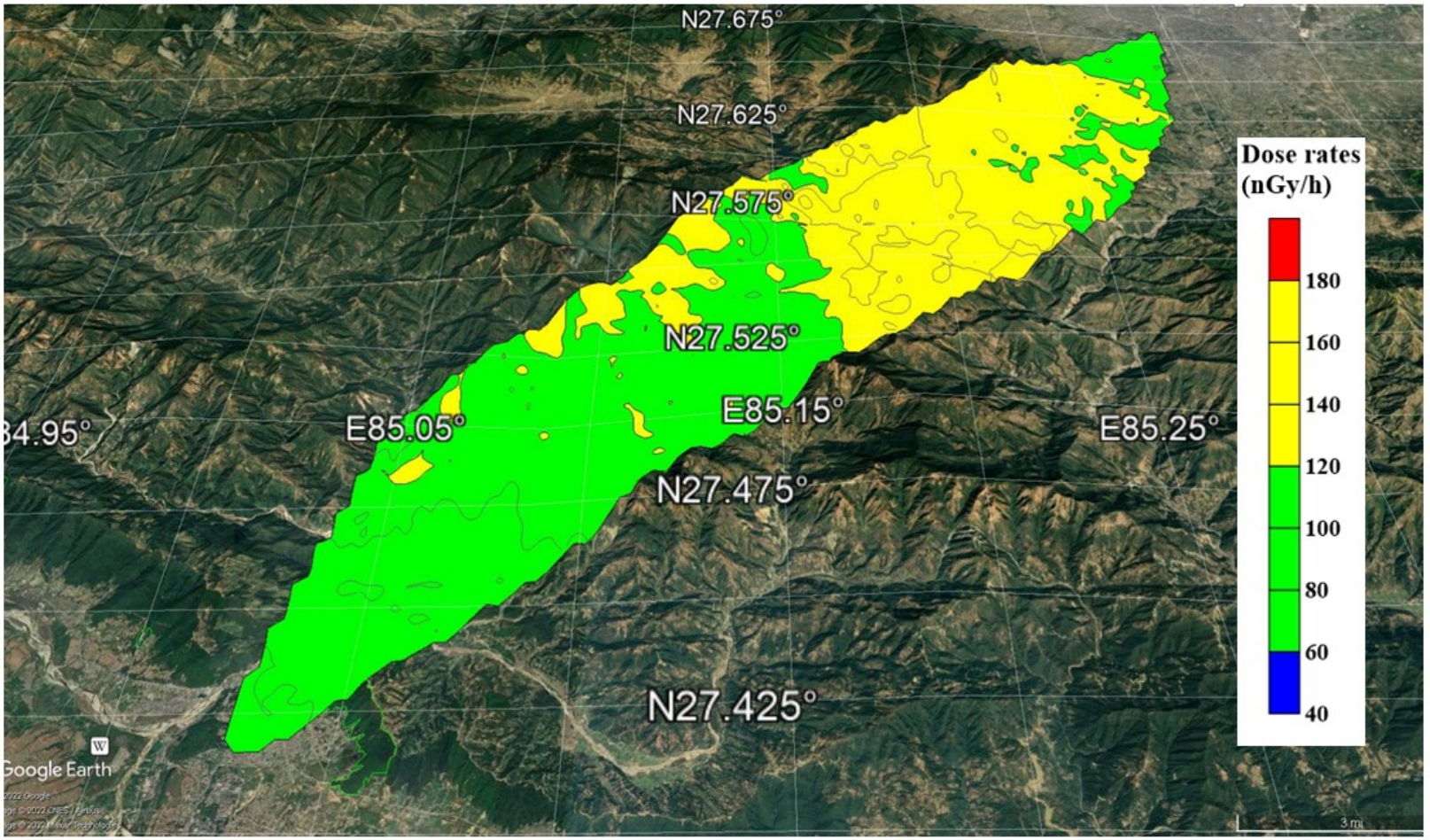

Figure 30: Contour map of dose rates in K-H overlaid on topography scenery

4.1.2 Dose Rates in K-L

The radiological map of the gamma dose rates between Kathmandu and Lamagaun is shown in Figure 31 and 32. The altitude varies from 1222 m to 1643 m ASL showing significant elevation.

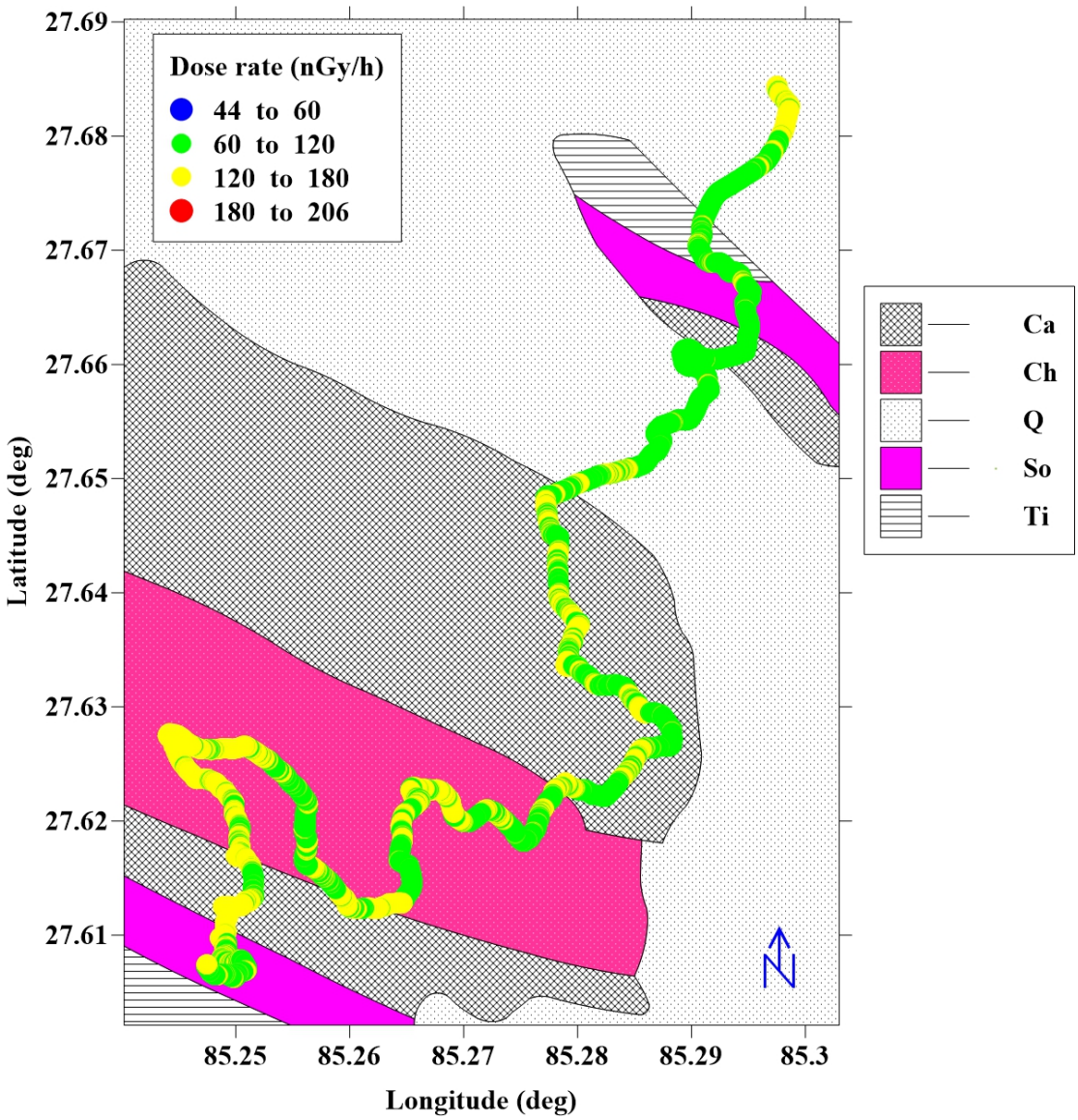

Figure 31: Radiological map of K-L overlaid on geological map

The average dose rate (116 nGy/h) measured along the road from Balkhu chowk of Kathmandu to Lamagaun (Pharping) via Chobhar was found above the world average. The dose rate ranges from 74 to 154 nGy/h with 58.8% of total dose rates above the world average and 41.2% above twice the world average. The region is mostly overlain by grained crystalline limestone, white quartzites, dark slates, trilobites, slates, limestones, alluvium, boulder, gravel, sand silt and clay. The radioelement (^{232}Th) is found to have a slightly higher contribution to dose rates in the area.

The spatial distribution of dose rates within the area with data interpolation was found smooth (Figure 33). The results obtained show a dependence of gamma dose rates on the geological properties of rocks and soil at higher altitude.

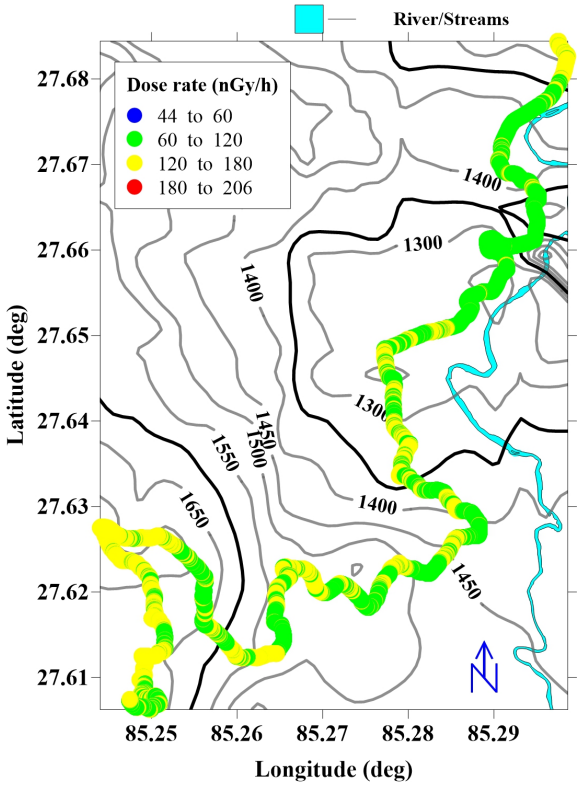

Figure 32: Dose rates in K-L overlaid on altitude contour

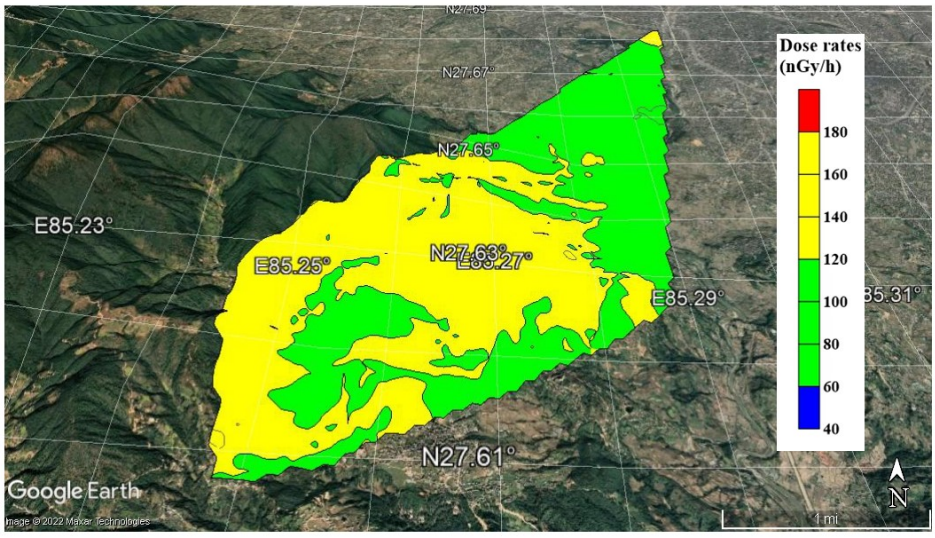

Figure 33: Contour map of dose rates in K-L overlaid on topography scenery

4.1.3 Dose Rates in L-K

The radiological map of the gamma dose rates between Lamagaun and Kulekhani is shown in Figure 34 and 35. The altitude varies from 1507 m to 1840 m ASL showing significant elevation.

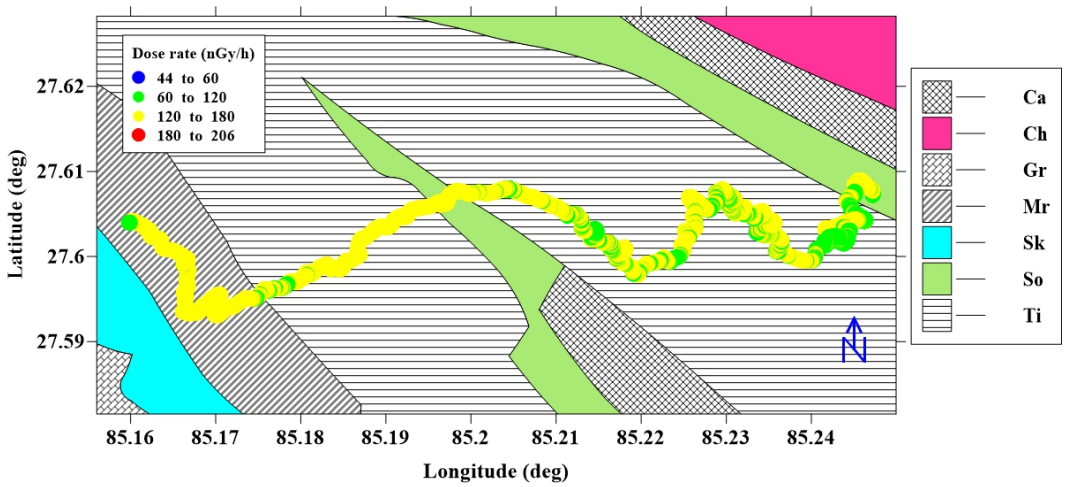

Figure 34: Radiological map of L-K overlaid on geological map

The average dose rate (130 nGy/h) measured along the road from Lamagaun (Pharping) to Kulekhani was found above the twice of world average. The dose rate ranges from 93 to 180 nGy/h with 23.8% of total dose rates above the world average and 76.2% above twice the world average. The region is mostly overlain by phyllites, sandstone, limestone, clay cracks, marbles, quartzites and slates. The radioelement (^{232}Th) have slightly higher contribution to dose rates in the area.

The spatial distribution of dose rates within the area with data interpolation was found smooth (Figure 36). The results obtained show a dependence of gamma dose rates on the geological properties of rocks and soil at higher altitude.

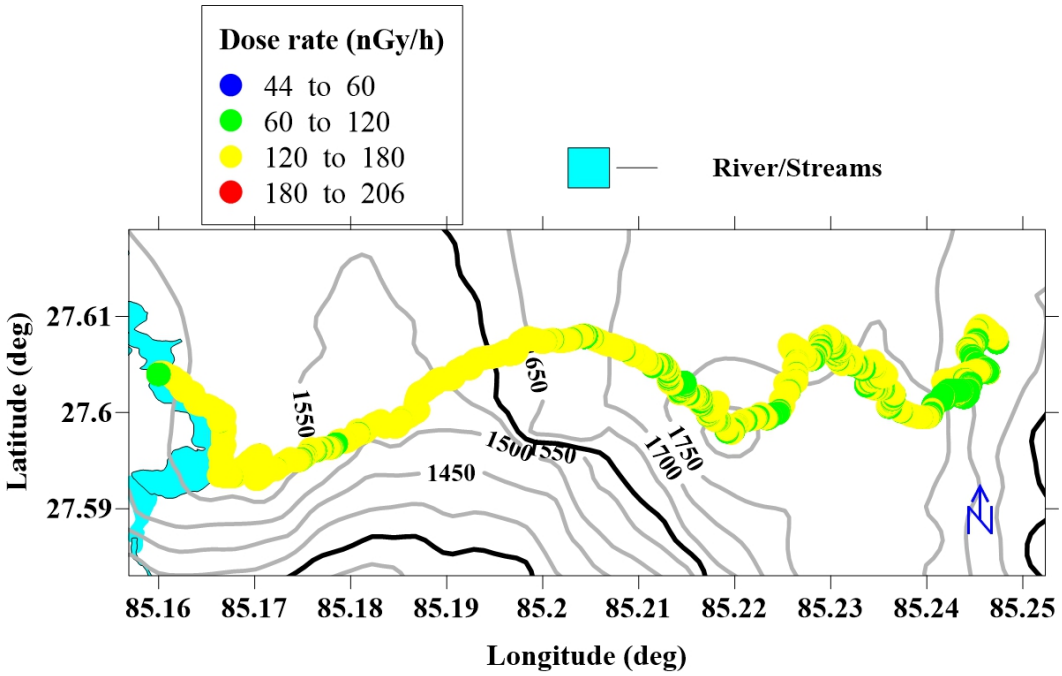

Figure 35: Dose rates in L-K overlaid on topographical map showing altitude contour

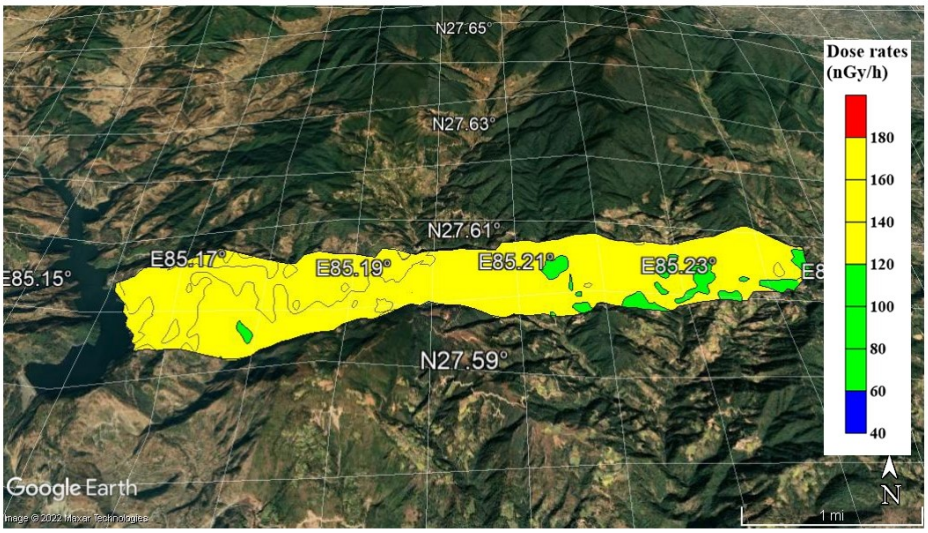

Figure 36: Contour map of dose rates in L-K overlaid on topography scenery

4.1.4 Dose Rates in D-K

The radiological map of the gamma dose rates between Dakshinkali and Kulekhani is shown in Figure 37 and 38. The altitude varies from 1086 m to 1789 m ASL showing significant elevation.

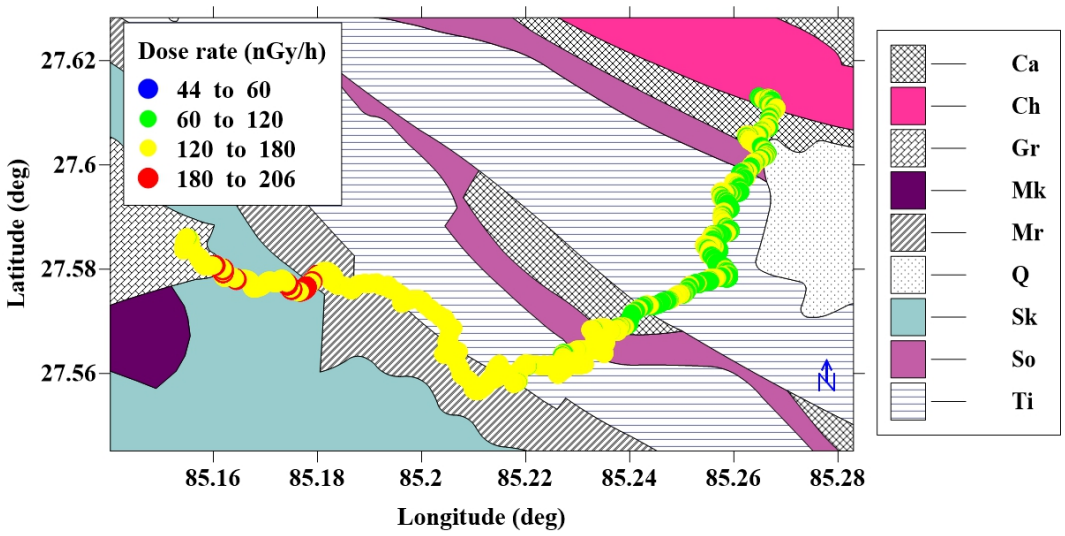

Figure 37: Radiological map of D-K overlaid on geological map

The average dose rate (139 nGy/h) measured along the road from Dakshinkali to Kulekhani via Sisneri was found above the twice of world average. The dose rate ranges from 92 to 206 nGy/h with 16.7% of total dose rates above the world average, 82.5% above twice the world average and 0.8% above thrice the world average. The region is mostly overlain by phyllites, sandstone limestone, clay cracks, marble, quartzite, slates, granites, slates, gravel, sand, boulder, silt and clay. The radioelement (^{232}Th) have a slightly higher contribution to dose rates in the area.

The spatial distribution of dose rates within the area with data interpolation was found smooth (Figure 39). The results obtained show a dependence of gamma dose rates on the geological properties of rocks and soil at higher altitude.

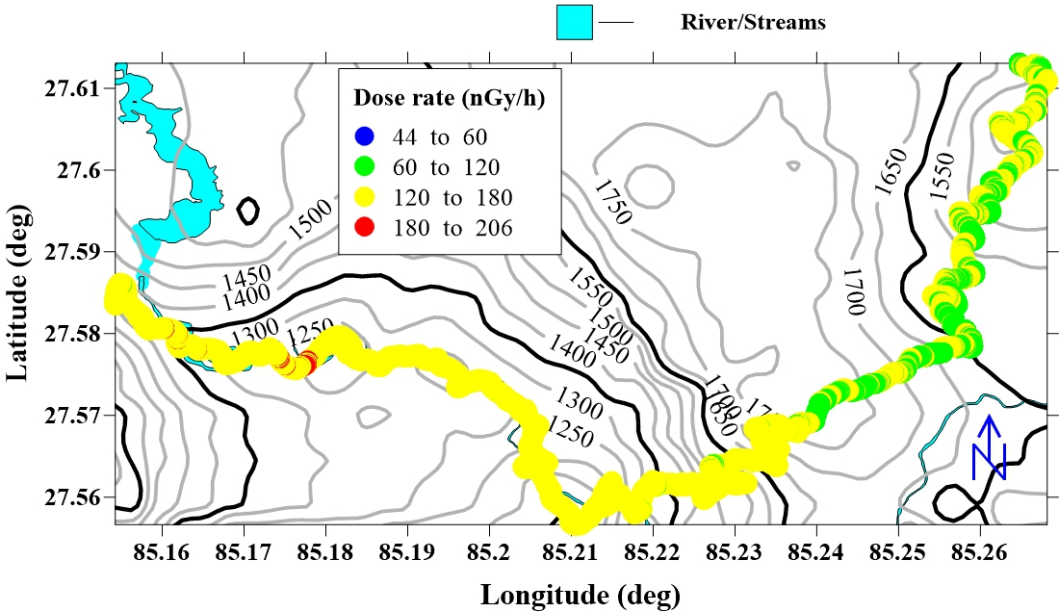

Figure 38: Dose rates in D-K overlaid on topographical map showing altitude contour

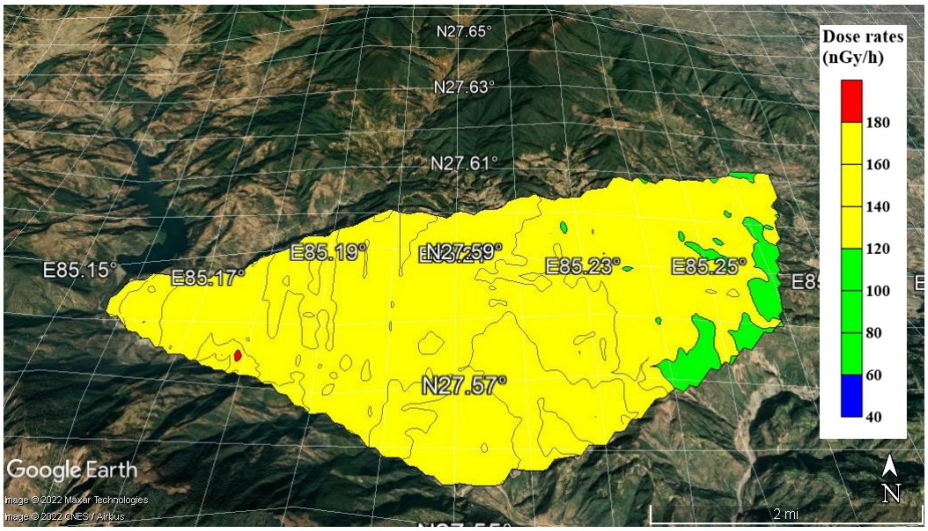

Figure 39: Contour map of dose rates in D-K overlaid on topography scenery

4.1.5 Dose Rates in K-B

The radiological map of the gamma dose rates between Kulekhani and Bhimphedi is shown in Figure 40 and 41. The altitude varies from 886 m to 1879 m ASL showing significant elevation.

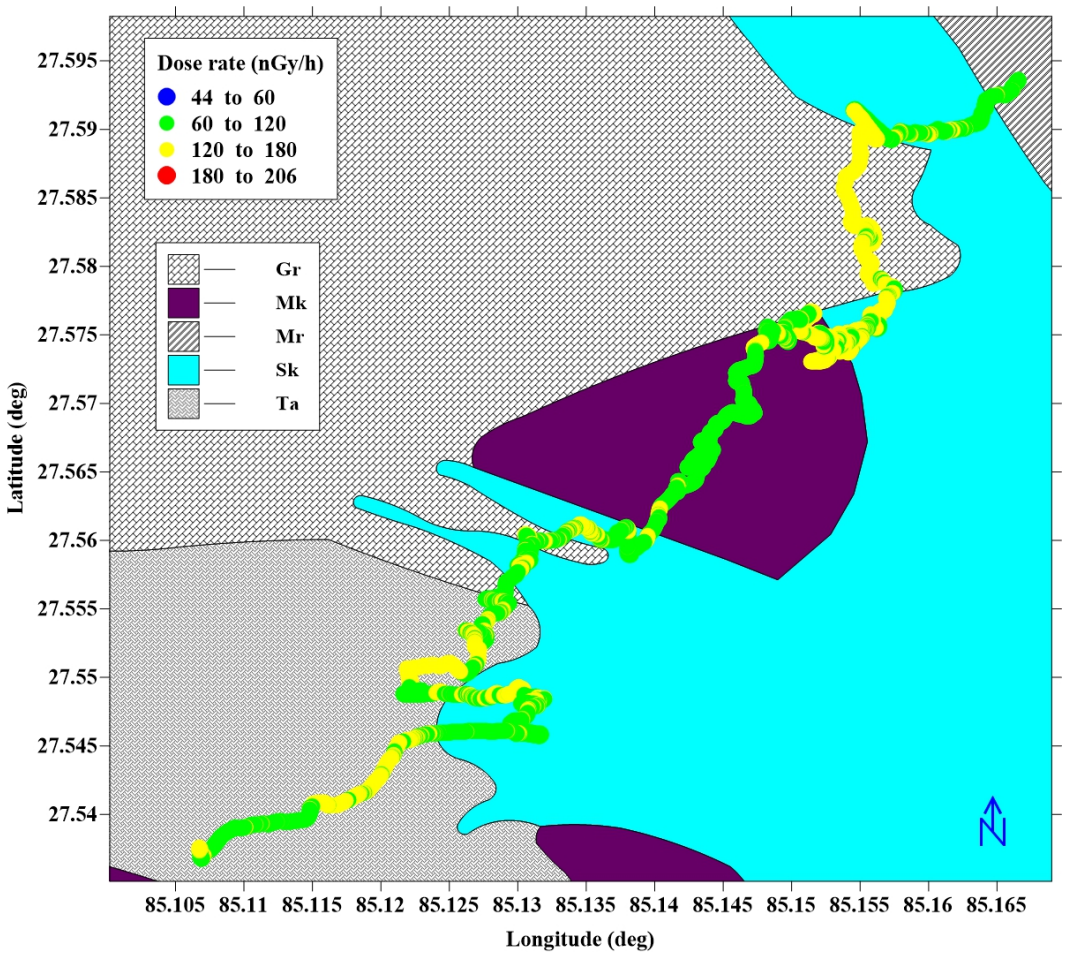

Figure 40: Radiological map of K-B overlaid on geological map

The average dose rate (119 nGy/h) measured along the road from Kulekhani to Bhimphedi was found nearly equal to the twice of world average. The dose rate ranges from 77 to 175 nGy/h with 55.7% of total dose rates above the world average and 44.3% above twice the world average. The region is mostly overlain by biotite quartz, quartzite, quartz feldspar, marble and granites. The radioelement (^{232}Th) have a slightly higher contribution to dose rates in the area.

The spatial distribution of dose rates within the area with data interpolation was found smooth (Figure 42). The results obtained show a dependence of gamma dose rates on the geological properties of rocks and soil at higher altitude.

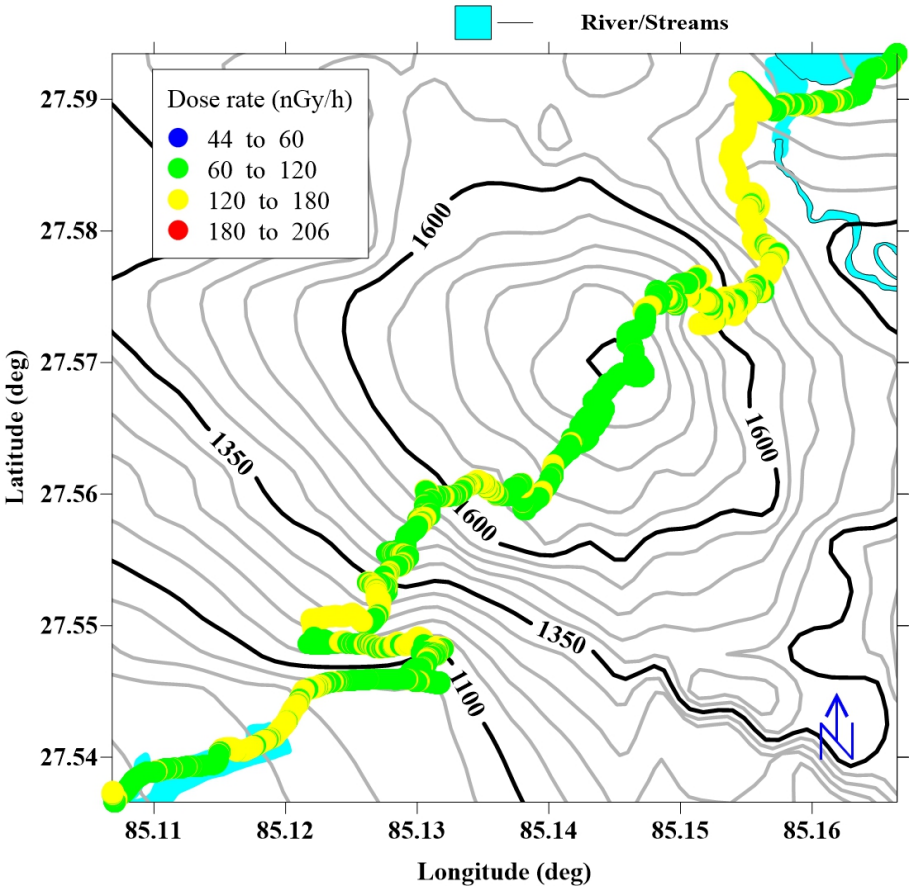

Figure 41: Dose rates in K-B overlaid on topographical map showing altitude contour

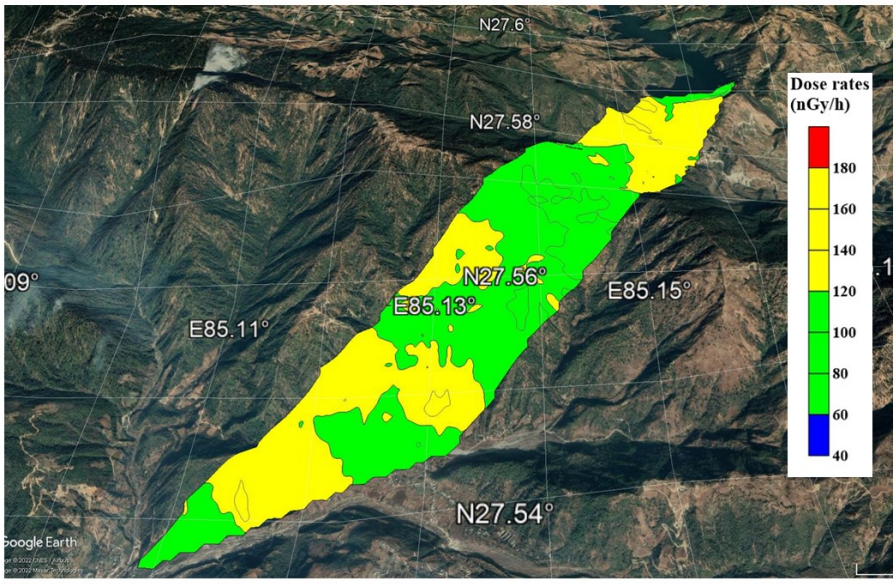

Figure 42: Contour map of dose rates in K-B overlaid on topography scenery

4.1.6 Dose Rates in B-H

The radiological map of the gamma dose rates between Bhimphedi and Hetauda is shown in Figure 43 and 44. The altitude varies from 395 m to 881 m ASL showing significant elevation.

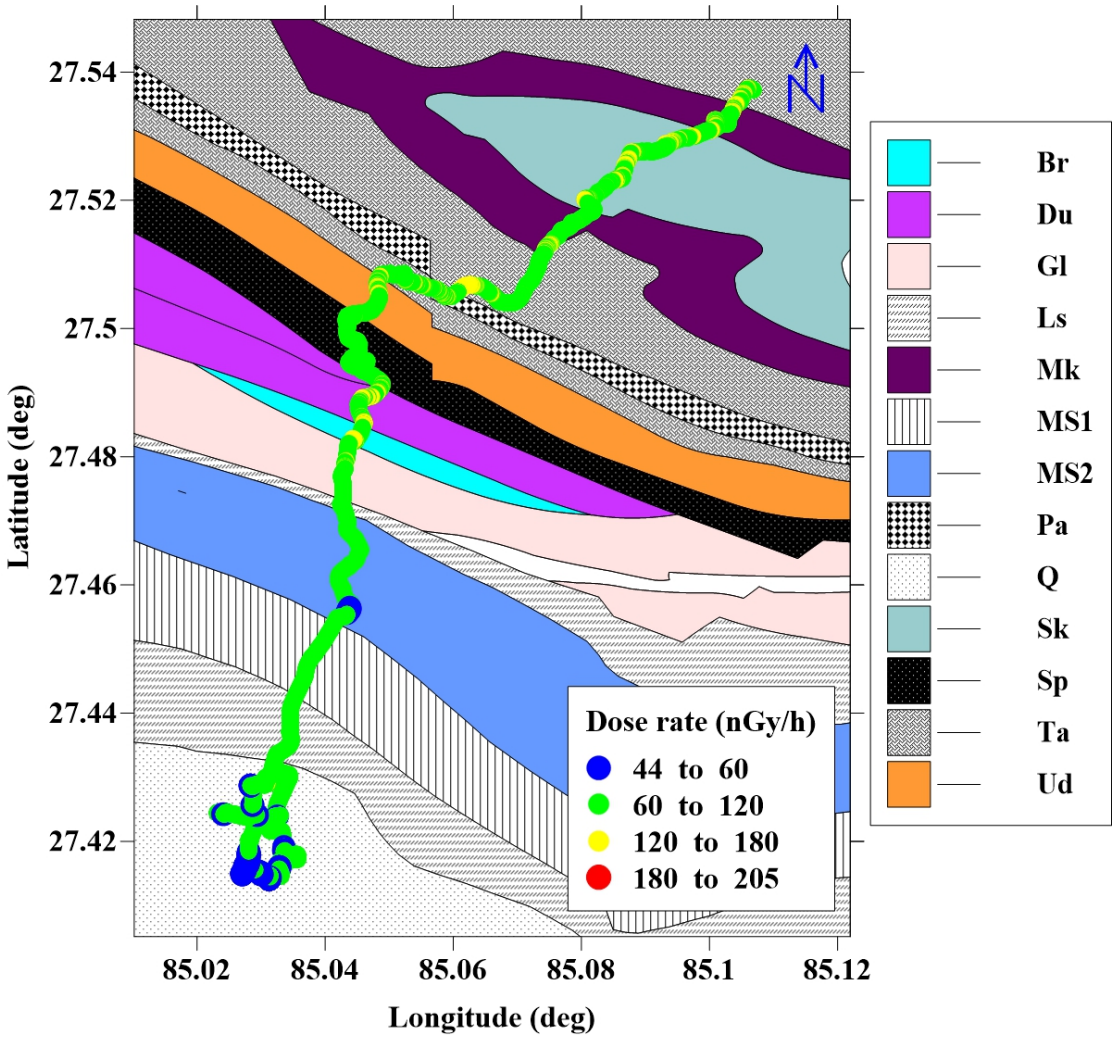

Figure 43: Radiological map of B-H overlaid on geological map

The average dose rate (87 nGy/h) measured along the road from Bhimphedi to the Hetauda city was found above the world average. The dose rate ranges from 45 to 149 nGy/h with 88.8% of total dose rates above the world average, 8.0% above twice the world average and 3.2% below the world average. The region is mostly overlain by basic rocks, dunga quartzites, slates, carbonates, sandstone, mudstone, siltstone, shale, coaly materials, quartzite, biotite, feldspar, alluvium, boulder, gravel, sand, silt, clay and crystalline marble. The radioelement (^{232}Th) have a little higher contribution to dose rates in the area.

The spatial distribution of dose rates within the area from data interpolation was found smooth (Figure 45). The results obtained show a dependence of gamma dose rates

on the geological properties of rocks and soil at higher altitude.

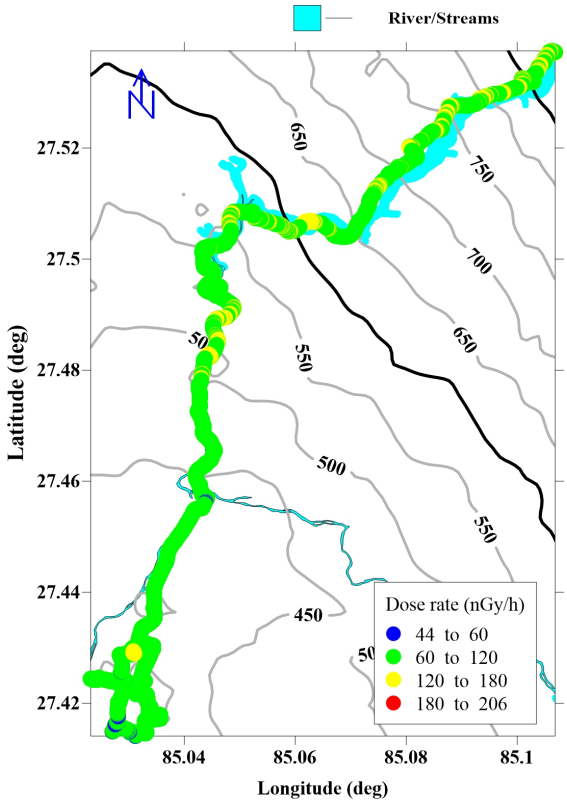

Figure 44: Dose rates in B-H overlaid on topographical map showing altitude contour

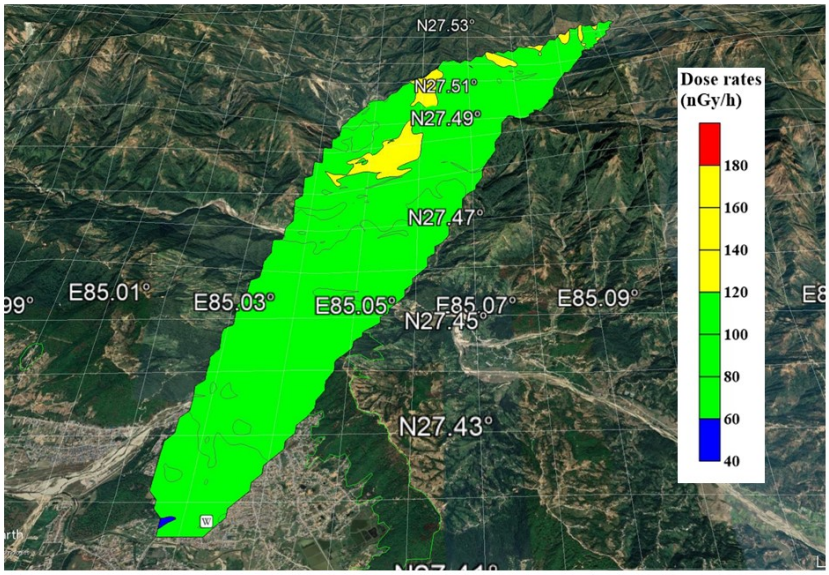

Figure 45: Contour map of dose rates in B-H overlaid on topography scenery

The lowest dose rate was measured in Hetauda and highest in Kulekhani while the average dose rate was found lowest in B-H and highest in D-K area. In addition to geology, geography, and topographical effects (i.e. vegetation, rock outcrops), anthropogenic activities like land cultivation and human settlements also influence to radiation exposure levels in the area. Increment of dose rates were also characterized by visible signs at erosion and weathering exposing bed rock. Storage of sand and stones for constructing road also have influenced the dose rates. The increase in ^{40}K and ^{238}U concentration can also be from the fertilizer (potash, urea and phosphate) used in agriculture. The elevated dose rates in the area implies that the area is highest value area (UNSCEAR, 2000).

4.2 Mass Concentrations of Primordial Radionuclides

The mass concentrations of primordial radionuclides (^{40}K,^{238}U and ^{232}Th) were measured higher than world average for soil (Table 10). The concentrations of ^{40}K ranges from 0.1 to 7.8% within the study area. The average concentration of ^{40}K (2.7%) was found above the twice of world average. The lowest and highest mass concentration of ^{40}K was measured in B-H and L-K while the average mass concentration of ^{40}K was found lowest in B-H and highest in D-K. The concentrations of ^{238}U ranges from 0.05 to 28 ppm within the study area. The average concentration of ^{238}U (6 ppm) was found above the twice of world average. The concentrations of ^{232}Th ranges from 0.1 to 57 ppm within the study area. The average concentration of ^{232}Th (18 ppm) was found above the world average. The lowest and highest mass concentration of ^{238}U and ^{232}Th were measured in B-H and D-K respectively. Similarly, the average mass concentrations of ^{238}U and ^{232}Th were found lowest in B-H and highest in D-K.

The radiological map of studied area with mass concentrations of primordial radionuclides is shown in Figure 46. The higher concentration of ^{40}K (higher than thrice of world average), ^{238}U and ^{232}Th (higher than twice of world average) were noticed in Kulekani area and lower (up to world average) at Hetauda. The average value of concentrations of ^{40}K, ^{238}U and ^{232}Th were measured above the world average (UNSCEAR, 2000). About 8.2% of mass concentrations of ^{40}K were measured within world average value (1.3%), 38.8% above the world average, 41.6% above twice of world average and 11.5% above thrice of the world average. About 11.7% of mass concentrations of ^{238}U were measured within the world average value (2.7 ppm), 34.9% above the world average, 30.4% above twice of world average and 23.1% above thrice of the world average. Similarly, the measured mass concentrations of ^{232}Th were found 16.5% within world average (11.1 ppm), 57.6% above world average, 23.5% above the twice of world average and 2.4% above thrice of world average. From geological map, it was found that the concentrations of ^{40}K, ^{238}U and ^{232}Th were measured higher on Sarung Khola Formation (Sk), Tistung Formation (Ti) and Markhu Formation (Mr) and lower on rocks

Quaternary (Q) rocks. The concentrations of ^{238}U were measured approximately similar and non-uniform with higher on rocks (Sk, Ti and Mr) and lower on rocks (Q). The concentrations of ^{232}Th were measured higher on rocks (Sk, Ti and Mr) and lower on Lower Middle Siwalik(MS1), Lower Siwalik (Ls) and (Q) rocks.

The Naturally occurring terrestrial radionuclides are members of the ^{238}U and ^{232}Th series, along with ^{40}K and their concentrations in soil depends on the nature of the parent rock during soil genesis. The variation of natural radioactivity levels of these radionuclides depends on the geological and geographical structure (UNSCEAR, 2000; Belivermis et al., 2010). Artificial fertilizers used in soil for agriculture can also change the level of terrestrial gamma radiation as they are made from phosphate rock containing an elevated level of natural radionuclides, especially ^{238}U (UNSCEAR, 1988; IAEA, 2003).

Table 10: Outdoor absorbed dose rates and mass concentrations of terrestrial radionuclides between Kathmandu and Makawanpur districts

Sites	Dose rate (nGy/h)			^{40} K (%)			^{238}U (ppm)			^{232}Th (ppm)		
	min	max	mean	min	max	mean	min	max	mean	min	max	mean
K - L	73.9	153.7	115.9 ± 11.5	0.6	5.6	2.8 ± 0.7	0.17	21.3	5.9 ± 2.8	1.9	47.9	17.5 ± 5.7
L - K	92.6	179.1	129.8 ± 13.1	0.5	7.8	3.2 ± 0.8	0.28	19.8	6.2 ± 2.9	4.0	50.0	20.8 ± 6.1
D - K	92.1	205.6	139.0 ± 17.5	0.7	7.7	3.4 ± 0.9	0.05	27.7	7.0 ± 3.2	2.2	57.5	22.1 ± 6.7
K - B	76.4	175.0	119.5 ± 13.8	0.6	5.4	2.5 ± 0.7	0.56	21.8	6.7 ± 3.0	2.0	51.4	17.9 ± 6.0
B - H	44.6	148.9	87.5 ± 19.1	0.1	5.2	1.7 ± 0.7	0.05	20.9	4.6 ± 2.4	0.1	41.1	12.2 ± 5.5
K - H	44.6	205.6	118.6 ± 23.4	0.1	7.8	2.7 ± 1.0	0.05	27.7	6.0 ± 3.0	0.1	57.5	18.1 ± 7.0
K - H*	56.4	205.6	123.5 ± 18.9	0.3	7.8	2.9 ± 0.9	0.05	27.7	6.3 ± 3.0	1.2	57.5	19.0 ± 6.6
World average[a]			59.0			1.3			2.7			11.1

* excluding adjoining environs, [a](UNSCEAR, 2000)

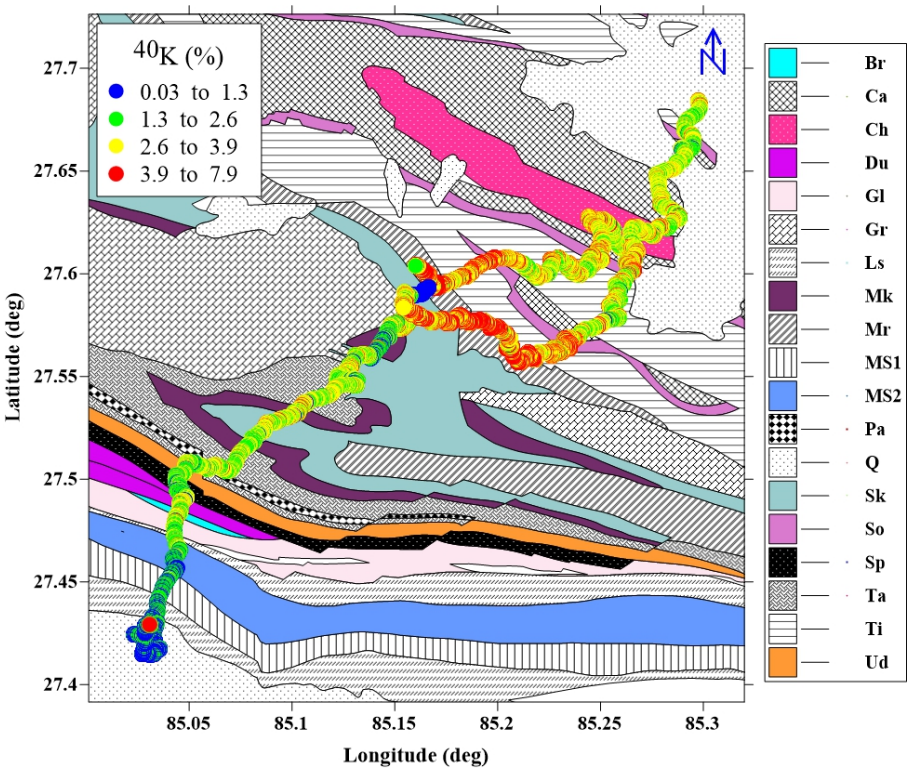

(a) Concentration of ^{40}K overlaid on geological map

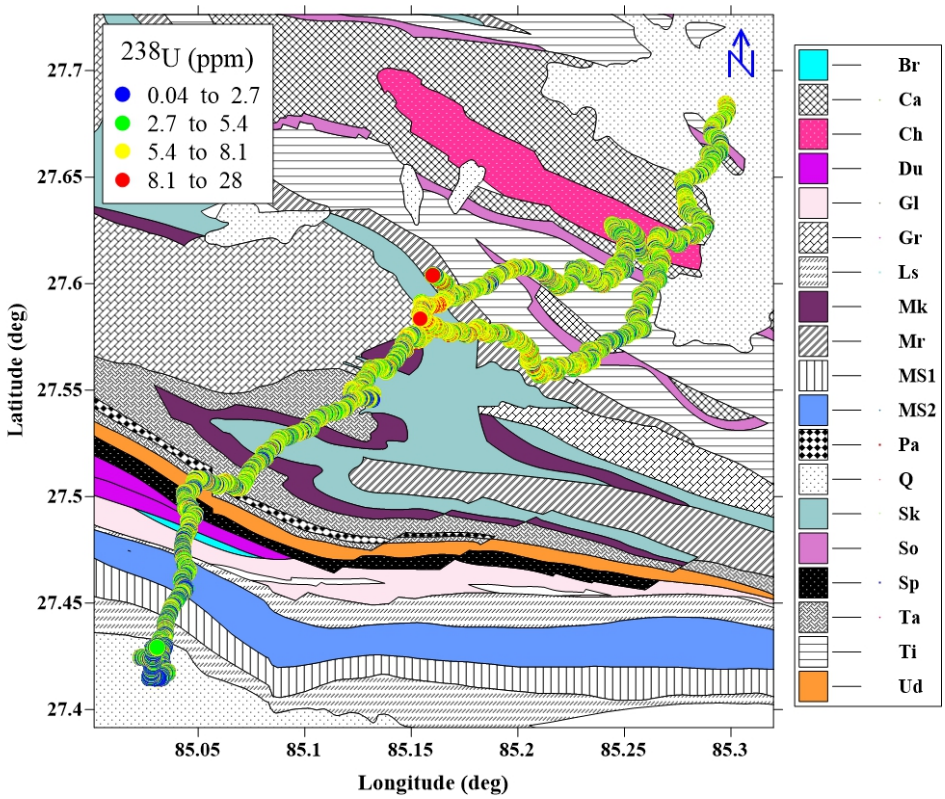

(b) Concentration of ^{238}U overlaid on geological map

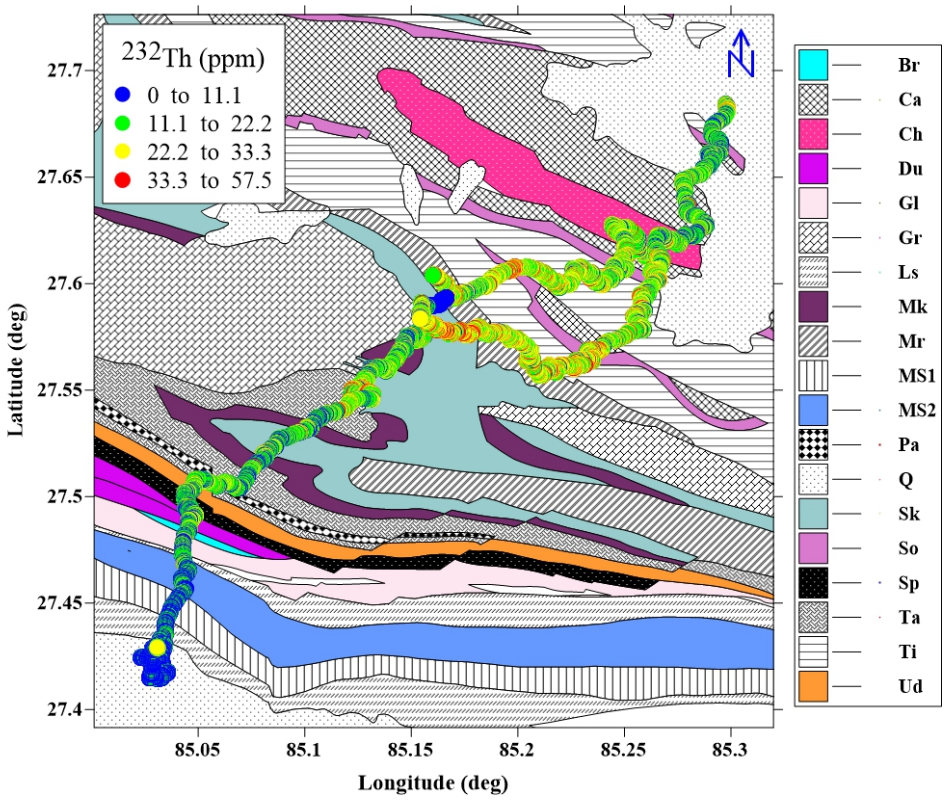

(c) Concentration of ^{232}Th overlaid on geological map

Figure 46: Radiological map of mass concentrations of primordial radionuclides in K-H

4.3 Activity Concentrations and Activity Ratios

The activity concentration of ^{40}K, ^{238}U and ^{232}Th were calculated from the mass concentration and found higher than the world average value 400, 35 and 30 for ^{40}K, ^{238}U and ^{232}Th respectively (UNSCEAR, 2000). These are attributed from geological, geographical and topography factors. The average value of activity concentrations of ^{40}K,^{238}U and ^{232}Th were found lowest in B-H and highest in D-K. The average activity concentrations of ^{40}K and ^{238}U were found higher than twice of the world average in all sites except B-H. The average activity concentration of ^{232}Th was found nearly twice of the world average in D-K and higher than world average in other sites.

The ratio of activities for members of the ^{238}U and ^{232}Th decay chain, like ^{232}Th to ^{238}U are typically equivalent to 1.1 in most environmental samples (Evans et al., 1997). Activity ratios for natural radionuclides ^{40}K and ^{232}Th were calculated taking the median value of activity concentration for ^{40}K and ^{232}Th reported by UNSCEAR (UNSCEAR, 2000) and the ^{232}Th to ^{40}K ratio was estimated 0.085 (Vukasinovic et al., 2010). The activity ratios calculated for the studied sites (Table 11) were found in good agreement with environmental samples which indicates no relocation of rocks and soils. In K-B and B-H slightly leaching of ^{238}U was noticed. But, no significant leaching of radionuclides

were noticed in the area.

The average activity concentrations of ^{40}K were found higher in D-K, L-K, K-L, K-B and B-H respectively. The activity concentrations of ^{238}U were found higher in D-K, K-B, L-K, K-L and B-H respectively. The activity concentrations of ^{232}Th were found higher in D-K, L-K, K-B, K-L and B-H respectively. The area of homogeneous lithology have a high correlation among natural radionuclide activity concentration (Navas et al., 2002a). The activity concentrations of ^{232}Th and ^{40}K were found significantly positively correlated in K-L (r = 0.90), B-H (r = 0.79), K-H (r = 0.82) moderately correlated in D-K (r = 0.60) and weakly correlated in L-K (r = 0.38). The activity concentrations of ^{238}U and ^{40}K were found significantly positively correlated in L-K (r = 0.71), K-B (r = 0.69), B-H (r = 0.83), moderately correlated in K-H (r = 0.55) and weakly correlated in K-L (r = 0.27). The activity concentrations of ^{232}Th and ^{238}U were found significantly positively correlated in L-K (r = 0.78), D-K (r = 0.67), B-H (r = 0.79), moderately correlated in K-H (r = 0.50), weakly correlated in K-L (r = 0.36) and negatively correlated in K-B (r = -0.46). This indicates that in K-B, ^{238}U increases as ^{232}Th decreases. This can be attributed to human activities such as road construction and land ploughing. Low and moderate correlation between the natural radionuclides activity concentrations were due to non homogeneous lithology.

Table 11: Activity concentrations and activity ratios between Kathmandu and Makawanpur

Sites	^{40}K (Bq/kg)			^{238}U (Bq/kg)			^{232}Th (Bq/kg)			Activity ratios		
	min	max	mean	min	max	mean	min	max	mean	Th/K	Th/U	U/K
K - L	199.4	1740.6	850.4 ± 210.8	2.1	263.4	72.5 ± 34.3	7.6	194.7	70.2 ± 23.1	0.08	0.97	0.09
L - K	146.8	2443.0	997.0 ± 260.1	3.4	243.9	76.7 ± 35.8	16.3	203.0	84.3 ± 24.9	0.08	1.10	0.08
D - K	234.1	2403.8	1060.4 ± 280.1	0.6	342.0	85.9 ± 40.1	9.1	233.4	89.9 ± 27.4	0.08	1.05	0.08
K - B	188.4	1699.3	773.9 ± 233.4	6.9	269.6	82.3 ± 37.2	8.1	208.8	73.0 ± 24.4	0.09	0.89	0.11
B - H	40.0	1630.7	541.2 ± 231.7	0.5	257.8	56.9 ± 30.3	0.4	166.9	49.6 ± 22.1	0.09	0.87	0.10
K - H	40.1	2443.0	850.2 ± 306.8	0.6	342.0	74.6 ± 37.1	0.4	233.4	73.5 ± 28.3	0.09	0.99	0.09
World average*			420.0			33.0			45.0			

* (UNSCEAR, 2000)

4.4 Dose Rate Calculated from Mass Concentration

The dose rates from particular radionuclides were calculated separately for each radionuclides. The dose rates from ^{40}K, ^{238}U and ^{232}Th are found higher than world averages (Table 12). The dose rates from ^{40}K ranges from 1.7 to 102.1 nGy/h with average of 35.5 nGy/h. The lowest value was found in B-H, and highest in L-K. The average dose rates from ^{40}K were found higher than world average with lowest value in B-H and highest in D-K. The average dose rates from ^{40}K were found higher than twice of the world average in L-K, D-K and nearly equal to twice of the world average in K-L, K-H. The dose rates from ^{238}U ranges from 0.3 to 157.2 nGy/h with average of 34.3 nGy/h. The lowest value was found in D-K, B-H and highest in D-K. The average dose rates from

^{238}U were found higher than twice of the world average with lowest value in B-H and highest in D-K. The average dose rates from ^{238}U were measured higher than twice of the world average in all sites except B-H. The dose rates from ^{232}Th ranges from 0.3 to 143.4 nGy/h with average of 45.2 nGy/h. The lowest value was found in B-H and highest in D-K. The average dose rates from ^{232}Th were found higher than world average with lowest value in B-H and highest in D-K. The average dose rates from ^{232}Th was found higher than the world average in all sites except D-K with dose rates higher than twice of the world average. The total dose rates (calculated dose rates) estimated by adding dose rates from ^{40}K, ^{238}U and ^{232}Th ranges from 12.3 to 268.4 nGy/h with average of 115 nGy/h. The lowest calculated dose rate was calculated in B-H and highest in D-K. The average calculated dose rates were estimated higher than world average with lowest in B-H and highest in D-K. The average calculated dose rates were estimated higher than twice of world average in L-K and D-K.

The dose rates contributed from ^{232}Th was found highest in all sites whereas the ^{238}U had lowest contribution to dose rates in K-L, L-K, D-K, K-H and ^{40}K had lower contribution in K-B and B-H.

The dose rates inferred from the concentrations (calculated dose rate) was found nearly equal to the dose rate measured from direct measurement (measured dose rate) as presented in Table 13. The ratio of calculated dose rates to measured dose rates were found nearly equal to one. The results of exposures inferred from the soil concentrations show reasonable agreement with the measured outdoor absorbed dose rates in air. The discrepancy lower than 30% indicates both data as representative data (UNSCEAR, 2000).

Table 12: Dose rates calculated from radionuclides concentrations

Sites	Dose rates from ^{40}K (nGy/h)			Dose rates from ^{238}U (nGy/h)			Dose rates from ^{232}Th (nGy/h)			Calculated dose rates		
	min	max	mean	min	max	mean	min	max	mean	min	max	mean
K - L	8.3	72.7	35.5 ± 8.8	1.0	121.0	33.3 ± 15.7	4.7	119.6	43.1 ± 14.2	41.7	207.8	111.9 ± 19.4
L - K	6.1	102.1	41.6 ± 10.9	1.6	112.1	35.2 ± 16.4	10.0	124.7	51.8 ± 15.3	60.2	224.9	128.7 ± 21.2
D - K	9.8	100.4	44.3 ± 11.7	0.3	157.2	39.5 ± 18.4	5.6	143.4	55.2 ± 16.8	63.1	268.4	139.0 ± 25.8
K - B	7.9	71.0	32.3 ± 9.7	3.2	123.9	37.8 ± 17.1	5.0	128.3	44.8 ± 14.9	53.8	204.9	115.0 ± 20.7
B - H	1.7	68.1	24.6 ± 9.9	0.3	118.5	27.5 ± 14.3	0.3	102.5	32.5 ± 13.9	12.3	199.8	84.6 ± 24.3
K - H	1.7	102.1	35.5 ± 12.8	0.3	157.2	34.3 ± 17.0	0.3	143.4	45.2 ± 17.4	12.3	268.4	114.9 ± 30.5
World average*			18			15			27			60

Table 13: Outdoor absorbed dose rates inferred from concentrations of soil radionuclides compared with direct measurements

Sites	Absorbed dose rates (nGy/h)		Ratio (calculated/measured)
	calculated from soil concentrations	measured by direct measurement	
K - L	111.9	117.3	0.95
L - K	128.7	129.8	0.99
D - K	139.0	139.0	1.00
K - B	115.0	119.5	0.96
B - H	84.6	87.5	0.97
K - H	114.9	118.6	0.97
World average*	60.0	59.0	1.02

* (UNSCEAR, 2000)

4.5 Anthropogenic Radionuclide in Environment between Kathmandu and Makawanpur

The spatial distribution of anthropogenic radionuclide (^{137}Cs) between Kathmandu and Makawanpur is shown in Figure 47. About 62.6% of total measured data of surface activity of ^{137}Cs lies below 0.9 kBq/m^2, 33.8% below 1.9 kBq/m^2, 3.5% below 2.83 kBq/m^2, and 0.1% above it.

The surface activity of ^{137}Cs ranges from 0.001 to 3.773 kBq/m^2 with average of 0.85 kBq/m^2 (Table 14). The both lowest and highest value was measured in D-K. The dose rate calculated from surface activity of ^{137}Cs ranges from 0.001 to 2.007 nGy/h with an average of 0.45 nGy/h. The dose rates was found homogeneous with slightly increase in L-K and D-K sites. The outdoor AED ranges from 0.001 to 2.462 µSv with average of 0.55 µSv. The homogeneous distribution and low surface activity of ^{137}Cs indicates that there is no contamination in the studied area and the trace of ^{137}Cs present was due to global fallout from weapon testing and nuclear accidents (UNSCEAR, 2000).

Table 14: Surface activity and absorbed dose rates of ^{137}Cs

Sites	^{137}Cs (kBq/m^2)			Dose rates (nGy/h)		
	min	max	mean	min	max	mean
K - L	0.010	3.151	0.84 ± 0.47	0.005	1.676	0.45 ± 0.25
L - K	0.003	3.603	0.90 ± 0.50	0.002	1.917	0.48 ± 0.27
D - K	0.001	3.773	0.95 ± 0.53	0.001	2.007	0.51 ± 0.28
K - B	0.005	3.356	0.85 ± 0.48	0.003	1.785	0.45 ± 0.26
B - H	0.003	3.294	0.68 ± 0.40	0.002	1.752	0.36 ± 0.21
K - H	0.001	3.773	0.85 ± 0.49	0.001	2.007	0.45 ± 0.26

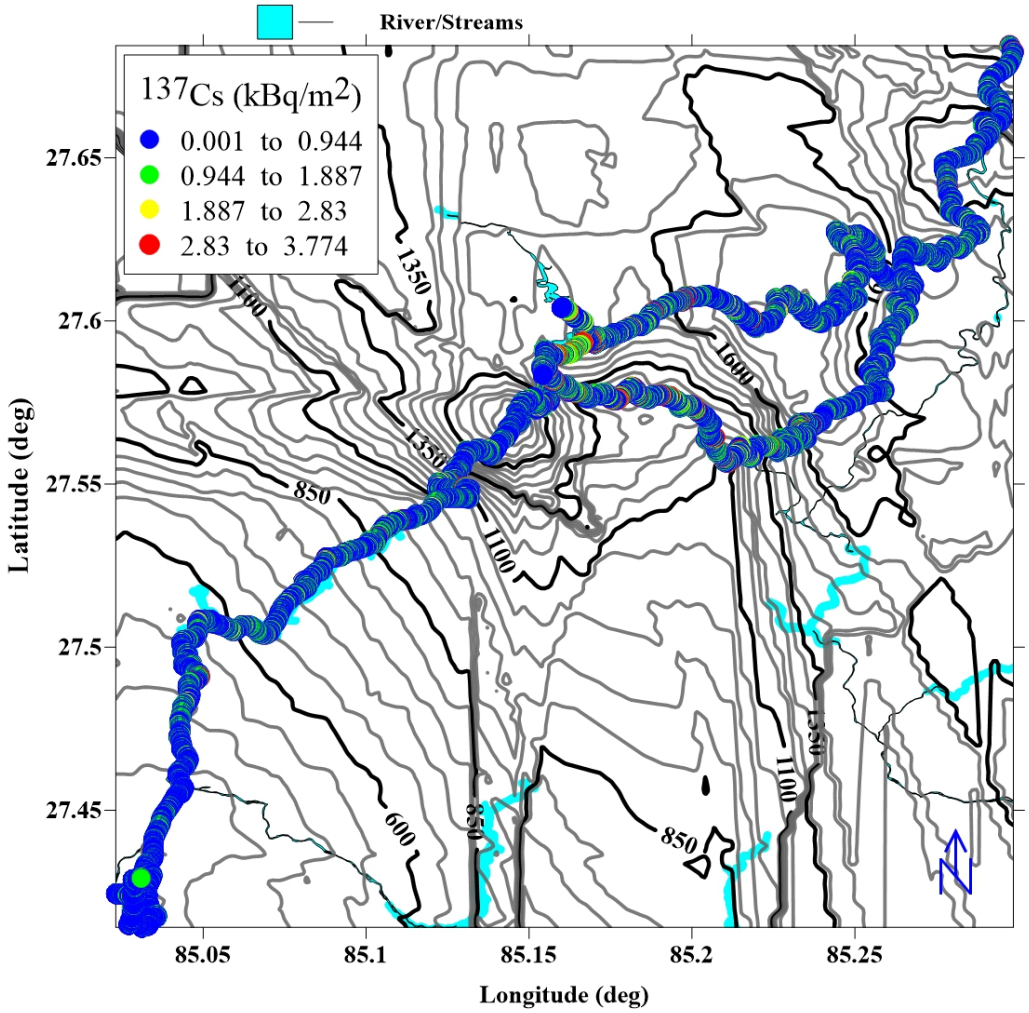

(a) Surface activity of ^{137}Cs overlaid on topographical map showing altitude contour

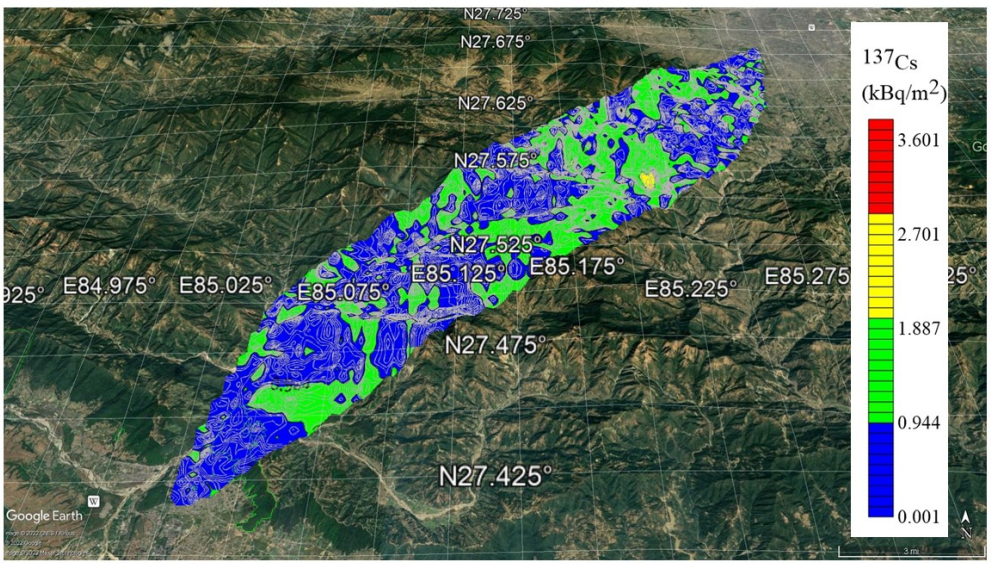

(b) Contour map of surface activity of ^{137}Cs overlaid on topography scenery

Figure 47: Radiological map of ^{137}Cs in K-H

4.5.1 Adjoining Environs

Ground based radiometric measurements were performed along the road between Kathmandu and Makawanpur. For the extent examination at radiation, the survey was conducted along the adjoining area of Rakash Khola (Fakhel), Bhimphedi, Golping Besi, Bhaise and Hetauda within the study area (Figure 48 and 49). In Rakash Khola, 52.4% of total dose rates were measured above the world average and 47.6% above twice of world average. In Bhimphedi, 79.3% of total dose rates were measured above the world average and 20.7% above twice of world average. In Golping Besi, 67.9% of total dose rates were measured above the world average and 32.1% above twice of world average. In Bhaise, 93.7% of total dose rates were measured above the world average and 6.3% above twice of world average. In Hetauda city, 91.9% of total dose rates were measured above the world average, 7.8% below the world average and 0.3% above twice of world average. The higher dose rates were measured at Golping Besi and lower at Hetauda. The higher dose rates were measured due to elevated radionuclides concentrations in Earth's crust (Table 15). The activity concentrations of (^{40}K, ^{238}U and ^{232}Th) were calculated from their mass concentrations and were found above the world average (Table 16). The ^{40}K, ^{238}U and ^{232}Th concentrations were measured higher at Golping Besi, Bhimphedi and Rakash Khola respectively. Similarly, the concentrations of ^{40}K, ^{238}U and ^{232}Th were measured lower at Hetauda. The activity ratio (Th/U) were found nearly equal to 1 and Th/K and U/K were found nearly 0.1 showing good agreement for environmental samples in adjoining area (Evans et al., 1997). The surface activity of ^{137}Cs were found similar with slightly lower value at Hetauda and higher at Golping Besi. This shows that there is no contamination in the environment and the trace found is due to global fallout.

The dose rates in Rakash Khola have strong positive correlation with ^{238}U and ^{232}Th ($r = 0.95$, $r^2 = 90\%$ and $r = 0.81$, $r^2 = 66\%$ respectively). The dose rates in Bhimphedi and Golping Besi have significant positive correlation with ^{238}U ($r = 0.81$, $r^2 = 66\%$ and $r = 0.8$, $r^2 = 63\%$ respectively). The dose rates in Bhaise have strong positive correlation with ^{40}K and ^{238}U ($r = 0.91$, $r^2 = 83\%$ and $r = 0.78$, $r^2 = 61\%$ respectively). The dose rates in Hetauda have significant positive correlation with ^{40}K, ^{238}U, ^{232}Th and ^{137}Cs ($r = 0.98$, $r^2 = 96\%$, $r = 0.90$, $r^2 = 81\%$, $r = 0.98$, $r^2 = 95\%$ and $r = 0.98$, $r^2 = 95\%$ respectively).

The villages were studied during the survey of adjoining environs, to get detail idea of radiation in environment. The paved road at Bhimphedi was noticed as to attenuate the gamma ray and act as a shielding resulting slightly lower dose rate compared to adjoining environs whereas the paved road at Rakash Khola was noticed to slightly increase the dose rates compared to adjoining environs. No, significant variation was observed in dose rates along the road and adjoining environs which indicates that the road construction materials were not brought from outside.

Table 15: outdoor absorbed dose rates and mass concentrations of radionuclides in the adjoining environs

Sites	Dose rate (nGy/h)			^{40}K (%)			^{238}U (ppm)			^{232}Th (ppm)			^{137}Cs (kBq/m^2)		
	min	max	mean	min	max	mean	min	max	mean	min	max	mean	min	max	mean
Rakash khola	89.0	149.6	116.0 ± 12.1	0.3	5.2	2.4 ± 0.8	0.2	19.21	5.9 ± 2.8	6.2	43.1	19.2 ± 5.8	0.01	2.6	0.8 ± 0.4
Bhimphedi	77.7	138.4	113.0 ± 8.3	0.5	4.4	2.2 ± 0.6	0.3	21.7	6.4 ± 2.8	3.2	40.1	17.2 ± 5.6	0.03	2.8	0.8 ± 0.4
Golping Besi	77.7	143.2	117.0 ± 7.8	0.6	4.7	2.7 ± 0.6	0.5	16.49	5.9 ± 2.6	2.4	37.4	16.6 ± 5.4	0.01	2.8	0.9 ± 0.5
Bhaise	71.2	134.4	105.0 ± 10.4	0.6	4.1	2.1 ± 0.5	0.4	16.17	5.5 ± 2.6	3.6	42.1	15.5 ± 5.1	0.01	2.7	0.7 ± 0.4
Hetauda	44.6	134.0	74.5 ± 10.4	0.1	4.2	1.3 ± 0.5	0.04	18.10	4.0 ± 2.1	0.1	34.8	10.1 ± 4.4	0.004	2.4	0.6 ± 0.3

Table 16: Activity concentrations and activity ratios in the adjoining environs

Sites	^{40}K (Bq/kg)			^{238}U (Bq/kg)			^{232}Th (Bq/kg)			Activity ratios		
	min	max	mean	min	max	mean	min	max	mean	Th/K	Th/U	U/K
Rakash khola	86.1	1636.4	759.4 ± 268.6	2.9	237.2	73.1 ± 34.9	25.1	175.1	78.0 ± 23.6	0.10	1.07	0.10
Bhimphedi	170.3	1389.7	692.8 ± 184.0	3.9	268.8	79.0 ± 34.8	13.2	162.7	70.0 ± 22.7	0.10	0.89	0.11
Golping Besi	185.6	1457.6	854.9 ± 188.1	6.1	203.7	72.5 ± 33.0	9.9	151.7	67.6 ± 21.9	0.08	0.93	0.08
Bhaise	190.0	1274.2	661.3 ± 181.4	5.2	199.7	68.1 ± 32.2	14.5	170.8	63.1 ± 20.6	0.09	0.93	0.10
Hetauda	40.1	1326.5	417.5 ± 155.5	0.6	223.5	49.5 ± 26.2	0.4	141.4	40.9 ± 18.0	0.10	0.83	0.12

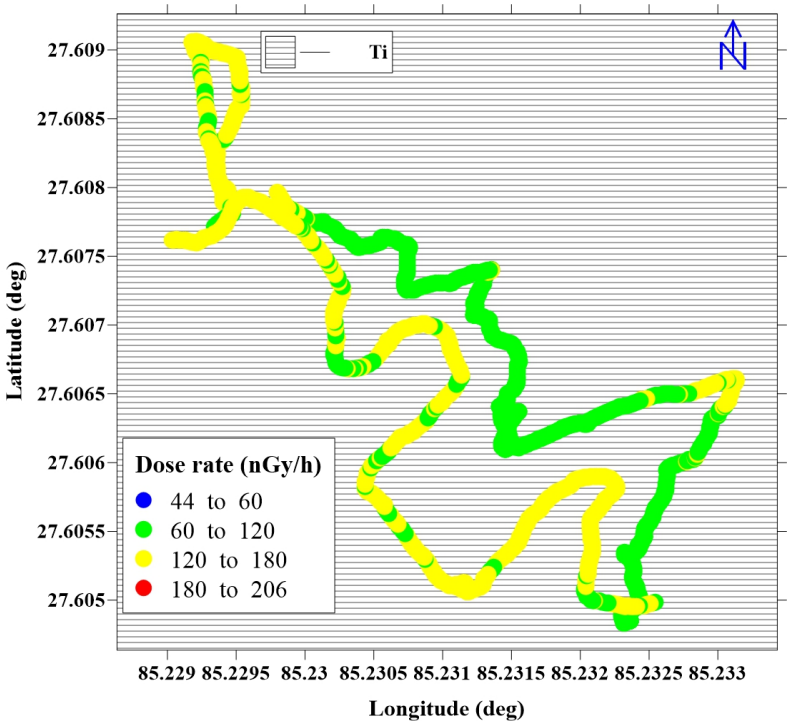

(a) Rakash Khola

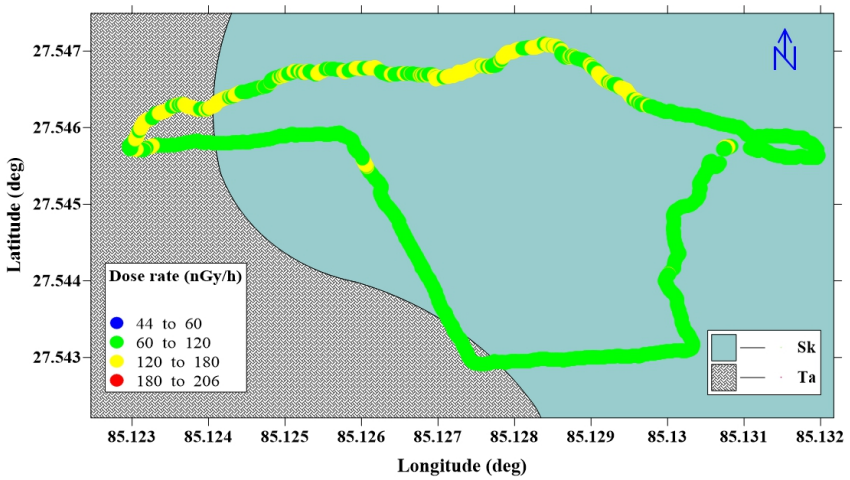

(b) Bhimphedi

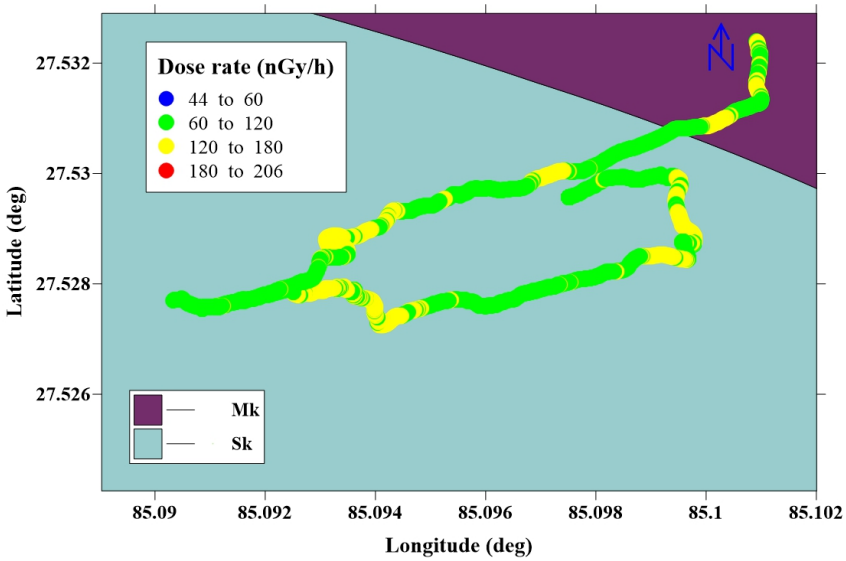

(c) Golping Besi

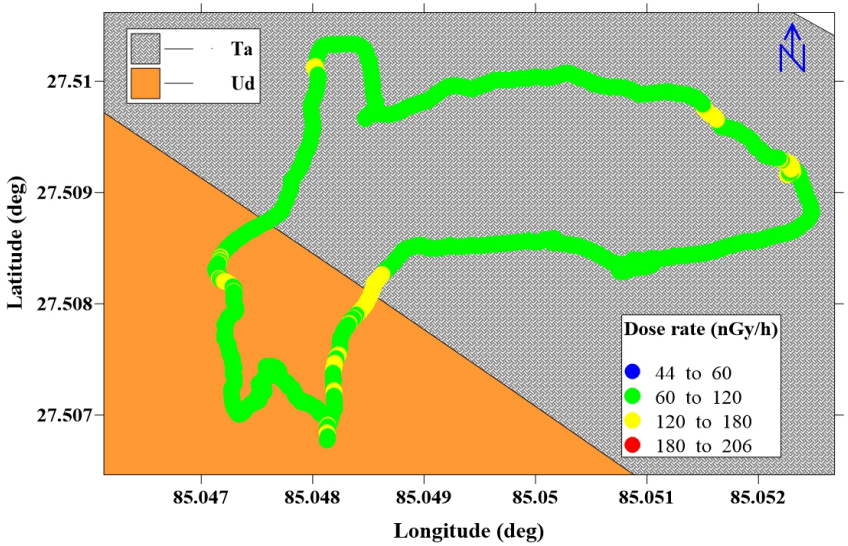

(d) Bhaise

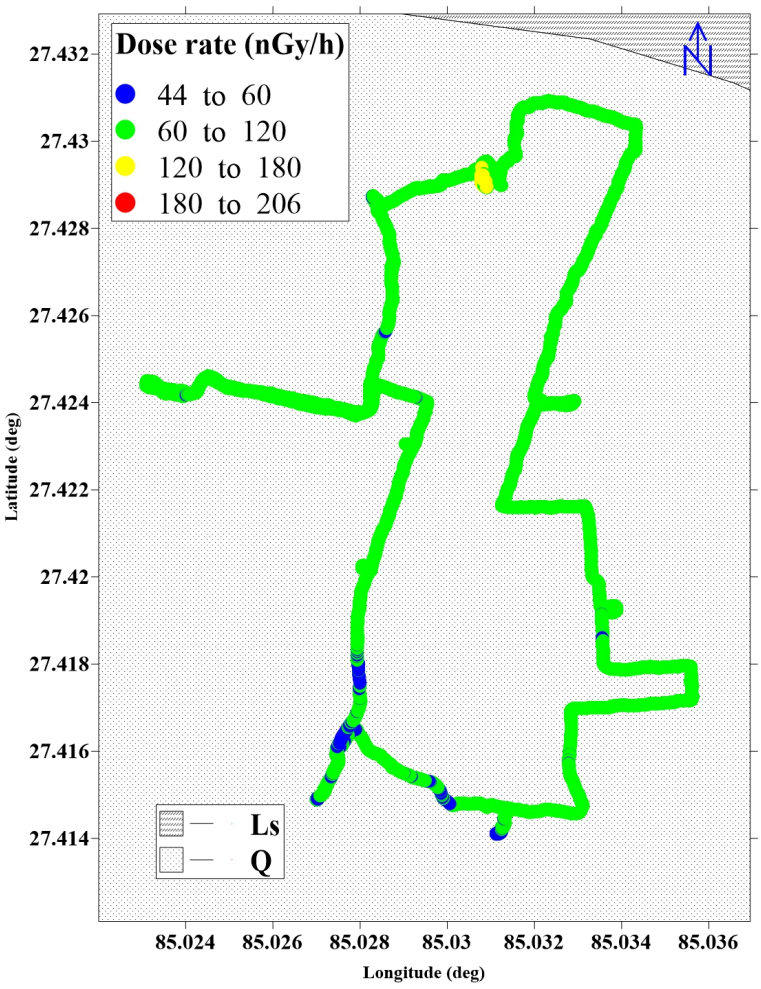

(e) Hetauda

Figure 48: Dose rates in adjoining environs overlaid on geological map

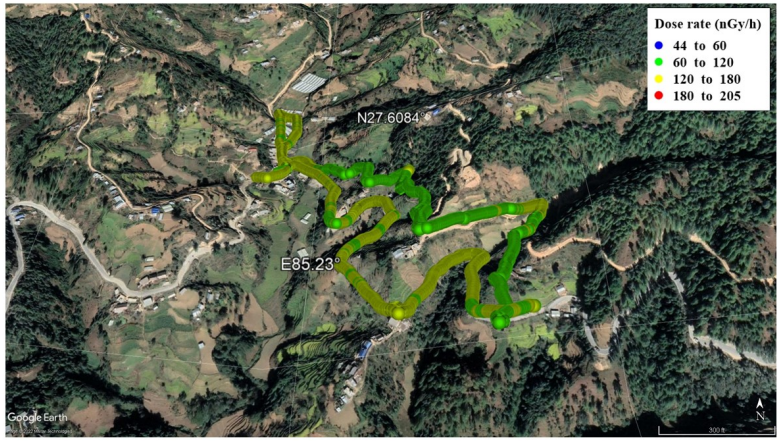

(a) Rakash Khola

(b) Bhimphedi

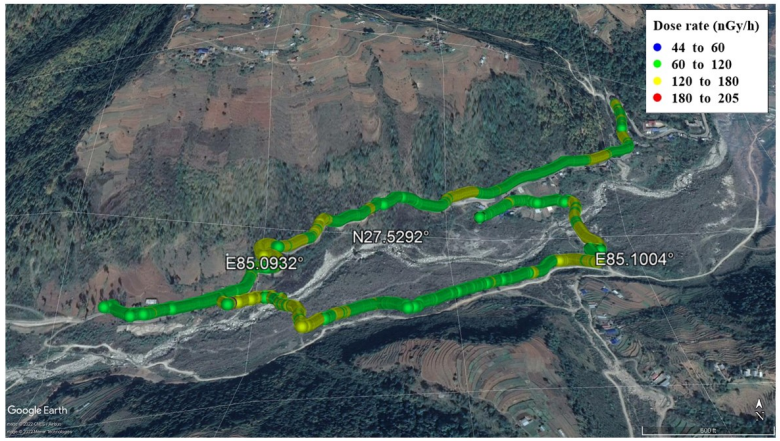

(c) Golping Besi

(d) Bhaise

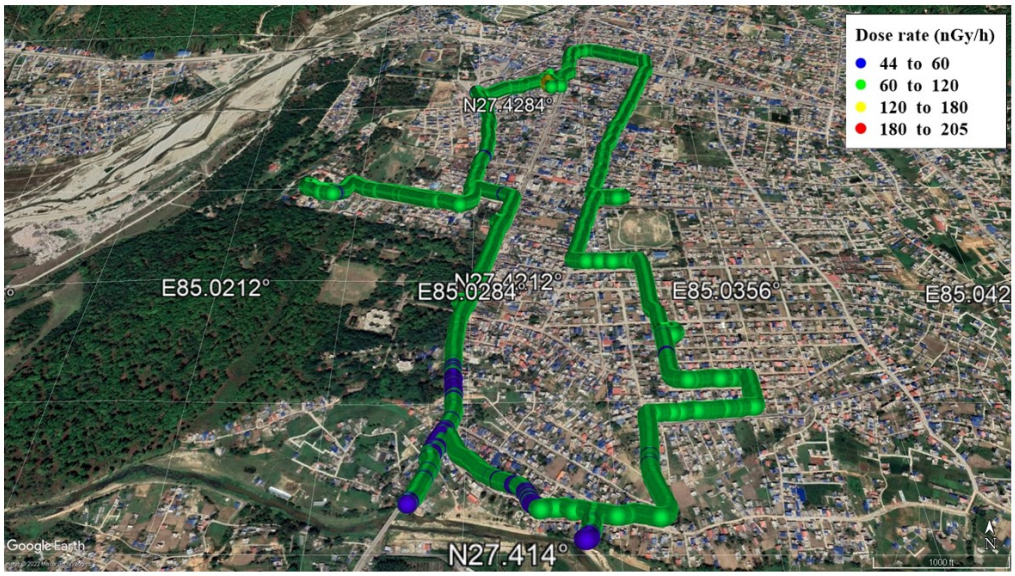

(e) Hetauda

Figure 49: Dose rates in adjoining environs overlaid on scenery

4.5.2 Radioactive Measurement around Water Resources

For the detail measurement of radiation in the environment within the area, the study was also conducted along the banks of water resources within the study area (Figure 50). The survey was conducted along six rivers (Chobhar, Sisneri (Dakshinkali), Mahalaxmi, Sisneri (Kulekhani), Bhaise Dobhan and Samari (Rapati) and around two lakes (Taudaha and Indra Sarovar). The measured dose rates along the banks were found similar to the dose rates measured along the road which shows no external material is leached or dissolved in water.

The dose rates along the banks of river were found higher than the world average. Along the bank of Chobhar river, 10.7% dose rates were measured above world average and 87.9% above twice the world average. Along the banks of Sisneri river (Dakshinkali) and Sisneri river (Kulekhani), all the dose rates were measured higher than the twice of world average. Along Mahalaxmi river, 1.5% of total dose rates were measured above the world average and 98.2% above the twice of world average. Along Bhaise Dobhan river, 96.4% of total dose rates were measured above the world average and 3.6% above twice of world average. Along, Samari (Rapati) river, 99.3% of total dose rates were measured above the world average and 0.7% above twice of world average. The highest dose rates were measured along the bank of Sisneri (Kulekhani) river and lowest along Samari (Rapati) river.

The higher dose rates were measured due to elevated radionuclides concentrations in the sands, rocks and sediments (Table 17). The activity concentrations of (^{40}K, ^{238}U and

^{232}Th) were calculated from their mass concentrations and were found above the world average (Table 18). The ^{40}K, ^{238}U and ^{232}Th concentrations were measured highest along the bank of Sisneri (Dakshinkali), Sisneri (Kulekhani) and Chobhar river respectively. Similarly, the ^{40}K, ^{238}U and ^{232}Th concentrations were measured lowest along the bank of Samari (Rapati) river. The activity ratio (Th/U) were found nearly equal to 1 and Th/K and U/K were found nearly 0.1 showing good agreement for environmental samples. Slightly, higher Th/K and U/K ratios were observed (nearly equal) along Chobhar river due to less content of ^{40}K due to leaching (Alfaro et al., 2004). Also, slightly lower Th/U and higher U/K ratios were noticed along the bank of Samari (Rapati) river due to accumulation of ^{238}U which can be due to the use of fertilizers (Takeda et al., 2006).

The surface activity of ^{137}Cs were found similar along the banks of all river with slightly lower value along Samari (Rapati) and higher along Mahalaxmi river. This shows that there is no contamination in the environment and the trace found is due to global fallout.

The dose rates along Chobhar river have strong positive correlation with ^{238}U, ^{232}Th and ^{137}Cs (r = 1, r^2 = 99%, r = 0.90, r^2 = 81%, r = 0.98, r^2 = 96% respectively). The dose rates along Sisneri (Dakshinkali) river have strong positive correlation with ^{40}K (r = 0.89, r^2 = 80%). The dose rates along Mahalaxmi river have strong positive correlation with ^{40}K and ^{238}U (r = 0.98, r^2 = 96%, r = 0.96, r^2 = 92% respectively). The dose rates along Sisneri (Kulekhani) river have significant positive correlation with ^{40}K, ^{137}Cs (r = 0.98, r^2 = 96%, r = 0.99, r^2 = 99% respectively). The dose rates along Bhaise Dobhan river have significant positive correlation with ^{40}K and ^{232}Th (r = 0.98, r^2 = 95%, r = 0.78, r^2 = 60% respectively). The dose rates along Samari (Rapati) river have significant positive correlation with ^{40}K, ^{238}U, ^{232}Th and ^{137}Cs (r = 0.94, r^2 = 89%, r = 0.91, r^2 = 83%, r = 0.75, r^2 = 57%, r = 0.74, r^2 = 55% respectively).

The dose rates and mass concentrations around the lakes were also found higher than the world average. The dose rates were found higher around Taudaha lake. The concentrations of ^{40}K and ^{232}Th were found higher around Taudaha and the concentrations of ^{238}U were found higher around Indra Sarovar lake. Around the Taudaha, 93.6% of total dose rates were measured above the world average and 6.4% above twice world average. Around the Indra Sarovar, 87.2% of total dose rates were measured above the world average and 12.8% above twice world average. The activity ratio (Th/U) were observed nearly equal to 1 and Th/K and U/K were found nearly 0.1 showing good agreement for environmental samples around the Taudaha lake. The lower activity ratios were observed around Indra Sarovar lake which shows relocation of rocks. This is because, the lake is artificial and rocks from outside were brought to construct it. The surface activity of ^{137}Cs were also found slightly higher than the other water resources. The dose rates around Taudaha lake have significant positive correlation with ^{40}K, ^{238}U, ^{232}Th and ^{137}Cs (r = 0.90, r^2 = 81%, r = 0.87,r^2 = 76%, r = 0.98, r^2 = 0.95, r = 0.94, r^2

Table 17: Outdoor absorbed dose rates and concentrations of radionuclides along the banks of water resources

Water resources	Dose rate (nGy/h)			^{40}K (%)			^{238}U (ppm)			^{232}Th(ppm)			^{137}Cs (kBq/m^2)		
	min	max	mean	min	max	mean	min	max	mean	min	max	mean	min	max	mean
Rivers															
Chobhar	94.8	192.4	136.9 ± 17.5	0.5	3.9	2.2 ± 0.6	0.7	27.8	7.8 ± 3.5	5.5	52.3	25.1 ± 8.4	0.003	3.199	0.956 ± 0.543
Sisneri (Dakshinkali)	127.4	157.6	143.3 ± 6.5	2.0	5.7	3.8 ± 0.6	1.5	15.4	6.7 ± 2.7	9.3	41.7	21.9 ± 6.3	0.095	2.917	0.994 ± 0.542
Mahalaxmi	99.8	185.0	147.1 ± 9.4	1.6	5.9	3.7 ± 0.7	0.3	23.5	6.7 ± 3.1	5.4	48.0	23.5 ± 6.8	0.044	2.988	1.062 ± 0.540
Sisneri (Kulekhani)	138.5	177.0	151.3 ± 6.2	2.1	5.7	3.7 ± 0.6	2.0	20.3	8.5 ± 3.3	10.2	44.9	22.6 ± 5.9	0.092	2.778	0.960 ± 0.524
Bhaise Dobhan	71.2	126.4	106.5 ± 7.8	0.6	3.8	1.9 ± 0.5	0.5	16.2	5.9 ± 2.7	4.1	33.0	16.5 ± 5.0	0.016	2.513	0.773 ± 0.451
Samari (Rapati)	60.2	141.6	91.0 ± 9.6	0.3	4.6	1.7 ± 0.5	0.4	16.0	5.6 ± 2.5	1.1	33.9	11.8 ± 4.5	0.012	2.206	0.673 ± 0.382
Lakes															
Taudaha	76.9	174.2	100.4 ± 16.9	1.0	5.6	2.2 ± 0.7	0.2	18.1	5.2 ± 2.7	2.0	42.6	13.8 ± 5.3	0.014	3.047	0.766 ± 0.431
Indra Sarobar	0.13	146.2	105.6 ± 15.0	0.03	1.5	0.4 ± 0.2	1.6	19.7	8.7 ± 3.3	BDL	5.9	0.8 ± 1.1	0.149	3.301	1.552 ± 0.577

Table 18: Activity concentrations and activity ratios along the banks of water resources

Water resources	^{40}K (Bq/kg)			^{238}U (Bq/kg)			^{232}Th (Bq/kg)			Activity ratio		
	min	max	mean	min	max	mean	min	max	mean	Th/K	Th/U	U/K
Rivers												
Chobhar	156.2	1233.5	702.3 ± 185.6	8.2	342.8	96.5 ± 43.9	22.3	212.4	102.0 ± 34.1	0.15	1.06	0.14
Sisneri (Dakshinkali)	625.1	1777.5	1191.2 ± 208.0	18.2	190.5	82.8 ± 33.1	37.6	169.3	88.8 ± 25.5	0.07	1.07	0.07
Mahalaxmi	497.4	1847.3	1154.0 ± 213.5	4.1	289.9	82.9 ± 38.2	22.1	194.8	95.6 ± 27.5	0.08	1.15	0.07
Sisneri (Kulekhani)	647.0	1778.5	1158.4 ± 199.4	24.6	251.3	105.7 ± 40.9	41.5	182.4	91.7 ± 24.2	0.08	0.87	0.09
Bhaise Dobhan	196.6	1200.4	614.2 ± 178.7	6.5	199.7	73.2 ± 33.6	16.7	134.2	67.0 ± 20.4	0.11	0.92	0.12
Samari (Rapati)	89.5	1427.9	548.4 ± 174.8	4.3	197.1	69.6 ± 31.6	4.4	137.7	48.1 ± 18.3	0.09	0.69	0.13
Lakes												
Taudaha	208.8	1756.2	710.1 ± 220.3	3.1	223.9	64.4 ± 33.6	7.9	173.0	56.1 ± 31.6	0.08	0.87	0.09
Indra Sarobar	10.3	473.6	145.3 ± 78.9	0.4	18.7	5.7 ± 3.1	BDL	23.8	3.4 ± 4.7	0.02	0.61	0.04

(a) Chobhar river

(b) Sisneri(Dakshinkali) river

(c) Mahalaxmi river

(d) Sisneri(Kulekhani) river

(e) Bhaise Dobhan river

(f) Samari (Rapati) river

(g) Taudaha lake

(h) Indra Sarovar lake

Figure 50: Water resources between Kathmandu and Makawanpur

= 89% respectively). The dose rates around Indra Sarovar lake have significant positive correlation with ^{40}K and ^{238}U (r = 0.91, r^2 = 82%, r = 0.96, r^2 = 92%).

4.6 The Associated Radiation Risk Factor

The associated radiological risk factor (AED, ELCR and H_{ex}) were calculated from the measured dose rates and the measured radioactivity (^{40}K, ^{238}U, ^{232}Th) in the study area. These were obtained by processing and aggregating the measured gamma ray spectra. The results were compared to the world average values. The AED, ELCR and H_{ex} were found greater than the world average (Table 19).

The outdoor AED varies from 0.05 to 0.25 mSv with average of 0.15 mSv. The lowest value was found in B-H and highest in D-K. The average AED was calculated highest in D-K and Lowest in B-H. The average AED was found higher than twice of world average in all sites except B-H. The Outdoor AED was calculated higher than world average but was lower than dose limit (1 mSv) recommended for public by ICRP (ICRP, 2007).

The ELCR varies from 0.2×10^{-3} to 0.92×10^{-3} with average of 0.53×10^{-3}. The lowest value was calculated in B-H and highest in D-K. The average value of ELCR was calculated lowest in B-H and highest in D-K. The ELCR was calculated higher than twice of world average in L-K, D-K and nearly equal to twice of world average in K-L and K-B. The average ELCR was reported 0.95 in Palestine, 3.27 times higher than the world average value but no risk of developing cancer has been stated (Thabayneh, 2012). In most of the study, mortality and ELCR has not been linked with the population of that area.

The H_{ex} varies from 0.07 to 1.57 with average of 0.66. The lowest value was calculated for B-H and highest for D-K. Similarly, the average H_{ex} was calculated lowest for B-H and higher for D-K. The external hazard index due to NORM were calculated < 1 which indicates no significant hazard in the area.

Table 19: The associated radiological risk factors

Sites	AED (mSv)			ELCR $\times 10^{-3}$			H_{ex}		
	min	max	mean	min	max	mean	min	max	mean
K-L	0.09	0.19	0.14 ± 0.01	0.33	0.69	0.52 ± 0.05	0.23	1.23	0.64 ± 0.11
L-K	0.11	0.22	0.16 ± 0.02	0.41	0.80	0.58 ± 0.06	0.34	1.31	0.74 ± 0.12
D-K	0.11	0.25	0.17 ± 0.02	0.41	0.92	0.62 ± 0.08	0.35	1.57	0.80 ± 0.15
K-B	0.09	0.21	0.15 ± 0.02	0.34	0.78	0.53 ± 0.06	0.09	1.18	0.64 ± 0.15
B-H	0.05	0.18	0.11 ± 0.02	0.20	0.67	0.39 ± 0.09	0.18	1.17	0.56 ± 0.12
K-H	0.05	0.25	0.15 ± 0.03	0.20	0.92	0.53 ± 0.10	0.07	1.57	0.66 ± 0.18
Adjoining environs									
Rakash Khola	0.11	0.18	0.14 ± 0.02	0.40	0.67	0.52 ± 0.05	0.21	4.42	1.50 ± 0.63
Bhimphedi	0.12	0.16	0.13 ± 0.01	0.43	0.60	0.49 ± 0.03	0.21	0.90	0.47 ± 0.10
Golping Besi	0.10	0.18	0.14 ± 0.01	0.35	0.64	0.52 ± 0.04	0.27	1.01	0.64 ± 0.10
Bhaise	0.09	0.16	0.13 ± 0.01	0.32	0.60	0.47 ± 0.05	0.24	0.93	0.57 ± 0.11
Hetauda	0.05	0.16	0.09 ± 0.01	0.20	0.60	0.33 ± 0.05	0.07	1.04	0.38 ± 0.10
Water resources									
Rivers									
Chobhar	0.12	0.24	0.17 ± 0.02	0.42	0.86	0.61 ± 0.08	0.39	1.42	0.80 ± 0.17
Sisneri (Dakshinkali)	0.16	0.19	0.18 ± 0.01	0.57	0.70	0.64 ± 0.03	0.55	1.23	0.82 ± 0.10
Mahalaxmi	0.12	0.23	0.18 ± 0.01	0.45	0.83	0.66 ± 0.04	0.45	1.21	0.83 ± 0.12
Sisneri (Kulekhani)	0.17	0.22	0.19 ± 0.01	0.62	0.79	0.68 ± 0.03	0.60	1.21	0.88 ± 0.11
Bhaise Dobhan	0.09	0.15	0.13 ± 0.01	0.32	0.56	0.48 ± 0.04	0.32	0.85	0.58 ± 0.09
Samari (Rapati)	0.07	0.17	0.11 ± 0.01	0.27	0.63	0.41 ± 0.04	0.18	0.94	0.49 ± 0.10
Lakes									
Taudaha	0.09	0.21	0.12 ± 0.02	0.34	0.78	0.45 ± 0.08	0.26	1.29	0.54 ± 0.13
Indra Sarovar	0.09	0.18	0.13 ± 0.02	0.32	0.65	0.47 ± 0.07	0.00	0.17	0.06 ± 0.03
World average (UNSCEAR, 2000)			0.07			0.29			0.35

The outdoor AED calculated from particular primordial radionuclides were found higher than world average (UNSCEAR, 1988). The outdoor AED from ^{40}K ranges from 0.002 to 0.13 mSv with an average of 0.04 mSv (Table 20). The average outdoor AED from ^{40}K was found highest in L-K, D-K and lowest in B-H. The average outdoor AED from ^{40}K was found higher than world average (0.03 mSv) in all sites and equal to world average in B-H. The outdoor AED from ^{238}U ranges from 0.0003 to 0.19 mSv with an average of 0.04 mSv. The average outdoor AED from ^{238}U was found higher than world average with highest in D-K and lowest in L-K. The average outdoor AED from ^{238}U was found higher than twice of world average (0.02 mSv) in D-K, K-B, K-H and equal to twice of world average in L-K, K-L. The outdoor AED from ^{232}Th ranges from 0.0003 to 0.18 mSv with an average of 0.05 mSv. The average outdoor AED from ^{232}Th was found higher than world average with lowest in B-H and highest in D-K. The average outdoor AED from ^{232}Th was found higher than twice of the world average (0.03 nGy/h) in L-K and D-K. (N.B.: World average outdoor AED was calculated from total AED by multiplying with outdoor occupancy factor, 0.2)

The outdoor AED from ^{137}Cs ranges from 0.0004 to 1.72 μSv with an average of 0.38 μSv. The outdoor AED from ^{137}Cs along the bank of water resources ranges from 0.002 to 2.15 μSv. The average outdoor AED from ^{137}Cs was found higher along Indra Sarovar lake and lower along Samari (Rapati) river. The ^{137}Cs had lower contribution to AED.

The higher associated radiation risk factor was calculated due to high radioactivity concentration of primordial radionuclides measured in the area due to geological and geographical factors. In some study, it is suggested that the low radiation exposure is beneficial for humans. Low radiation is used for curing of infections, rapid wound healing, relief in pain of arthritis and prevention of tumour growth (Cuttler, 2013). Low radiations exposures prevents occurrence of tumours (Mishra et al., 2008; Sharma et al., 2014). The observed dose shows no any associated health risk effects in these sites and the surrounding inhabitants.

Table 20: Outdoor AED from particular terrestrial and anthropogenic gamma radionuclides

Sites	AED (mSv)									AED (μSv)		
	^{40}K			^{238}U			^{232}Th			^{137}Cs		
	min	max	mean	min	max	mean	min	max	mean	min	max	mean
K-L	0.010	0.09	0.04 ± 0.02	0.0012	0.15	0.04 ± 0.02	0.0057	0.15	0.05 ± 0.02	0.004	1.44	0.38 ± 0.21
L-K	0.008	0.13	0.051 ± 0.01	0.0019	0.14	0.043 ± 0.02	0.0123	0.15	0.06 ± 0.02	0.001	1.64	0.41 ± 0.23
D-K	0.012	0.12	0.05 ± 0.01	0.0004	0.19	0.05 ± 0.02	0.0068	0.18	0.07 ± 0.02	0.0004	1.72	0.43 ± 0.24
K-B	0.010	0.09	0.04 ± 0.01	0.0039	0.15	0.05 ± 0.02	0.0061	0.16	0.05 ± 0.01	0.002	1.53	0.39 ± 0.22
B-H	0.002	0.08	0.03 ± 0.01	0.0003	0.15	0.03 ± 0.02	0.0003	0.13	0.04 ± 0.02	0.001	1.50	0.31 ± 0.18
K-H	0.002	0.13	0.04 ± 0.01	0.0003	0.19	0.04 ± 0.02	0.0003	0.18	0.05 ± 0.02	0.0004	1.72	0.38 ± 0.22
Adjoining environs												
Rakash Khola	0.004	0.08	0.04 ± 0.01	0.002	0.13	0.04 ± 0.02	0.0189	0.132	0.06 ± 0.02	0.005	1.72	0.51 ± 0.30
Bhimphedi	0.009	0.07	0.04 ± 0.01	0.002	0.15	0.04 ± 0.02	0.0099	0.123	0.05 ± 0.02	0.019	1.83	0.52 ± 0.29
Golping Besi	0.010	0.07	0.04 ± 0.01	0.003	0.11	0.04 ± 0.02	0.0074	0.114	0.05 ± 0.02	0.008	1.85	0.59 ± 0.30
Bhaise	0.010	0.07	0.03 ± 0.01	0.003	0.11	0.04 ± 0.02	0.0109	0.129	0.05 ± 0.02	0.009	1.77	0.49 ± 0.28
Hetauda	0.002	0.07	0.02 ± 0.01	0.0003	0.13	0.03 ± 0.01	0.0003	0.106	0.03 ± 0.01	0.002	1.55	0.38 ± 0.22
Water resources												
Rivers												
Chobhar	0.008	0.06	0.04 ± 0.01	0.005	0.19	0.05 ± 0.02	0.017	0.16	0.08 ± 0.03	0.002	2.09	0.62 ± 0.35
Sisneri (Dakshinkali)	0.032	0.09	0.06 ± 0.01	0.010	0.11	0.05 ± 0.02	0.028	0.13	0.07 ± 0.02	0.062	1.90	0.65 ± 0.35
Mahalakshmi	0.025	0.09	0.06 ± 0.01	0.002	0.16	0.05 ± 0.02	0.017	0.15	0.07 ± 0.02	0.029	1.95	0.69 ± 0.35
Sisneri (Kulekhani)	0.033	0.09	0.06 ± 0.01	0.014	0.14	0.06 ± 0.02	0.031	0.14	0.07 ± 0.02	0.060	1.81	0.63 ± 0.34
Bhaise Dobhan	0.010	0.06	0.03 ± 0.01	0.004	0.11	0.04 ± 0.02	0.013	0.10	0.05 ± 0.02	0.010	1.64	0.50 ± 0.29
Samari (Rapati)	0.005	0.07	0.03 ± 0.01	0.002	0.11	0.04 ± 0.02	0.003	0.10	0.04 ± 0.01	0.008	1.44	0.44 ± 0.25
Lakes												
Taudaha	0.011	0.090	0.04 ± 0.011	0.002	0.1262	0.04 ± 0.02	0.006	0.130	0.04 ± 0.016	0.009	1.99	0.50 ± 0.28
Indra Sarovar	0.001	0.024	0.003 ± 0.004	0.011	0.1372	0.02 ± 0.02	BDL	0.018	0.003 ± 0.004	0.097	2.15	1.01 ± 0.38
World average (UNSCEAR, 1988)			0.03			0.02			0.03			

4.7 Statistical Analysis of Radioactive Measurements

4.7.1 Descriptive Statistics

The numerical insights about the in-situ radiometric data of study area is presented in Table 21. The summarized value of the numerical variables were studied for descriptive analysis of the data of dose rates, activity concentrations of primordial radionuclides, outdoor AED, ELCR and H_{ex} in survey area. The central tendency and the dispersion of the numerical variables of the data were studied. The important technologies of descriptive analysis like mean, median, inter quartile range, deviation, skewness and kurtosis were analysed for the data of studied area.

As the median is robust than mean for skewed distribution (Reimann & Filzmoser, 2000), it was used for descriptive statistical analysis. The mean of the data of dose rates, AED and ELCR in the survey area (K-H) were found lower than the median, and hence the data were negatively skewed.

The mean and median of dose rates, AED and ELCR in all sites were found nearly equal with mean slightly greater than median except in D-K. The distribution of dose rates in all sites were found approximately symmetric as coefficient of skewness lies between -0.5 to +0.5 (Bulmer, 1979). The data in the L-K, K-B and K-H sites were found leptokurtic as excess kurtosis were found > 0 except in K-L, D-K and B-H where the distribution were platykurtic as excess kurtosis were < 0 (Westfall, 2014). The mean of activity concentrations of ^{40}K, ^{238}U and ^{232}Th in all sites were found greater than the median and thus, the data were found positively skewed. The distribution of ^{40}K were found approximately symmetric in all sites except B-H where the distribution were found moderately skewed. The distribution of ^{238}U were found moderately skewed in all sites. The distribution of ^{232}Th were found approximately symmetric for all sites except K-B and B-H where the distribution were moderately skewed. The distribution of ^{40}K, ^{238}U and ^{232}Th were found leptokurtic for all sites. The H_{ex} distribution were found approximately symmetric with positive skewness in all sites except in D-K where it is negatively skewed. The distribution were found leptokurtic for all sites except D-K and B-H where the distribution were found platykurtic.

4.7.2 Exploratory Analysis

After descriptive data analysis, exploratory data analysis (the visual way to analyze the data) is performed.

Univariate Analysis

In univariate exploratory analysis, histogram and box plot were used for analyzing the data. For univariate analysis, the data along the road between Kathmandu and

Makawanpur were analysed (excluding adjoining environs for K-H).

For histogram, the p-value is less than the significance level (.05) in all sites, and hence it is concluded that the data do not follow a normal distribution. The distribution of dose rates were found approximately symmetric with Kurtosis. The location and shape parameter provided in graph gives the center (mean) and spread (SD) of the data respectively (Figure 51). The D-K and B-H histograms appear to be bimodal because D-K and B-H data sets have two distinct cluster as dose rates in Dakshinkali have one center (lower) and near Kulekhani have another (higher). Similarly, Hetauda has lower dose rates than Bhimphedi.

The box plot of dose rates data is shown in Figure 52. The median and inter quartile range are the measure of the centre and spread of the data respectively. The median of the dose rates was found highest for D-K and lowest for B-H. The data were dispersed highest in D-K (long box) and lowest in K-L (small box). Since, the median is approximately in the middle of the box, and the whiskers are approximately about the same on both sides of the box, the distribution is approximately symmetric. The median of dose rates data in L-K, K-B and K-H sites is slightly shifted towards to the lower quartile, hence the distribution is slightly skewed right (positively skewed). In K-L, D-K and B-H where the median is shifted towards upper quartile, the distribution is slightly skewed left (negatively skewed). The overall spread (extreme value of the whisker) is higher for D-K (larger range) and lower for K-L (smaller range) which indicates wider distribution and more scattered data in D-K and less scattered in K-L. Outlier indicates observation point that is distant from other observations (not the wrong value).

The box plot of concentration of gamma radionuclides and dose rate calculated from the concentration of particular gamma radionuclides are shown in Figure 53 and 54 respectively.

The distribution of concentrations of ^{40}K is found approximately symmetric in all sites with slightly positive skewness as mean is slightly greater than median. The distribution of ^{238}U concentrations is found moderately positively skewed for all sites. The distribution of concentrations of ^{232}Th has positive skewness and is found approximately symmetric in K-L and L-K sites whereas moderately skewed in other sites. The distribution of concentrations of ^{137}Cs is found moderately and positively skewed in all sites.

Table 21: Descriptive statistics

	Dose rates (nGy/h)						^{40}K (Bq/kg)						^{238}U (Bq/kg)						^{232}Th (Bq/kg)					
	K-H	K-L	L-K	D-K	K-B	B-H	K-H	K-L	L-K	D-K	K-B	B-H	K-H	K-L	L-K	D-K	K-B	B-H	K-H	K-L	L-K	D-K	K-B	B-H
Number of values	87587	19658	14546	21366	12594	31341	87587	19658	14546	21367	12594	31341	87587	19658	14546	21367	12594	31341	87587	19658	14546	21367	12594	31341
Minimum	44.6	73.9	92.6	92.1	76.4	44.6	40.1	199.4	146.8	234.1	188.4	40.1	0.6	2.1	3.4	0.6	6.9	0.6	0.4	7.6	16.3	9.1	8.1	0.4
Maximum	205.6	153.7	179.1	205.6	175.0	148.9	2443.0	1740.6	2443.0	2403.8	1699.3	1630.7	342.0	263.4	243.9	342.0	269.6	257.8	233.4	194.7	203.0	233.4	208.8	166.9
Range	161.0	79.8	86.5	113.5	98.6	104.4	2402.9	1541.2	2296.2	2169.7	1510.9	1590.7	341.5	261.3	240.5	341.4	262.7	257.3	233.0	187.0	186.7	224.3	200.7	166.5
Mean	118.6	115.9	129.8	139.1	119.6	87.5	850.2	850.4	997.0	1060.4	773.9	541.2	74.6	72.5	76.7	86.0	82.3	56.9	73.5	70.2	84.3	89.9	73.0	49.6
Median	119.8	116.3	128.2	140.3	118.7	84.3	839.5	842.0	976.6	1047.9	758.1	508.6	69.5	68.1	72.0	80.7	78.1	52.5	71.5	68.4	82.7	87.5	70.9	47.2
First quartile	106.4	107.2	120.5	125.2	109.7	72.8	636.6	702.7	815.4	860.4	609.1	369.7	47.2	47.2	50.1	56.1	54.4	34.4	53.5	53.8	66.5	70.1	55.8	33.6
Third quartile	133.2	123.8	137.7	152.4	128.8	102.2	1048.2	986.0	1158.1	1241.7	916.8	684.8	96.9	93.5	98.7	110.3	105.9	74.7	91.3	84.7	100.3	107.1	87.7	63.1
Variance	548.7	133.8	172.2	307.1	191.1	364.7	94130.2	44438.2	67632.6	78451.0	54471.6	53730.5	1376.8	1179.0	1286.3	1612.5	1385.9	917.6	799.5	535.3	619.7	751.4	594.8	491.5
Average deviation	18.0	9.4	10.4	14.6	11.1	15.8	244.2	168.1	205.7	223.6	185.1	185.7	29.5	27.4	28.7	31.9	29.8	23.9	22.5	18.4	19.9	21.8	19.2	17.6
Standard deviation	23.4	11.6	13.1	17.5	13.8	19.1	306.8	210.8	260.1	280.1	233.4	231.8	37.1	34.3	35.9	40.2	37.2	30.3	28.3	23.1	24.9	27.4	24.4	22.2
Coefficient of variation	0.197	0.100	0.101	0.126	0.116	0.218	0.361	0.248	0.261	0.264	0.302	0.428	0.497	0.473	0.468	0.467	0.452	0.532	0.385	0.330	0.295	0.305	0.334	0.447
Skew	-0.296	0.032	0.52	-0.006	0.343	0.407	0.287	0.283	0.451	0.328	0.466	0.655	0.772	0.706	0.653	0.722	0.649	0.876	0.448	0.471	0.396	0.509	0.625	0.667
Kurtosis	0.107	-0.387	0.106	-0.534	0.257	-0.624	0.075	0.068	0.453	0.167	0.224	0.267	0.702	0.534	0.267	0.637	0.37	1.055	0.274	0.326	0.142	0.361	0.855	0.556
Critical K-S stat, α = .05	0.005	0.01	0.011	0.009	0.012	0.008	0.005	0.01	0.011	0.009	0.012	0.008	0.005	0.01	0.011	0.009	0.012	0.008	0.005	0.01	0.011	0.009	0.012	0.008

	AED (mSv)						ELCR $\times 10^{-3}$						H_{ex}					
	K-H	K-L	L-K	D-K	K-B	B-H	K-H	K-L	L-K	D-K	K-B	B-H	K-H	K-L	L-K	D-K	K-B	B-H
Number of values	87587	19658	14546	21366	12594	31341	87587	19658	14546	21366	12594	31341	87587	19658	14546	21367	12594	31341
Minimum	0.055	0.091	0.114	0.113	0.094	0.055	0.199	0.330	0.413	0.411	0.341	0.199	0.067	0.233	0.338	0.349	0.312	0.067
Maximum	0.252	0.188	0.220	0.252	0.215	0.183	0.918	0.686	0.800	0.918	0.782	0.665	1.575	1.228	1.306	1.575	1.183	1.166
Range	0.197	0.098	0.106	0.139	0.121	0.128	0.719	0.356	0.386	0.507	0.440	0.466	1.508	0.995	0.968	1.226	0.871	1.099
Mean	0.145	0.142	0.159	0.171	0.147	0.107	0.530	0.518	0.580	0.621	0.534	0.391	0.662	0.644	0.740	0.800	0.665	0.458
Median	0.147	0.143	0.157	0.172	0.146	0.103	0.535	0.519	0.572	0.627	0.530	0.376	0.663	0.638	0.733	0.795	0.660	0.445
First quartile	0.130	0.131	0.148	0.153	0.135	0.089	0.475	0.478	0.538	0.559	0.490	0.325	0.550	0.564	0.652	0.693	0.582	0.356
Third quartile	0.163	0.152	0.169	0.187	0.158	0.125	0.595	0.553	0.615	0.681	0.575	0.457	0.777	0.718	0.820	0.900	0.743	0.551
Variance	0.0008	0.0002	0.0003	0.0005	0.0003	0.0005	0.0109	0.0027	0.0034	0.0061	0.0038	0.0073	0.0312	0.0131	0.0154	0.0227	0.0147	0.0195
Average deviation	0.022	0.012	0.013	0.018	0.014	0.019	0.080	0.042	0.047	0.065	0.049	0.070	0.139	0.091	0.099	0.121	0.096	0.113
Standard deviation	0.029	0.014	0.016	0.021	0.017	0.023	0.105	0.052	0.059	0.078	0.062	0.085	0.177	0.115	0.124	0.151	0.121	0.140
Coefficient of variation	0.197	0.100	0.101	0.126	0.116	0.218	0.197	0.100	0.101	0.126	0.116	0.218	0.267	0.178	0.168	0.188	0.182	0.305
Skew	-0.296	0.032	0.520	-0.006	0.343	0.407	-0.296	0.032	0.520	-0.006	0.343	0.407	0.022	0.293	0.368	0.241	0.323	0.397
Kurtosis	0.107	-0.387	0.106	-0.534	0.257	-0.624	0.107	-0.387	0.106	-0.534	0.257	-0.624	0.074	0.161	0.181	-0.121	0.254	-0.083
Critical K-S stat, α = .05	0.005	0.010	0.011	0.009	0.012	0.008	0.005	0.010	0.011	0.009	0.012	0.008	0.005	0.010	0.011	0.009	0.012	0.008

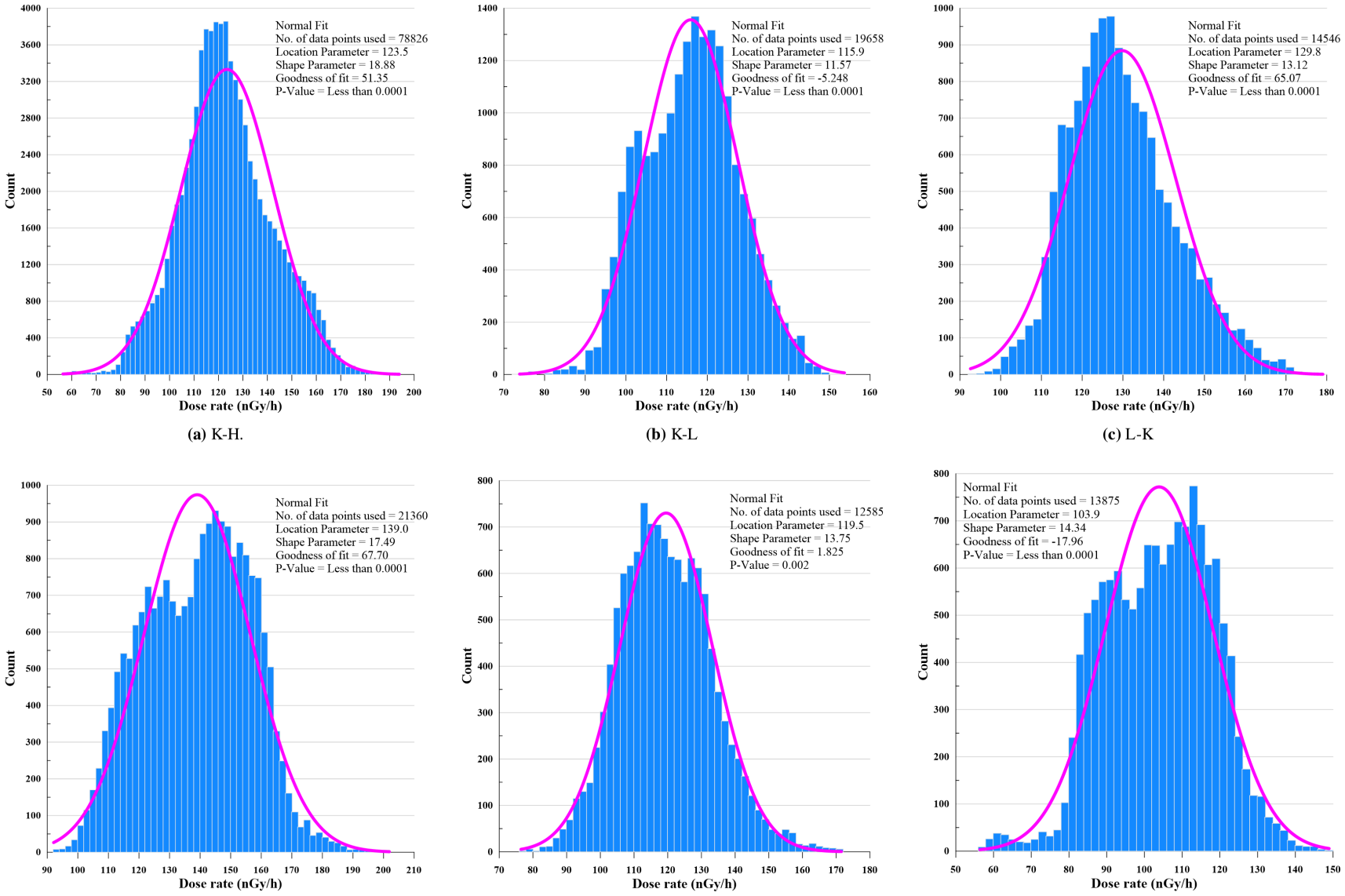

Figure 51: Histogram of the dose rates distribution in studied area with corresponding normal curve

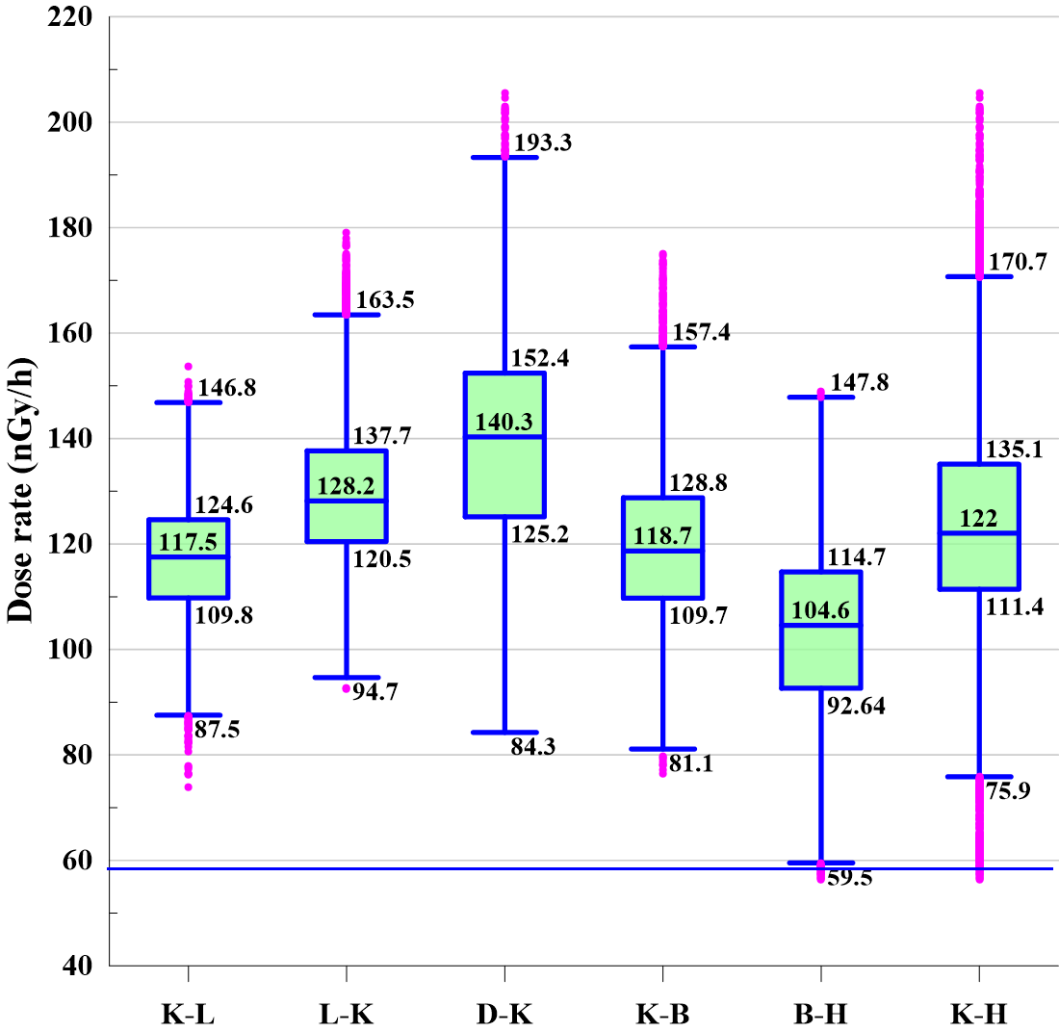

Figure 52: Dose rates distribution in studied area

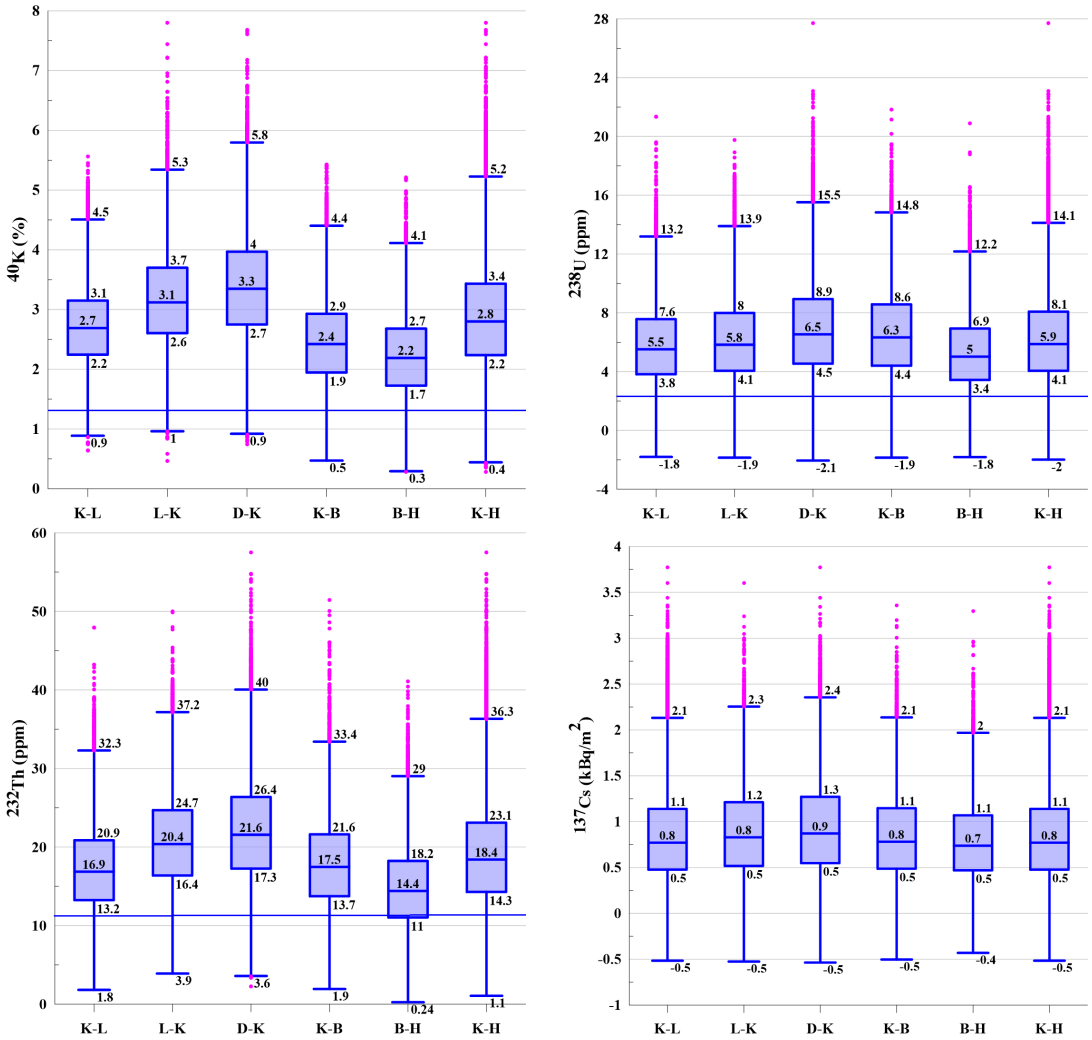

Figure 53: Concentrations of gamma radionuclides distribution in studied area

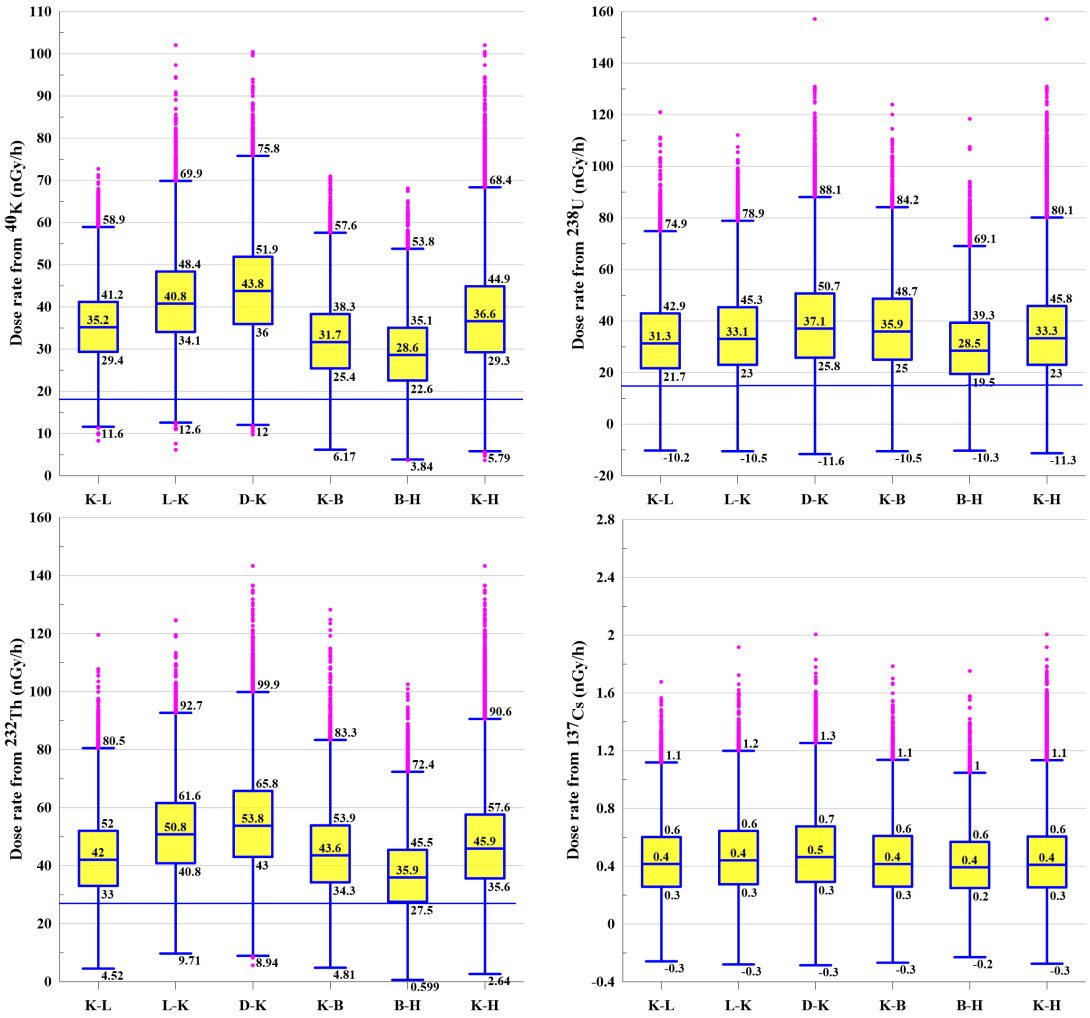

Figure 54: Dose rates calculated from gamma radionuclides concentrations

The distribution of dose rates contributed from ^{40}K in all sites is found slightly positively skewed as mean is greater than median (median is slightly shifted downward). The distribution of dose rates contributed from ^{40}K is found approximately symmetric in all sites. The distribution of dose rates contributed from ^{238}U is found positively and moderately skewed in all sites. The distribution of dose rates contributed from ^{232}Th is found approximately symmetric in K-L, L-K, and K-H whereas moderately skewed in D-K, K-B and B-H sites. The distribution of dose rates contributed from ^{137}Cs is found positively moderately skewed in all sites.

The distribution were found to be generally asymmetric due to presence of outliers and spatial nature of the data measured.

4.7.3 Statistics of Adjoining Environs and Water Resources

The statistics of the in-situ radiometric data of adjoining environs and water resources are written as representative value for study area (Table 22). The mean of dose rates, outdoor AED and ELCR were found lower than the median for all adjoining environs sites, and hence were negatively skewed except for Hetauda. The distribution of outdoor AED and ELCR were found approximately symmetric except for Bhaise and Bhimphedi where the data distribution were found moderately skewed. The H_{ex} data distribution were found approximately symmetric for all adjoining environs sites. The box plot of dose rates in adjoining environs is shown in Figure 55. The distribution of dose rates is found approximately symmetric in Rakash Khola, Golping Besi (with slightly negative skewness) and Hetauda (with slightly positive skewness) whereas moderately negatively skewed in Bhaise and highly negatively skewed in Bhimphedi. The median value is find higher in Rakash Khola and lower in Hetauda. The distribution of dose rates, AED and ELCR were found leptokurtic for all adjoining environs except for Rakash Khola where the distribution were found platykurtic. The distribution of H_{ex} data in adjoining environs were found positively skewed, approximately symmetric and Leptokurtic for all sites.

The dose rates and outdoor AED distribution along the banks of rivers within survey area were found negatively skewed except for Chobhar and Sisneri (Kulekhani) where the data were skewed positively (Table 22). The distribution of data were found approximately symmetric along the banks of the rivers except for Sisneri (Kulekhani) and Bhaise Dobhan where the distribution of data were found moderately symmetric. The distribution of dose rates and AED were found leptokurtic along all banks of the rivers except Sisneri (Dakshinkali) where the distribution were found platykurtic. Around the Indra Sarovar lake, the distribution of dose rates and AED were found negatively skewed, approximately symmetric and platykurtic. Around the Taudaha lake, the distribution were found positively highly skewed and leptokurtic.

Table 22: Descriptive statistics of adjoining environs and water resources

Adjoining environs																				
	Dose rate (nGy/h)					AED (mSv)					ELCR $\times 10^{-3}$					H_{ex}				
	Rakash Khola	Bhimphedi	Golping Besi	Bhaise	Hetauda	Rakash Khola	Bhimphedi	Golping Besi	Bhaise	Hetauda	Rakash Khola	Bhimphedi	Golping Besi	Bhaise	Hetauda	Rakash Khola	Bhimphedi	Golping Besi	Bhaise	Hetauda
Number of values	1966	1504	2054	1530	8732	1966	2091	2054	1530	8732	1966	2091	2054	1530	8732	1966	2091	2054	1530	8732
Minimum	89.0	74.4	77.7	71.2	44.6	0.109	0.095	0.095	0.087	0.055	0.397	0.347	0.347	0.318	0.199	0.339	0.358	0.274	0.240	0.067
Maximum	149.6	138.4	143.2	134.4	134.0	0.183	0.170	0.176	0.165	0.164	0.668	0.618	0.640	0.600	0.598	1.146	1.089	1.013	0.931	1.039
Range	60.5	64.1	65.5	63.2	89.4	0.074	0.074	0.080	0.077	0.110	0.270	0.271	0.293	0.282	0.399	0.808	0.731	0.739	0.691	0.972
Mean	116.0	106.4	117.1	105.0	74.5	0.142	0.139	0.144	0.129	0.091	0.518	0.505	0.523	0.469	0.333	0.657	0.628	0.635	0.565	0.379
Median	118.6	108.5	116.8	106.0	74.6	0.145	0.139	0.143	0.130	0.092	0.530	0.505	0.521	0.473	0.333	0.656	0.626	0.631	0.564	0.376
First quartile	105.1	103.9	112.0	99.6	67.7	0.129	0.132	0.137	0.122	0.083	0.469	0.481	0.500	0.445	0.302	0.572	0.559	0.569	0.496	0.311
Third quartile	125.3	112.6	121.7	111.2	81.4	0.154	0.146	0.149	0.136	0.100	0.560	0.531	0.544	0.497	0.364	0.736	0.689	0.699	0.630	0.442
Variance	147.6	115.2	61.8	108.5	109.1	0.000	0.000	0.000	0.000	0.000	0.003	0.001	0.001	0.002	0.002	0.014	0.010	0.009	0.011	0.010
Average deviation	10.5	7.5	6.1	7.8	8.2	0.013	0.008	0.007	0.010	0.010	0.047	0.029	0.027	0.035	0.036	0.096	0.078	0.077	0.082	0.077
Standard deviation	12.1	10.7	7.9	10.4	10.4	0.015	0.010	0.010	0.013	0.013	0.054	0.037	0.035	0.047	0.047	0.119	0.099	0.096	0.105	0.098
Coefficient of variation	0.105	0.101	0.067	0.099	0.140	0.105	0.073	0.067	0.099	0.140	0.105	0.073	0.067	0.099	0.140	0.182	0.158	0.151	0.186	0.258
Skew	-0.201	-1.162	-0.074	-0.74	0.363	-0.201	-0.715	-0.074	-0.74	0.363	-0.201	-0.715	-0.074	-0.74	0.363	0.219	0.353	0.168	0.069	0.33
Kurtosis	-1.022	1.309	1.521	1.382	2.184	-1.022	2.149	1.521	1.382	2.184	-1.022	2.149	1.521	1.382	2.184	0.029	0.62	0.132	0.258	0.706
Critical K-S stat, α = .05	0.031	0.035	0.03	0.035	0.015	0.031	0.03	0.03	0.035	0.015	0.031	0.03	0.03	0.035	0.015	0.031	0.03	0.03	0.035	0.015

Water resources																	
	Dose rate (nGy/h)								AED (mSv)								
	Chobhar	Sisneri (Dakshinkali)	Mahalaxmi	Sisneri (Kulekhani)	Bhaise Dobhan	Samari (Rapati)	Indra Sarovar	Taudaha	Chobhar	Sisneri (Dakshinkali)	Mahalaxmi	Sisneri (Kulekhani)	Bhaise Dobhan	Samari (Rapati)	Indra Sarovar	Taudaha
Number of values	717	316	1604	669	466	1918	898	2398	717	316	1604	669	466	1918	898	2398
Minimum	94.8	127.4	99.8	138.5	71.2	60.2	71.0	76.9	0.116	0.156	0.122	0.170	0.087	0.074	0.087	0.094
Maximum	192.4	157.6	185.0	177.0	126.4	141.6	146.2	174.2	0.236	0.193	0.227	0.217	0.155	0.174	0.179	0.214
Range	97.6	30.3	85.1	38.6	55.2	81.4	75.3	97.4	0.120	0.037	0.104	0.047	0.068	0.100	0.092	0.119
Mean	137.0	143.3	147.1	151.4	106.6	91.1	105.8	100.5	0.168	0.176	0.180	0.186	0.131	0.112	0.130	0.123
Median	135.6	144.1	146.6	150.6	106.7	91.6	109.1	97.1	0.166	0.177	0.180	0.185	0.131	0.112	0.134	0.119
First quartile	126.3	139.0	141.8	147.0	102.7	87.1	94.7	90.9	0.155	0.170	0.174	0.180	0.126	0.107	0.116	0.112
Third quartile	148.5	148.0	153.0	154.8	111.5	95.5	115.2	104.3	0.182	0.181	0.188	0.190	0.137	0.117	0.141	0.128
Variance	307.0	43.1	90.0	38.7	61.9	92.7	213.1	288.0	0.0005	0.0001	0.0001	0.0001	0.0001	0.0001	0.0003	0.0004
Average deviation	13.7	5.4	7.1	4.9	5.8	6.6	11.9	10.8	0.017	0.007	0.009	0.006	0.007	0.008	0.015	0.013
Standard deviation	17.5	6.6	9.5	6.2	7.9	9.6	14.6	17.0	0.021	0.008	0.012	0.008	0.010	0.012	0.018	0.021
Coefficient of variation	0.128	0.046	0.064	0.041	0.074	0.106	0.138	0.16891	0.128	0.046	0.064	0.041	0.074	0.106	0.138	0.169
Skew	0.191	-0.397	-0.266	0.813	-0.89	-0.053	-0.228	2.343	0.191	-0.397	-0.266	0.813	-0.89	-0.053	-0.228	2.343
Kurtosis	0.349	-0.543	2.032	1.245	2.867	3.055	-0.329	6.081	0.349	-0.543	2.032	1.245	2.867	3.055	-0.329	6.081
Critical K-S stat, α = .05	0.05	0.076	0.034	0.052	0.063	0.031	0.045	0.028	0.05	0.076	0.034	0.052	0.063	0.031	0.045	0.028

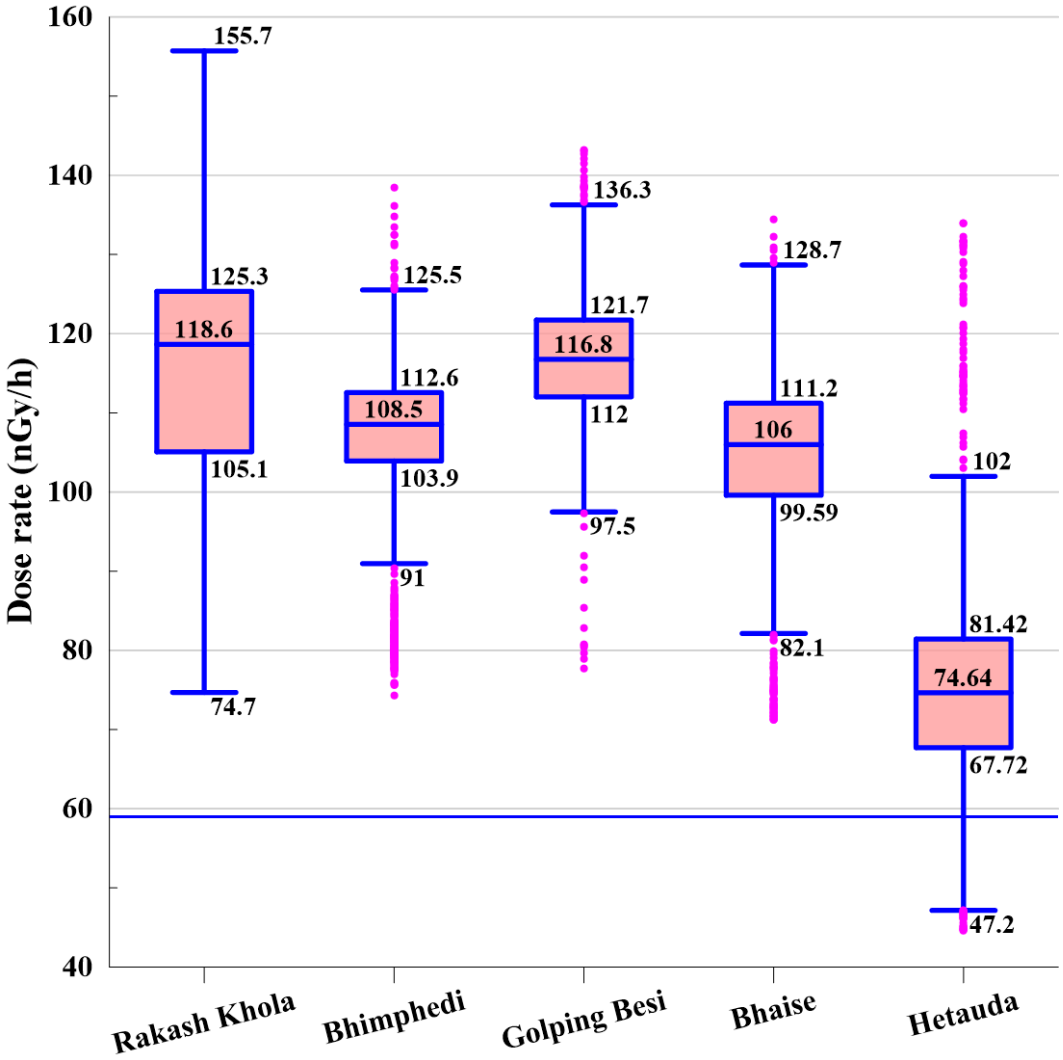

Figure 55: Dose rates distribution in adjoining environs

Bivariate Exploratory Analysis

The relationship between dose rates and concentrations of gamma radionuclides were shown in scatter plot with error bar (standard error) (Figure 56 - 62). The average of 300 s data is taken for analysis in all sites except K-H where the average of 900 s data is taken for analysis. The instrument record spectra every second and therefore the data will give the measurement of average of 5 minute and 15 minute respectively. The dose rates in the studied area showed positive (linear) and strong correlations with the concentrations of gamma radionuclides. The correlation analysis between gamma radionuclides and outdoor absorbed dose rates showed that the elevated dose rates in the area is due to higher level of terrestrial radionuclides concentrations. The regression output below showed that the variables had statistically significant relationship as their p-value is less than significance level (.05). The p-value was 0.001 for all except for Th in B-H where p-value was 0.048. The precision of the predictions can be seen from standard error of the slope (standard error of estimate) as it represents the average distance that the observed values deviate from the regression line. The smaller value indicates that the values are closer to the regression line.

The dose rates in the area have strong and positive correlation with ^{40}K, ^{232}Th and ^{238}U (r = 0.92, 0.90 and 0.85 respectively). The regression analysis showed that the dose rates in the studied area depends 85% , 81% and 73% on concentrations of ^{40}K, ^{232}Th and ^{238}U respectively.

In K-L, the dose rates were strongly and positively correlated with concentrations of ^{40}K (r = 0.89), ^{232}Th (r = 0.91) and weakly correlated with ^{238}U (r = 0.59). In L-K, the dose rates had strong and positive correlation with concentrations of ^{40}K (r = 0.87) and moderate correlation with ^{232}Th (r = 0.76) and ^{238}U (r = 0.74). In D-K, the dose rates had strong and positive correlation with ^{40}K (r = 0.86), ^{238}U (r = 0.87) and ^{232}Th (r = 0.82). In K-B, the dose rate had strong and positive correlation with concentrations of ^{40}K (r = 0.79), ^{238}U (r = 0.81) and very weak correlation with ^{232}Th (r = 0.31). In B-H, the dose rates showed strong and positive correlation with ^{40}K (r = 0.95), ^{238}U (r = 0.90) and ^{232}Th (r = 0.90).

Similarly, the dose rates dependence on concentrations of ^{40}K, ^{232}Th and ^{238}U in K-L, L-K, D-K, K-B and B-H was 80%, 84% and 34%, 76%, 58% and 55%, 73%, 67% and 76%, 63%, 9.4% and 66%, 91%, 81% and 80% respectively.

The dose rates in studied area shows strong and positive correlation with surface activity of ^{137}Cs (r = 0.91, r^2 = 82%). The dose rates had moderate positive correlation with surface activity of ^{137}Cs in K-L (r = 0.64, r^2 = 41%), L-K (r = 0.72, r^2 = 52%) and K-B (r = 0.76, r^2 = 58%) while strong and positive correlation in D-K (r = 0.78, r^2 = 62%) and B-H (r = 0.83, r^2 = 69%).

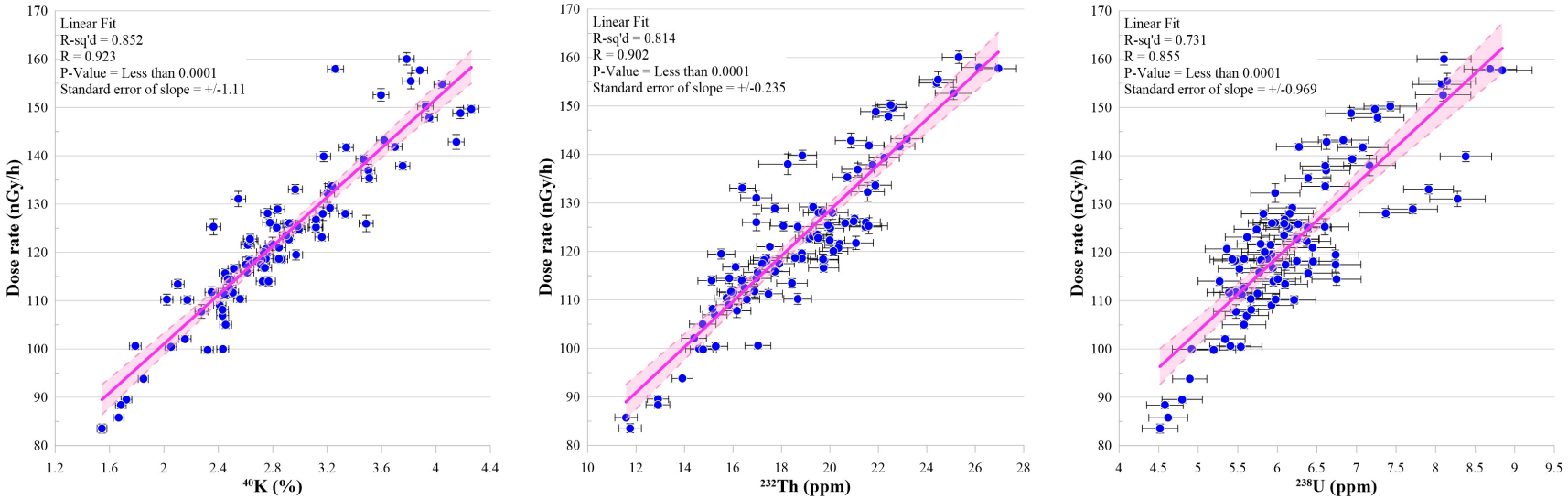

Figure 56: Dose rates and mass concentration in K-H

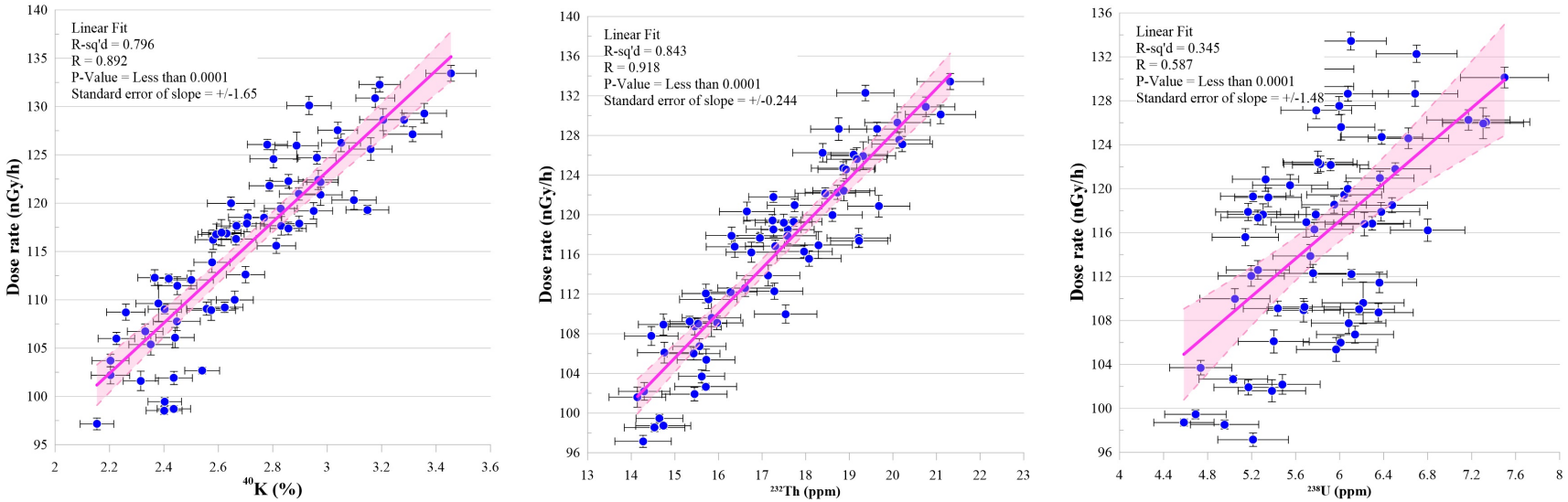

Figure 57: Dose rates and mass concentration in K-L

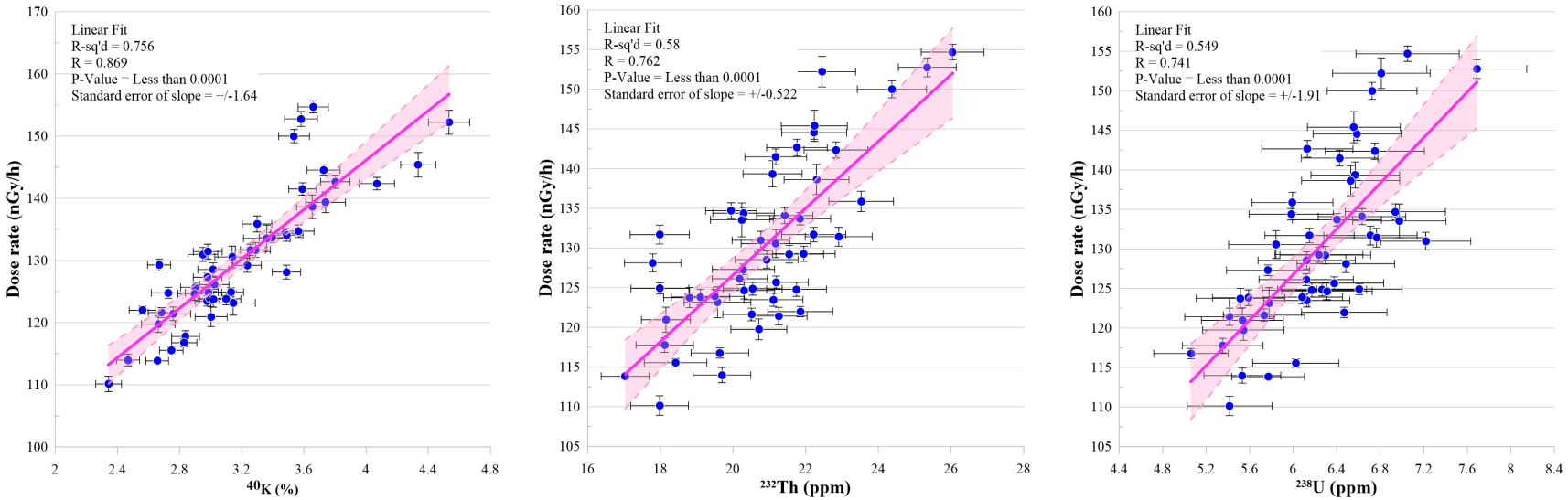

Figure 58: Dose rates and mass concentration in L-K

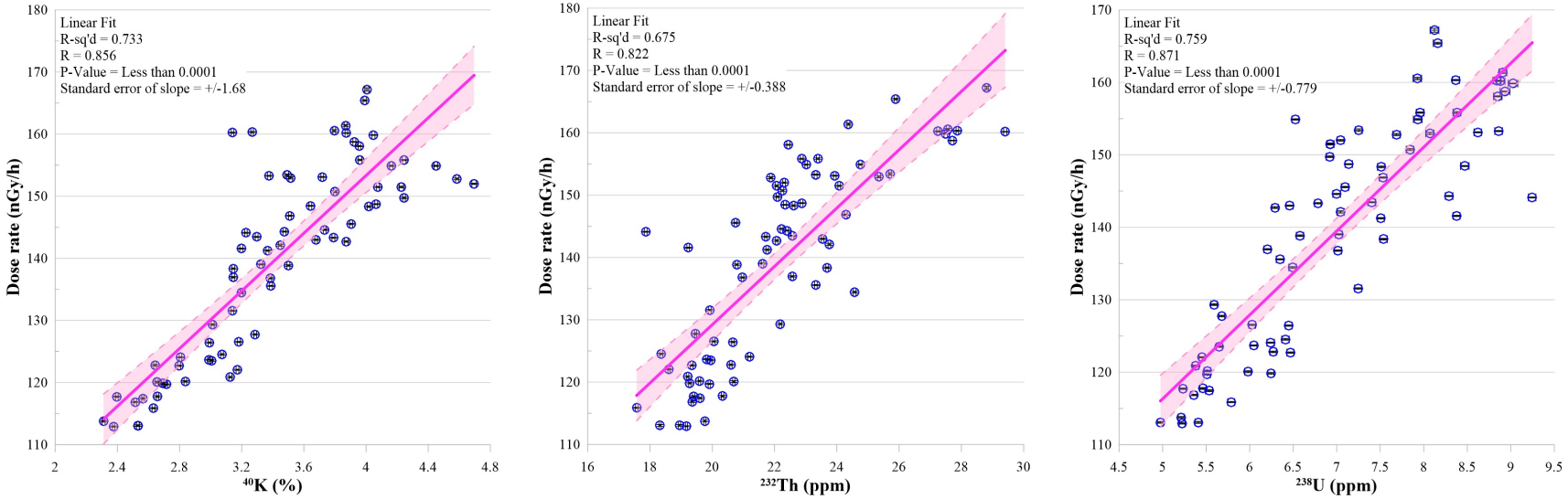

Figure 59: Dose rates and mass concentration in D-K

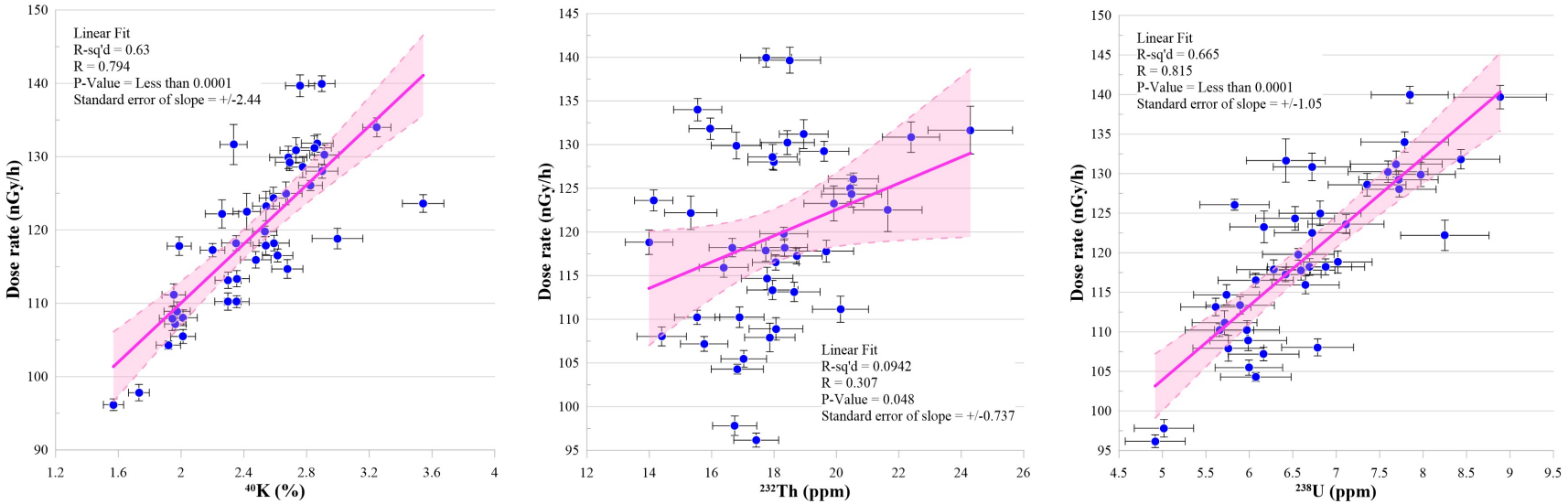

Figure 60: Dose rates and mass concentration in K-B

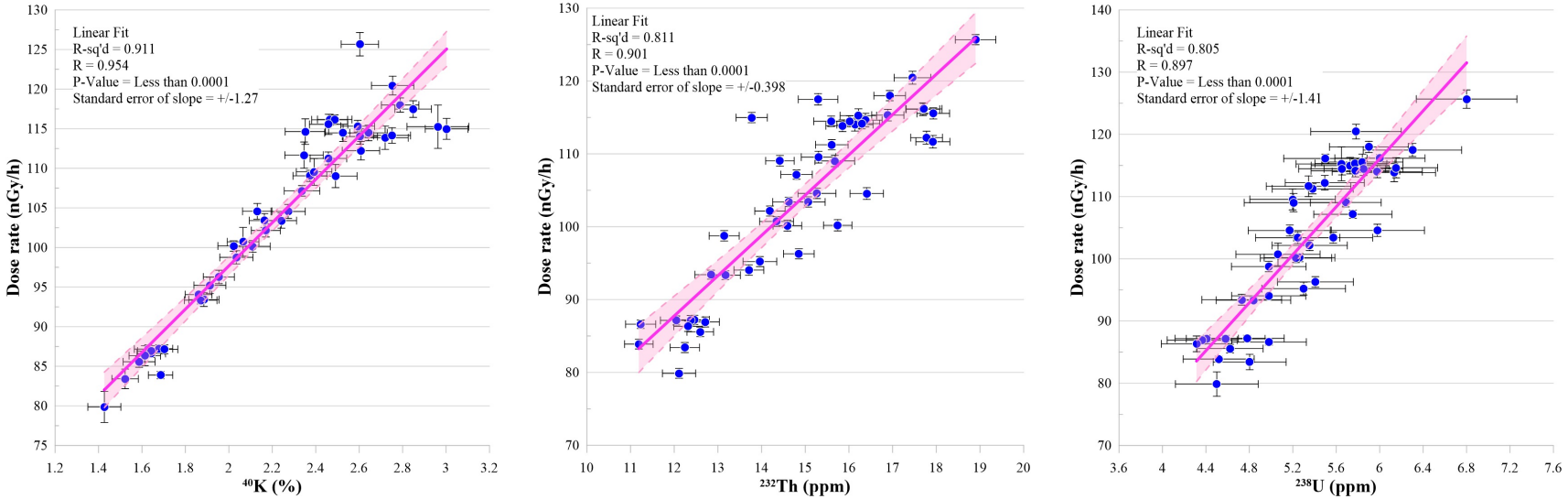

Figure 61: Dose rates and mass concentration in B-H

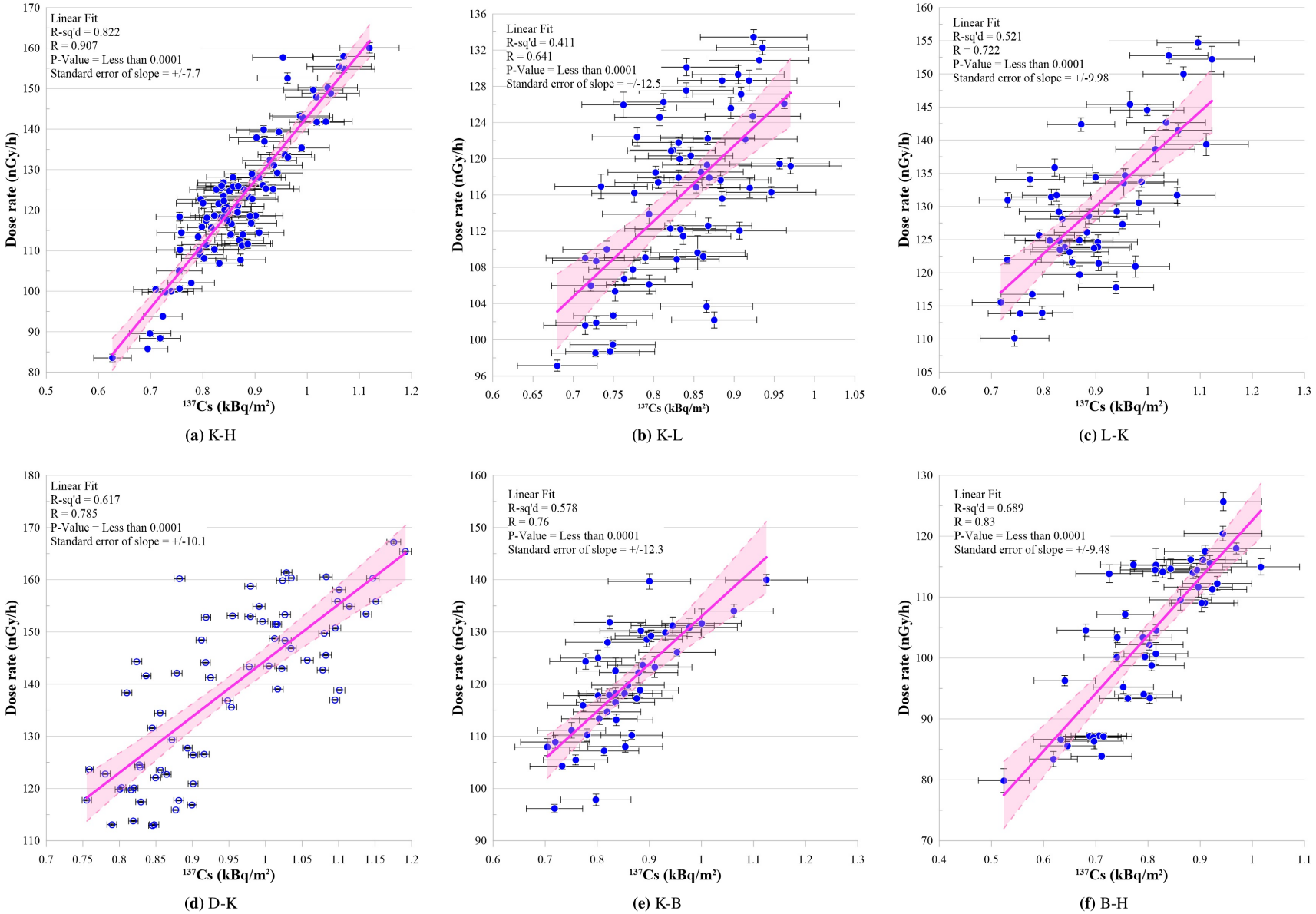

Figure 62: Dose rates and surface activity concentrations of ^{137}Cs between Kathmandu and Makawanpur

Multivariate Exploratory Analysis

The results of multivariate exploratory analysis of activity concentrations and dose rates are performed using PCA and ternary diagram. The spatial variability of the elevated level of radioactivity in the study area is mainly constrained by underlying geology and geochemical process at high altitude.

PCA

The Pearson correlation matrix is given in Table 23 where D is the dose rates, K, U, Th and Cs are the concentrations of ^{40}K, ^{238}U, ^{232}Th and ^{137}Cs in the studied sites. The variables are found highly correlated. The PCA results show that 88.70% of total variance in the studied data can be explained by the Factor F1 (first principal component) and Factor F2 (second principal components) (Figure 63). It is found that all variables have positive projection on F1 and accounts 79.31% of the total variance and thus, explains the main process about radioactivity levels in the study area. F1 is positively correlated with variables means F1 increases with increase in five variables suggesting that these five variables vary together. If one increases, other also tend to increase. F1 is measure of these variables. F2 accounts 9.39% variance and have positive projection for D, U and Th and negative for K and Cs (Table 24) . The loadings are the weights of variable in principal component analysis. The variables are seen to be positively correlated (Figure 63). From PCA biplot, it is seen that the lowest gamma dose rates are projected with lowest F1 values and highest with higher at other end of the axis.

Table 23: Pearson's correlation matrix

Variables	D	K	U	Th	Cs
D	**1.000**	**0.914**	**0.819**	**0.889**	**0.794**
K	**0.914**	**1.000**	**0.634**	**0.759**	**0.740**
U	**0.819**	**0.634**	**1.000**	**0.630**	**0.550**
Th	**0.889**	**0.759**	**0.630**	**1.000**	**0.634**
Cs	**0.794**	**0.740**	**0.550**	**0.634**	**1.000**

Values in bold are different from 0 with a significance level α = 0.05

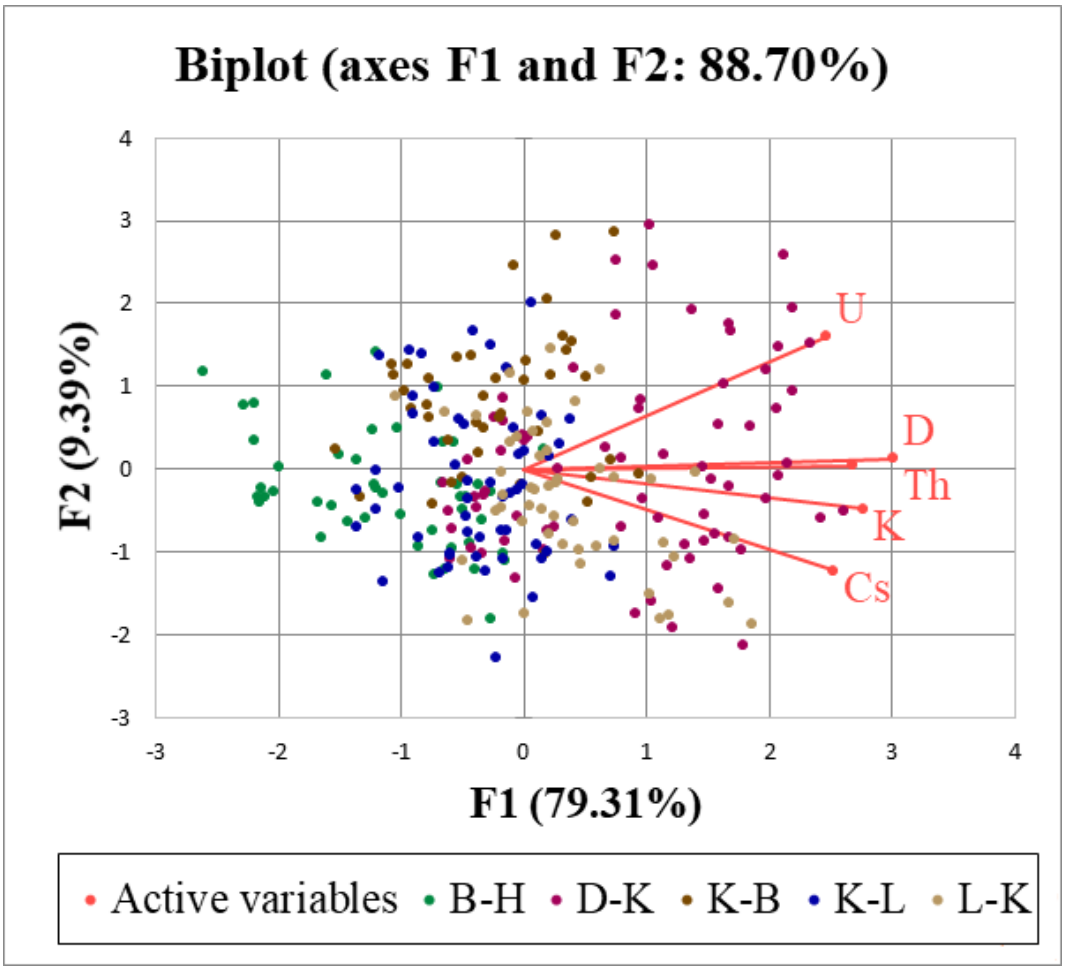

Figure 63: PCA biplot of concentrations of gamma radionuclides and dose rates in Kathmandu and Makawanpur

Table 24: PCA loading factor

	F1	F2	F3	F4	F5
D	0.995	0.043	0.042	0.026	0.075
K	0.915	-0.160	0.078	0.361	-0.027
U	0.813	0.528	-0.244	-0.019	-0.022
Th	0.884	0.013	0.411	-0.222	-0.025
Cs	0.834	-0.404	-0.332	-0.172	-0.011

Ternary Diagram

The relative proportions of dose rates contributions from primordial radionuclides between Kathmandu and Makawanpur is shown in Figure 64. The studied sites show a relatively uniform trend characterised by nearly equal dose rates contributions with slightly high contribution from ^{232}Th (28 to 48%). The dose rates contributions from ^{238}U and ^{40}K are between 22 to 42% and 20 to 40% respectively. In K-L, the dose rates contribution from ^{232}Th, ^{238}U and ^{40}K are between 34 to 44%, 24 to 36% and 28 to 38% respectively. In L-K, the dose rates contribution from ^{232}Th, ^{238}U and ^{40}K are between 34 to 46%, 24 to 32% and 26 to 40% respectively. In D-K, the dose rates contribution from ^{232}Th, ^{238}U and ^{40}K are between 30 to 48%, 24 to 40% and 24 to 40% respectively. In K-B, the dose rates contribution from ^{232}Th, ^{238}U and ^{40}K are between 30 to 48%, 26 to 42% and 22 to 40% respectively. In B-H, the dose rates contribution from ^{232}Th, ^{238}U and ^{40}K are between 32 to 44%, 28 to 38% and 24 to 38% respectively. In K-B, near Indra Sarovar lake the dose rate contribution from ^{238}U is between 82 to 88% while from ^{40}K and ^{232}Th are between 8 to 12% and 2 to 6% respectively. This anomaly can be due to the rocks brought from outside to built the artificial lake (dam). The ternary diagrams of relative proportions of dose rates contributions from primordial radionuclides in K-L, L-K, D-K, K-B and B-H is shown separately in appendix (Figure A.10).

The relative proportions of activity concentrations of primordial radionuclides between Kathmandu and Makawanpur is shown in Figure 65. The studied sites show a relatively uniform trend characterised by high ^{40}K (78 to 90%) and low ^{238}U and ^{232}Th contribution (4 to 14%). In K-L, ^{40}K contribution is between 80 to 90%, ^{238}U and ^{232}Th contribution are $< 10\%$. In L-K, ^{40}K contribution is between 82 to 90%, ^{238}U and ^{232}Th contribution are $< 10\%$. In D-K, ^{40}K contribution is between 80 to 90%, ^{238}U and ^{232}Th contribution are $< 10\%$. In K-B, ^{40}K contribution is between 78 to 90%, ^{238}U and ^{232}Th contribution are $< 14\%$. In B-H, ^{40}K contribution is between 80 to 90%, ^{238}U is $< 12\%$ and ^{232}Th contribution is $< 10\%$. The ternary diagrams of relative proportions of activity concentrations of primordial radionuclides in K-L, L-K, D-K, K-B and B-H is shown separately in appendix (Figure A.11).

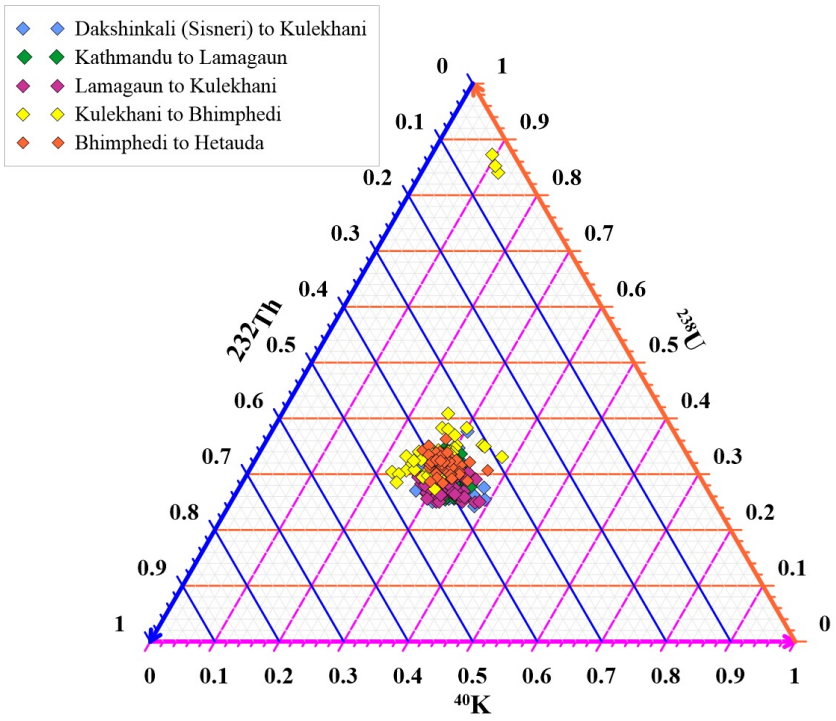

Figure 64: Dose rates from ^{40}K, ^{238}U and ^{232}Th

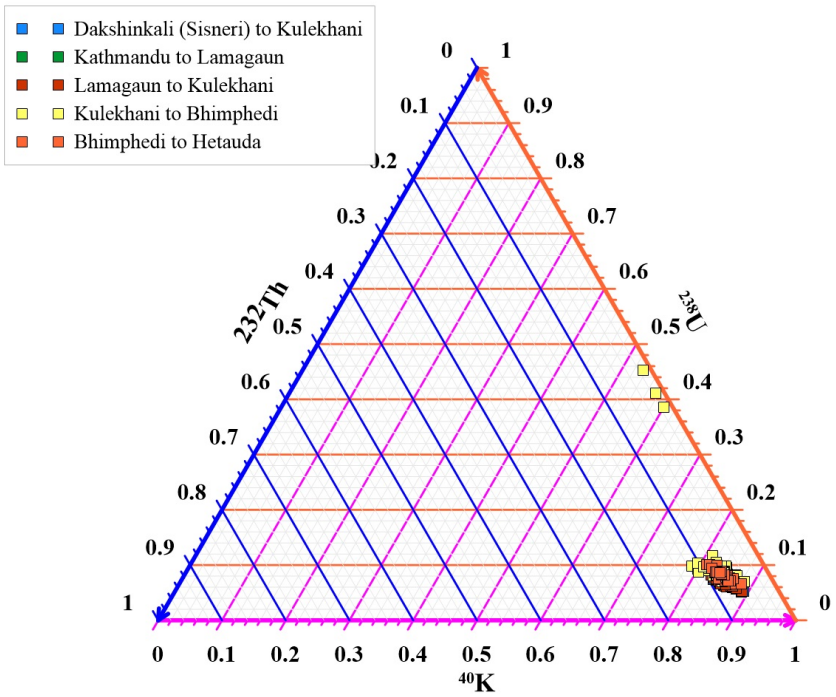

Figure 65: Activity Concentration of ^{40}K, ^{238}U and ^{232}Th

4.8 Comparison of Measured Results with Other Country Worldwide

The outdoor AED of the study area was found 2.14 times higher than the world average. The terrestrial radiation dose rates were found higher in many states of India which touches the boundary of Nepal like (885-900) μGy/y for Bihar, 800 μGy/y for Uttar Pradesh and 877 μGy/y for West Bengal (Sankaran et al., 1986). The results obtained is compared with published values of neighbouring country and worldwide (Table 25). The concentration of ^{40}K, ^{238}U and ^{232}Th is found comparable with Bangladesh, Malaysia and Islamabad of Pakistan and China respectively. It is noticed that the outdoor AED is found higher than world average but comparable with the neighbouring country India, China and Bangladesh (touching the boundary of Nepal). The AED is also found comparable with Pakistan, Malaysia and Turkey.

Table 25: Comparative study of activity concentration and AED

S.N.	Sites	Activity concentration (Bq/kg)			Outdoor AED (mSv)	References
		^{40}K	^{238}U(^{226}Ra)	^{232}Th		
1	Hetauda, Nepal	318	51	94	0.12	(Wallova et al., 2010)
2	Northern Rajasthan, India	1627	52	19	0.13	(Duggal et al., 2014)
3	Una, India	1535	46	17	0.10	(Bala et al., 2014)
4	Kirklarele, Turkey	667 ± 282	28 ± 13	40 ± 18	0.14	(Taskin et al., 2009)
5	Kohistan, Pakistan	418 ± 16	42 ± 1	43 ± 2	0.12	(Khan et al., 2011)
6	Islamabad, Pakistan	325	74	153	0.16	(Rahman et al., 2009)
7	Terengganu, Malaysia	545 ± 55	79 ± 3	84 ± 3	0.18	(Garba et al., 2016)
8	Xiazhuang, China	672	112	71	0.15	(Yang et al., 2005)
9	Southern district, Bangladesh	833 ± 358	42 ± 7	81 ± 14	0.13 ± 0.03	(Chowdhury et al., 2006)
10	Haryana, India	592	48	66	0.10	(Kansal & Mehra, 2015)
11	Present Study	850 ± 307	75 ± 37	73 ± 28	0.15 ± 0.03	
12	World average	420	33	45	0.07	(UNSCEAR, 2000)

4.9 Depth Profile of Gamma Radionuclides

4.9.1 Vertical Distribution of Primordial Radionuclides in Soil

The distribution of natural gamma radionuclides in the 10 cm depth intervals of soil profiles up to 50 cm at eight selected location within the study area were studied (Table 26). The distribution of primordial radionuclides ^{40}K, ^{238}U and ^{232}Th showed usual constant depth distribution trend with depth (Figure 66). For depth profile map, equal interval method is used for colour coding. The obtained values of dose rates and activity concentrations are found higher than the recommended values for background gamma radiation reported for soils worldwide (UNSCEAR, 2000).

The average dose rates and average concentrations of ^{40}K, ^{238}U and ^{232}Th in the soil profiles ranges from 84.4 to 246.0 nGy/h, 1.4 to 9.2 %, 4.7 to 10.6 ppm and 12.6 to 43.3 ppm respectively. The lowest average dose rate, ^{238}U and ^{232}Th concentrations

were measured in Hetauda whereas lowest average ^{40}K concentration was measured in Hetauda and Chisapani Gadhi. The highest dose rate, ^{40}K and ^{232}Th concentration were measured in Salle whereas highest ^{238}U concentration was measured in Rakash Khola. The average dose rates were measured within the range 119.2 to 125.0 nGy/h, 112.6 to 147.3 nGy/h, 114.8 to 157.4 nGy/h, 186.3 to 246.0 nGy/h, 108.3 to 164.2 nGy/h, 103.1 to 130.1 nGy/h, 117.6 to 132.8 nGy/h and 84.4 to 101.6 nGy/h in soil profile of Chobhar, Pharping, Rakash Khola, Salle, Chisapani Gadhi, Dhorsingh, Baghjhora and Hetauda respectively. The concentrations of ^{40}K were measured within the range 2.9 to 3.9%, 2.6 to 3.6%, 2.1 to 3.4%, 6.7 to 9.2%, 1.4 to 2.4%, 2.7 to 3.5%, 2.6 to 3.4%, 1.4 to 1.8% in soil profile of Chobhar, Pharping, Rakash Khola, Salle, Chisapani Gadhi, Dhorsingh, Baghjhora and Hetauda respectively. The concentrations of ^{238}U were measured within the range 6.0 to 6.5 ppm, 6.4 to 7.1 ppm, 6.2 to 9.1 ppm, 6.1 to 9.0 ppm, 6.3 to 10.6 ppm, 5.2 to 7.8 ppm, 5.4 to 7.2 ppm and 4.7 to 5.8 ppm in soil profile of Chobhar, Pharping, Rakash Khola, Salle, Chisapani Gadhi, Dhorsingh, Baghjhora and Hetauda respectively. The concentration of ^{232}Th were measured within the range 16.7 to 19.5 ppm, 20.3 to 27.0 ppm, 20.1 to 29.9 ppm, 33.3 to 43.3 ppm, 19.2 to 33.3 ppm, 13.5 to 20.9 ppm, 16.7 to 20.1 ppm and 12.6 to 18.0 ppm in soil profile of Chobhar, Pharping, Rakash Khola, Salle, Chisapani Gadhi, Dhorsingh, Baghjhora and Hetauda respectively.

The dose rates and the concentrations of ^{232}Th were noticed slightly increasing with depth while ^{40}K and ^{238}U concentrations showed a slight non- uniformity in some and all profiles respectively. This can be due to mobility (leaching and accumulation) of those radionuclides. The significant variation of radionuclide levels with depth as radionuclide content in soil is affected by the number of factors and processes. Variation in concentration with depth in the same profile can be due to the different physical, chemical and geochemical properties of the sediments. The soil texture is expected for variability of the distribution of natural radionuclides.

The distribution of natural radionuclides in the depth profiles of the studied sites showed slight variations. In the soil depth profiles, the concentrations of natural radionuclides were noticed slightly enriched in depth. These variation can be related to the movement of radionuclides through the soil column. The radionuclides are connected with the soil particles and are moving along with them through the soil column (Vukasinovic et al., 2010). The variability of gamma radionuclides in depth profile of soil can be due to sand fraction in soil as vertical mobility of radionuclides is enhanced by soil fraction (Golmakani et al., 2008). Humus fraction in soil have also significant effect on the variability of the radionuclides. The distribution of radionuclides also depends on particle size distribution, which is correlated to water infiltration in the layer from 20 to 60 cm (Vukasinovic et al., 2010).

Table 26: Dose rates, mass concentrations and activity concentrations of primordial radionuclides and activity ratios with depth

Depth	Dose rate (nGy/h)			^{40}K (%)			^{238}U (ppm)			^{232}Th (ppm)			^{40}K (Bq/kg)			^{238}U (Bq/kg)			^{232}Th(Bq/kg)			Th/K	Th/U	U/K
(cm)	min	max	mean	min	max	mean	min	max	mean	min	max	mean	min	max	mean	min	max	mean	min	max	mean			
Chobhar, Latitude: 27.6487°, Longitude: 85.27858°, Altitude:1234 m																								
0-10	109.9	127.4	119.2 ± 3.0	1.5	4.7	2.9 ± 0.6	1.1	16.6	6.0 ± 2.8	4.0	30.8	16.7 ± 5.3	474.5	1459.8	923.6 ± 185.5	13.9	205.5	74.1 ± 34.2	16.1	124.8	67.9 ± 21.5	0.07	0.92	0.08
10-20	113.6	127.5	120.6 ± 3.4	1.5	5.1	3.0 ± 0.6	0.7	17.7	6.2 ± 3.3	7.4	32.8	17.2 ± 5.4	463.2	1595.7	957.0 ± 195.0	8.1	218.3	77.3 ± 40.4	30.2	133.2	69.9 ± 22.0	0.07	0.90	0.08
20-30	108.7	131.9	121.9 ± 3.9	1.8	4.6	3.0 ± 0.6	1.7	13.9	6.5 ± 2.7	6.7	32.3	18.4 ± 5.4	572.2	1427.6	949.9 ± 190.6	20.8	172.2	80.7 ± 33.6	27.3	130.9	74.7 ± 22.2	0.08	0.93	0.09
30-40	114.2	134.1	124.6 ± 3.3	1.9	4.5	3.9 ± 0.5	0.7	12.8	5.4 ± 2.5	7.9	36.4	18.6 ± 4.8	579.1	1400.4	966.7 ± 153.3	8.4	157.6	66.8 ± 31.2	32.2	147.7	75.7 ± 19.5	0.08	1.13	0.07
40-50	115.6	130.8	125.0 ± 3.2	1.6	4.3	3.0 ± 0.6	1.5	16.9	6.4 ± 2.9	9.0	35.3	19.5 ± 5.5	509.6	1330.9	936.5 ± 192.0	18.0	208.6	79.7 ± 35.9	36.4	143.4	79.1 ± 22.2	0.08	0.99	0.09
Pharping, Latitude: 27.62014° , Longitude: 85.25592° , Altitude: 1617 m																								
0-10	115.2	129.4	122.6 ± 2.6	1.4	3.8	2.6 ± 0.5	1.3	15.5	6.4 ± 2.9	7.3	33.7	20.5 ± 5.1	431.9	1182.8	805.0 ± 164.8	16.0	191.3	79.1 ± 36.3	29.7	136.8	83.2 ± 20.9	0.10	1.05	0.10
10-20	119.3	130.4	125.2 ± 2.3	1.4	4.0	2.7 ± 0.5	0.9	15.2	6.5 ± 3.0	8.9	38.9	22.1 ± 5.5	424.4	1252.3	835.7 ± 169.2	10.9	187.3	80.2 ± 36.7	36.1	157.8	89.7 ± 22.4	0.11	1.12	0.10
20-30	120.3	131.2	125.4 ± 2.3	1.5	4.1	2.7 ± 0.5	2.1	13.3	6.9 ± 2.8	10.1	33.3	20.3 ± 4.9	481.1	1274.5	852.0 ± 150.1	25.7	164.2	84.9 ± 34.8	41.2	135.3	82.6 ± 19.9	0.10	0.97	0.10
30-40	118.3	153.8	134.6 ± 9.2	1.7	4.8	3.0 ± 0.6	1.3	15.7	6.1 ± 3.1	7.3	43.9	22.2 ± 7.8	545.9	1487.1	947.0 ± 194.7	15.8	193.4	75.1 ± 39.0	29.7	178.3	90.2 ± 29.1	0.10	1.20	0.08
40-50	127.6	159.6	147.3 ± 5.1	2.2	5.0	3.6 ± 0.5	1.9	15.6	7.1 ± 2.5	13.0	52.5	27.0 ± 6.0	686.4	1556.2	1124.3 ± 175.3	23.3	192.3	88.0 ± 31.4	53.0	213.0	109.5 ± 24.5	0.10	1.24	0.08
Rakash Khola, Latitude: 27.60482°, Longitude: 85.23236°, Altitude: 1743 m																								
0-10	94.7	123.5	114.8 ± 4.6	0.5	3.7	2.1 ± 0.5	0.8	20.6	6.2 ± 3.3	9.1	33.5	20.1 ± 5.3	156.8	1150.0	671.7 ± 174.4	9.8	254.0	76.5 ± 40.4	36.8	135.8	81.5 ± 21.3	0.12	1.07	0.11
10-20	107.6	139.1	122.3 ± 5.8	0.9	3.6	2.2 ± 0.5	0.9	16.0	6.6 ± 3.2	8.0	51.0	22.5 ± 6.2	294.5	1123.7	695.2 ± 145.7	10.5	197.5	82.2 ± 39.1	32.6	207.1	91.4 ± 25.3	0.13	1.11	0.12
20-30	110.9	142.1	130.6 ± 5.2	1.3	3.9	2.6 ± 0.5	2.1	15.4	6.7 ± 2.7	12.3	46.8	23.2 ± 6.2	418.2	1227.3	810.2 ± 159.0	16.5	48.4	32.0 ± 6.3	49.9	190.0	94.3 ± 25.3	0.12	1.14	0.10
30-40	123.5	155.7	144.9 ± 4.6	1.4	4.4	3.0 ± 0.6	1.1	14.3	6.6 ± 3.0	9.1	49.2	28.1 ± 7.8	437.6	1379.4	955.5 ± 187.9	13.0	176.9	81.8 ± 37.5	36.9	199.8	114.3 ± 31.5	0.12	1.40	0.09
40-50	127.7	167.8	157.4 ± 4.2	1.6	5.2	3.4 ± 0.6	1.9	28.9	9.1 ± 3.9	12.4	49.4	29.9 ± 6.7	504.9	1627.6	1054.8 ± 187.0	23.3	356.6	113.1 ± 48.4	50.5	200.6	121.5 ± 27.1	0.12	1.07	0.11
Salle, Latitude: 27.5932°, Longitude: 85.16837°, Altitude: 1579 m																								
0-10	154.0	199.1	186.3 ± 9.3	5.2	8.7	6.7 ± 0.8	1.2	13.6	6.1 ± 3.0	16.4	54.2	33.3 ± 9.1	1629.8	2738.1	2097.7 ± 258.0	14.7	167.6	75.5 ± 36.8	66.8	220.1	135.3 ± 36.8	0.06	1.79	0.04
10-20	152.1	228.0	207.4 ± 12.5	4.9	9.6	7.6 ± 0.9	1.5	14.7	6.0 ± 2.9	19.6	60.9	37.5 ± 9.4	1537.5	3010.7	2367.8 ± 279.9	18.2	181.9	74.8 ± 35.9	79.6	247.2	152.2 ± 38.4	0.06	2.04	0.03
20-30	181.0	245.8	228.7 ± 11.3	6.3	10.6	8.6 ± 0.9	1.9	19.5	9.1 ± 3.7	20.8	65.9	38.0 ± 7.6	1987.2	3305.3	2699.7 ± 282.5	23.4	240.5	112.0 ± 46.4	84.5	267.7	154.5 ± 30.8	0.06	1.38	0.04
30-40	179.0	250.2	237.6 ± 11.8	6.6	11.2	8.9 ± 0.8	0.9	18.9	8.9 ± 3.9	25.7	69.1	42.0 ± 8.1	2068.9	3503.1	2789.9 ± 265.2	11.0	233.2	109.7 ± 48.3	104.4	280.7	170.4 ± 32.9	0.06	1.55	0.04
40-50	203.9	255.0	246.0 ± 6.2	6.0	11.2	9.2 ± 1.0	0.7	24.0	9.0 ± 4.0	27.5	63.9	43.3 ± 7.5	1886.5	3495.6	2868.4 ± 318.1	9.2	296.7	111.6 ± 49.2	111.6	259.5	175.9 ± 30.3	0.06	1.58	0.04

Table 26: Dose rates, mass concentrations and activity concentrations of primordial radionuclides and activity ratios with depth

Depth	Dose rate (nGy/h)			^{40}K (%)			^{238}U (ppm)			^{232}Th (ppm)			^{40}K (Bq/kg)			^{238}U (Bq/kg)			^{232}Th(Bq/kg)			Th/K	Th/U	U/K
(cm)	min	max	mean	min	max	mean	min	max	mean	min	max	mean	min	max	mean	min	max	mean	min	max	mean			
Chishapani Gadhi, Latitude:27.55965° , Longitude: 85.13616°, Altitude: 1656 m																								
0-10	94.9	125.1	108.3 ± 7.6	0.7	2.6	1.4 ± 0.4	1.6	16.9	6.3 ± 2.7	7.6	36.2	19.2 ± 5.8	232.2	826.0	445.0 ± 114.0	19.9	208.9	78.1 ± 33.9	31.0	146.8	77.9 ± 23.6	0.18	1.00	0.18
10-20	116.6	149.2	138.1 ± 6.4	1.2	3.5	2.0 ± 0.4	3.1	16.1	8.0 ± 3.0	16.5	46.2	28.8 ± 6.4	386.9	1083.6	624.9 ± 120.2	38.3	199.0	98.3 ± 37.4	67.1	187.7	116.8 ± 25.9	0.19	1.19	0.16
20-30	135.2	172.4	164.2 ± 4.6	1.1	4.7	2.4 ± 0.7	1.9	24.7	10.6 ± 5.0	16.2	51.2	33.3 ± 6.7	352.4	1470.2	768.4 ± 211.6	22.9	305.1	131.6 ± 61.7	65.8	207.9	135.1 ± 27.1	0.18	1.03	0.17
30-40	146.2	163.2	154.9 ± 3.0	0.9	4.4	2.4 ± 0.6	2.1	24.7	9.0 ± 3.5	14.1	52.7	31.0 ± 7.1	274.8	1364.4	740.7 ± 181.6	26.3	305.2	111.4 ± 43.7	57.4	213.9	125.8 ± 28.8	0.17	1.13	0.15
40-50	142.5	167.1	157.5 ± 3.5	0.8	3.8	2.2 ± 0.6	2.7	21.4	10.6 ± 3.9	15.1	54.0	31.4 ± 7.2	255.7	1179.1	683.3 ± 192.3	33.9	264.6	130.5 ± 48.1	61.2	219.3	127.7 ± 29.4	0.19	0.98	0.19
Dhorsing, Latitude: 27.53241° , Longitude: 85.10242° , Altitude: 862 m																								
0-10	98.6	109.5	103.1 ± 2.1	1.3	4.1	2.7 ± 0.5	0.3	12.8	5.2 ± 2.7	5.6	27.9	13.5 ± 4.4	395.0	1289.9	841.4 ± 177.1	4.1	158.2	64.6 ± 33.9	22.8	113.2	54.7 ± 17.8	0.07	0.85	0.08
10-20	105.2	118.6	114.0 ± 2.5	1.7	4.6	3.1 ± 0.5	1.2	14.4	6.0 ± 2.6	4.0	32.5	16.2 ± 5.0	526.8	1429.2	961.8 ± 170.2	15.1	177.8	74.3 ± 31.7	16.1	132.0	66.0 ± 20.2	0.07	0.89	0.08
20-30	111.8	127.2	119.6 ± 3.0	1.6	4.9	3.0 ± 0.5	1.1	15.8	6.5 ± 3.0	4.8	33.1	19.2 ± 5.7	515.5	1533.7	935.9 ± 172.1	14.2	194.8	80.3 ± 37.0	19.6	134.4	77.9 ± 23.0	0.08	0.97	0.09
30-40	123.1	137.5	129.6 ± 3.1	2.2	5.2	3.5 ± 0.7	1.6	16.7	7.2 ± 3.3	6.3	40.5	20.7 ± 6.3	673.0	1627.0	1088.5 ± 208.0	20.2	206.1	88.5 ± 40.3	25.6	164.3	83.9 ± 25.5	0.08	0.95	0.08
40-50	124.0	135.5	130.1 ± 2.5	1.4	4.8	3.3 ± 0.7	0.8	16.7	7.8 ± 3.1	7.8	35.6	20.9 ± 6.0	439.1	1514.3	1038.0 ± 224.4	10.2	206.9	96.2 ± 38.7	31.7	144.6	84.7 ± 24.2	0.08	0.88	0.09
Baghjhora, Latitude: 27.48216° , Longitude: 85.04504° , Altitude: 483 m																								
0-10	112.9	125.5	119.5 ± 2.5	1.3	4.5	2.9 ± 0.6	2.1	18.0	7.2 ± 3.1	8.1	29.0	16.7 ± 4.8	415.0	1396.6	900.3Âś ± 191.4	26.4	221.9	89.3 ± 37.8	32.8	117.8	67.7 ± 19.4	0.08	0.76	0.10
10-20	109.7	123.9	117.6 ± 2.6	1.2	3.9	2.6 ± 0.4	1.6	17.3	6.4 ± 2.6	7.6	36.0	16.9 ± 5.4	388.7	1228.5	821.4 ± 140.3	19.5	213.2	78.5 ± 32.0	30.9	146.3	68.7 ± 21.8	0.08	0.87	0.10
20-30	118.3	130.7	123.8 ± 2.8	1.8	4.6	3.0 ± 0.5	1.0	13.9	5.4 ± 2.8	6.2	34.0	19.2 ± 5.2	560.6	1425.4	947.3 ± 169.0	12.7	171.9	66.3 ± 34.1	25.2	138.0	77.9 ± 21.2	0.08	1.17	0.07
30-40	124.7	136.2	130.3 ± 2.6	1.6	4.7	3.3 ± 0.6	0.9	15.7	7.0 ± 3.2	9.9	39.5	21.3 ± 6.1	498.3	1483.0	1027.9 ± 199.8	10.6	193.3	87.0 ± 39.8	40.4	160.4	86.4 ± 24.9	0.08	0.99	0.08
40-50	127.3	140.2	132.8 ± 2.6	1.9	4.8	3.4 ± 0.5	1.1	16.1	7.1 ± 3.1	7.1	37.2	20.1 ± 6.1	606.3	1517.4	1060.6 ± 170.1	14.0	198.6	87.8 ± 38.2	29.0	151.1	81.6 ± 24.7	0.08	0.93	0.08
Hetauda, Latitude: 27.4276° , Longitude: 85.04584° , Altitude: 388 m																								
0-10	79.5	89.1	84.4 ± 2.0	0.8	2.5	1.5 ± 0.3	0.9	10.6	4.7 ± 2.2	3.4	25.8	12.6 ± 4.6	255.1	789.1	461.1 ± 107.3	10.8	130.9	58.1 ± 27.8	14.0	104.8	51.3 ± 18.7	0.11	0.88	0.13
10-20	82.8	95.2	89.3 ± 2.4	0.5	2.5	1.4 ± 0.4	1.0	12.7	4.8 ± 2.2	5.1	30.0	15.3 ± 4.3	149.6	786.9	456.6 ± 131.2	12.7	157.0	59.3 ± 27.8	20.6	121.9	62.0 ± 17.4	0.14	1.04	0.13
20-30	91.6	102.6	96.2 ± 2.2	0.7	2.6	1.5 ± 0.4	0.7	15.2	5.6 ± 3.1	6.1	32.5	17.8 ± 5.2	223.5	813.5	477.6 ± 120.7	8.2	188.1	69.6 ± 38.4	24.9	131.8	72.4 ± 21.2	0.15	1.04	0.15
30-40	93.0	105.2	99.0 ± 2.4	0.8	2.6	1.6 ± 0.4	0.8	15.9	5.0 ± 2.4	6.3	38.1	18.0 ± 5.8	252.6	823.5	491.9 ± 121.2	10.3	196.1	61.7 ± 30.3	25.8	154.8	73.0 ± 23.7	0.15	1.18	0.13
40-50	96.2	107.5	101.6 ± 2.3	0.4	2.9	1.8 ± 0.5	1.1	12.6	5.8 ± 2.3	7.5	34.9	17.6 ± 5.3	140.5	910.5	552.2 ± 147.5	13.1	156.2	71.5 ± 28.1	30.6	141.6	71.7 ± 21.7	0.13	1.00	0.13

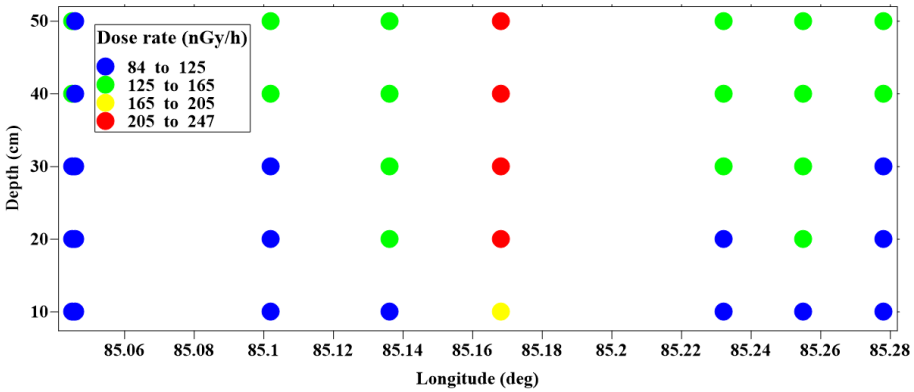

(a) Vertical distribution of dose rates

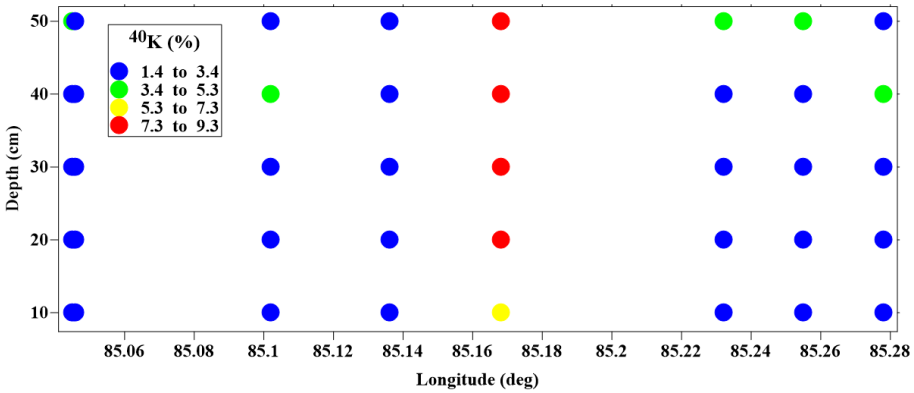

(b) Vertical distribution of ^{40}K

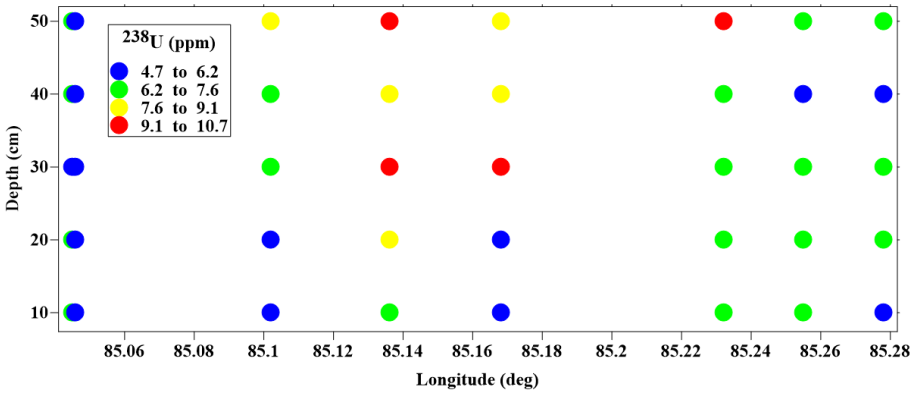

(c) Vertical distribution of ^{232}U

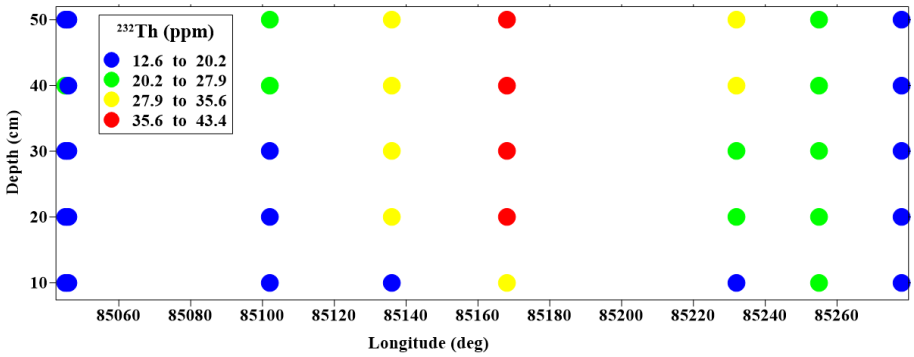

(d) Vertical distribution of ^{232}Th

Figure 66: Depth profiles of dose rates and primordial radionuclides in soil

No significant variation of radionuclides distribution was observed with depth. The homogeneous depth distribution of the natural radionuclides are related with the lower mobility of radionuclides which is associated with the small variations of mineral composition of the parent materials (Navas et al., 2002b).

The Th/U ratio in all soil profiles except Salle, were found approximately equal to 1.1 whereas the Th/K and U/K ratios were found approximately equal to 0.085. In Salle, slightly high Th/U ratios and slightly low Th/K and U/K ratios were found which can be due to leaching of ^{238}U and enriched ^{40}K respectively. The activity ratio in soils can be used as a reliable index for assessing the fertilizer's influence on radionuclides enrichment in soil (Takeda et al., 2004). In Chisapani Gadhi, Th/K and U/K ratios were found slightly high which can be due to less content of ^{40}K due to weathering (Chan et al., 2007).

In the studied depth profiles of soil, usual trend i.e. homogeneous depth distribution (no significant variation of dose rates and radionuclides concentrations) of natural radionuclides were observed with depth. The activity ratios Th/U (approximately equal to 1.1), Th/K and U/K ratios (approximately equal to 0.085) of soil depth profiles indicates the soil profiles as environmental profile (Evans et al., 1997). Also, the activity ratios in the soil profiles were found approximately constant which indicates that radionuclides have same geochemical origin (Navas et al., 2002b).

4.9.2 Vertical Distribution of Anthropogenic Radionuclides in Soil

The distribution of ^{137}Cs with soil depth up to 50 cm at every 10 cm is presented in Table 27 and Figure 67. Low surface activity of ^{137}Cs were measured which can be a global fallout from nuclear weapon testing and Chernobyl accident (UNSCEAR, 2000).

The average surface activity of ^{137}Cs ranges from 0.65 to 1.31 kBq/m^2. The lowest average value was measured in Baghjhora and highest in Salle. The average surface activity of ^{137}Cs were found within the range 0.77 to 0.96 kBq/m^2, 0.83 to 1.18 kBq/m^2, 0.76 to 1.01 kBq/m^2, 1.16 to 1.31 kBq/m^2, 0.80 to 1.19 kBq/m^2, 0.77 to 0.87 kBq/m^2, 0.65 to 1.16 kBq/m^2 and 0.73 to 0.79 kBq/m^2 in soil profile of Chobhar, Pharping, Rakash Khola, Salle, Chisapani Gadhi, Dhorsingh, Baghjhora and Hetauda respectively. The vertical depth distributions of ^{137}Cs for all soil profile were found unnatural (does not decreases exponentially) and homogeneous. Vertical movement of radionuclides is affected by physical and chemical properties of soil and biological processes operating in the soil system itself. Homogeneous and unnatural vertical depth distribution can be due to disturbed soil due to cultivation (tilled soil), road construction, erosion, small animals like earthworms and rodents (He & Walling, 1997; Matsuda et al., 2015).

Table 27: Depth profile of ^{137}Cs

Depth	^{137}Cs (kBq/m^2)		
(cm)	min	max	mean
Chobhar, Latitude: 27.6487°, Longitude: 85.27858°, Altitude:1234 m			
0-10	0.19	2.51	0.96 ± 0.45
10-20	0.05	1.98	0.85 ± 0.44
20-30	0.09	2.27	0.77 ± 0.48
30-40	0.07	2.31	0.92 ± 0.49
40-50	0.14	2.20	0.86 ± 0.43
Pharping, Latitude: 27.62014° , Longitude: 85.25592° , Altitude: 1617 m			
0-10	0.12	2.40	0.97 ± 0.51
10-20	0.09	2.30	0.83 ± 0.51
20-30	0.12	2.28	0.87 ± 0.44
30-40	0.19	2.77	1.18 ± 0.55
40-50	0.12	2.72	0.98 ± 0.53
Rakash Khola, Latitude: 27.60482°, Longitude: 85.23236°, Altitude: 1743 m			
0-10	0.05	1.88	0.82 ± 0.38
10-20	0.04	2.30	0.76 ± 0.46
20-30	0.05	2.67	1.01 ± 0.52
30-40	0.12	2.81	1.08 ± 0.52
40-50	0.04	3.25	0.99 ± 0.52
Salle, Latitude: 27.5932°, Longitude: 85.16837°, Altitude: 1579 m			
0-10	0.21	3.40	1.16 ± 0.65
10-20	0.30	3.39	1.30 ± 0.63
20-30	0.14	2.89	1.31 ± 0.59
30-40	0.14	3.51	1.27 ± 0.60
40-50	0.15	2.92	1.30 ± 0.59
Chishapani Gadhi, Latitude:27.55965° , Longitude: 85.13616°, Altitude: 1656 m			
0-10	0.06	2.37	0.80 ± 0.49
10-20	0.10	2.42	1.01 ± 0.60
20-30	0.06	2.98	1.18 ± 0.63
30-40	0.13	2.87	1.19 ± 0.59
40-50	0.18	2.99	1.16 ± 0.57
Dhorsing, Latitude: 27.53241° , Longitude: 85.10242° , Altitude: 862 m			
0-10	0.16	1.91	0.78 ± 0.38
10-20	0.03	2.96	0.77 ± 0.45
20-30	0.17	2.15	0.80 ± 0.43
30-40	0.05	1.84	0.80 ± 0.39
40-50	0.08	2.20	0.87 ± 0.53
Baghjhora, Latitude: 27.48216° , Longitude: 85.04504° , Altitude: 483 m			
0-10	0.04	1.66	0.65 ± 0.39
10-20	0.04	2.10	0.89 ± 0.45
20-30	0.10	2.40	1.03 ± 0.51
30-40	0.08	2.41	0.82 ± 0.59
40-50	0.09	2.87	1.16 ± 0.56
Hetauda, Latitude: 27.4276° , Longitude: 85.04584° , Altitude: 388m			
0-10	0.12	1.87	0.77 ± 0.34
10-20	0.08	2.20	0.76 ± 0.43
20-30	0.10	1.83	0.73 ± 0.38
30-40	0.08	2.11	0.78 ± 0.42
40-50	0.03	2.14	0.79 ± 0.44

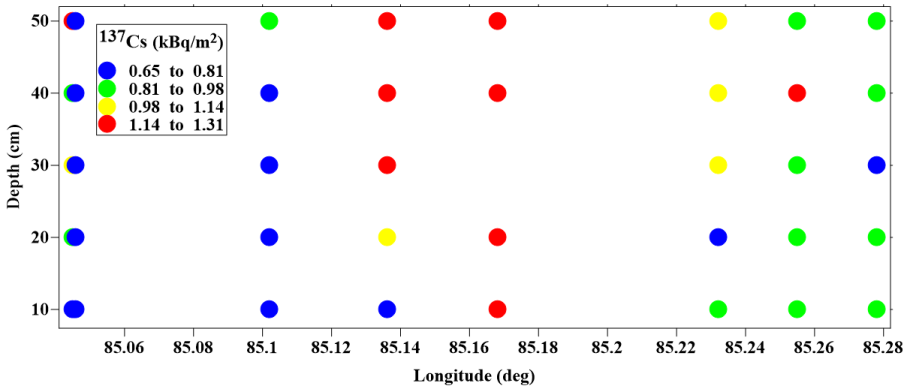

Figure 67: Depth profiles of ^{137}Cs

4.10 Scattering of Gamma Radiation in Air

The mass attenuation coefficient of air were calculated using the NIST XCOM computer program (Table 28). The corresponding linear attenuation coefficients and the attenuation lengths in air were calculated from it. The attenuation of gamma ray in air is mainly due to scattering as absorption is very less compared to scattering. Also, coherent scattering is not considerable for high energy. The attenuation length in air for 1.41 MeV (^{40}K), 1.76 MeV (^{238}U) and 2.61 MeV (^{232}Th) gamma rays were calculated to be 10775.9 cm, 12087.9 cm and 14934.6 cm respectively which justifies no significant attenuation was measured up to 300 cm in air for these energy range.

The intensity of gamma radiation in ambient environment was found decreasing with the air thickness as total count was decreasing with detector's height (Table 29). In ambient atmosphere, the attenuation nature of terrestrial gamma radiation in air is as shown in Figure 68. The nature of energy of terrestrial gamma radionuclides is found similar for high energy (Badawy & Abd El-Latif, 2017). The gamma rays attenuation changes with thickness and energy (Figure 69). The attenuation of ^{40}K is found higher than ^{238}U and ^{232}Th as ^{40}K has lower energy. Also, intensity decreases with the energy of gamma radionuclides and increasing thickness of air. As up to 100 cm height between detector and ground, no significant attenuation was noticed, the height of the detector from ground is always maintained below 1 m during in-situ survey (Mishra & Khanal, 2021).

Table 28: Attenuation coefficient calculated from NIST XCOM

Edge	Photon Energy	Scattering		Photoelectric absorption	Pair production		Total attenuation	
		Coherent	Incoherent		in Nuclear field	in Electron field	with Coherent scattering	without Coherent scattering
	MeV	cm^2/g	cm^2/g	cm^2/g	cm^2/g	cm^2/g	cm^2/g	cm^2/g
18 K	1.41E+00	2.73E-05	5.34E-02	1.84E-06	6.20E-05	0.00E+00	5.35E-02	5.35E-02
	1.76E+00	1.75E-05	4.74E-02	1.26E-06	2.34E-04	0.00E+00	4.77E-02	4.76E-02
	2.61E+00	7.96E-06	3.77E-02	6.98E-07	8.28E-04	3.60E-06	3.86E-02	3.86E-02

Table 29: Intensity of terrestrial gamma radiation with height of detector

Thickness of air (cm)	Total count rate (cps)		
	Range	Mean	S.E.
50	91 to 130	107	0.1
100	86 to 130	107.7	0.1
150	82 to 127	105.6	0.1
200	71 to 126	98.1	0.1
250	71 to 115	98.2	0.1
300	65 to 109	88.9	0.1

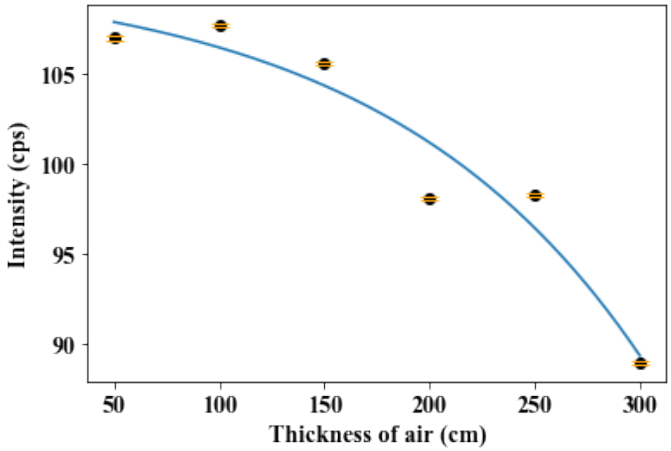

Figure 68: Scattering of gamma ray in air (Mishra & Khanal, 2021)

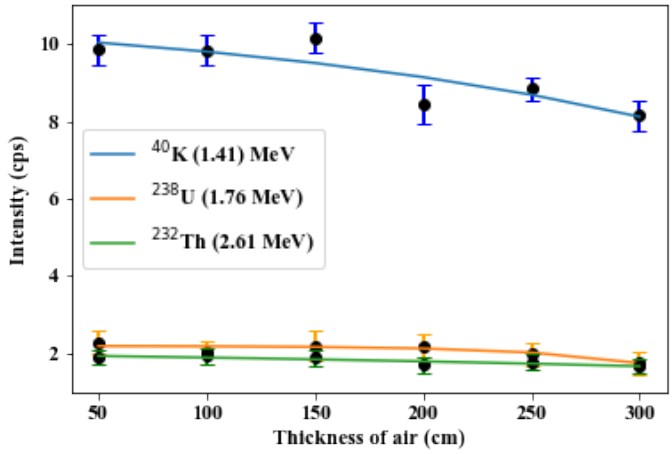

Figure 69: Scattering of gamma ray from particular terrestrial radionuclides in air (Mishra & Khanal, 2021)

CHAPTER 5

CONCLUSION AND RECOMMENDATIONS

5.1 Conclusion

A mobile in-situ radiometric study was conducted using GPS and GIS equipped portable gamma ray spectrometer. The survey conducted covers more than 120 km along the road between Balkhu and Hetauda via Kulekhani. For comprehensive study and analysis, the surveyed sites was divided in four sections (Kathmandu to Lamagaun (Pharping) (K-L), Lamagaun to Kulekhani (L-K), Kulekhani to Bhimphedi (K-B) and Bhimphedi to Hetauda (B-H) region for about approximately 20 km distance and the survey was also conducted along some selected adjoining environs and along the water resources. The survey was also conducted from Dakshinkali to Kulekhani via Sisneri (D-K). The depth profiles of radionuclides at eight selected location up to 50 cm were studied for understanding migration and distribution of radionuclides as they are important for environmental studies. In addition, the scattering of gamma radiations in air up to 300 cm were also studied.

The average dose rate in Kathmandu and Makawanpur area varies from 45 to 206 with an average of 119 $\pm$ 23 nGy/h. In K-L, dose rate varies from 74 to 154 with an average of 116 $\pm$ 11 nGy/h. In L-K, dose rate varies from 93 to 179 with an average of 130 $\pm$ 13 nGy/h. In D-K, dose rate varies from 92 to 206 with an average of 139 $\pm$ 17 nGy/h. In K-B, dose rate varies from 76 to 175 with an average of 119 $\pm$ 14 nGy/h. In B-H, dose rate varies from 45 to 149 with an average of 87 $\pm$ 19 nGy/h. The average mass concentrations of ^{40}K, ^{238}U and ^{232}Th in Kathmandu and Makawanpur area were found 3%, 28 ppm and 18 ppm respectively. The average mass concentrations of ^{40}K in K-L, L-K and D-K were found 3% and 2% in K-B and B-H. The average mass concentrations of ^{238}U were found 21, 20, 28, 22 and 21 ppm respectively in K-L, L-K, D-K, K-B and B-H. Similarly, the average mass concentrations of ^{232}Th were found 17, 21, 22, 18 and 13 ppm respectively in K-L, L-K, D-K, K-B and B-H. The activity ratios calculated for the studied sites were found in good agreement with environmental samples which indicates no relocation of rocks and soils. The dose rates inferred from the concentrations (calculated dose rates) were found nearly equal to the dose rates measured from direct measurement (measured dose rates) and the ratio of calculated dose rates

to measured dose rates were found nearly equal to one. The surface activity of ^{137}Cs ranges from 0.001 to 3.8 kBq/m^2 with average of 0.8 kBq/m^2. The dose rate calculated from surface activity of ^{137}Cs ranges from 0.001 to 2.0 nGy/h with an average of 0.4 nGy/h. The homogeneous distribution and low surface activity of ^{137}Cs in environment indicates that there is no contamination in the studied area and the trace of ^{137}Cs present was due to global fallout from weapon testing and nuclear accidents.

Along adjoining environs, the higher dose rates were measured at Golping Besi and lower at Hetauda. The higher dose rates were measured due to elevated radionuclides concentrations in Earth's crust. The ^{40}K, ^{238}U and ^{232}Th concentrations were measured higher at Golping Besi, Bhimphedi and Rakash Khola respectively. Similarly, the concentrations of ^{40}K, ^{238}U and ^{232}Th were measured lower at Hetauda. The activity ratio (Th/U) were found nearly equal to 1 and Th/K and U/K were found nearly 0.1 showing good agreement for environmental samples in adjoining area. The activity ratio (Th/U) were found nearly equal to 1 and Th/K and U/K were found nearly 0.1 showing good agreement for environmental samples along the banks of rivers and around the lakes also.

The outdoor AED in Kathmandu and Makawanpur district varies from 0.05 to 0.25 mSv with average of 0.15 mSv. The lowest and highest AED was estimated in B-H and D-K respectively whereas the average AED was calculated highest and lowest in D-K and B-H respectively. The average AED was found higher than twice of world average in all sites except B-H (higher than world average) but was lower than dose limit (1 mSv) recommended for public by ICRP. The ELCR varies from 0.2 $\times$ 10^{-3} to 0.9 2 $\times$ 10^{-3} with average of 0.53 $\times$ 10^{-3}. In most of the study, mortality and ELCR has not been linked with the population of that area. The external hazard index (H_{ex}) due to NORM were calculated < 1 which indicates no significant hazard in the area. The average AED from ^{40}K, ^{238}U and ^{232}Th were calculated 0.04 $\pm$ 0.01, 0.04 $\pm$ 0.02 and 0.05 $\pm$ 0.02 mSv respectively. The higher associated radiation risk factor was calculated due to high radioactivity concentration measured in the area due to geological and geographical factors. The exploratory analysis enabled the assessment of the variability of the measured data of study area in detail.

The activity ratios in the soil depth profiles for terrestrial radionuclides were found approximately constant which indicates that radionuclides have same geochemical origin. The vertical depth distribution of ^{137}Cs for all soil profile were found unnatural (does not decreases exponentially) and homogeneous which can be due to disturbed soil due to cultivation (tilled soil), road construction, erosion, small animals like earthworms and rodents. The scattering of gamma radiation in air was measured and also calculated using computer program NIST XCOM. The gamma ray intensity was found decreasing with the increase in thickness of air and energy of gamma radiation. No significant attenuation was noticed up to 100 cm.

The spatial variability of the data in the Kathmandu and Makawanpur district is mainly due to underlying geology and geochemical process in the terrestrial environment. The finding of the study are useful to establish baseline data for radioactivity levels and exposure.

5.2 Recommendations

The results obtained in this study can be used as a baseline data for gamma radionuclides concentrations and exposures in Kathmandu and Makawanpur district. The findings of the present work can be used as a base map to assess any changes in background radiation levels due to weathering, geological and anthropogenic activities. Due to time and technical limitations, the study was mainly conducted only along the road and in some selected adjoining area and water resources. More comprehensive survey is recommended for more information in the area. All villages between Kathmandu and Makawanpur district should be surveyed. Also, indoor gamma survey is also recommended to assess more information about exposure. Gamma ray spectrometric study for ground water is also recommended. Moreover, the study related to simulation and modelling of environmental gamma photon energy using Monte Carlo techniques or others are worthwhile.

Exposure to natural radiation sources are more significant for public than artificial sources. The database should be broaden to determine representative values as there is wide variation in natural exposure even for relatively small area. Therefore, more effort is required for detail information of representative data and dosimetric procedure improvement. The uncertainties in the natural dose assessment is due to limited number of measurement rather than dosimetric complication (UNSCEAR, 2000).

CHAPTER 6

SUMMARY

The mobile in-situ gamma ray measurement have been carried in the Kathmandu and Makawanpur district along the road via Kulekhani using portable gamma ray spectrometer equipped with GPS and GIS. The instrument used is auto calibrated and measures spectra every second. The spectrometer is carried in backpack pointing downward and walked at a maximum pace of 2 km/h along the study area for continuous measurement.

The radiological maps in the region between Kathmandu and Makawanpur along the road via Kulekhani are prepared. The radiological map showing dose rates are overlaid on geological and geographical map. For comprehensive study, the study area are divided into four sections and the radiological maps are prepared for all sections. The contour maps of dose rates in the study area shows smooth spatial distribution. The radiological map showing the concentration of ^{40}K, ^{238}U, ^{232}Th and ^{137}Cs are also overlaid on geological map for more information of radionuclide distributions. For better understanding of radiation in the study area, the radiological maps are prepared also in adjoining environs and along the water resources. The higher dose rates are seen over Sk (Sarung Khola formation), Mr (Markhu formation), Ti (Tistung formation) and Gr (Granites) rocks (Kulekhani area) which consists quartz, biotite, feldspar, marble, phyllites, sandstone, limestone and granites and the lower dose rates are noticed on Q (Quaternary) rocks (Hetauda) which contains alluvium, boulder, gravel, sand, silt and clay. The exploratory data analysis (descriptive statistics, regression, PCA, ternary diagram) are performed to find the pattern and anomalies.

The dose rates and concentrations of radionuclides (^{40}K, ^{238}U, ^{232}Th and ^{137}Cs) are measured and no associated radiological risk factors (AED, ELCR and H_{ex}) are assessed in the study area. The outdoor AED estimated is found higher than world average but is comparable with the neighbouring country India, China and Bangladesh (touching the boundary of Nepal).

No unusual high or low activity are detected in the study area. The lowest dose rate is measured in Hetauda and highest in Kulekhani. The higher (than world average as reported by UNSCEAR) radioactivity are measured in rocks, soils and waters and the cause of elevated activity is the underlying geology and geochemical factors. No possibility of radioactive deposit is noticed in the area.

For the understanding of distribution and migration of radionuclides in the soil, the depth profile of soils up to 50 cm at every 10 cm are studied at eight selected locations within the study area. The depth profile indicates usual homogeneous distribution of radionuclides in the soil for primordial radionuclides (^{238}U, ^{232}Th and ^{40}K) while the depth distribution of anthropogenic radionuclides (^{137}Cs) is found unnatural (not decreases exponentially). The approximately constant activity ratios in the soil depth profiles for terrestrial radionuclides indicates the same geochemical origin of radionuclides.

The relative intensity of gamma radiation in the ambient environment of study area are measured up to 300 cm and also calculated using computer program NIST XCOM. The gamma ray attenuation was found increasing with the increase in thickness of air with no significant attenuation up to 100 cm. Also, the gamma ray intensity is found decreasing with increase in energy of gamma radiation.

The activity ratios in the studied sites are found in good agreement with environmental samples and indicates no relocation of rocks and soils. The homogeneous distribution and low surface activity of ^{137}Cs in the environment of study area indicates no contamination in the area and the trace of ^{137}Cs present is due to global fallout from weapon testing and nuclear accidents. The spatial variability of the data noticed in Kathmandu and Makawanpur district is generally due to underlying geology and geochemical process in the terrestrial environment.

The results obtained in this study can be used as a baseline data for gamma radionuclides concentrations and exposures in Kathmandu and Makawanpur district. The findings can be used as a base map to assess any changes in background radiation levels due to weathering, geological and anthropogenic activities. Due to time constraint and technical limitations, the study was mainly conducted only along the road and in some selected adjoining area and water resources. For, more comprehensive study and broad information in the area, all villages between Kathmandu and Makawanpur district should be surveyed. Also, indoor gamma survey and gamma ray spectrometric study for ground water are also suggested to assess more information about exposure. Moreover, the study related to simulation and modelling of environmental gamma photon energy using Monte Carlo techniques or others are desirable.

REFERENCES

Aage, H. K., & Korsbech, U. (2003). Search for lost or orphan radioactive sources based on NaI gamma spectrometry. *Applied Radiation and Isotopes*, *58*(1), 103–113.

Adam, A. M. A., & Eltayeb, M. A. H. (2012). Multivariate statistical analysis of radioactive variables in two phosphate ores from Sudan. *Journal of Environmental Radioactivity*, *107*, 23–43.

Adhikari, K. P. (2012). *Current status of radiation protection in different hospitals in Nepal* (Doctoral dissertation). Tribhuvan University, Nepal.

Adhikari, K. P., Benini, A., Malla, R., & Chaurasia, P. (2013). First data about radiation level & evaluation of doses to medical staff working at the catheterization laboratory at Katmandu, Nepal. In *World Congress on Medical Physics and Biomedical Engineering May 26-31, 2012,Beijing, China* (pp. 1191–1194).

Adhikari, K. P., Jha, L., & Montenegro, P. G. (2009). Study and analysis of radiation level at different hospitals in Nepal. In *World Congress on Medical Physics and Biomedical Engineering, September 7-12, 2009, Munich, Germany* (pp. 110–113).

Aitchison, J. (1982). The statistical analysis of compositional data. *Journal of the Royal Statistical Society: Series B (Methodological)*, *44*(2), 139–160.

Akingboye, A. S., Ogunyele, A. C., Jimoh, A. T., Adaramoye, O. B., Adeola, A. O., & Ajayi, T. (2021). Radioactivity, radiogenic heat production and environmental radiation risk of the basement complex rocks of Akungba-Akoko, Southwestern Nigeria: insights from in situ gamma-ray spectrometry. *Environmental Earth Sciences*, *80*(6), 1–24.

Alfaro, M., Jarvis, S., & Gregory, P. (2004). Factors affecting potassium leaching in different soils. *Soil Use and Management*, *20*(2), 182–189.

Allen, C. W., & Cox, A. N. (2000). *Allen's astrophysical quantities*. United States: Springer Science & Business Media.

Anspaugh, L. R. (1976). In situ methods for quantifying specific radionuclides. *IEEE Transactions on Nuclear Science*, *23*(3), 1190–1196.

Aryal, B. (1994). *Estimation of uranium in rocks collected from central Siwalik of Nepal* (Unpublished master's thesis). Tribhuvan University, Nepal.

Asfahani, J., Aissa, M., & Al-Hent, R. (2005). Statistical factor analysis of aerial spectrometric data, Al-Awabed area, Syria: a useful guide for phosphate and uranium exploration. *Applied Radiation and Isotopes*, *62*(4), 649–661.

Asfahani, J., Aissa, M., & Al-Hent, R. (2007). Uranium migration in a sedimentological phosphatic environment in Northern Palmyrides, Al-awabed area, Syria. *Applied Radiation and Isotopes*, *65*(9), 1078–1086.

Ashley, R., & Lloyd, J. (1978). An example of the use of factor analysis and cluster analysis in groundwater chemistry interpretation. *Journal of Hydrology*, *39*(3-4), 355–364.

Astel, A. (2007). Chemometrics based on fuzzy logic principles in environmental studies. *Talanta*, *72*(1), 1–12.

Badawy, S. M., & Abd El-Latif, A. (2017). Synthesis and characterizations of magnetite nanocomposite films for radiation shielding. *Polymer Composites*, *38*(5), 974–980.

Bala, P., Mehra, R., & Ramola, R. (2014). Distribution of natural radioactivity in soil samples and radiological hazards in building material of Una, Himachal Pradesh. *Journal of Geochemical Exploration*, *142*, 11–15.

Bavarnegin, E., Moghaddam, M. V., & Fathabadi, N. (2013). Natural radionuclide and radiological assessment of building materials in high background radiation areas of Ramsar, Iran. *Journal of Medical Physics/Association of Medical Physicists of India*, *38*(2), 93.

Beamish, D. (2016). *Mapping the terrestrial gamma radiation dose*. Dublin: Royal Irish Academy.

Beck, H. L., Gogolak, C., & DeCampo, J. (1972). *In situ Ge (Li) and NaI (T1) gamma-ray spectrometry* (Report no. HASL-258). New York, United Nations: United States Atomic Energy Commission, Health and Safety Lab.

Belivermis, M., Kılıç, Ó., Çotuk, Y., & Topcuoğlu, S. (2010). The effects of physic-ochemical properties on gamma emitting natural radionuclide levels in the soil profile of Istanbul. *Environmental Monitoring and Assessment*, *163*(1), 15–26.

Beretka, J., & Matthew, P. (1985). Natural radioactivity of Australian building materials, industrial wastes and by-products. *Health Physics*, *48*(1), 87–95.

Bezuidenhout, J. (2015). In situ gamma ray measurements of radionuclides at a disused phosphate mine on the West Coast of South Africa. *Journal of Environmental Radioactivity*, *150*, 1–8.

Bhatt, C. R., Koirala, B., Gupta, D. K., & Vives i Batlle, J. (2012). Environmental radiation–an important concern in the Himalayas (Nepal). *Journal of Environmental Radioactivity*, *112*, 171.

Bierwirth, P. (1996). *Investigation of airborne gamma-ray images as a rapid mapping tool for soil and land degradation-Wagga Wagga, NSW*. Canberra City, Australia: Australian Geological Survey Organisation.

Buccianti, A., Mateu-Figueras, G., & Pawlowsky-Glahn, V. (2006). Compositional data analysis in the geosciences: from theory to practice..

Bulmer, M. G. (1979). *Principles of statistics*. New York: United States: Dover Publications.

Chan, L., Wong, P., & Chen, Q. (2007). Abundances of radioelements (K, U, Th) in weathered igneous rocks in Hong Kong. *Journal of Geophysics and Engineering*, *4*(3), 285–292.

Charro, E., Pardo, R., & Peña, V. (2013). Statistical analysis of the spatial distribution of radionuclides in soils around a coal-fired power plant in Spain. *Journal of Environmental Radioactivity*, *124*, 84–92.

Chowdhury, M., Kamal, M., Alam, M., Yeasmin, S., & Mostafa, M. (2006). Distribution of naturally occurring radionuclides in soils of the southern districts of Bangladesh. *Radiation Protection Dosimetry*, *118*(1), 126–130.

Clark, R. B., Duval Jr, J. S., & Adams, J. A. (1972). Computer simulation of an air-borne gamma-ray spectrometer. *Journal of Geophysical Research*, *77*(17), 3021–3031.

Cook, S., Corner, R., Groves, P., & Grealish, G. (1996). Use of airborne gamma radiometric data for soil mapping. *Soil Research*, *34*(1), 183–194.

Corbacho, J., & Baeza, A. (2022). In situ gamma spectrometry using a portable HPGe detector. radiological characterisation and environmental surveillance around an operating nuclear power plant. possibilities and limits. *Journal of Radiological Protection*, *42*(2), 021501.

Cresswell, A., & Sanderson, D. (2009). The use of difference spectra with a filtered rolling average background in mobile gamma spectrometry measurements. *Nuclear Instruments and Methods in Physics Research Section A: Accelerators, Spectrometers, Detectors and Associated Equipment*, *607*(3), 685–694.

Cuttler, J. M. (2013). Commentary on Fukushima and beneficial effects of low radiation. *Dose-Response*, *11*(4), dose–response.

Darnley, A., Björklund, A., Bölviken, B., Gustavsson, N., Koval, P., Plant, J., ... others (1995). A global geochemical database for environmental and resource management. final report of IGCP project 259. *Earth Sciences*, *19*, 122.

Debertin, K., & Helmer, R. G. (1988). *Gamma-and x-ray spectrometry with semiconductor detectors*. Netherlands:Holland.

De Meijer, R., James, I., Jennings, P., & Koeyers, J. (2001). Cluster analysis of radionuclide concentrations in beach sand. *Applied Radiation and Isotopes*, *54*(3), 535–542.

Dickson, B. L., & Scott, K. (1997). Interpretation of aerial gamma-ray surveys-adding the geochemical factors. *AGSO Journal of Australian Geology and Geophysics*, *17*(2), 187–200.

DMG. (1994). *Geological map of Nepal*. Department of Mines and Geology, Kathmandu, Nepal.

Dragovic, S., & Onjia, A. (2007). Classification of soil samples according to geographic origin using gamma-ray spectrometry and pattern recognition methods. *Applied Radiation and Isotopes*, *65*(2), 218–224.

Duggal, V., Rani, A., Mehra, R., & Ramola, R. (2014). Assessment of natural radioactivity levels and associated dose rates in soil samples from Northern Rajasthan, India. *Radiation Protection Dosimetry*, *158*(2), 235–240.

Einax, J. W., Zwanziger, H. W., & Geiss, S. (1997). *Chemometrics in environmental analysis*. United States: John Wiley & Sons.

Eisenbud, M., & Gesell, T. F. (1997). *Environmental radioactivity from natural, industrial and military sources: from natural, industrial and military sources*. United States: Elsevier.

Evans, C., Morton, L., & Harbottle, G. (1997). Pedologic assessment of radionuclide distributions: Use of a radio-pedogenic index. *Soil Science Society of America Journal*, *61*(5), 1440–1449.

Fujimoto, K. (1986). Shielding effect of snow cover on terrestrial gamma exposure rate. *Japanese Journal of Health Physics*, *21*(1), 3–8.

Fujitaka, K., Matsumoto, M., Kaiho, K., & Abe, S. (1992). Effect of rain interval on wet deposition of radon daughters. *Radiation Protection Dosimetry*, *45*(1-4), 333–336.

Garba, N., Ramli, A., Saleh, M., Sanusi, M., Gabdo, H., & Aliyu, A. (2016). The potential health hazards of chronic exposure to low-dose natural radioactivity in Terengganu, Malaysia. *Environmental Earth Sciences*, *75*(5), 1–12.

Gilmore, G. (2008). *Practical gamma-ray spectroscopy*. United States: John Wiley & Sons.

Golmakani, S., Moghaddam, M. V., & Hosseini, T. (2008). Factors affecting the transfer of radionuclides from the environment to plants. *Radiation Protection Dosimetry*, *130*(3), 368–375.

Grasty, R., & Cox, J. (1997). *A carborne gamma-ray spectrometer system for natural radioactivity mapping and environmental monitoring* [Resume 95, DK9800029].

Groeneveld, R. A., & Meeden, G. (1984). Measuring skewness and kurtosis. *Journal of the Royal Statistical Society: Series D (The Statistician)*, *33*(4), 391–399.

Hatakka, J., Paatero, J., Viisanen, Y., & Mattsson, R. (1998). Variations of external radiation due to meteorological and hydrological factors in Central Finland. *Radiochemistry*, *40*(6), 534–538.

He, Q., & Walling, D. (1997). The distribution of fallout ^{137}Cs and ^{210} Pb in undisturbed and cultivated soils. *Applied Radiation and Isotopes*, *48*(5), 677–690.

Hendriks, P., Limburg, J., & De Meijer, R. (2001). Full-spectrum analysis of natural γ-ray spectra. *Journal of Environmental Radioactivity*, *53*(3), 365–380.

IAEA. (1989). *Construction and use of calibration facilities for radiometric field equipment* (Technical Report, Series No. 309). Austria: International Atomic Energy Agency.

IAEA. (1990). *The use of gamma ray data to define the natural radiation environment* (Technical Report, IAEA TECDOC-566). Austria: International Atomic Energy Agency.

IAEA. (2000). *Generic procedures for assessment and response during radiological emergency* (Technical Report, IAEA TECDOC-1162). Austria: International Atomic Energy Agency.

IAEA. (2003). *Guidelines for radioelement mapping using gamma ray spectrometry data* (Technical Report, IAEA TECDOC-1363). Austria: International Atomic Energy Agency.

ICRP. (2007). The 2007 recommendations of the international commission on radiological protection. *ICRP Publication 103, Annals of the ICRP 37*, *37*(2.4), 2.

Jackson, J. E. (2005). *A user's guide to principal components*. New York: United States: John Wiley & Sons, Inc.

Jacob, P., Debertin, K., Miller, K., Roed, J., Saito, K., & Sanderson, D. (1994). *Gamma-ray spectrometry in the environment* (ICRU Report No. 53). Maryland, USA: International Commission on Radiation Units and Measurements.

Jaques, A., Wellman, P., Whitaker, A., & Wyborn, D. (1997). High-resolution geophysics in modern geological mapping. *AGSO Journal of Australian Geology and Geophysics*, *17*(2), 159–173.

Ji, Y.-Y., Ochi, K., Hong, S. B., Nakama, S., Sanada, Y., & Mikami, S. (2021). Performance of in situ gamma-ray spectrometry in the assessment of radioactive cesium deposition around the Fukushima Daiichi nuclear power plant. *Radiation Physics and Chemistry*, *179*, 109205.

Kanevski, M., Parkin, R., Pozdnukhov, A., Timonin, V., Maignan, M., Demyanov, V., & Canu, S. (2004). Environmental data mining and modeling based on machine learning algorithms and geostatistics. *Environmental Modelling & Software*, *19*(9), 845–855.

Kaniu, M. (2017). *Rapid in-situ gamma-ray spectrometry and associated radiometric assessment of the Mrima-Kiruku complex (Kenya) high background radiation anomaly* (Doctoral dissertation). University of Nairobi, Kenya.

Kansal, S., & Mehra, R. (2015). Evaluation and analysis of ^{226}Ra, ^{232}Th and ^{40}K and radon exhalation rate in the soil samples for health risk assessment. *International Journal of Low Radiation*, *10*(1), 1–13.

Kastlander, J. (2010). *In situ measurements of radionuclide concentration in soil: An investigation into detector properties and methods* (Doctoral dissertation). Department of Physics, Stockholm University, Sweden.

Khabar, A. (2014, June 2). *Uranium kills locals people with cancer - Makwanpur.* Retrieved from `https://www.youtube.com/watch?v=x_4d3DJE5O0&t=74s`

Khan, H. M., Ismail, M., Khan, K., & Akhter, P. (2011). Radioactivity levels and gamma-ray dose rate in soil samples from Kohistan (Pakistan) using gamma-ray spectrometry. *Chinese Physics Letters*, *28*(1), 019301.

Klemic, G. (1996). Environmental radiation monitoring in the context of regulations on dose limits to the public. In *Proceedings of 1996 congress of the international radiation protection association (IRPA 9)* (pp. 321–328). Vienna.

Klusoň, J., & Thinova, L. (2011). Contribution of atmospherical radon to in-situ scintillation gamma spectrometry data. *Applied Radiation and Isotopes*, *69*(8), 1143–1145.

Knoll, G. F. (2010). *Radiation detection and measurement*. United States: John Wiley & Sons.

Kobayashi, S., Shinomiya, T., Kitamura, H., Ishikawa, T., Imaseki, H., Oikawa, M., ... Uchihori, Y. (2015). Radioactive contamination mapping of northeastern and eastern Japan by a car-borne survey system, radi-probe. *Journal of Environmental Radioactivity*, *139*, 281–293.

Kogan, R. M., Nazarov, I. M., & Fridman, S. D. (1971). *Gamma spectrometry of natural environments and formations: Theory of the method applications to geology and geophysics*. Israel Program for Scientific Translations;[available from the US Department].

Krane, K. S. (1988). *Introductory nuclear physics*. New York: United States: John Wiley & Sons.

Laaksoharju, M., Skårman, C., & Skårman, E. (1999). Multivariate mixing and mass balance (m3) calculations, a new tool for decoding hydrogeochemical information. *Applied Geochemistry*, *14*(7), 861–871.

Laedermann, J. P., Byrde, F., & Murith, C. (1998). In-situ gamma-ray spectrometry: the influence of topography on the accuracy of activity determination. *Journal of Environmental Radioactivity*, *38*(1), 1–16.

Landa, E. R. (2007). Naturally occurring radionuclides from industrial sources: characteristics and fate in the environment. *Radioactivity in the Environment*, *10*, 211–237.

Lilley, J. (2013). *Nuclear physics: principles and applications*. England: United States: John Wiley & Sons Ltd.

Liu, W., Li, X., Shen, Z., Wang, D., Wai, O., & Li, Y. S. (2003). Multivariate statistical study of heavy metal enrichment in sediments of the pearl river estuary. *Environmental Pollution*, *121*(3), 377–388.

Løvborg, L. (1984). *The calibration of portable and airborne gamma-ray spectrometers-theory, problems, and facilities* (Report). Denmark: Risoe National Lab.

Matsuda, N., Mikami, S., Shimoura, S., Takahashi, J., Nakano, M., Shimada, K., ... Saito, K. (2015). Depth profiles of radioactive cesium in soil using a scraper plate over a wide area surrounding the Fukushima Dai-ichi Nuclear Power Plant, Japan. *Journal of Environmental Radioactivity*, *139*, 427–434.

Meglen, R. R. (1992). Examining large databases: a chemometric approach using principal component analysis. *Marine Chemistry*, *39*(1-3), 217–237.

Miller, K. M., & Shebell, P. (1993). *In situ gamma-ray spectrometry: a tutorial for environmental radiation scientists* (Report). New York, United States: USDOE Environmental Measurements Lab.

Mishra, A., & Khanal, R. (2019). Outdoor effective dose and associated health risk in the premises of Tribhuvan University in-situ gamma ray spectrometry. *Himalayan Physics*, *8*, 47–52.

Mishra, A., & Khanal, R. (2021). Scattering of gamma radiation by air in the ambient environment using gamma ray spectrometry: 10.48129/kjs.17253. *Kuwait Journal of Science*.

Mishra, A., & Khanal, R. (2023). In-situ radiometric assessment of UNESCO world heritage sites in Kathmandu valley of Nepal using gamma ray spectrometry. *Jordan Journal of Physics*, *16*(2), https://journals.yu.edu.jo/jjp/Accepted%20articles-%20unpublished.html.

Mishra, K. P., Ahmed, M., & Hill, R. P. (2008). Low-dose radiation effects on human health with implications to radioprotection and cancer radiotherapy. *International Journal of Radiation Biology*, *84*(5), 441–444.

Mlwilo, N. A. (2010). *Radiometric characterisation of vineyard soils, Western Cape, South Africa* (Doctoral dissertation). University of the Western Cape, Africa.

Navas, A., Gaspar, L., López-Vicente, M., & Machín, J. (2011). Spatial distribution of natural and artificial radionuclides at the catchment scale (South Central Pyrenees). *Radiation Measurements*, *46*(2), 261–269.

Navas, A., Machín, J., & Soto, J. (2005). Mobility of natural radionuclides and selected major and trace elements along a soil toposequence in the Central Spanish Pyrenees. *Soil Science*, *170*(9), 743–757.

Navas, A., Soto, J., & Machín, J. (2002a). Edaphic and physiographic factors affecting the distribution of natural gamma-emitting radionuclides in the soils of the Arnás catchment in the Central Spanish Pyrenees. *European Journal of Soil Science*, *53*(4), 629–638.

Navas, A., Soto, J., & Machın, J. (2002b). ^{238}U, ^{226}Ra, ^{210}Pb, ^{232}Th and ^{40}K activities in soil profiles of the Flysch sector (Central Spanish Pyrenees). *Applied Radiation and Isotopes*, *57*(4), 579–589.

NCRP. (1976). *Environmental radiation measurements* (Report No. 050). United States: National council on Radiation Protection and Measurements.

NG. (2017). *Mines & minerals sector profile* (Report). Nepal: Government of Nepal Office of the Investment Board.

Nilsson, J. M., Östlund, K., Söderberg, J., Mattsson, S., & Rääf, C. (2014). Tests of HPGe and scintillation-based backpack γ-radiation survey systems. *Journal of Environmental Radioactivity*, *135*, 54–62.

O'Brien, R., & Cooper, M. (1998). Technologically enhanced naturally occurring radioactive material (NORM): pathway analysis and radiological impact. *Applied Radiation and Isotopes*, *49*(3), 227–239.

Okeji, M. C., Agwu, K. K., & Idigo, F. U. (2012). Assessment of natural radioactivity in phosphate ore, phosphogypsum and soil samples around a phosphate fertilizer plant in Nigeria. *Bulletin of Environmental Contamination and Toxicology*, *89*(5), 1078–1081.

Olagbaju, P., Okeyode, I., Alatise, O., & Bada, B. (2021). Background radiation level measurement using hand held dosimeter and gamma spectrometry in Ijebu-Ife, Ogun State Nigeria. *International Journal of Radiation Research*, *19*(3), 591–598.

Ouseph, P. (1975). *Introduction to nuclear radiation detectors*. New York, United States: Plenum Press.

Pantha, P., Bhusal, T. P., Shah, B. R., & Koirala, R. P. (2019). Study of natural background radiation in Kathmandu valley. *BIBECHANA*, *16*, 187–195.

Paschoa, A. S. (1998). Potential environmental and regulatory implications of naturally occurring radioactive materials (NORM). *Applied Radiation and Isotopes*, *49*(3), 189–196.

PEI. (2008). *Montaj plus Praga 4 tutorial and user guide* [Software manual]. Canada: Pico Envirotec Inc.

PEI. (2010). *AGRS1 portable spectrometer calibration program user manual* [Software manual]. Canada: Pico Envirotec Inc.

PEI. (2013). *PEI DATA VIEWER program for fast field data verification and PEI format conversion to Geosoft GBN or ASCII formats user manual* [Software manual]. Canada: Pico Envirotec Inc.

PEI. (2014). *PEICore and PGIS-2 operation manual, version 5.2.5* [Software and instrument operational manual]. Canada: Pico Envirotec Inc.

Podgorsak, E., & Hendee, W. (2010). Radiation physics for medical physicists-2nd ed. *Medical Physics*, *37*(9), 5148.

Rahman, S., Faheem, M., Anwar, J., Ziafat, M., Nasir, T., & Matiullah. (2009). External dose assessment from the measured radioactivity in soil samples collected from the Islamabad capital territory, Pakistan. *Journal of Radiological Protection*, *29*(4), 499.

Ramzaev, V., Bernhardsson, C., Dvornik, A., Barkovsky, A., Vodovatov, A., & Jönsson, M. (2021). In situ determination of ^{137}cs inventory in soil using a field-portable scintillation gamma spectrometer-dosimeter. *Journal of Environmental Radioactivity*, *231*, 106562.

Reimann, C., & Filzmoser, P. (2000). Normal and lognormal data distribution in geochemistry: death of a myth. consequences for the statistical treatment of geochemical and environmental data. *Environmental Geology*, *39*(9), 1001–1014.

Rostron, P. D., Heathcote, J. A., & Ramsey, M. H. (2014). Optimising in situ gamma measurements to identify the presence of radioactive particles in land areas. *Journal of Environmental Radioactivity*, *138*, 162–169.

Sankaran, A., Jayaswal, B., Nambi, K., & Sunta, C. (1986). *U, Th and K distributions inferred from regional geology and the terrestrial radiation profiles in India* (Report). India: Bhabha Atomic Research centre.

Shah, B. R. (1994). *Rapid determination of K-40 in sample of soil from within Kathmandu valley using multichannel spectrometer* (Unpublished master's thesis). Tribhuvan University, Nepal.

Sharma, P., Kumar Meher, P., & Prasad Mishra, K. (2014). Terrestrial gamma radiation dose measurement and health hazard along river Alaknanda and Ganges in India. *Journal of Radiation Research and Applied Sciences*, *7*(4), 595–600.

Smetsers, R., & Blaauboer, R. (1997). A dynamic compensation method for natural ambient dose rate based on 6 years data from the Dutch radioactivity monitoring network. *Radiation Protection Dosimetry*, *69*(1), 19–31.

Software, G. (2020). *A basic understanding of surfer gridding methods- part 1,* [Golden software support]. Retrieved from `https://support.goldensoftware.com/hc/en-us/articles/231348728-A-Basic-Understanding-of-Surfer-Gridding-Methods-Part-1`

Sohrabi, M. (2000). Environments with elevated radiation levels from natural radioactive substances. In *Restoration of environments with radioactive residues. papers and discussions. proceedings of an international symposium,IAEA-SM-359.* Arlington, Virginia.

Stöcklin, J. (1980). Geology of Nepal and its regional frame: Thirty-third William Smith Lecture. *Journal of the Geological Society*, *137*(1), 1–34.

Taira, Y., Hayashida, N., Tsuchiya, R., Yamaguchi, H., Takahashi, J., Kazlovsky, A., . . . Takamura, N. (2013). Vertical distribution and estimated doses from artificial radionuclides in soil samples around the Chernobyl nuclear power plant and the Semipalatinsk nuclear testing site. *PLoS One*, *8*(2), e57524.

Takeda, A., Kimura, K., & Yamasaki, S.-i. (2004). Analysis of 57 elements in Japanese soils, with special reference to soil group and agricultural use. *Geoderma*, *119*(3-4), 291–307.

Takeda, A., Tsukada, H., Takaku, Y., Hisamatsu, S., & Nanzyo, M. (2006). Accumulation of uranium derived from long-term fertilizer applications in a cultivated andisol. *Science of the Total Environment*, *367*(2-3), 924–931.

Taskin, H., Karavus, M., Ay, P., Topuzoglu, A., Hidiroglu, S., & Karahan, G. (2009). Radionuclide concentrations in soil and lifetime cancer risk due to gamma radioactivity in Kirklareli, Turkey. *Journal of Environmental Radioactivity*, *100*(1), 49–53.

Thabayneh, K. (2012). Natural radioactivity levels and estimation of radiation exposure in environmental soil samples from Tulkarem Province–Palestine. *Open Journal of Soil Science*.

Tsikritzis, L. (2005). Chemometrics of the distribution and origin of ^{226}Ra, ^{228}Ra, ^{40}K and ^{137}Cs in plants near the West Macedonia Lignite Center (Greece). *Journal of Radioanalytical and Nuclear Chemistry*, *264*(3), 651–656.

Tsoulfanidis, N., & Landsberger, S. (2021). *Measurement & detection of radiation*. United States: CRC press.

Tsujimoto, T. (1988). A comparison between in-situ and sampling methods for the determination of radionuclides in soil. *Journal of Radiation Research*, *29*(4), 229–237.

Tyler, A. N., & Copplestone, D. (2007). Preliminary results from the first national in situ gamma spectrometry survey of the United Kingdom. *Journal of Environmental Radioactivity*, *96*(1-3), 94–102.

UNSCEAR. (1988). *Sources, effects and risks of ionizing radiation* (Report to the General Assembly, with annexes). New York: United Nations: United Nations Scientific Committee on the Effects of Atomic Radiation.

UNSCEAR. (2000). *Sources and effects of ionizing radiation* (Report to the General Assembly, with scientific annexes). New York: United Nations: United Nations Scientific Committee on the Effects of Atomic Radiation.

van Velzen, L. (2015). *Environmental remediation and restoration of contaminated nuclear and NORM sites*. United States: Elsevier.

Varmuza, K., & Filzmoser, P. (2016). *Introduction to multivariate statistical analysis in chemometrics*. United States: CRC press.

Veiga, L. H., Amaral, E., Magalhaes, M. H., Sachet, I., & Mello, V. (1999). Brazilian areas of elevated levels of natural radiation: a critical review and relevant future studies. *Second Symposium on Technologically Enhanced Natural Radiation*.

Vukasinovic, I., Djordjevic, A., Rajkovic, M., Todorovic, D., & Pavlovic, V. (2010). Distribution of natural radionuclides in anthrosol-type soil. *Turkish Journal of Agriculture and Forestry*, *34*(6), 539–546.

Wallova, G., Acharya, K., & Wallner, G. (2010). Determination of naturally occurring radionuclides in selected rocks from Hetaunda area, central Nepal. *Journal of Radioanalytical and Nuclear Chemistry*, *283*(3), 713–718.

Webster, R., & Oliver, M. A. (2007). *Geostatistics for environmental scientists*. United States: John Wiley & Sons.

Wenning, R. J., & Erickson, G. A. (1994). Interpretation and analysis of complex environmental data using chemometric methods. *TrAC Trends in Analytical Chemistry*, *13*(10), 446–457.

Westfall, P. H. (2014). Kurtosis as peakedness, 1905–2014. RIP. *The American Statistician*, *68*(3), 191–195.

Wilford, J. (1996). Airborne gamma-ray spectrometry as a tool for assessing relative landscape activity and weathering development of regolith, including soils. In *International journal of rock mechanics and mining sciences and geomechanics abstracts* (Vol. 5, p. 214A).

Wilford, J., Bierwirth, P., & Craig, M. (1997). Application of airborne gamma-ray spectrometry in soil/regolith mapping and applied geomorphology. *AGSO Journal of Australian Geology and Geophysics*, *17*(2), 201–216.

Wilford, J. R. (1992). *Regolith mapping using integrated Landsat TM imagery and high resolution gamma-ray spectrometric imagery: Cape York Peninsula*. Australia: Australian Geological Survey Organisation.

Wu, Z., Wang, B., Sun, J., Wang, Y., & Zhao, C. (2022). In-situ γ-ray analysis of ground surface radioactivity using portable HPGe γ spectrometer. *Scientific Reports*, *12*(1), 1–11.

Yadav, P., Rajbhandari, P., & Shrestha, K. (2012). Estimation of concentration of k-40 by gamma spectroscopy and atomic emission spectroscopy in the environmental samples of northern Kathmandu valley. *Journal of Nepal Chemical Society*, *29*, 75–80.

Yang, Y., Wu, X., Jiang, Z., Wang, W., Lu, J., Lin, J., ... Hsia, Y. (2005). Radioactivity concentrations in soils of the Xiazhuang granite area, China. *Applied Radiation and Isotopes*, *63*(2), 255–259.

APPENDIX 1

A. Academic Activities

A.1 Attended Courses Recommended by Supervisor

1) "Training on Nuclear and Atomic Physics" by International Atomic Energy Agency (IAEA), Department of Nuclear Sciences and Applications, Nuclear Science and Instrumentation Laboratory, Seibersdorf, Austria, 28 November to 16 December 2016.

2) "Lecture Series on Research Methodology" by Prof. Dr. Subodh R. Shenoy, Central Department of Physics, Tribhuvan University, Kirtipur, Nepal, 6 November to 22 December 2017.

3) "Postgraduate Educational Courses on Radiation Protection and Safety of Radiation Sources", organised by International Atomic Energy Agency (IAEA) and hosted by Malaysian Nuclear Agency, 23 April to 19 October 2018.

A.2 Paper Publications

1) Mishra, A., & Khanal, R. (2019). Outdoor effective dose and associated health risk in the premises of Tribhuvan University in-situ gamma ray spectrometry. *Himalayan Physics*, *8*, 47-52.

2) Mishra, A., & Khanal, R. (2021). Scattering of Gamma Radiation by Air in the Ambient Environment Using Gamma Ray Spectrometry: 10.48129/kjs.17253. *Kuwait Journal of Science*.

3) Mishra, A., & Khanal, R. (2023). In-situ radiometric assessment of UNESCO world heritage sites in Kathmandu valley of Nepal using gamma ray spectrometry. *Jordan Journal of Physics*, *16*(2).

A.3 Paper Communicated

1) Mishra, A., & Khanal, R. Radiometric assessment of Bagh Bhairav temple in Kirtipur, Nepal using in-situ gamma ray spectrometry (under review).

2) Mishra, A., & Khanal, R. Assessment of ^{137}Cs in the environment of Hetauda City, Nepal by in-situ gamma ray spectrometry.

3) K. C. Nirmal, Chalise, R., Mishra A. & Khanal R. Background Radiation at Different Bridges over the River Bishnumati, Kathmandu, Nepal by in-situ gamma ray spectrometry.

A.4 Participations and Presentations

1) Participated in the “Workshop on Scientific Writing ” Tri-Chandra Multiple Campus, 22 July, 2017

2) Participated in the Workshop on "Emergency Preparedness Response Related to Nuclear Radiation" conducted by IAEA in Kathmandu Nepal in cooperation with Department of Hydrology and Meteorology, 7-9 June, 2017.

3) Poster presentation entitled “ Estimation of Background Radiation in the Premises of Tribhuvan University, Kirtipur, Nepal by In-Situ Gamma-Ray Spectrometry” in International Conference on Nano-Material and Computational Physics, Central Department of Physics, Tribhuvan University, Kirtipur, Nepal, 27-29 December 2017.

4) Oral presentation entitled “Estimation of Background Radiation in the Premises of Tribhuvan University, Kirtipur, Nepal by In-situ Gamma Ray Spectrometry", organised by Nepal Physical Society, Nepal, 23 December, 2017.

5) Oral presentation entitled “Environmental Monitoring Surrounding TRIGA Puspati Research Reactor in Nuclear Malaysia", in 15th Postgraduate Educational Course on Radiation Protection and Safety of Radiation Sources (PGEC-15), organised by Malaysian Nuclear Agency, Malaysia, 14 October, 2018.

6) Oral presentation entitled “Radiological Survey of Kathmandu by In-situ Gamma Ray Spectrometry", organised by Nepal Physical Society, Nepal, 24 November, 2018.

7) Participated in the Workshop on "IAEA Outreach Workshop for Nepal: Safe, Secure and Peaceful Applications of Nuclear Science and Technology to reach National Development Goals", Kathmandu, Nepal, 10-11 December, 2018.

8) Oral presentation entitled “Radiological Survey of Kathmandu By In-situ Gamma Ray Spectrometry” in International Conference on Nanosciences and High Energy Physics (ICNHEP-2019), Central Department of Physics, Tribhuvan University, Kirtipur, Nepal, 4-6 February, 2019.

9) Oral presentation entitled “Estimation of Background Radiation in the Premises of Tribhuvan University, Kirtipur Nepal by In-situ Gamma Ray Spectrometry” in

Second Regional Conference on Women in Physics (RCWIP-2019), Kathmandu, Nepal, 27-29 March, 2019.

10) Team member of the project work entitled "In-situ Radiological Mapping of Kathmandu and Lalitpur within the Ring Road" with research grant from Ministry of Education, Science and Technology; Government of Nepal, 2019.

11) Participated in the Workshop on "National Workshop on Current status, Needs and Challenges of Nuclear Sources and Technology on Nepal", Kathmandu, Nepal, 11 February, 2020.

12) Oral presentation entitled “Radiological assessment of Bagh Bhairav in Kirtipur, Nepal by in-situ gamma ray spectrometry” in the ANPA Conference 2020 organized by The Association of Nepali Physicists in America (ANPA), during 17–19 July 2020.

13) Poster presentation entitled “ Assessment of ^{137}Cs in the environment of Hetauda, Nepal by in-situ gamma ray spectrometry” in ICRP International Conference on Recovery after Nuclear Accidents, organised by the International Commission on Radiological Protection (ICRP) and hosted by Japan Atomic Energy Agency (JAEA), 1-4 December, 2020.

14) Participated in the Workshop on "Basic Training in Radiation Protection", Kirtipur, 1-8 February, 2021.

15) Poster presentation entitled “ In-situ radiometric assessment of UNESCO world heritage sites in Kathmandu valley of Nepal by gamma spectrometry” in 7^{th} IUPAP International Conference for Women in Physics (ICWIP 2020), organised by the International Union of Pure and Applied Physics (IUPAP), 11 - 16 July, 2021.

16) Oral presentation entitled “Presentation on Depth Profile of ^{137}Cs in Cultivated Land in Eight Different Locations of Kathmandu and Makwanpur District, Nepal” in International Conference on Frontiers of Physics (ICFP) - 2022, 22-24 January, 2022.

A.5 M.Sc. Term Paper under Joint Supervision

1) Background Radiation on different bridges of Bishnumati river from Balaju to Teku, 2020 by Nirmal KC.

2) Natural background radiation in Rani Pokhari, Kathmandu during reconstruction, 2020 by Hari Adhikari.

3) Background radiation exposure around Manjushree statue at Chobhar, 2020 by Ishwor Datt Bhatt.

4) Background radiation at Sisdol landfill site in Okharpauwa, Nuwakot, 2021 by Niranjan Dahal.

APPENDIX 2

A. Decay Series of Primordial Radionuclides

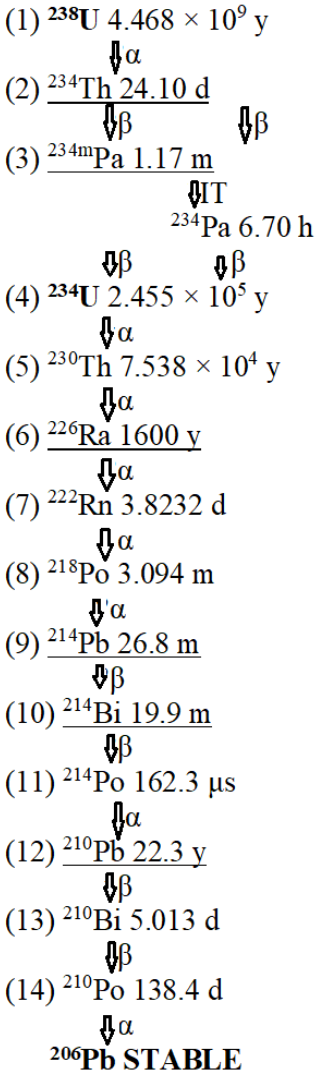

14 decay stages

8 alpha particles

Nuclides underlined are measurable by gamma spectrometry

Figure A.1: The uranium decay series ^{238}U (Gilmore, 2008)

(1) **^{235}U** 7.04×10^8 y

⇩ α

(2) ^{231}Th 25.52 h

⇩ β

(3) ^{231}Pa 3.276×10^4 y

⇩ α

(4) ^{227}Ac 21.772 y

⇩ β

(5) ^{227}Th 18.718 d

+ α (1.38 %) to ^{223}Fr 22.00 m, then β

⇩ α

(6) ^{223}Ra 11.43 d

⇩ α

(7) ^{219}Rn 3.96 s

⇩ α

(8) ^{215}Po 1.781 ms

⇩ α

(9) ^{211}Pb 36.1 m

⇩ β

(10) ^{211}Bi 2.14 m

⇩ α

(11) ^{207}Tl 4.77 m

+ β (0.273%) ^{211}Po 516 ms then α

⇩ β

^{207}Pb STABLE

11 decay stages
7 alpha particles
Only ^{235}U is measurable by gamma spectrometry

Figure A.2: The actinium decay series ^{235}U (Gilmore, 2008)

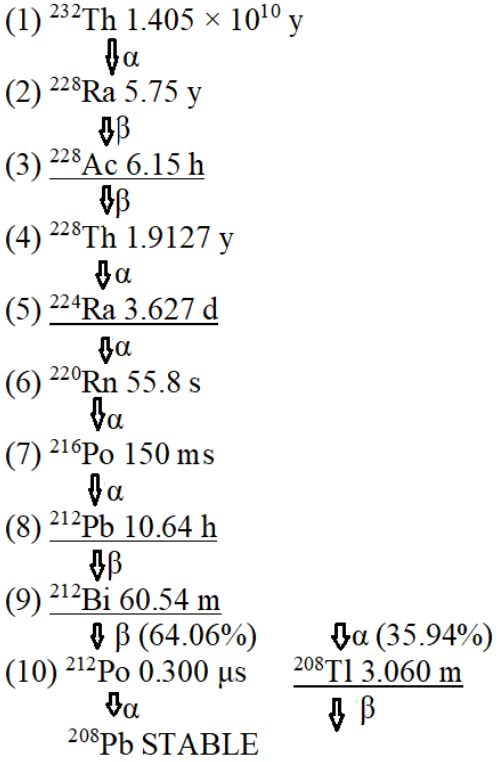

Figure A.3: The thorium decay series ^{232}Th (Gilmore, 2008)

B. In-situ Measurement of Vertical Depth profile for Gamma Radionuclides

Figure A.4: In-situ measurement of vertical depth profile for gamma radionuclides

C. Accumulated Spectrum During Data Analysis

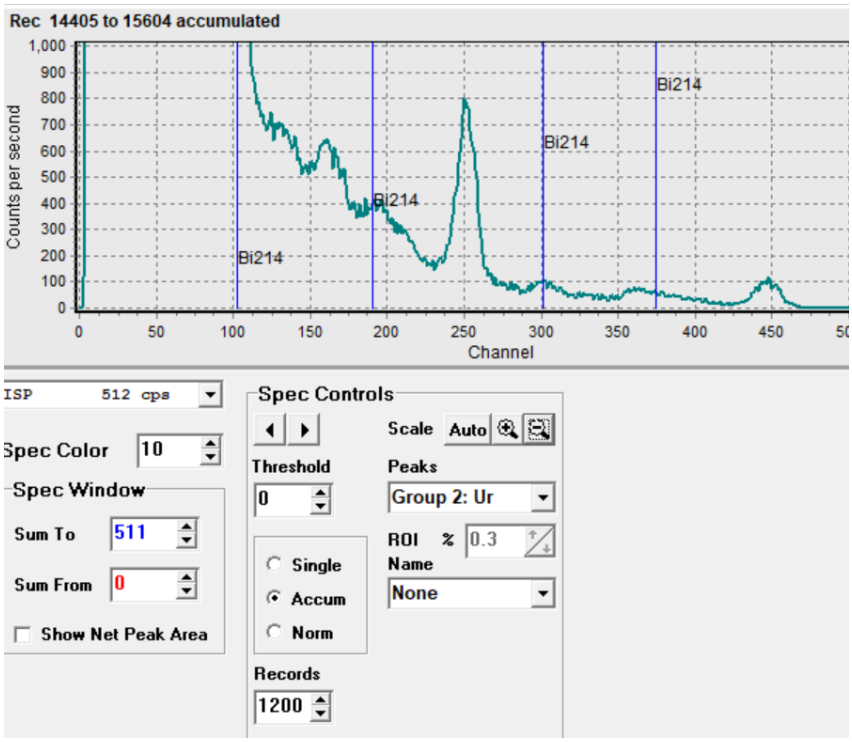

(a) ^{238}U peak

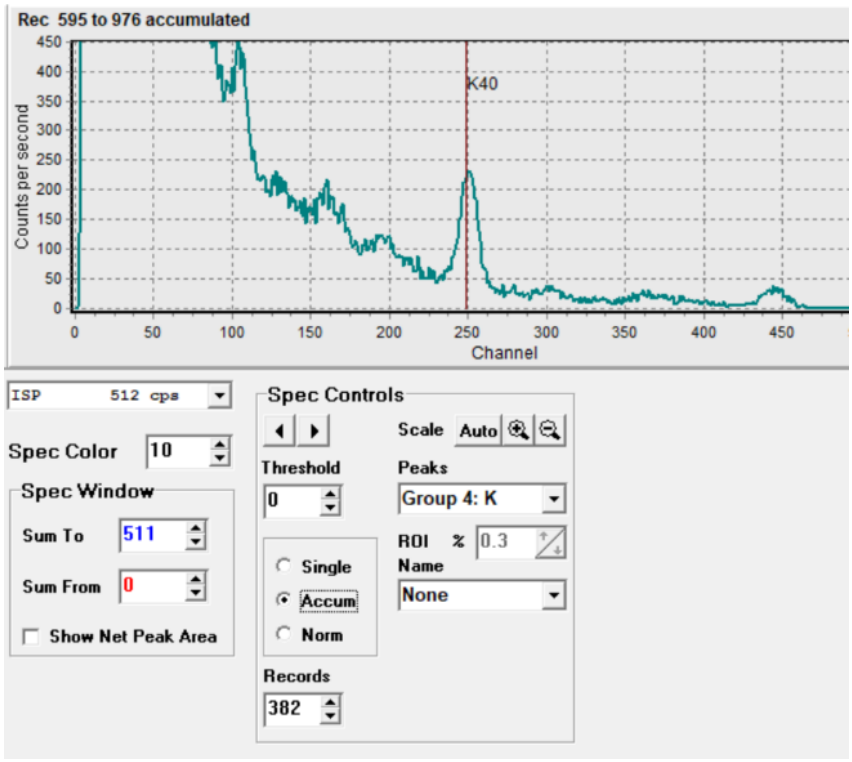

(b) ^{40}K peak

Figure A.5: Accumulated spectrum

D. Tuning Status of PGIS 2

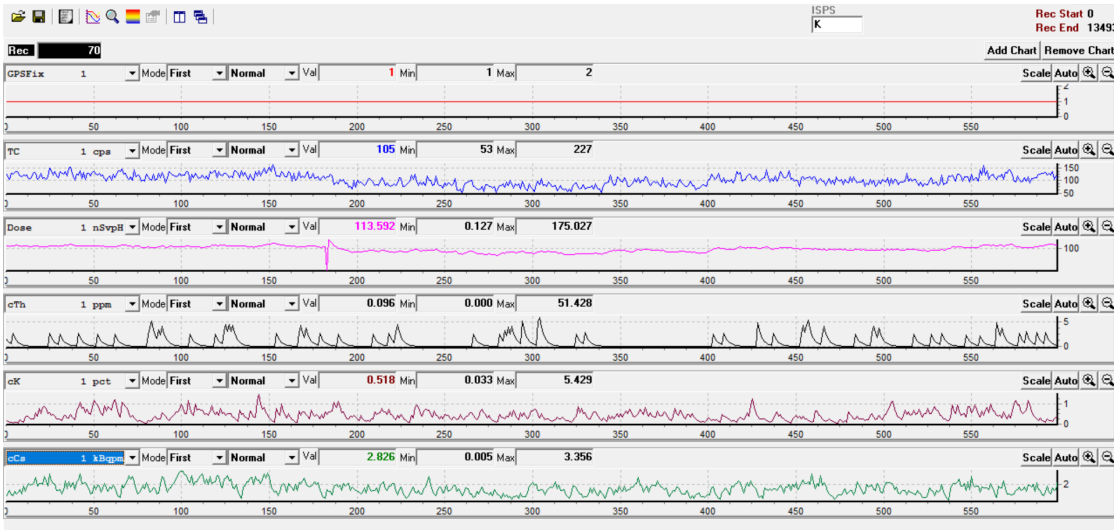

(a) Tuning status with K peak

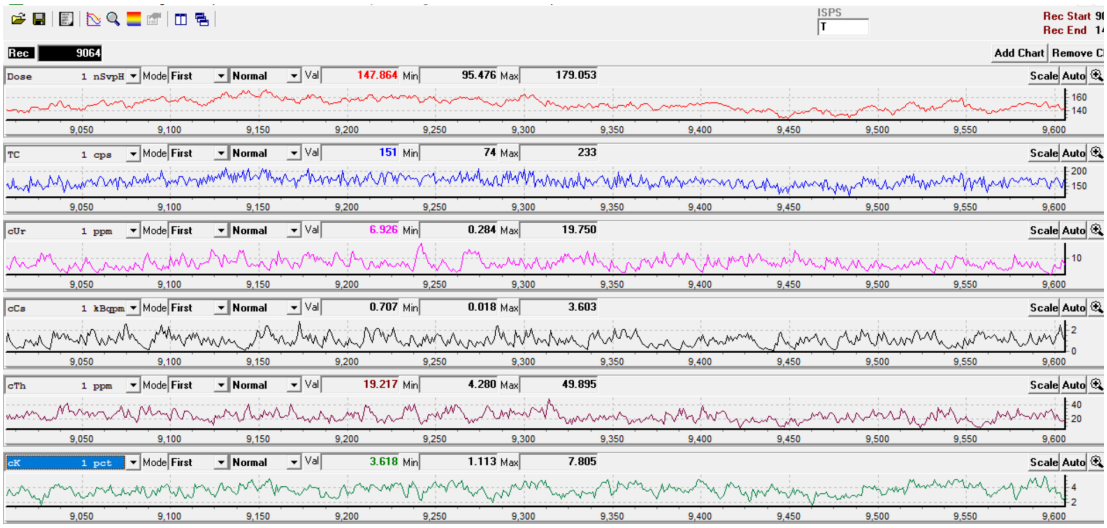

(b) Tuning status with Th peak

Figure A.6: Chart file showing the tuning status

E. Photographs of Rocks and Soils in Studied Area Taken During Survey

Figure A.7: Rocks and soils in the studied area

F. Photographs of Vegetation, Lake, Paddy Field and Rivers

Figure A.8: Some photos of vegetation, lake, paddy field and rivers taken during survey

G. Map Indicating the Locations of Depth profile Sites

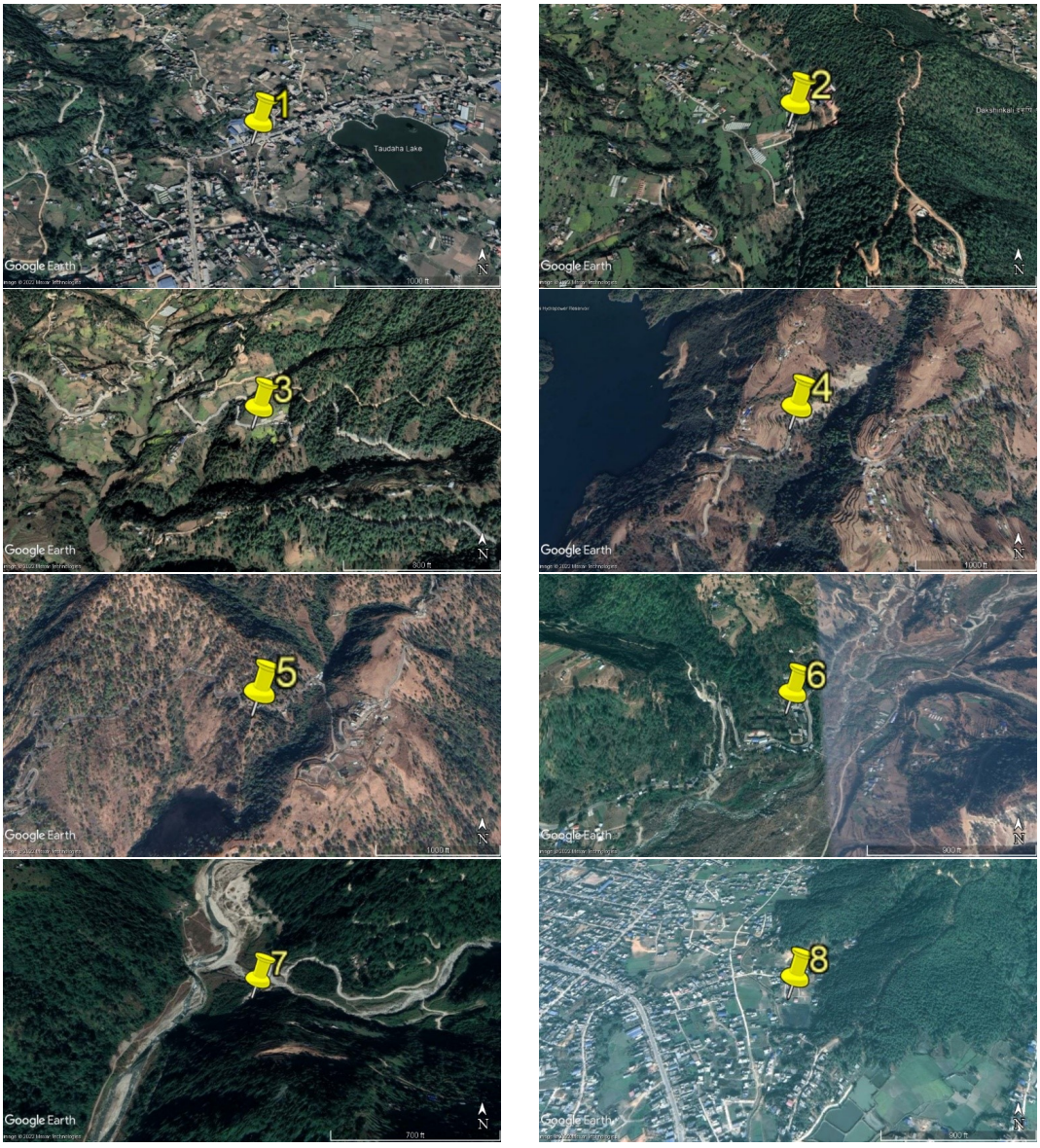

Figure A.9: Map showing the location of vertical depth measurement sites (1. Chobhar, 2. Pharping, 3. Rakash Khola, 4. Salle, 5. Chisapani Gadhi, 6. Dhorsingh, 7. Baghjhora, 8. Hetauda)

H. Ternary Diagram of Dose Rates in K-L, L-K, D-K, K-B and B-H

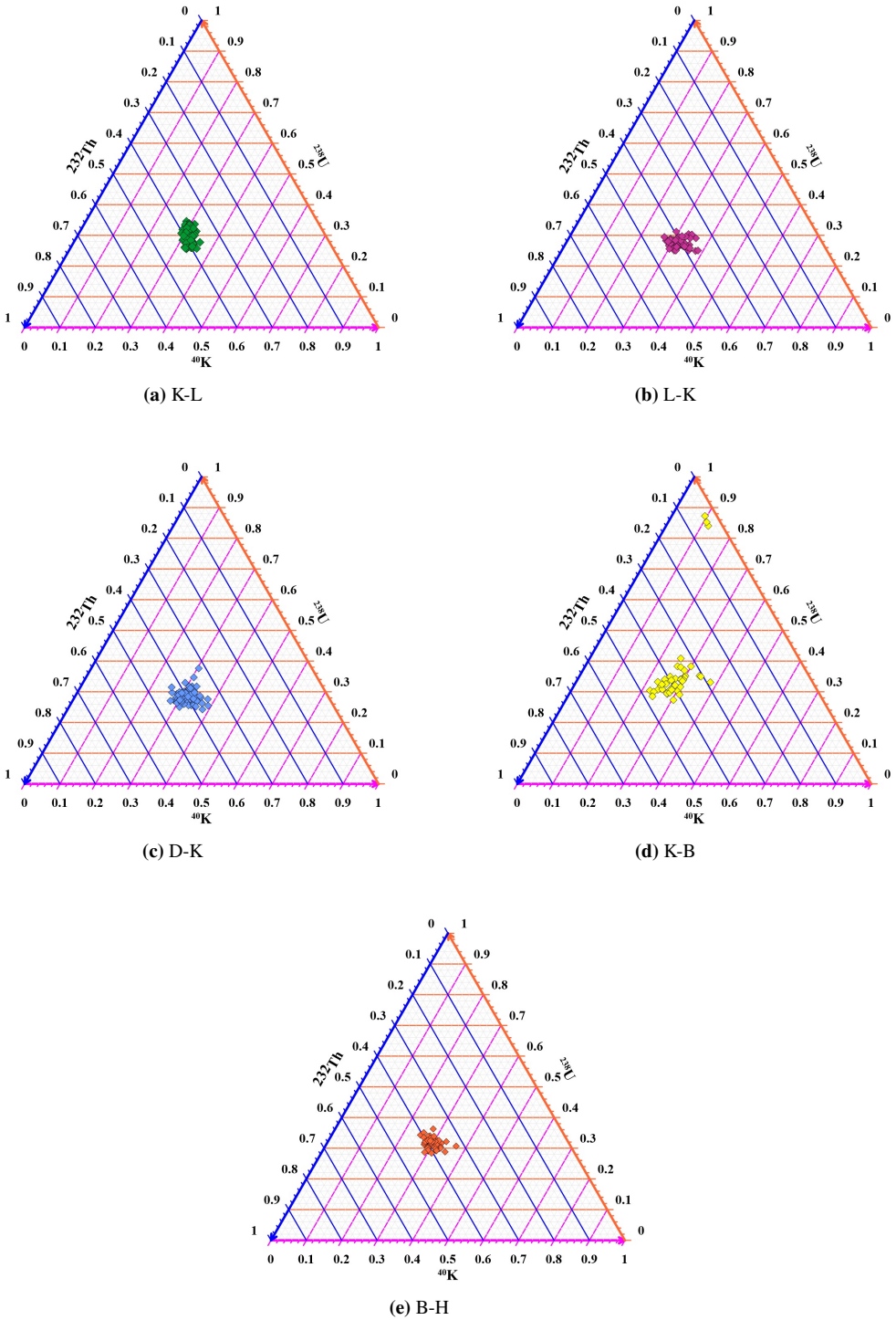

(a) K-L

(b) L-K

(c) D-K

(d) K-B

(e) B-H

Figure A.10: Dose rates from ^{40}K, ^{238}U and ^{232}Th between Kathmandu and Hetauda

I. Ternary Diagram of Activity Concentrations in K-L, L-K, D-K, K-B and B-H

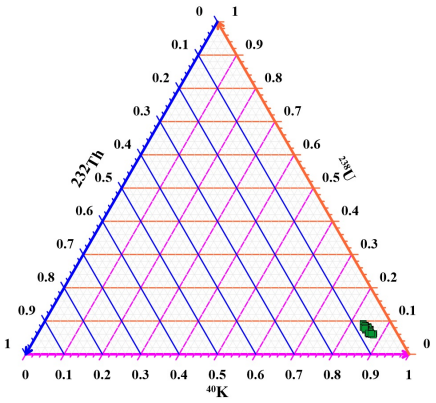

(a) K-L

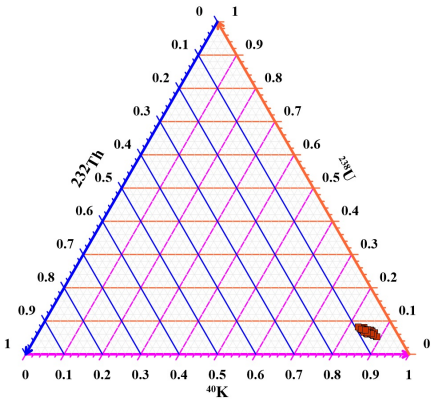

(b) L-K

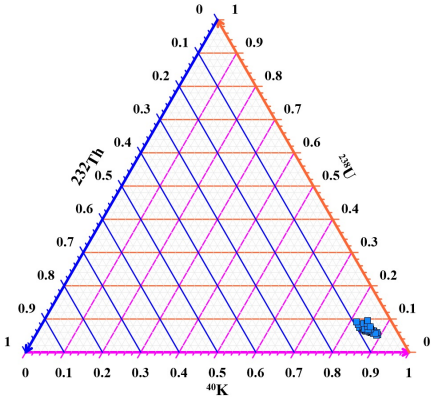

(c) D-K

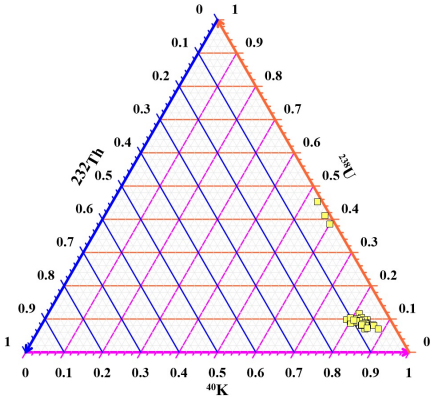

(d) K-B

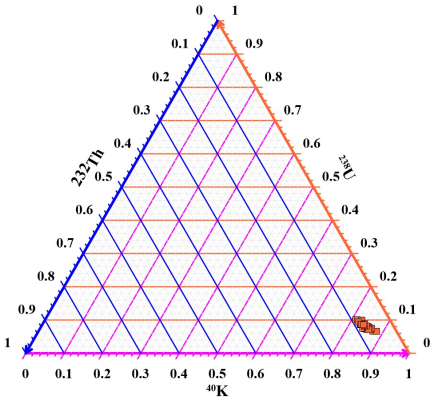

(e) B-H

Figure A.11: Activity Concentration of ^{40}K, ^{238}U and ^{232}Th between Kathmandu and Hetauda